

UNIVERSITÀ DEGLI STUDI DI NAPOLI FEDERICO II



SCUOLA POLITECNICA E DELLE SCIENZE DI BASE

Department of Industrial Engineering

DOCTORAL THESIS

**CFD STUDY OF A DIESEL ENGINE
OPERATING IN DUAL FUEL MODE**

Tutor

Prof. Maria Cristina Cameretti
Prof. Raffaele Tuccillo

Ph.D. Candidate

Roberta De Robbio

Ph.D. School Coordinator

Prof. Michele Grassi

XXXII CYCLE

Index

Introduction	4
Abbreviations	7
Chapter 1 – DUAL FUEL	10
1.1 Diesel Engine.....	10
1.2 Dual Fuel Systems.....	21
1.3 Fuels	24
1.3.1 Diesel oil	24
1.3.2 Natural gas	26
1.4 State of the art.....	27
Chapter 2 – MODELLING.....	39
2.1 Fluid Dynamics	39
2.1.1 Numerical analysis.....	42
2.1.2 Discretization	43
2.1.3 Meshing.....	45
2.1.4 Solution methods.....	47
2.1.5 Errors.....	48
2.2 Turbulence.....	48
2.3 Turbulence models	51
2.4 Combustion models.....	53
2.4.1 Finite rate – Eddy dissipation model	54
2.4.2 Non-premixed combustion models	56
2.4.2.1 Mixture fraction theory	57
2.4.2.2 Laminar flamelet model.....	60
2.4.3 Premixed combustion models	64
2.5 Flame Models: G-equation.....	71
2.6 Liquid Jet Atomisation and Breakup models	73
2.6.1 TAB Model	74
2.6.2 WAVE Model	75
2.6.3 KHRT Model	76
2.7 Combustion features and problems	77
Chapter 3 – PRELIMINARY EXPERIENCE	81
3.1 Micro gas turbine.....	81
3.2 Dual Fuel diesel engines.....	96
Chapter 4 – LIGHT DUTY ENGINE	121
4.1 Methodology.....	121
4.2 One-dimensional Model	122
4.3 Three-dimensional Model	125

4.4 Test Cases	127
4.5 Full Diesel Results.....	129
4.6 Dual Fuel Results	135
Chapter 5 – OPTICALLY ACCESSIBLE ENGINE	147
5.1 Experimental results	147
5.2 Methodology.....	155
5.3 Case study.....	162
5.4 Two-step mechanism results	164
5.5 Li and Williams mechanism results	178
5.5.1 Case RP = 15%	178
5.5.2 Case RP = 22%	182
5.5.3 Comparison RP =10, 15, 22%.....	189
5.5.4 Comparison of Autoignition model vs 2-step model.....	192
5.5.5 Comparison RP = 80% vs RP = 22%	194
Chapter 6 – HEAVY DUTY ENGINE	201
6.1 Experimental Setup	201
6.2 Experimental Results.....	206
6.3 CFD Methodology.....	209
6.4 CFD results.....	215
6.4.1 Medium Load: Li and Williams model.....	215
6.4.2 High Load: Li and Williams model	217
6.4.3 High Load vs Medium load: Li and Williams	219
6.4.4 High Load: Ra and Reitz model.....	220
6.4.5 Li and Williams vs Ra and Reitz model	223
Chapter 7 – DEFINITE IMPROVEMENTS TO THE RESEARCH ENGINE SIMULATION.....	227
7.1 Geometry	227
7.2 Crevices	229
7.3 Autoignition induced flame propagation.....	232
7.4 Results	234
Conclusions	242
Acknowledgments	245
References	246
Appendix	256

Introduction

In the last years climate change has become an emergency that united countries of the world to make agreements to reduce pollutant emissions. the Kyoto Protocol and the Paris Agreement dictated the purposes to limit the global warming, respectively for the periods 2013 – 2020 and up to 2030 [1]. In the European Union the targets were transposed into the Climate and Energy package 2020 that plans the achievement of 20% share of renewables in energy consumption, an improvement of 20% in energy efficiency and a 20% reduction in greenhouse emissions by the 2020 with respect to the 1990. While the targets of the Paris Agreement are defined in the Clean Energy package with an increase of share of renewable energy of 27%, an increase of 27% for the energy efficiency and a 40% reduction of greenhouse emission by 2030 compared again to the levels of 1990.

In this context, the diesel engine, whose combustion is characterised by high emissions of particulate matter and nitric oxides, is likely to disappear from the future automotive market. However, the high performances of this well established engine may still represent a resource in terms of power, efficiency and reliability. In this regard, a possible solution is to readapt the engine to operate in Dual Fuel mode. As the name suggests, by supplying the engine with a second fuel, such as natural gas, it is possible to combine the above mentioned advantages of the diesel engine with the advantages of a gaseous fuel like natural gas, achieving a good compromise between the necessity to guarantee high performances and the necessity to use low carbon fuels with lower impact on the environment.

In order to assess the benefits and limits of this technology, it is necessary a deep investigation of the phenomena that characterise the combustion development that results further complicated, due to the interaction of two

burning fuels. As a matter of fact, they present different features and, above all, they burn in different ways: diesel vapour in a diffusive flame while natural gas in a premixed flame.

To this purpose, Computational Fluid Dynamics is the most powerful tool allowing investigation of the different processes that take place inside the cylinder such as turbulence, fuel atomisation and chemical kinetics. Clearly, major difficulties are encountered in the choice of a combustion model suitable for both fuels. In this regard, kinetics plays a key role in the description of the oxidation process. Much work must be done to implement a reaction scheme that includes both fuels and that allows to predict the interaction of the two fuels.

Based on the outcomes of an activity carried out by some researchers of University of Naples “Federico II”, this thesis aimed at a progressive improvement of the methodology and more detailed kinetic mechanism were utilised to better comprehend the actual combustion mechanism and pollutants formation. Starting from a simplified kinetics scheme for diesel oil and natural gas oxidation, firstly a new mechanism including 9 reactions was introduced for the ignition of methane (considered as the main component of natural gas), in this way it was possible to release from empirical correlations for the ignition of at least one of the two fuels. Finally, this model was compared with a more detailed scheme consisting of 100 species and 432 reactions.

Further criticalities arise from the wide operating range of the engine, especially for automotive applications. To overcome the typical problem related to the computational cost of the CFD based approach, the utilisation of different tools such as a one-dimensional model demonstrated to be helpful for extending the numerical investigations to multiple cases

characterised by either different load levels or changes in the fuel injection settings.

In this framework the experimental activity represented an effective tool for the validation of the numerical outcomes, since experimental data provided important information on the behaviour of three distinct diesel engines, say: a light-duty common rail engine, an optically accessible research engine and a heavy-duty engine. The main point to be highlighted is that the study of three engines with different characteristics allowed a wide investigation on different operating conditions.

Abbreviations

0D	Zero-Dimensional
1D	One-Dimensional
3D	Three-Dimensional
ATDC	After Top Dead Centre
BMEP	Brake Mean Effective Pressure
BTDC	Before Top Dead Centre
CAD	Crank Angle Degrees
CE	Chemical Equilibrium
CFD	Computational Fluid Dynamics
CI	Compression Ignition
CNG	Compressed Natural Gas
DAQ	Data Acquisition
DES	Detached Eddy Simulation
DF	Dual Fuel
DI	Direct Injection
DNS	Direct Numerical Simulation
DOC	Diesel Oxidation Catalyst
DPF	Diesel Particulate Filter
ECU	Electronic Control Unit

EDC	Eddy Dissipation Concept
EGR	Exhaust Gas Recirculation
EOI	End of Injection
EVO	Exhaust Valve Opening
FBR	Fuel Burning Rate
FD	Full Diesel
FRED	Finite Rate – Eddy Dissipation
HCCI	Homogeneous Charge Compression Ignition
HD	Heavy Duty
HRR	Heat Release Rate
IDI	Indirect Injection
IMEP	Indicated Mean Effective Pressure
IVC	Intake Valve Closing
KHRT	Kelvin-Helmholtz and Rayleigh-Taylor
LES	Large Eddy Simulation
LHV	Low Heating Value
LTC	Low Temperature Combustion
MGT	Micro Gas Turbine
NG	Natural Gas
PCCI	Premixed Charge Compression Ignition
PDF	Probability Density Function

PFI	Port Fuel Injection
PID	Proportional Integral Derivative
PM	Particulate Matter
PN	Particulate Number
PPC	Partially Premixed Combustion
PRF	Primary Reference Fuel
RANS	Reynolds Averaged Navier-Stokes
RCCI	Reactivity Controlled Compression Ignition
RNG	Renormalization Group
RP	Premixed Ratio
RSM	Reynolds Stress Model
SCR	Selective Catalytic Reduction
SI	Spark Ignition
SLF	Steady Laminar Flamelet
SOC	Start of Combustion
SOI	Start of Injection
SOP	Start of Pilot
TDC	Top Dead Centre
THC	Total Unburned Hydrocarbons
UHC	Unburned Hydrocarbons
VVA	Variable Valve Actuation

Chapter 1

DUAL FUEL

In this section, a summary of the main characteristics of the Diesel engine and its evolution in the years is illustrated, explaining the motivations and the advantages that could lead the introduction of the Dual Fuel system in the current European automotive scenario.

1.1 Diesel Engine

The invention of the Diesel engine is dated back to 1892 when Rudolf Diesel published an essay describing a thermodynamic cycle where combustion occurred with an isothermal compression [2]. The idea was to introduce the finely atomised fuel into air taken at a temperature above the igniting-point of the fuel, which ignites on introduction. In order to exceed the temperature of combustion, air must be tightly compressed. However, the compression required must be at a level that an engine operating following this cycle could never perform any usable work. Then in 1893 Diesel adopted the constant pressure cycle. In his 1895 patent application it is simply stated that compression must be sufficient to trigger ignition. Also, the degree of compression is lower than that needed for isothermal ignition.

With the efforts of Diesel and the resources of M.A.N. in Augsburg combined, after five years (1897) a practical engine was finally developed [3]. His concept permitted a doubling of efficiency due to much greater expansion ratios without detonation or knock. The first diesel engine was a four-stroke single-cylinder engine with a bore and stroke respectively of 250 mm and 400 mm, with a final compression of 32 bar, rated 14 kW at 150 rpm with a specific fuel consumption of 324 g/kWh resulting in an effective

efficiency of 26.2% [4]. Since then, engine developments have continued to contribute to the steadily widening internal combustion engines markets.

The Diesel engine presents some advantages with respect to the Otto engine; the most important are reported below [5]:

1. Higher overall efficiency, to allow the self-ignition of diesel oil, the diesel engine usually operates with lean air/fuel ratio of 18 to 70 (or $F/A=0.014$ to 0.056) and with compression ratios doubled (12 to 24) compared to the Otto engine ones (8 to 12).
2. Higher flexibility, the efficiency decreases slower when the load decreases, indeed the load level is controlled by the air/fuel ratio, so when it is necessary to reduce the power produced it is possible to simply reduce the amount of fuel injected in the cylinder without pressure drops due to the throttle valve. Also, the pumping work requirements are low.
3. Use of low value fuels, their production in refinery requires lower energy consumption. This aspect combined with the previous one allows a more efficient and cost-effective management of the engine.

On the other hand, the diesel engine presents a higher weight-power ratio. The higher compression ratios and consequently the higher pressure reached, highlighted in point 1, demands to the various components to be stronger and more rigid to withstand the mechanical and thermal stresses. These stresses are represented by the noise and vibrations caused by the harshness of combustion which develops in this kind of engine. Indeed, in this engine, combustion is not characterised by the propagation of a flame front through the combustion chamber but, as already stated, by the auto-ignition of a fuel, that after a small ignition delay burns rapidly. Moreover, the use of heavier materials, not only increases the weight of the engine but also, enhances the inertia of the moving components preventing them to reach high engine

speeds, thus lower power is obtained, and this contributes to further reduce the weight-power ratio.

It follows that the diesel engine is more suitable for medium-high power applications where the weight and the size are secondary to operating costs, such as on road industrial transports, agricultural vehicles, earth moving machines, rail and marine propulsion, as well as fixed installations for electrical power generation. However, the previously mentioned operating flexibility at different load levels allowed the adoption of diesel engines also for applications at lower power such as heavy-duty diesel engines which generally include lorries and buses and passenger cars which usually operate at partial load.

Therefore, the diesel engine has an extremely wide range of utilisation and it can be used both in a 2-stroke and 4-stroke cycles. Of course, depending on the application and the power needed a certain configuration is preferred. Usually large size engines operate on the 2-stroke cycle in contrast to the small- and medium-size diesels.

As reported in Table 1.1, the different types of engines can be categorised on the base of their size; as already stated dimensions and thus weight of the engine influence every other characteristic or operating condition, so it results that a large size engine produces high power but performs at low speed. In this regard, the compression-ignition combustion is an unsteady, heterogeneous, three-dimensional process and the details of this process depend on the characteristics of many factors such as the fuel, the injection-system and design of the combustion chamber. All these factors influence and manage combustion development; a correct combination of them can promote an efficient combustion (complete oxidation and low emissions) in the entire operating range.

Tab. 1.1: Characteristics of common diesel engines [3, 4].

Size	Large	Medium	Small
Cycle	2-stroke	4-stroke	4-stroke
Bore [mm]	150 – 1,000	200 – 650	60 – 120
Stroke/Bore	1.2 – 3.5	0.9 – 1.3	0.9 – 1.1
Max speed [rpm]	60 – 120	300 – 800	1,000 – 5,000
Compression ratio	12 – 15	15 – 22	22 – 24
Power [kW]	5,000 per cylinder	150 – 20,000	5 – 400
Injection pressure	Very high	Medium	High/Low
Chamber	Quiescent	Bowl-in-piston	Deep bowl-in-piston/ Pre-chamber

Firstly, the injection timing is used to control combustion timing. Actually, before the fuel starts to burn a delay period occurs, it is necessary to keep this delay short to hold the maximum cylinder gas pressure below the maximum the engine can tolerate. The measure of the ease of ignition of a specific fuel is indicated by its cetane number which must be above a certain value in a typical diesel environment.

Secondly, the injection pressure level must be properly chosen with the aim to provide a sufficient velocity to the fuel jet, so that it is efficiently atomised, that it can cross the combustion chamber in the time available and that it can fully utilise the air charge. When the necessary injection pressure cannot be achieved due to technological limits or to high costs of the injection system, in order to meet the requirements of an efficient combustion, the lack of sufficient pressure can be compensated by a right design of the combustion chamber shape, able to generate a certain level of air motion which promotes

a good vaporisation and mixing of the charge. In fact, the major problem is to achieve sufficiently rapid mixing between the injected fuel and the air in the appropriate crank angle interval close to the top dead centre but this crank angle interval varies with the engine speed and then with the engine size. For this reason, as reported in Table 1.1 the largest size engines usually present a quiescent combustion chamber (Figure 1.1.a), which means that the chamber is not designed with the particular aim to generate high turbulence, but the injection pressure must increase to allow the fuel to reach every part of the chamber due to the increased dimensions of the cylinder.

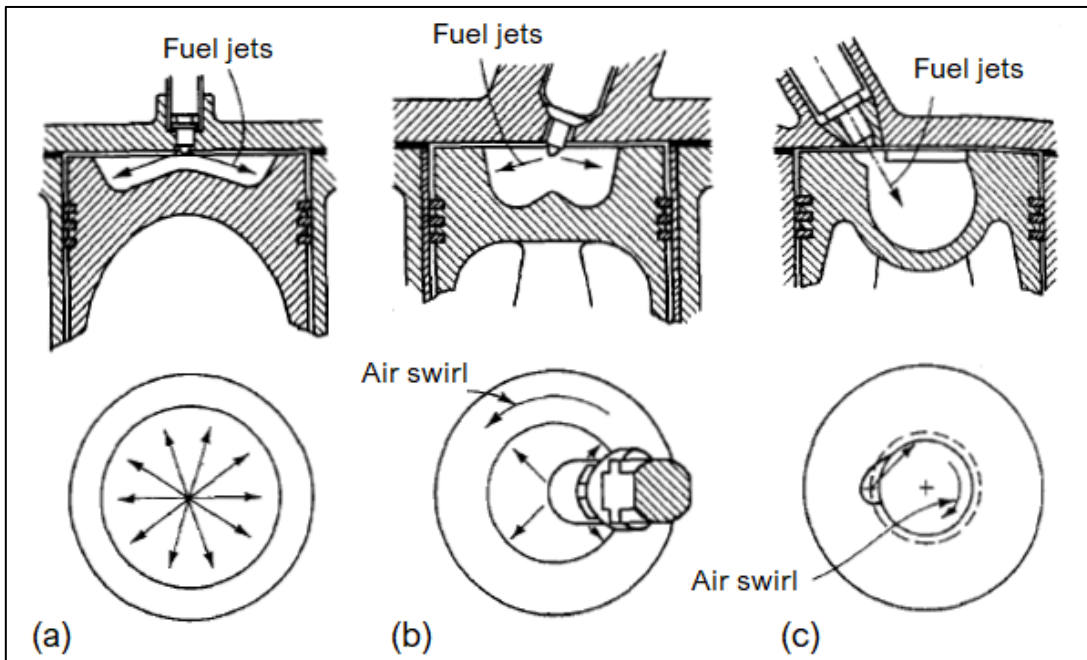


Fig. 1.1: Diesel engine combustion chamber, (a) quiescent chamber, (b) and (c) bowl-in-piston chamber [3].

On the other side, as engine size decreases, less fuel jet penetration is necessary while more vigorous air motion is necessary, and it can be obtained with the aid of more complex geometry of the combustion chamber (Figures 1.1.b and c). Also, swirl motion can be enhanced by enhancing the compression ratio, which has higher values for small size engines (Table 1.1).

Over the years, different changes have been made to improve the diesel engine performances in efficiency, power, and degree of emission control. In 1905 the first turbochargers are manufactured by Büchi. Turbocharging and supercharging consist in compress the inlet air with the use of an exhaust-driven-turbine-compressor combination and a mechanically driven pump respectively. Turbocharging and supercharging increase the air mass flow per unit displaced volume, then more fuel can be injected and burned, and more power can be delivered while avoiding excessive black smoke in the exhaust. The brake mean effective pressure (BMEP) can increase from 700 – 900 kPa to 1,000 – 1,200 kPa. These methods are mainly used in larger engine, to reduce engine size and weight for a given power output, so to reduce the weight to power ratio. In this way, for the same dimensions the 2-stroke cycle is competitive with the 4-stroke one because only air is lost in the cylinder scavenging process.

An important change is the indirect injection (IDI), introduced in the 1909 on engines that need a vigorous charge motion, such as small high-speed ones used in automobiles; it is the division of the combustion chamber into two parts: the main chamber and the auxiliary pre-chamber. During the compression stroke air is forced to enter in the auxiliary chamber from the main one above the piston through a set of orifices, the connecting passage between the two chamber is properly shaped so that the flow gains high turbulence within the auxiliary chamber. Usually, fuel is injected into the pre-chamber so the pressure of the injector can be lower than the one required by direct injection systems (DI). In the pre-chamber combustion starts and the consequent pressure rise forces the fluid to mix back with the air into the main chamber.

The evolution of diesel engine is closely linked to the development of the injection system with the assistance of electronical devices which ensure a better control on pressure, timing and quantity of fuel. The basic

configuration consists of an injection pump, delivery pipes and fuel injector nozzles. The earlier injection pumps were crankshaft driven via a series of gears and chains.

In the Unit injector the injector nozzle and the high-pressure injection pump are combined in a compact assembly installed directly in the cylinder head. An individual pump is assigned to each cylinder where an electric valve ensures an accurate timing of injection. This configuration eliminates the need for high-pressure pipes and their associated failures but at the same time allows much higher injection pressure (up to 2,200 bar) then, ideal combination of air-fuel mixture, high efficiency, low consumption and emissions against high power.

Nowadays the better performances are attained by the utilisation of the common-rail injection system (Figure 1.2) where fuel at high pressure (up to 2,500 bar) is stored in a distribution pipe (rail) common to all injectors. The first prototype was implemented on a low-speed 2-stroke crosshead engine in the 1979 but the first mass-produced common rail diesel engine for passenger car is dated 1997 (Fiat 1.9 JTD). The purpose of the pressure pump is to maintain a target pressure in the rail which is constant and not affected by fluctuations caused by the nozzle opening. Injection is controlled by solenoid or piezoelectric valves, governed by an electronic control unit (ECU), due to their precision they make possible fine electronic control over timing and fuel quantity and allow pressure to maintain a constant value from the start till the end of the injection, equal to the pressure in the rail. This permits to provide an efficient atomisation of the fuel and then a decreasing of emissions. Moreover, advanced common-rail systems can perform multiple injections per stroke. By injecting a small amount of fuel before the real injection it is possible to reduce the explosiveness of compressed ignition combustion, so to reduce vibrations and noise.

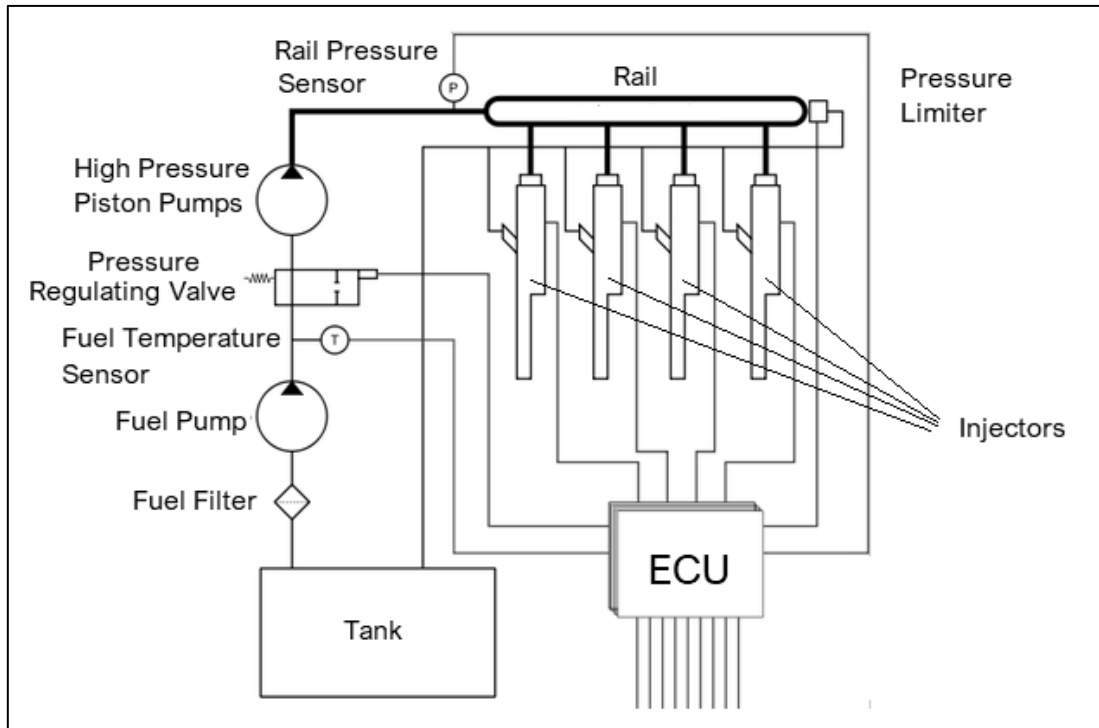


Fig. 1.2: Common rail injection system scheme [6].

In the latest decades the main improvements made on the diesel engine include technologies and devices that aim to reduce emissions, by operating an after-treatment of the exhaust gases. They can also be used as silencers to reduce noise. The first device, introduced in 1980 on non-road machines and in 1985 on automobiles [7], is the Diesel Particulate Filter (DPF). The oxidation of CO and unburned hydrocarbon can be achieved with the utilisation of the Diesel Oxidation Catalyst (DOC). For the reduction of NO_x emissions the Lean NO_x trap was introduced in 2008 on passenger cars with the VW 2.0 TDI engine by Volkswagen, and, in 2006 Daimler-Chrysler launched the first series-production passenger car engine with the Selective Catalytic Reduction (SCR) exhaust gas after-treatment, the Mercedes-Benz OM 642. The development of these devices is extremely important since greater attention must be put on the pollutants problem. In this regard, the European Union established the acceptable limits for exhaust emissions of new vehicles sold in the member states. These limitations, as reported in Tables 1.2 to 1.4 for the different categories of diesel engines, due to the

escalating greenhouse gas and pollutants emergency of the recent years, are becoming constantly more stringent. Compliance is determined by running the engine at a standardized test cycle. It is worth-noting that starting from 2009 (directive Euro V) also the number of particles of soot has been regulated.

Tab. 1.2: UE emission standards for light commercial vehicles with a reference mass ≤ 1305 kg (in g/km and particles/km for PN) [8].

Engine	Pollutant	Euro 1 (1992)	Euro 2 (1996)	Euro 3 (2000)	Euro 4 (2005)	Euro 5 (2009)	Euro 6 (2014)
Diesel Engine	CO	2.72	1.00	0.64	0.50	0.50	0.50
	HC	-	-	-	-	-	-
	NO _x	-	-	0.50	0.25	0.18	0.08
	HC + NO _x	0.97	0.70	0.56	0.30	0.23	0.17
	PM	0.14	0.08	0.05	0.025	0.005	0.0045
	PN	-	-	-	-	6.0 e11	6.0 e11

Tab. 1.3: UE emission standards for light commercial vehicles with a reference mass ≥ 1305 kg and ≤ 3500 kg (in g/km and particles/km for PN) [8].

Engine	Pollutant	Euro 1 (1994)	Euro 2 (1999)	Euro 3 (2002)	Euro 4 (2006)	Euro 5 (2012)	Euro 6 (2016)
Diesel Engine	CO	6.9	1.5	0.95	0.74	0.74	0.74
	HC	-	-	-	-	-	-
	NO _x	-	-	0.78	0.39	0.28	0.125
	HC + NO _x	1.7	1.2	0.86	0.46	0.35	0.215
	PM	0.25	0.17	0.10	0.06	0.005	0.0045
	PN	-	-	-	-	6.0 e11	6.0 e11

Tab. 1.4: UE emission standards for heavy duty diesel engines (in g/km, ppm for NH₃, particles/km for PN and m⁻¹ for Smoke) [8].

Engine	Pollutant	Euro 1 (1992)	Euro 2 (1995)	Euro 3 (2000)	Euro 4 (2005)	Euro 5 (2008)	Euro 6 (2012)
Diesel Engine	CO	4.5	4.0	2.1	1.5	1.5	1.5
	HC	1.1	1.1	0.66	0.46	0.46	0.13
	NO _x	8.0	7.0	5.0	3.5	2.0	0.4
	NH ₃	-	-	-	-	-	10
	PM	0.612	0.25	0.10	0.02	0.02	0.01
	PN	-	-	-	-	-	8.0 e11
	Smoke	-	-	0.8	0.5	0.5	-

The main issue that researchers are facing is to reduce emissions without affecting engine performances and driving expectations. Even though a lot of options are available, not always it is possible to achieve this target. Unfortunately, the costs related to the management of these technologies result burdensome in terms of potential emission reduction effectively obtained with an evident drop of performances. Indeed, a study of the latest diesel cars by the International Council for Clean Transportation (ICCT) reported that the nitric oxides emissions produced by diesel cars are, on average, seven times higher than safety limits allow [9]. In addition, it is important to mention the scandal that hit the automotive sector in 2015, where some car manufactures programmed software to recognise when the standardised emission test was being done and manipulated the engine to emit less during the test [10]. All these factors led to a significant impact on market penetration. While in United States diesel engines have never spread, due to cheap cost of gasoline and the great focus of automakers on hybrid and electric vehicles [9], in Europe the latest data registered an increase of 3% for

sales of new passenger cars and for the first year, petrol cars became the most sold vehicles constituting almost 53% against the 45% for diesel cars [11], that have undergone an overall reduction of sales as illustrated in Figure 1.3.

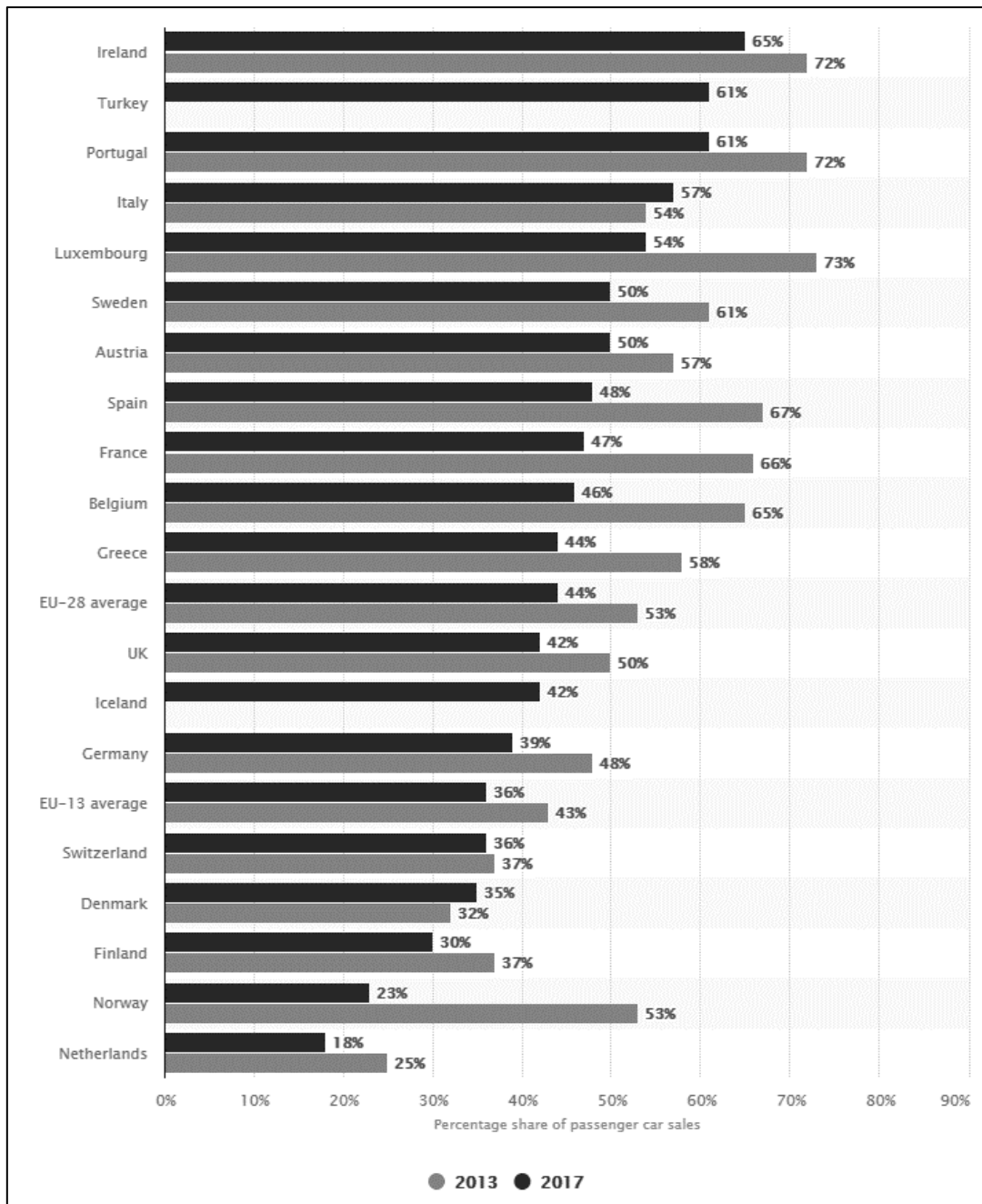


Fig. 1.3: Statistics of sales share of diesel engines in European Union [12].

Moreover, many countries are planning to ban fossil fuel cars, by prohibiting the sale of all petrol and diesel vehicles in the next decades [13].

Despite of all these issues a great part of cars in Europe are still sold and equipped with Diesel engines so they will not disappear soon from the transport scenario. Also, after over a century of development, new strategies have still a little potential for further improvements. In particular, low temperature combustion (LTC) strategies such as Homogeneous Charge Compression Ignition (HCCI), Premixed Charge Compression Ignition (PCCI) and Reactivity Controlled Compression Ignition (RCCI) produce near zero oxides of nitrogen and particulate matter emissions since in all the LTC strategies the fuel-air mixture is premixed and they exhibit a characteristic low temperature heat release followed by main heat release without any diffusion phase combustion [14]. Furthermore, much work is being done on the use of alternative fuels like biodiesel (vegetable oils), synthetic diesel made from shale oil and coal, or fuels used as diesel supplement fractions such as natural gas, methanol and ethanol (methyl and ethyl alcohols).

1.2 Dual Fuel Systems

In this context, the introduction of a Dual Fuel (DF) system represents a possible solution to some typical problems that are still unsolved for the conventional diesel engines, with particular reference to its environmental impact. Indeed, Dual Fuel system results from the need to readapt a well-established technology like internal combustion engine, in a period characterised by new requirements of emission dictated by more and more stringent regulations. In addition, the depletion and the consequent rising cost of petroleum pushed the scientific research in the direction of more eco-friendly and available fuels. Also, the main challenge is to keep the same performances (efficiency, durability, reliability and specific power output) of a standard engine. Actually, it is important to highlight that both compression and spark ignition engines can operate in Dual Fuel mode with different configurations depending on the fuels used and their way of introduction inside the cylinder (DI or IDI).

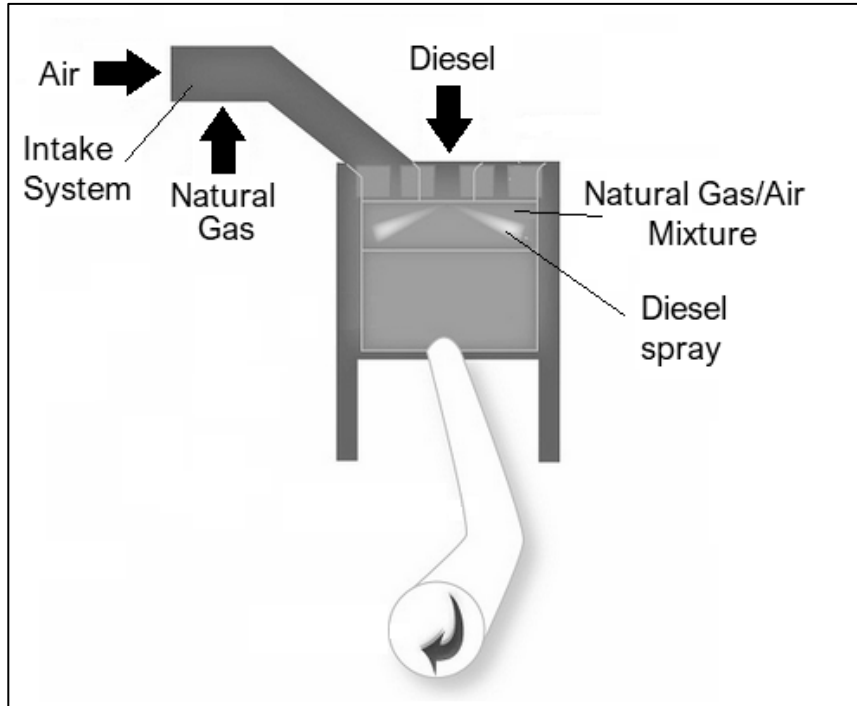


Fig. 1.4: Dual Fuel scheme [15].

However, in this thesis, a diesel engine supplied with natural gas (NG) as primary fuel is studied while other solutions are illustrated in section 1.4. In particular, as shown in Figure 1.4, natural gas is premixed with air inside the intake manifold, then at the end of compression stroke a little amount of diesel oil is injected to ignite the mixture causing multiple flame fronts that propagate through the combustion chamber. In this sense, the Dual Fuel technology could be considered as a particular application of PCCI concept, above mentioned.

In this case, only slight modifications can be implemented on existing engines, a high level of thermal efficiency can be still ensured, since NG, thanks to its high resistance to knock, can easily withstand the typical high compression ratio of this kind of engine.

Also, natural gas represents a good solution to all the problem previously described: it is available worldwide, it is expected to remain less expensive than gasoline and its use leads to different benefits in terms of emissions.

Indeed, its combustion is relatively clean since it is a mixture of different species whose major component is methane (almost 95% of mass fraction), that has the lowest carbon/hydrogen ratio among hydrocarbons, thus for the same amount of burned fuel less CO₂ is produced.

Moreover, as it is known, there are three mechanisms of NO_x formation: thermal, prompt and fuel. In engines, NO_x are mainly produced by the thermal mechanism. In Dual Fuel, being NG port fuel injected, a lean premixed charge is formed, and lower temperatures are achieved because combustion occurs at an equivalent ratio far from stoichiometric value ($\phi \ll 1$), as shown in Figure 1.5.

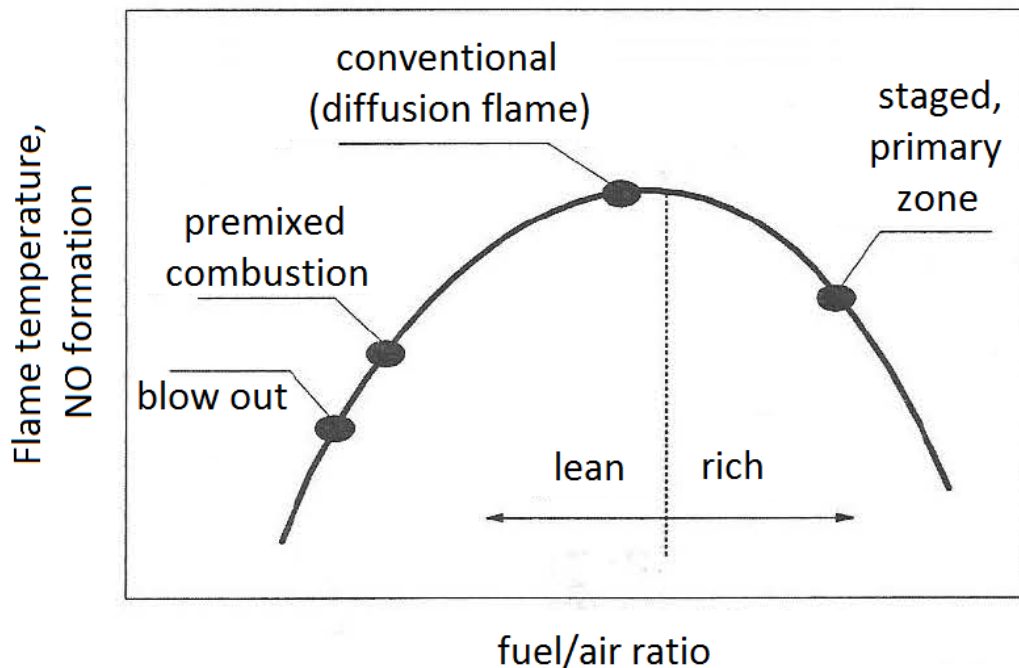


Fig. 1.5: Equivalence ratio – Flame temperature [16].

In the last years, great attention has been paid on the effect of particulate matter, especially in the cities, where, often, a stop of traffic is imposed to cars equipped with diesel engines. Also, in this regard Dual Fuel technology can represent a viable solution since only the reduced amount of diesel oil necessary to ignite the mixture, is injected to start the combustion of the main fuel that is a gas, and then, does not produce PM at the exhaust. Usually

Selective Catalytic Reduction and Diesel Particulate Filter are used to reduce PM and NO_x but these methods are based on the use of precious and expensive metals, while in this case, by only increasing NG energy contribution, it is possible to obtain the same effect.

On the other hand, the main drawback of DF combustion is the high level of carbon monoxide and unburned hydrocarbons emitted in the exhaust. As a matter of fact, the NG/air mixture is lean and it becomes leaner with the load decrease, it can happen that equivalence ratio falls outside the flammability limits so to prevent the achievement of an efficient flame propagation, especially at part load. This could imply a performances' decrease with respect to the original configuration.

In this sense, an appropriate optimization of the engine operating parameters is needed, by deepening the complex combustion phenomenon of two fuels.

1.3 Fuels

As already stated, one of the characteristics of a certain Dual Fuel configuration is the couple of fuels used. Of course, different combinations provide different results in terms of performances, emissions and above all different combustion developments. In the next paragraphs, the features of the main fuels utilised for the DF technology are illustrated.

1.3.1 Diesel oil

In order to ensure a correct start of combustion (SOC) in diesel engines, the fuel must present suited characteristics of atomisation, vaporisation and autoignition. The most common type of diesel oil derives from the distillation of petroleum, but it is important to highlight that other sources such as biomass, animal fat and coal liquefaction are increasingly being exploited. Petrodiesel (or fossil diesel) is composed of about 75% saturated hydrocarbons (paraffins including n-, iso- and cycloparaffins), and 25%

aromatic hydrocarbons (naphthalenes and alkylbenzenes). The average chemical formula ranges from $C_{10}H_{20}$ to $C_{15}H_{28}$ [17].

Tab. 1.5: Diesel oil and Gasoline properties [4, 17].

Fuel	Diesel oil	Gasoline
Distillation range [°C]	200 – 350	30 – 200
Carbon atoms per molecule	9 to 25	4 to 11
LHV [MJ/kg]	43.1	43.2
Density @ 15 °C [kg/m ³]	840	720
Volumetric energy density [MJ/l]	35.86	32.18
Viscosity [cSt]	2.0 – 5.35	0.37 – 0.44
Flash Point [°C]	52 – 96	< 21
CO ₂ emission [g/MJ]	73.25	73.38

In Table 1.3 the characteristics of diesel oil and gasoline are reported. Gasoline includes hydrocarbons of the lighter fraction of the petroleum distillation. Indeed, the temperature range is lower and less carbon atoms per molecule are contained. Components at higher boiling point, burn less easily, this is the reason why diesel engines typically produce smoke at the exhaust. The Lower Heating Value (LHV) is almost the same, but the higher diesel density implies a higher volumetric energy density and consequently a lower fuel consumption. Also, a high fuel viscosity prevents the correct flow inside the injection system and a good level of atomisation which influence all the jet formation and distribution process. Both fuels should have low sulphur content in order to avoid corrosion due to the formation of sulphuric acid.

In diesel engine the main issue is the fuel autoignition. It defines the start and development of combustion and consequently the performance and emission output. In order to achieve a good control on these parameters it is necessary to have a short ignition delay when sprayed into hot compressed air. The ignition delay is caused by physical and chemical factors. Physical delay is

due to the actual time necessary for two parcels (fuel and oxidiser) to meet and react. The chemical delay is a property of the fuel and depends on the readiness to the self-ignition and it is measured by the cetane number. A higher cetane number indicates a short ignition delay. European (EN 590 standard) road diesel has a minimum cetane number of 51 [17]. However, the cetane number for standard diesel ranges between 47 and 60 [4].

1.3.2 Natural gas

Natural Gas is a gas mixture consisting primarily of hydrocarbons (alkanes) such as methane, ethane, propane, butane and pentanes. It may present, also, little amount of hydrogen sulphide, carbon dioxide, water vapor and sometimes helium and nitrogen [18]. In Table 1.4 a typical composition of Natural is reported.

Tab. 1.6: Typical composition of Natural Gas [19].

Component	Formula	Volume [%]
Methane	CH ₄	> 85
Ethane	C ₂ H ₆	3 – 8
Propane	C ₃ H ₈	1 – 2
Butane	C ₄ H ₁₀	< 1
Pentane	C ₅ H ₁₂	< 1
Carbon dioxide	CO ₂	1 – 2
Hydrogen sulphide	H ₂ S	< 1
Nitrogen	N ₂	1 – 5
Helium	He	< 0.5

As it is possible to notice, the main constituent of NG is methane, for this reason, usually, it is possible to consider only this component to describe the properties of the whole mixture and use the two terms indifferently. Methane is widely used in residential, commercial and industrial heating, industrial

feedstock, power generation and vehicle transportation. In this last field, the use of a gaseous fuel can bring significant advantages since it can easily mix with air to form a homogeneous charge. In this way the adiabatic flame temperature reaches lower value with important benefits in terms of NO_x emissions. Also, methane is characterised by a high resistance to knock (octane number of 120 – 130) that allows its utilisation in engines with high compression ratio such as diesel engine in Dual Fuel mode. In this regard, the interest on the utilisation of this fuel is given by the high stability of the molecule structure that prevents the autoignition of the fuel before the pilot injection. Gasoline and diesel vehicle can be easily converted to run on natural gas with slight modifications to the original engine. However, an engine properly designed to operate with this specific fuel can provide better performance outputs. Methane has a Lower Heating Value of 49,8 MJ/kg, higher than both gasoline and diesel oil (Table 1.2) and the highest stoichiometric ratio among the hydrocarbons ($\alpha_{st} = 17.24$). On the other hand, the introduction of a gaseous fuel reduces the maximum engine power achievable with respect to the same engine supplied with gasoline (10%), since it reduces the filling coefficient. Moreover, the gaseous nature of this fuel penalises the storage and transportation by vehicle. Indeed, critical temperature of methane is -83 °C, then tanks suitable to withstand pressures of 200 – 250 bar, are required, with a quadruple enhancement of size [4].

1.4 State of the art

In the last years several researchers have been interested into the Dual Fuel technology, analysing the behaviour of the combustion in different operating conditions, and also studying different configurations and solutions in order to overcome the limits that affect its operation. In particular, the development of models and correlations between the fuel properties, operating parameters and emissions can be beneficial for the optimization of the process. The models used for the simulations include 0D, 1D, multi-zone and 3D

approaches. The 0D and 1D models are mainly used for the prediction of performances and emissions based on empirical models [20, 21] and they can be useful to provide the boundary conditions for the multidimensional simulations or even experiments [22]. However, a good description of the phenomena and prediction of emissions is achieved by models that study in detail the evolution of the combustion throughout the cylinder. Although, multi-zone models have shown reasonable results [23], it is clear that the best information can be retrieved from 3D CFD [24]. In literature computational fluid dynamics is widely exploited in combination with experimental activities for the investigation of the Dual Fuel combustion. Indeed, Akbarian et al. [25] compared emissions and performances in full diesel and dual fuel mode. After finishing the experimental tests in full diesel mode, the engine was converted with few modifications to dual mode. The experimental tests were carried out under different loads (10, 25, 50, 75, and 100%) and different pilot to gaseous fuel ratios (30, 40 and 50%). Results showed that at constant engine speed, dual fuel mode has lower CO₂, NO_x and PM under all load conditions and port gaseous fuel ratio when compared to full diesel mode. At full load, the dual fuel engine has relatively lower CO emission and higher HC emission while the specific energy consumption is similar to that for the diesel engine. The CFD simulations were performed on a mesh that does not present valves and allows only closed cycles. 13 species are included in the 10 kinetic reactions and 6 equilibrium equation were employed. Numerical results showed good agreement with the experimental ones. Finally, the authors suggested a pilot fuel ratio of 30% in full load and to raise it to 50% in half load operation.

Huang et al. [26] studied the effects of multiple injection on the combustion at low load condition in order to improve the thermal efficiency and reduce emissions. Results showed that, when the first diesel injection timing is advanced, the indicated thermal efficiency and nitrogen oxide emissions

increase first and then decrease, while the maximum pressure rise rate, carbon monoxide and methane emissions reduce initially and then increase, attaining a relatively high indicated thermal efficiency. Indeed, the proportion of premixed combustion of the first injected diesel and the duration of flame propagation of natural gas has considerable influence on methane emissions. The kinetic mechanism involves 45 components and 142 reactions where diesel and natural gas are, respectively represented by n-heptane and methane. The computation efforts were reduced thanks to the symmetry of the combustion chamber, since the injector has eight equally spaced nozzle orifices, a 45° sector mesh was generated to simulate one spray plume. In their research Shu et al. [27] demonstrated that the peak cylinder pressure increases as the spray angle increases from 60° to 140°, but it slightly decreases by the further increase of the spray angle to 160°. Generally, combustion duration decreases with the spray angle. Also, the NO_x emissions ascend when spray angle increases. On the other hand, the unburned methane is almost unchangeable while the CO emissions keep at lower level for all spray angles. The Reynolds Averaged Navier-Stokes (RANS) approach was used for the turbulence modelling and a modified rapid distortion renormalization group (RNG) k-ε turbulence model. The SAGE model was used to simulate the combustion process of the NG-diesel dual fuel engine, the chemical kinetics mechanism of which consists of 76 species and 464 reactions. The Kelvin-Helmholtz and Rayleigh-Taylor (KHRT) model was chosen to simulate the break-up of diesel fuel. Once again, since eight nozzle holes are distributed symmetrically, the cylinder model was simplified as a 45° fan-shaped area where the single fuel spray is located in the centre. In [28] the authors implemented a new simulation model with the aim to understand the mechanisms behind soot formation in diesel-CNG combustion. The soot evolution was investigated under different natural gas substitution ratios with single and split fuel injection and integrated with a reduced heptane/methane polycyclic aromatic hydrocarbons mechanism.

They affirmed that, as the CNG substitution ratio increases the equivalence ratio distribution becomes more homogenous and the ignition delay gets extended while the combustion duration gets shorter both with single and split injection. A slight increase of pressure is observed when the split injection is used. Indeed, split injection changes fuel distribution and vaporisation. Consequently, the prolonged ignition delay in higher CNG substitution ratios provides more time to fuel and air for the mixing, which reduces drastically soot mass formation. Papagiannakis et al. [29] studied the effects of different air oxygen enrichment degree (addition of oxygen in the intake air) on dual fuel combustion. In particular, it can accelerate the burning rate and reduce the ignition delay, in this way the specific energy consumption and CO emissions decrease too, without impairing the soot and NO emissions. Ghazal et al. [30] proposed to use a turbocharger to enhance fuel saving. Since methane has high octane number, it can well withstand the high compression ratios of the diesel engines. However, to avoid knock occurrence Sremec et al. [31] suggested not exceeding a compression ratio of 16 for turbocharged intake condition but this limit rises to 18 for ambient intake condition.

As already mentioned, NG can be directly introduced in the combustion chamber. In [32] the authors analysed direct and indirect CNG injection methods influence on combustion process and heat transfer. Direct injection provides advantages in terms of thermal efficiency and a higher degree of fuel consumption while through indirect injection a homogeneous mixture is produced in the combustion chamber and a reduction of soot formation is obtained, especially in poor combustion areas. Moreover, they affirmed that a proper direct injection can be more efficient than indirect injection in terms of engine economy (higher cycle efficiency) and can reduce emissions of harmful substances. Indeed, as demonstrated by Zoldak et al. [33] direct injection of natural gas creates a stratification of this fuel portion and avoids

excessive premixing, which tempers the rate of pressure rate. They studied several azimuthal angles between NG and diesel fuel nozzles, diesel pilot injection timing and quantity splits. The results indicated that the direct injection of natural gas can successfully control the rate of pressure rise while improving the NO_x, HC and soot emissions to meet the targets for engines equipped with modern aftertreatment systems. Also, the optimization of the piston bowl geometry is required to ensure a good combustion efficiency. The direct injection of NG needs the design and the testing of new injectors. In this regard paper [34] presented the tests results of the prototype design of hydraulically assisted injector that is designed for gas supply into diesel engines.

Stettler et al. [35] evaluated the emissions reduction obtained with the oxidation catalyst. They compared energy consumption, greenhouse gas and noxious emissions for five after-market dual fuel configurations of two heavy goods vehicles were compared relative to their full diesel baseline values over transient and steady state testing. Over a transient cycle, CO₂ emissions are reduced by up 9% while methane emissions due to incomplete combustion are 50 – 127% higher; results showed that the oxidation catalyst can reduce emissions by at most 15%.

Since the presence of the gaseous fuel affects considerably the features and the development of the combustion, one of the main goals of research is the modelling of the interaction between the two fuels. Mousavi et al. [36] investigated and compared some important combustion's characteristics at part load and full load. Ignition delay and combustion duration time at part load are longer due to insufficient methane concentration which could not be burned completed because of lower combustion speed. A significant amount of the unburned methane usually remains in the most remote areas from diesel fuel injector such as the piston bowl. The slow progress of combustion process at part load, leads the heat release to be drawn more toward the

expansion stroke which causes incomplete combustion, and consequently high amounts of UHC and CO are emitted. Also, at part load, low temperature gas surrounds diesel spray and interferes with a rapid liquid droplet evaporation. The KIVA-3V was used to simulate the closed part of the cycle with tetradecane ($C_{14}H_{30}$) and methane (CH_4) as representatives of diesel and natural gas fuels, respectively. A mechanism consisting of three reactions describes the combustion, one for diesel vapour and two for the methane. Also, six equilibrium reactions and the extended Zel'dovich NO formation complete the chemical model. Finally, they suggested increasing the amount of diesel fuel, with the assumption of constant input energy, to overcome the part load disadvantages, since diffusion flame penetration is increased. Hence, very lean methane/air mixture could be ignited suitably and propagated quickly due to size enlargement of diesel combustion region. Talekar et al. [37] affirmed that traces of gaseous fuel can affect ignition delay, temperature of auto-ignition process, duration of first-stage ignition and laminar burning velocity. This influence is dependent on the diesel substitution ratio, as this ratio increases beyond 95%, authors have found that traditional auto ignition models, which are created for diesel-like fuels, do not predict major combustion phases. Below this threshold value the first stage of dual fuel combustion, which is the auto-ignition, is assumed not affected by the presence of another fuel species and standard models can be applied without any change. Indeed, the main focus of their simulation is the creation of a unified modelling approach for Dual Fuel combustion. The G-equation flame propagation model and LES turbulent model are used combined with a detailed chemistry: the LLNL of n-heptane and the GRIMECH 3.0 for methane oxidation. The intermediate chemical mechanism obtained consists of 181 species and 1,714 reactions, which is still computationally expensive to run 3D combustion simulations, hence a further reduction was obtained by considering only the strongest reaction paths, this is the path flux analysis (PFA). Their new overall combustion model proved

to effectively predict most extreme dual fuel combustion mode including three major intertwined processes of slow kernel development, flame propagation and end-gas ignition. In this way substitution up to 98-99% can be achieved. Barro et al. [38] focused on the evaluation of the phases in which the combustion is split: the auto-ignition phase and the premixed flame propagation phase. The distribution of fuel burnt in the auto-ignition phase and in the premixed flame propagation is provided by the trapped natural gas within the spray volume. In order to investigate the effects of the dilution heat capacity and fuel chemistry impact during the ignition delay period of the NG-diesel dual fuel engine on dual fuel engine ignition process, Li et al. [39] replaced methane with two artificial species representing the unique features of methane: one for the examination of diluting impact due to decreased O₂ concentration and the other for the evaluation of the heat capacity impact. Also, the contributions of the key radicals such as OH, HO₂ and H to chemical reactions are analysed. The addition of NG retards the start of combustion and elongates the ignition delay at low and medium load conditions. It was believed that the elongated ignition delay was due only to the displacement of a portion of intake air by NG, which decreases the concentration of O₂ in cylinder. Nevertheless, the introduction of CH₄ to intake air also increases the heat capacity of the air-fuel mixture formed. The fuel chemistry coupled was a reduced primary reference fuel (PRF) mechanism consisting of 45 species and 142 reactions. The simulation started from the intake valve closing (IVC) with the assumed homogeneous mixture of methane, air, and residue gas and completed at exhaust valve opening (EVO).

As matter of fact, the choice of the model has a fundamental role in the CFD analysis. Nowadays several well-established models have been implemented and, depending on the operating conditions certain models can be more suitable than others to describe the processes inside the combustion chamber.

Kusaka et al. [40] performed numerical studies using a multi-dimensional model combined with detailed chemical kinetics, including 43 species and 173 elementary reactions. Instead, in [41] the combustion mechanism for natural gas/diesel oil mixture includes 81 species and 421 reactions. In paper [42] methane and n-heptane were used as representative of natural gas and diesel fuels in a chemical kinetics mechanism which consists of 42 species and 57 reactions for prediction of n-heptane oxidation with the addition of a series of major methane oxidation pathways. Huang et al. [43] developed a reduced n-heptane-n-butylbenzene-NG-polycyclic aromatic hydrocarbon (PAH) mechanism with 746 reactions and 143 species. Therefore, to model diesel fuel a mixture of n-heptane and n-butylbenzene was used while to model NG, a mixture of methane, ethane and propane was used. Combustion process was simulated by combining the mentioned mechanism with the SAGE combustion model. The renormalized group (RNG) k- ϵ model, the turbulence model was used to simulate the turbulence characteristics. The spray atomisation and droplet breakup processes were predicted by the Kelvin-Helmholtz and Rayleigh-Taylor (KHRT) models, respectively. Kahila et al. [44] performed large-eddy simulations (LES) together with a finite-rate chemistry model of two diesel surrogate (n-dodecane) mechanisms consisting respectively of 54 species and 269 reactions, and 96 species and 993 reactions. It is stated that dual fuel ignition can be separated into three stages: the first is the ignition due to low temperature chemistry which results delayed with both mechanisms by the methane presence in the ambient; the second is the ignition at the spray tips; the last is represented by the full oxidation of available CH₄ and premixed flame. Chemical decomposition of n-dodecane produces heat, intermediate species and radicals, enabling a faster ignition compared to homogeneous ignition of pure methane-air mixtures. On the other hand, the ambient methane influences the early decomposition of n-dodecane mainly by consuming OH radical and forming methyl radicals which activate other inhibiting reactions. Therefore, ambient methane

influences the low- and high-temperature chemistry throughout the ignition process. Both first- and second-stage ignition processes are inhibited compared to the single-fuel reference case. The high-temperature ignition process begins near the most reactive mixture fraction conditions. The role of low-temperature reactions is of particular importance for initiation of the production of intermediate species and heat, required in methane oxidation and both applied mechanisms yield qualitatively the same features in the DF configuration. The primary breakup is considered by sampling computational parcels from the Rosin- Rammler size distribution while the secondary breakup is modelled by the KHRT model. Also, laminar 1D igniting counter-flow flamelet computations resemble the LES results, indicating their applicability to understand the DF ignition process.

However, it is clear that the simple replacement of diesel fuel with natural gas does not allow to optimize the performance of the engine due to the high THC emissions particularly at lower loads. Increasing the injection timing of pilot diesel fuel helps to reduce THC but causes an increase of the nitrogen oxides. Therefore, more complex combustion strategies should be realized to meet vehicles emission standards. In paper [45], the benefits obtainable through the activation of the low combustion temperatures were evaluated. LTC can be activated by means of very early diesel injection timings and with the maximum by natural gas share tolerable for stable combustion. The experimental activity was also focused to analyse the particle emissions. The activation of LTC showed the potential to simultaneously reduce both THC and NO_x emissions as well as ensuring ultra-low particle emissions. Hence, LTC should be considered as a key-strategy to make DF engines compliant with the limits imposed for the vehicles approval.

Dual fuel configurations can be implemented also on Spark Ignition engines. This is the case illustrated in [46] where gasoline is injected in the intake manifold, while the CNG is injected in the combustion chamber, in order to

have a charge stratification without the impingement of liquid fuels on the piston and cylinder walls.

Moreover, it is important to mention that the natural gas is not the only fuel used for diesel substitution. Indeed, Vipavanich et al. [47] investigated a different configuration such as the port fuel injection of gasoline to form a premixed charge prior to induction into the combustion chamber and ignition by the main diesel fuel. In this way an enhancement of the engine thermal efficiency over the diesel baseline combustion was attained. However, the real purpose of Dual Fuel strategy is to utilise renewable and clean fuels. Zang et al. [48] compared the ignition characteristics of natural gas and methanol in a Dual Fuel mode in a diesel engine. Results show that both methane and methanol retard the ignition of diesel vapour, but this effect is more significant when methanol is used. Hydroxyl radical is an important ignition promoter, during dehydrogenation process of methanol, the production of OH is possible only through the decomposition of H_2O_2 , which is stable at lower temperature; then the reaction activity of methanol is decreased, compared to natural gas.

Zhao et al. [49, 50, 51, 52] deeply studied the effects of ethanol burning in a Heavy Duty diesel engine. They demonstrated that the characteristics of ethanol such as high knock resistance and high latent heat of vaporisation, increase the reactivity gradient. However, ethanol-diesel dual-fuel combustion suffers from poor engine efficiency at low load due to incomplete combustion. Several ethanol energy fractions were explored in conjunction with the effect of different diesel injection strategies, and internal and external EGR on combustion, emissions, and efficiency. For the best emissions case, NO_x and soot emissions were reduced by 65% and 29%, respectively.

Another important strategy is the utilisation of hydrogen and methane blends or syngas in a compression ignition engine. Karagoz et al. [53] injected a gas

with a composition of 30% of H₂ and 70% of CH₄. Different energy inputs from the gas were tested (0, 15, 40 and 75% of the total fuel energy content) in full load conditions. Both NO_x and soot emissions are taken under control with 15% and 40% energy content rates in the gas fuel compared to the diesel-only condition. Although an increase is observed in CO and THC emissions with gas fuel addition compared to the diesel only condition, an improvement is considered compared to the results obtained for only methane fuel usage with diesel fuel. Moreover, in the 75% energy content case, combustion assumes features typical of a gasoline engine. In addition to the tri-fuel configuration Alrazen et al. [54] investigate a dual fuel mode when only H₂ is injected as gaseous fuel. Although a significant CO₂ reduction is achieved, the emissions of nitric oxides drastically increase and, it is important to take in account that the addition of CNG in hydrogen is necessary to produce a smoother combustion of hydrogen, and to ensure a safe operation of the engine and mechanical durability. In [55] a chemical kinetics and CFD analysis was performed to evaluate the combustion of syngas derived from biomass and coke-oven solid feedstock in a micro-pilot ignited supercharged dual-fuel engine under lean conditions. The syngas mixture consists of H₂, CO, CO₂, CH₄ and N₂. Results show that the NO_x formation is driven mostly by hydrogen while CH₄, have also important effects on combustion parameters such as laminar flame speed and ignition delay. Finally, in [56], also part of diesel oil is constituted by a renewable liquid fuel such as n-butanol. The authors demonstrated that the higher evaporation latent heat of n-butanol combined with the better homogeneity obtained due to natural gas can be beneficial for the reduction of NO_x emissions.

In this framework, experimental and numerical studies on dual fuel engine are addressed by the authors in [57, 58, 59] who discussed the effects of different fuel ratios (natural gas/diesel), up to 90%, on the performances and

emission levels of a light duty diesel engine. In papers [60, 61], the same authors tested two different load levels (50 and 100 Nm) with different injection timings which influence the combustion development of the mixture natural gas/air. The results of these studies are better illustrated and discussed in Chapter 3.

Chapter 2

MODELLING

In this chapter, an overview of the main principles of the computational fluid dynamics was provided, pointing out the models utilised in this thesis.

2.1 Fluid Dynamics

The study of the fluids (liquids, gases and plasmas) and their interactions with surfaces is suggested by the necessity to foresee the flow of a fluid in a lot of applications of engineering, physical sciences and even arts [62].

Examples of these applications include: the interaction of fluid with the blades of a turbine, the mass flow through pipelines, the air flow around a wing and consequently the forces and moments on the aircraft, the prediction of the weather, some of its principles are even used in traffic engineering, where traffic is seen as a continuous fluid, and the modelling of a wide variety of natural phenomena in video games.

The discipline that makes possible to understand and analyse the development of the motion of the fluids is the Fluid Dynamics.

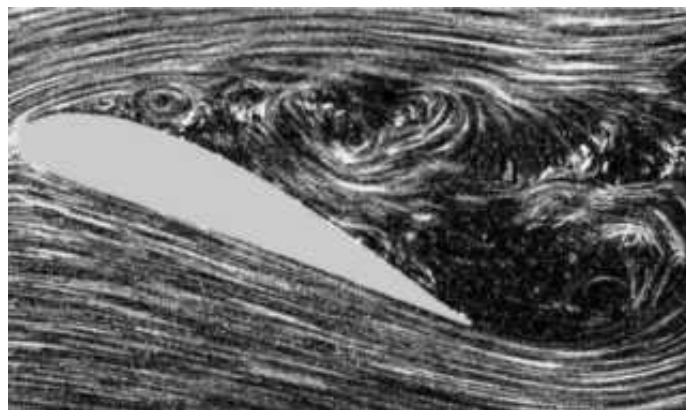


Fig. 2.1: Air flow around a wing [63].

The solution of a fluid dynamics problem is obtained by writing a complex system of differential equations, which describe the motion of a fluid from the macroscopic point of view.

The fundamental axioms of fluid dynamics are the conservation laws [64], which in their most general form can be written as follow:

- Conservation of mass:

$$\frac{\partial \rho}{\partial t} + \frac{\partial(\rho u)}{\partial x} + \frac{\partial(\rho v)}{\partial y} + \frac{\partial(\rho w)}{\partial z} = \frac{\partial \rho_s}{\partial t}$$

Where ρ is fluid density and u , v and w represent flow velocity vector components $\mathbf{v} = (u, v, w)$. The source $\frac{\partial \rho_s}{\partial t}$ is the mass added to the continuous phase from a dispersed second phase (e.g., due to vaporisation of liquid droplet).

- Conservation of momentum (Navier-Stokes equations):

$$\begin{aligned} \frac{\partial(\rho u)}{\partial t} + \frac{\partial(\rho u^2)}{\partial x} + \frac{\partial(\rho uv)}{\partial y} + \frac{\partial(\rho uw)}{\partial z} \\ = -\frac{\partial p}{\partial x} + \frac{\partial(\sigma_x)}{\partial x} + \frac{\partial(\tau_{yx})}{\partial y} + \frac{\partial(\tau_{zx})}{\partial z} + \rho f_x + (\mathbf{F}_s)_x \end{aligned}$$

$$\begin{aligned} \frac{\partial(\rho v)}{\partial t} + \frac{\partial(\rho vu)}{\partial x} + \frac{\partial(\rho v^2)}{\partial y} + \frac{\partial(\rho vw)}{\partial z} \\ = -\frac{\partial p}{\partial y} + \frac{\partial(\tau_{xy})}{\partial x} + \frac{\partial(\sigma_y)}{\partial y} + \frac{\partial(\tau_{zy})}{\partial z} + \rho f_y + (\mathbf{F}_s)_y \end{aligned}$$

$$\begin{aligned} \frac{\partial(\rho w)}{\partial t} + \frac{\partial(\rho wu)}{\partial x} + \frac{\partial(\rho wv)}{\partial y} + \frac{\partial(\rho w^2)}{\partial z} \\ = -\frac{\partial p}{\partial z} + \frac{\partial(\tau_{xz})}{\partial x} + \frac{\partial(\tau_{yz})}{\partial y} + \frac{\partial(\sigma_z)}{\partial z} + \rho f_z + (\mathbf{F}_s)_z \end{aligned}$$

Where p is the static pressure, ρf_i is the gravitational body force, F_s is the external body forces and σ_i and τ_{ij} are the terms of the stress tensor.

$$\begin{aligned}\boldsymbol{\tau} &= \begin{pmatrix} \sigma_x & \tau_{xy} & \tau_{xz} \\ \tau_{yx} & \sigma_y & \tau_{yz} \\ \tau_{zx} & \tau_{zy} & \sigma_z \end{pmatrix} \\ &= \mu \cdot \begin{pmatrix} 2 \cdot \frac{\partial u}{\partial x} & \left(\frac{\partial u}{\partial y} + \frac{\partial v}{\partial x}\right) & \left(\frac{\partial w}{\partial x} + \frac{\partial u}{\partial z}\right) \\ \left(\frac{\partial u}{\partial y} + \frac{\partial v}{\partial x}\right) & 2 \cdot \frac{\partial v}{\partial y} & \left(\frac{\partial w}{\partial y} + \frac{\partial v}{\partial z}\right) \\ \left(\frac{\partial w}{\partial x} + \frac{\partial u}{\partial z}\right) & \left(\frac{\partial w}{\partial y} + \frac{\partial v}{\partial z}\right) & 2 \cdot \frac{\partial w}{\partial z} \end{pmatrix}\end{aligned}$$

Where μ is the dynamic viscosity.

- Conservation of energy:

$$\begin{aligned}\frac{\partial \rho E}{\partial t} + \frac{\partial [(\rho E + p)u]}{\partial x} + \frac{\partial [(\rho E + p)v]}{\partial y} + \frac{\partial [(\rho E + p)w]}{\partial z} \\ = \nabla \left(-(\lambda_c \cdot \nabla T) - \sum_j h_j \cdot \mathbf{J}_j + (\boldsymbol{\tau}_{ij} \mathbf{v}) \right) + S_h\end{aligned}$$

The left hand represents the local variation and transport in the total energy including the work done on or by the system via pressure, so E is total energy, $-\nabla(\lambda_c \cdot \nabla T)$ is diffusive heat flow through system's boundaries, $-\nabla \sum_j h_j \cdot \mathbf{J}_j$ is the internal source of energy (e.g. radiation), $\nabla(\boldsymbol{\tau}_{ij} \mathbf{v})$ total energy variation due to dissipative forces and S_h is the work done on or by the system due to mass force.

This is a non-linear set of partial differential equations which can be analytically solved only for laminar flows and simpler geometries such spheres or flat plates, but in practical cases the flow very often is turbulent and the geometries are more complicated. For these reasons, in the last

decades, the numerical analysis has been widely spread; it is, indeed, a different approach to the resolution of mathematical problems, enabled by the development of the electronic calculators which allow to do longer and more complex calculations in short time. In particular, the solution of fluid dynamics problems using electronic machines is called Computational Fluid Dynamics (CFD).

The use of CFD to simulate a great part of phenomena related to fluid mechanics as flow, heat and mass transfer and chemical reactions, clearly, implies great economical and practical advantages:

- conceptual studied of new design in reduced time;
- redesign;
- product development;
- preliminary analysis of system in conditions hardly replicable;
- assessment of quantities difficult to measure directly;
- troubleshooting.

For example, it is possible to know how a machine will respond before performing a test and thus to avoid conditions that can take damage, or simply to understand how the product's performances are affected by this flows and the changes of arrangement which caused them.

Several commercial software solves fluid dynamics equations, in this thesis FLUENT, KIVA and FORTE are used. Each of them can be specialised in a particular application, like KIVA and FORTE that are used for internal combustion engines simulations.

2.1.1 Numerical analysis

The aim of numerical analysis is not to seek exact answers but it wants to attain results which can properly approximate the real solutions through the study of algorithms; as consequence, the presence of errors must be taken

into account, maintaining them within reasonable bounds to give a good representation of the analysed phenomena [65].

Usually the solution is reached through the same basic procedure:

1. The geometry of the problem is defined.
2. The volume occupied by the fluid is divided into discrete cells (mesh).
3. The equations that represent the physical modelling are defined.
4. Boundary conditions are determined. This means that the behaviour and the properties of the fluid must be specified at the limits of the domain. For transient cases there must be also an initial condition.
5. Equations are solved.
6. A postprocessor is used for the analysis and visualization of the results.

2.1.2 Discretization

Through a discretization process a continuous problem is replaced by a discrete one whose results approximate the solution of the continuous problem. This is done by dividing the domain into a series of volumes of infinitesimal dimensions so to generate a calculation grid, the so-called *mesh*, and for each volume, by writing conservation laws.

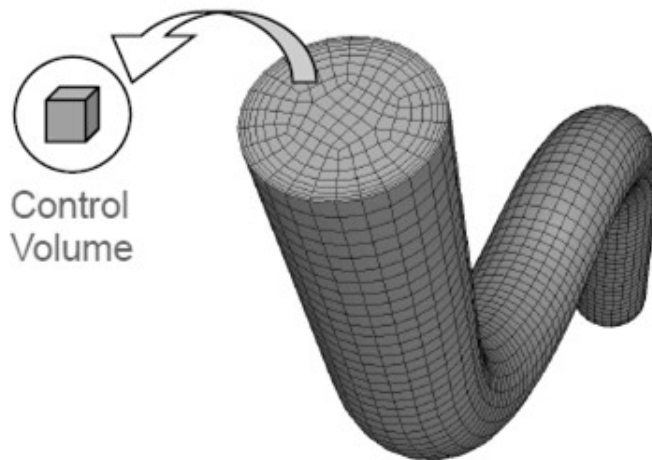


Fig. 2.2: Generic mesh [66].

The assumption behind this process is that all the points belonging to a certain volume are characterised by the same value of pressure, temperature and density, this is an acceptable approximation given the extremely small size. In this way conservation laws can be seen as a simple system of algebraic equations and no longer as partial differential equations, because the generic derivative is now a finite difference:

$$\frac{du_i}{dx} = \frac{u_{i+1} - u_i}{\Delta x}$$

For every case it is possible to create an infinite number of grids by enhancing or reducing the number of nodes.

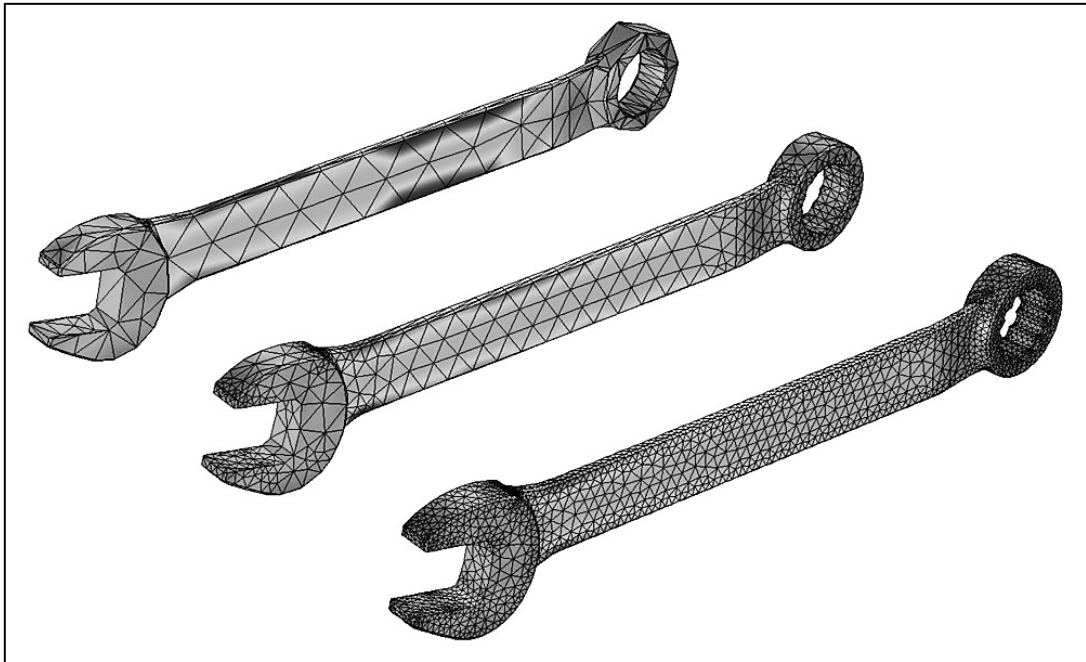


Fig. 2.3 : Different mesh resolutions [67].

Of course the mesh must be generated according to appropriate criteria; indeed it represents the domain, so the features of the original subject must be preserved and this occurs by enhancing the number of nodes and consequently the number of volumes and equations to solve, but conversely all this involves the increase of computational costs. Therefore, the optimal

choice is dictated by economic needs, available time, degree of accuracy required and power of electronic machines.

The most common discretization methods are:

- Finite volume method: this is the standard approach used in the greatest part of commercial CFD codes, it is characterised by high solution speed, high Reynolds number turbulent flow and it is particularly effective in combustion problems.
- Finite element method (FEM): this is mainly used in structural analysis but is also used in fluid dynamics where the Reynolds number are of the order of ten thousands.
- Finite difference method: it is used only in specialized codes with complex geometries.

Aside from these, there are other methods as the spectral element method, the boundary element method and the high-resolution discretization schemes.

2.1.3 Meshing

There are numerous ways to generate a mesh (e.g. starting from the surfaces or from the interior solid) and several types of meshes characterised by a different shape of cells. The most common grids are triangular and quadrangular (Figures 2.4.a and b), or respectively tetrahedral and hexahedral in a three-dimensional environment: usually the second type is preferred because with the same number of nodes, a better accuracy can be provided, despite triangular cells can better follow the border of the domain. However, it is possible to mix different shapes of cell in the same grid exploiting the features of each type (Figure 2.4.c).

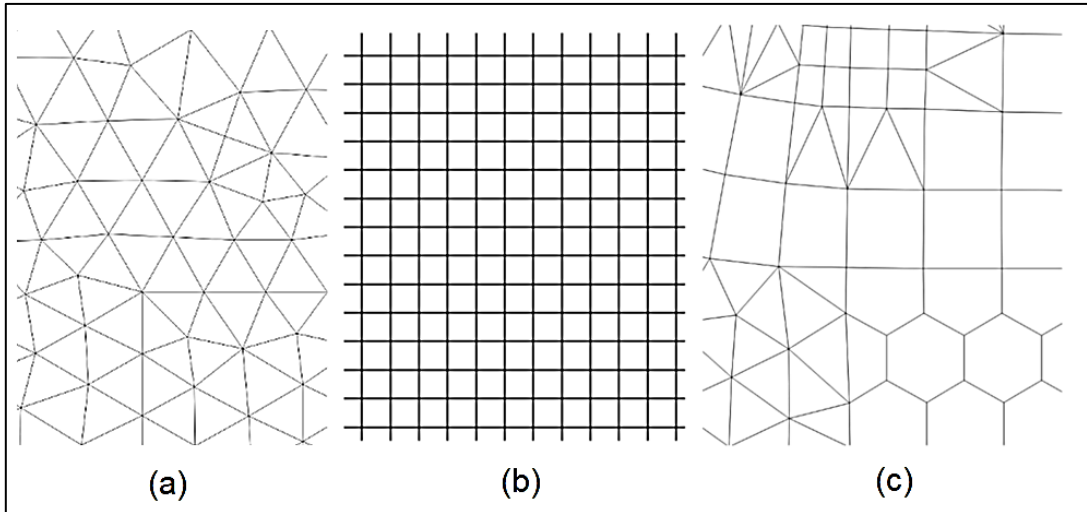


Fig. 2.4: Different shapes of cell: a) Triangular b) Quadrangular c) Mesh with mixed element types [68].

The generation of the mesh can be further complicated when parts of the geometry or boundaries move rigidly, deform or deflect. In this case the domain changes over time and then the mesh must adapt to the variations; for this reason, the mesh is called “dynamic”. This is the case of a piston inside the cylinder, during the stroke from the top dead centre to the bottom dead centre cells must be created to increase the volume and vice versa.

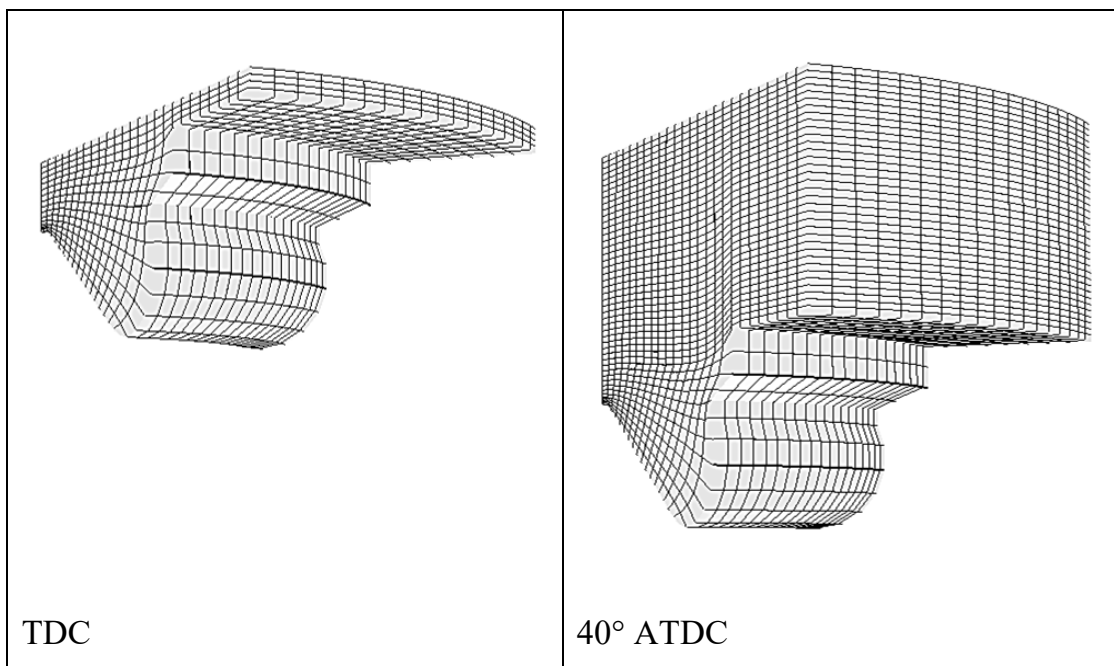


Fig. 2.5: Dynamic mesh at two different crank angles.

Also, the generic conservative equations must be modified to take into account the movement of the mesh:

$$\frac{d}{dt} \int_V \rho \phi dV + \int_{\partial V} \rho \phi (\mathbf{u} - \mathbf{u}_g) \cdot d\vec{A} = \int_{\partial V} \Gamma \nabla \phi \cdot d\vec{A} + \int_V S_\phi dV$$

Where \mathbf{u} is the velocity of the fluid, \mathbf{u}_g is the velocity of the mesh and ∂V represents the boundary of the control volume V.

2.1.4 Solution methods

The solution of the equations can be accomplished with direct or iterative methods.

Direct methods solve all the equations directly and reach the solution in a finite number of steps. These methods would give the precise answer if they were performed in infinite precision arithmetic. Examples include Gaussian elimination, the QR factorization method for solving system of linear equations, and the simplex method of linear programming.

In contrast, iterative methods start from an initial guess and iteratively give successive approximations that converge to the exact solution only at the limit, that is after an endless number of steps, but in practice the calculation is interrupted after is reached the desired degree of accuracy. So even using infinite precision arithmetic these methods would not reach the true solution but there always will be residuals. Among these methods there are Newton's method, the bisection method and Jacobi iteration.

Furthermore, some methods are direct in principle but are usually used as iterative ones because the number of steps needed to obtain the exact solution is so large that an approximation can be well accepted; GMRES and the conjugate method are examples.

Usually, in CFD and numerical analysis simulations iterative methods are commonly used to solve the equations for steady or transient state.

2.1.5 Errors

Both direct and iterative methods are affected by errors:

- Round off errors: arise because it is impossible to represent all real numbers exactly in reality or on a machine with finite memory.
- Truncation errors: are committed when an iterative method is terminated or a mathematical procedure is approximated, and the approximated solution differs from the exact solution.
- Discretization errors: these are intrinsic to numerical approaches, the solution of the discrete problem does not coincide with the solution of the continuous problem.

Once an error is generated, it will generally propagate through the calculation, so due to their presence it is important to introduce the notion of numerical stability. An algorithm is called numerically stable if an error, whatever its cause is, does not increase during the calculation. When this condition is fulfilled the problem is well-conditioned, meaning that if the problem data change by a small amount, the solution changes by only a small amount too. On the contrary when any small error in the data grows to be a large error, the problem is ill-conditioned. Both the original problem and the algorithm used can be well-conditioned and/or ill-conditioned and any combination is possible.

2.2 Turbulence

As already stated in practice cases fluid flows are very often turbulent.

In laminar flows kinetic energy is dissipated because of the action of molecular viscosity and the fluid streamlines do not mix laterally. On the

contrary in turbulent flows the inertia forces prevail over the viscous so that the particles move chaotically.

The transition from the first regime to the other is dependent on velocity of the fluid which is conventionally indicated by the non-dimensional Reynolds number:

$$Re = \frac{\rho \mathbf{v} L}{\mu} = \frac{\mathbf{v} L}{\nu}$$

Where L is a characteristic length and ν is cinematic viscosity.

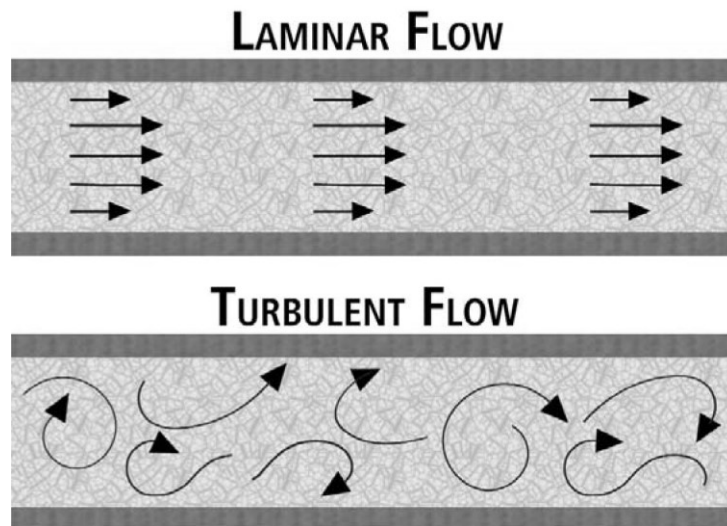


Fig. 2.6: Laminar and turbulent flow [69].

Turbulence is a very complex phenomenon characterised by a fluctuating velocity that consequently causes the fluctuation of other quantities as momentum, energy and species concentration, and develops on a wide range of length scales. The flow field is characterised by a continuous transfer of energy between these various whirling structures of different size.

In fluid dynamics studies energy can be classified in three basic forms:

- Enthalpy: energy added to the system as heat and dependent on temperature ($h = c_p \cdot T$).
- Potential: energy associated to a geodetic head ($w = g \cdot z$).

- Kinetic: energy manifesting in the speed of particles of the fluid
($k = \frac{1}{2} \cdot \mathbf{v}^2$).

In combustion phenomena that are the object of this work, kinetic energy is widely predominant while the other two can be considered negligible.

All the modelling is based on the idea formulated by Richardson, that all kinetic energy k entering the system owned by larger vortices is transferred to the ones of gradually decreasing size and at least dissipated as heat in the smaller eddies where the viscous forces prevail on inertial forces. The dissipation term is given by the derivative of kinetic energy with respect to time: $\varepsilon = \frac{\partial k}{\partial t}$. For this reason, this theory is called “energy cascade mechanism” of turbulent flow.

Under general conditions it is not possible to quantify the dimensions of the smaller length scales and the entity of dissipation. An important solution was given by Kolmogorov, who in 1941 published his theory applicable to fluids with high Reynolds number.

The first hypothesis is represented by considering turbulence as homogenous and isotropic, this means that the components of velocity along the three directions have the same value ($u = v = w$) and kinetic energy can be written as follow:

$$k = \frac{1}{2} \cdot (\overline{u^2} + \overline{v^2} + \overline{w^2}) = \frac{1}{2} \cdot (\overline{u^2} + \overline{u^2} + \overline{u^2}) = \frac{3}{2} \cdot (\overline{u^2})$$

The second hypothesis is that all characteristics of smaller length scales of all turbulent flows are universal and are determined by viscosity ν and dissipation ε . By combining these two parameters, it is possible to define quantitatively a characteristic length called “Kolmogorov scale”, time and velocity:

- $\eta = \left(\frac{\nu^3}{\varepsilon}\right)^{1/4}$
- $t_\eta = \left(\frac{\nu}{\varepsilon}\right)^{1/2} = \frac{\eta^2}{\nu}$
- $u_\eta = (\nu \cdot \eta)^{1/4}$

Given the stationarity of the process, which implies that the energy dissipated is the same entering the system, it is possible to identify also for larger eddies a characteristic length L_I , time t_t and velocity u' , but unlike the previous case, as the phenomena are governed by inertial parameters, cinematic viscosity is not utilised. In fact for macrovortices L_I , called “integral scale”, is known and is given by the dimensions of the larger scales which are delimited by the geometry at issue; velocity is easily measurable knowing the mass flows and the surfaces of passage; the time is given by the ratio of length and velocity and is called “turnover time”; finally it is also possible to express the dissipation energy as $\varepsilon = \frac{u'^3}{L_I}$.

Thus, comparing the characteristics of the various length scales, it is possible to understand the flow field and to select the best suited solution model to the problem.

2.3 Turbulence models

Since resolving all the instantaneous exact governing equations is computationally impossible due to the excessive expenses, in such cases the primary approach is for example to bypass this obstacle creating models capable of time-averaging, ensemble-averaging or manipulating the equations by removing smaller scales so that they may be easily solved.

However the modified equations are the result of analytical and experimental studies in which it is necessary to introduce new variables which require new equations and constants to close the problem, so the turbulence models are

needed to determine and approximate also these unsolved phenomena, by assigning a certain value to these terms.

However, there is not a universal model best suited to describe all classes of problems. The choice is made considering different factors as computing resources, the established practice for a certain class of problem, the level of accuracy required, the amount of time available and of course the physics of the flow. Beside computational costs depend on the range of scales modelled, the wider is this range the higher are the costs.

Below are briefly shown the main models used in CFD:

Direct numerical simulation (DNS) is not a real model as the equations are numerically solved in all time and spatial scales; this means that it is the most accurate but also the most expensive process.

The *Reynolds-averaged Navier-Stokes* (RANS) equations are the time-averaged equations that describe the motion of fluid flows; the basic concept behind this model is that the solution variables are decomposed in a mean and a fluctuating component:

$$\phi_i = \bar{\phi}_i + \phi'_i$$

Where $\bar{\phi}'_i = 0$

This approach introduces a new term which represents the effect of turbulence, it is called “Reynolds stresses” and other correlations are required in order to close the problem. For this reason, RANS models can be divided into two groups:

- The Boussinesq hypothesis uses few algebraic equations to determine turbulent viscosity μ_t , turbulent kinetic energy k and turbulent dissipation ε . Among these there are the Spalart-Allmaras model, the k - ε models and the k - ω models.

- Reynolds stress model (RSM) attempts to actually solve transport equations for each of the terms in the Reynolds stress tensor, this implies the addition of equations that increase further CPU effort.

Large eddy simulation (LES) solves only larger eddies which are strongly influenced by the geometry of the domain, the Kolmogorov scales, are previously numerically filtered and then properly modelled. Resolving larger eddies allows to utilise a coarser mesh and broader time-steps size, this means to reduce computational costs which fall between DNS and RANS approaches.

Detached eddy simulation (DES) is a hybrid formulation which combines RANS and LES models, the domain is divided into two zones: the region located near the boundary layer, where the turbulent length scale is less than the maximum grid dimension, is solved with RANS; while to the core region where the turbulent length scales exceed the grid dimension is assigned the LES mode solution, thereby a sub-grid scale formulation is required only in this zone and the cost of the computation is considerably cut down. However, the RANS/LES switch complicates the generation of the mesh because a single smooth velocity field must be provided across the two regions.

Other turbulence models which will be only mentioned are: coherent vortex simulation, vortex method, vorticity confinement method and linear eddy model.

2.4 Combustion models

Combustion models describe all chemical and physical reactions which derive from combustion. Clearly these phenomena are extremely complex as interaction between particles must be simulated considering turbulence's effects.

The starting consideration concerns the fuel and oxidizer streams entering the reaction zone, if they are separated the combustion is called non-premixed (or diffusion), otherwise if they are mixed, before burning, the combustion is defined as premixed.

The first approach aims to model the mixing and the transport of each chemical species by solving conservation equations that represent convection, diffusion and sources, so for the i th component:

$$\frac{\partial(\rho Y_i)}{\partial t} + \nabla \cdot (\rho \mathbf{v} Y_i) = -\nabla \cdot \mathbf{J}_i + R_i$$

Y is mass fraction, \mathbf{J} is the diffusion flux and R is the rate of production.

Actually, all mass fractions must sum to unity, if there are N chemical species in the system, $N-1$ equations will be solved and the last component's mass fraction is obtained as 1 minus the sum of the $N-1$ solved mass fractions. Usually the N th species is the one with the largest mass fraction thereby numerical errors are reduced.

The diffusion flux is generated by gradients of concentration and temperature and is given by Fick's law:

$$\mathbf{J}_i = -\left(\rho D_{m,i} + \frac{\mu_t}{Sc_t}\right) \nabla Y_i - D_{T,i} \frac{\nabla T}{T}$$

$D_{m,i}$ is the mass diffusion coefficient, μ_t is the turbulent viscosity, Sc_t is the Schmidt number and $D_{T,i}$ is thermal diffusion coefficient.

Several models were formulated to describe the source term. The most important are the finite-rate and the eddy-dissipation model.

2.4.1 Finite rate – Eddy dissipation model

The finite-rate model ignores the effect of turbulence and determines the reactions rate by the Arrhenius kinetic expression:

$$R_k = R_f - R_b = k_f \prod_{j=1}^N [C_j]^{a_j} - k_b \prod_{j=1}^N [C_j]^{b_j}$$

C_j is the molar concentration, a_j and b_j are stoichiometric coefficient, k_f and k_b are the forward and backward rate constants which are obtained using Arrhenius' expression:

$$k = AT^x \exp\left(-\frac{E_a}{RT}\right)$$

A is the pre-exponential factor, x is temperature exponent, E_a is the activation energy and R is universal gas constant.

On the contrary the eddy-dissipation model, formulated by Magnussen and Hjertager [70], neglects the kinetic rate and considers the problem linked only to fluid dynamics which means that is mixing-limited; this is possible when the fuel burns rapidly or at least when reactions are quicker than mixing phenomena. In this case reactions rate of all species are calculated and the one that limits the process, that is the smallest, is chosen:

$$R_t = C \frac{\varepsilon}{k} \cdot \min(Y_R, Y_P)$$

C is a factor proportional to turbulent combustion, Y_R and Y_P are mass fractions of reactants and products, k is the turbulent kinetic energy and ε is turbulent energy dissipation. The ratio $\frac{k}{\varepsilon}$ is called "characteristic mixing time" and indicates that the chemical reaction rate is governed by the large-eddy time scales and the combustion extinguishes if there is not turbulence, thus clearly this model is not suited to describe laminar flames. Moreover, an ignition source is not required which is acceptable for diffusion flames but in premixed flames the reactants will burn as soon as they enter the computational domain.

For these reasons usually CFD codes use a combination of these two models to describe the turbulence-chemistry interaction. The finite-rate/eddy-dissipation model calculates both kinetic and turbulent rates and takes as net rate the minimum. In this way slower chemical reactions are prevented to complete unlike happened in the ED model. Usually as the flame starts the ED rate is smaller than the one predicted by Arrhenius and reactions are controlled by turbulent effects.

Moreover, an extension of the ED model is represented by the Eddy Dissipation Concept (EDC) where the detailed Arrhenius chemical kinetics are incorporated in turbulent flames. It is assumed that reactions occur in small turbulent structures, defined by the previously illustrated fine Kolmogorov scales η . Then the source term is expressed as follow:

$$R_i = \frac{\rho(\eta^3)^2}{t_\eta[1 - (\eta^3)^3]} (Y_i^* - Y_i)$$

η^3 indicates the volume fraction of the fine scale where the species are assumed to react over a time scale t_η and after this time the species mass fraction is given by the term Y_i^* .

2.4.2 Non-premixed combustion models

In non-premixed combustion fuel and oxidizer enter the reaction zone as distinct streams. Combustion reaction occurs only when particles of these two streams come in contact. Combustion of pulverized coal and diesel internal-combustion engines are examples.

The flame develops on a thin surface called “inner layer” where the mixing of fuel and oxidizing reaches the stoichiometric value. At the opposite sides of the layer there are a rich and a lean zone where the mixture departs from stoichiometric value and unavoidably the flame extinguishes.

For this reason, it is noticeable the strong dependence of non-premixed flames on convection and diffusion caused by turbulence, which allows a more intimate mixing between reactants. This phase requires larger time than the time necessary for combustion, thus the problem can be reduced to a single variable able to represent the trend of mixing and independent of the chemical: this parameter is called mixture fraction.

Once mixed, the chemistry can be modelled as being in chemical equilibrium with the Equilibrium model, being near chemical equilibrium with Steady Laminar Flamelet or significantly far from chemical equilibrium with the Unsteady Laminar Flamelet model.

2.4.2.1 Mixture fraction theory

The mixture fraction is the mass fraction originated from the fuel stream, that is the local mass fraction of burned and unburned fuel elements (C, H, etc.) in all species (CO₂, H₂O, O₂, etc.). The greatest advantage of this approach is that atomic elements are conserved in chemical reactions, thus the mixture fraction is a conserved scalar quantity, in this way the solution involves only transport equations for one or two conserved scalars and source terms are equal to zero. Equation for individual species are not solved. Instead, species concentrations are derived from the predicted mixture fraction fields. At least, to save computational time, the thermochemistry calculations are pre-processed and then stored in a look-up table.

Moreover, interaction of turbulence and chemistry is accounted for with an assumed-shape Probability Density Function (PDF).

The mixture can be written in term of atomic mass fraction as:

$$f = \frac{Z_i - Z_{i,ox}}{Z_{i,fuel} - Z_{i,ox}}$$

Z_i is the elemental mass fraction for element i , the subscript ox is for the oxidizer and the subscript $fuel$ denotes the value for the fuel both at stream inlet. The sum of all mixture fractions in the system is always equal to 1.

Under the hypothesis of equal diffusivities, which is problematic for laminar flows but acceptable for turbulent flows because convection overwhelms molecular diffusion, the species equations can be reduced to a single equation for the mixture fraction. The Favre mean (density-averaged) mixture fraction equation is:

$$\frac{\partial}{\partial t}(\rho \bar{f}) + \nabla \cdot (\rho \mathbf{v} \bar{f}) = \nabla \cdot \left(\frac{\mu_t}{\sigma_t} \nabla \bar{f} \right)$$

At this point in condition of chemical equilibrium, all thermochemical scalar ϕ (species, density and temperature) are uniquely related to the mixture fractions.

$$\phi_i = \phi_i(f)$$

To give a closure to the problem it is necessary to solve another conservation equation for mixture fraction variance which describe turbulence-chemistry interaction:

$$\frac{\partial}{\partial t}(\rho \overline{f'^2}) + \nabla \cdot (\rho \mathbf{v} \overline{f'^2}) = \nabla \cdot \left(\frac{\mu_t}{\sigma_t} \nabla \overline{f'^2} \right) + C_g \mu_t (\nabla \bar{f})^2 - C_d \rho \frac{\varepsilon}{k} \overline{f'^2}$$

Where $f' = f - \bar{f}$, σ_t , C_g and C_d are constants.

Actually, due to the unpredictability of this parameter, in numerical analysis the solution of this equation is reached imposing a Probability Density Function (PDF). The PDF is the fraction of time that the fluid spends in the vicinity of the state f .

In fact, the fluctuating value of f spends some time in a range denoted as Δf . The function $p(f)$ represents the frequency with which f is found in such

range, in particular the area under its curve delimited in the band Δf , is equal to the fraction of time that f spends in this range. Written mathematically:

$$p(f)\Delta f = \lim_{T \rightarrow \infty} \frac{1}{T} \sum_i \tau_i$$

T is the time scale and τ is the amount of time that f spends in the Δf band.

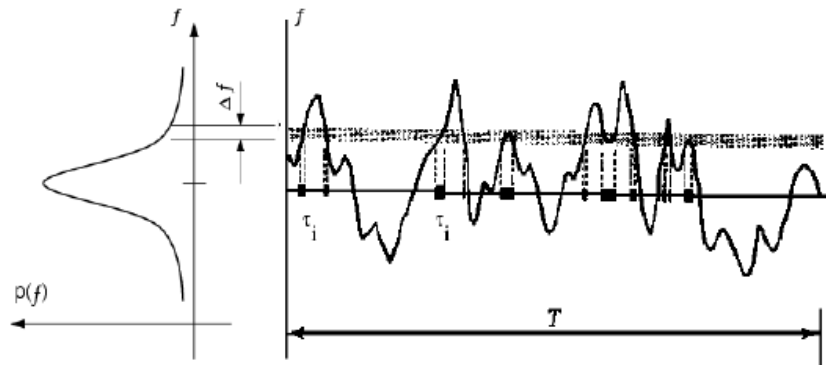


Fig. 2.7: Graphical description of the probability density function $p(f)$ [64].

Figure 2.7 plots on the right the time trace of mixture fraction at a point in the flow and on the left the probability density function of f .

The shape of the function depends on the nature of the turbulent fluctuations in f . In practice $p(f)$ is unknown but it can be modelled as mathematical function that approximates the actual PDF shapes that have been observed experimentally.

The most utilised shape is the β -function because it is the closer to experimental results.

$$p(f) = \frac{f^{\alpha-1}(1-f)^{\beta-1}}{\int f^{\alpha-1}(1-f)^{\beta-1}df}$$

$$\alpha = \bar{f} \left[\frac{\bar{f}(1-\bar{f})}{\bar{f}'^2} - 1 \right]$$

$$\beta = (1 - \bar{f}) \left[\frac{\bar{f}(1 - \bar{f})}{\overline{f'^2}} - 1 \right]$$

Thus, the PDF shape $p(f)$ is a function dependent only on the mean mixture fraction \bar{f} and the mixture fraction variance $\overline{f'^2}$. In turn this function can be used to determine the mean values of species mass fraction, density and temperature.

The PDF is used to compute averaged values of variables that depend on f (mass fraction, density and temperature):

$$\bar{\phi}_i = \int_0^1 p(f) \phi_i(f) df$$

To save significant computational time these integrals can be computed once, stored in a look-up table and retrieved during the simulation.

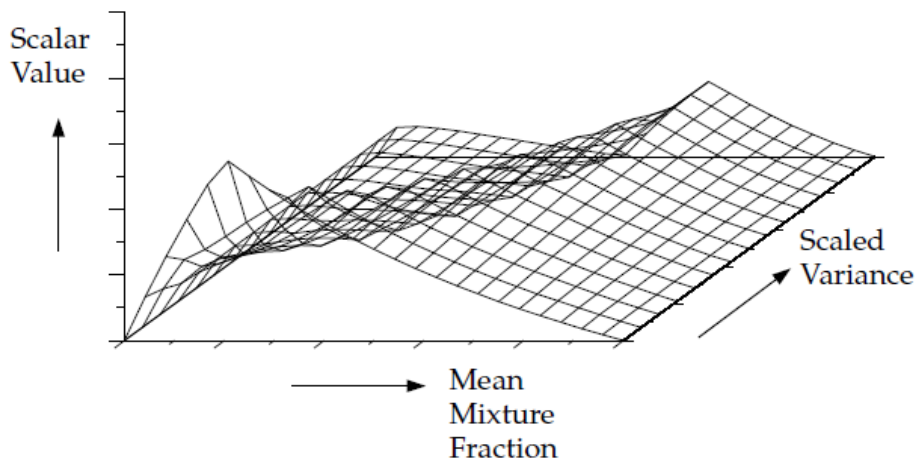


Fig. 2.8: Visual representation of a look-up table for a generic scalar [64].

2.4.2.2 Laminar Flamelet model

In many reacting systems, the combustion is not in chemical equilibrium. To simulate this state of chemical non-equilibrium is necessary another approach represented by the Laminar Flamelet models. The advantage of this approach is that realistic chemical kinetic effects can be incorporated into turbulent

flames. In fact, the chemistry is pre-processed and tabulated, offering huge computational savings.

Moreover it is possible to distinguish the Steady Flamelet model to describe the phenomena of diffusion flame stretched by turbulence with a relatively fast chemistry and the Unsteady Laminar Flamelet model to follow the slow-forming product species that are far from chemical equilibrium, this last is the case of gaseous pollutants (NO_x and low-temperature CO oxidation).

The basic concept of this theory is that the turbulent flame is seen as an ensemble of thin, laminar, locally one-dimensional flamelet located within the turbulent flow field.

In particular the individual flamelet is an independent thin reactive-diffusive layer whose structure is the same of a simple laminar flame which configuration is easy to perform by experiments or to calculate.

The location of the flamelet is identified through statistical PDF methods; in fact as the distribution of mixture fraction is known, for example using a β -function, it is possible to situate the layer where f reach the stoichiometric value.

After defining the stoichiometric surface on which reactions take place, the next step is to describe the combustion itself. Usually to represent a flamelet, it is used a common laminar diffusion flame type in a turbulent counterflow. The geometry is very simple and consists of opposed fuel and oxidizer jets. As the distance between the jets is decreased and/or the velocity of the jets is increased, the flame is strained and increasingly departs from chemical equilibrium until it is eventually extinguished.

This flame is easy to perform experimentally so that mass fraction and temperature fields can be measured. Otherwise due to simplicity of this configuration it is possible to calculate these parameters because the

governing equations are simplified to one-dimension along the axis of the fuel and oxidizer jets, and to neglect all variations of mixture along the isosurfaces at a constant value of f .

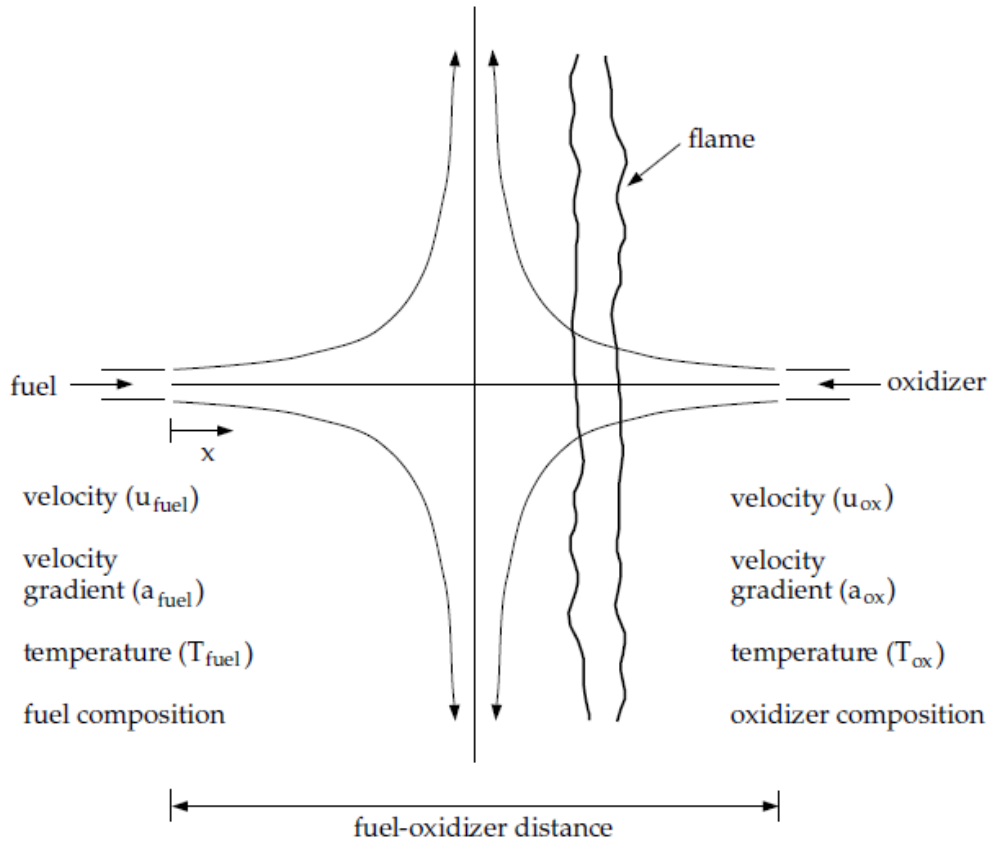


Fig. 2.9: Laminar opposed-flow diffusion flamelet [64].

In the laminar counterflow flame, the mixture fraction decreases monotonically from unity at the fuel jet to zero at the oxidizer jet. If the species mass fraction and temperature along the principal direction are mapped from physical space, they can be described by only two parameters: the mixture fraction and the scalar dissipation χ .

$$\frac{\partial Y_i}{\partial t} = \frac{\chi}{2} \cdot \frac{1}{Le_i} \left(\frac{\partial^2 Y_i}{\partial f^2} \right) + \frac{\omega_i}{\rho}$$

$$c_p \frac{\partial T}{\partial t} = \frac{\chi}{2} \left(\frac{\partial^2 h}{\partial f^2} \right) - \sum_{i=1}^N h_i \left\{ \frac{\chi}{2} \left(\frac{\partial^2 Y_i}{\partial f^2} \right) + \frac{\omega_i}{\rho} \right\}$$

These are the Flamelet Equations, the first is relative to conservation of mass fractions for i th species and the second is relative to conservation of energy.

Also, in this case the reduction of the complex chemistry to two variables (f and χ) allows the flamelet calculations to be pre-processed, and stored in look-up tables.

The scalar dissipation is given by:

$$\chi = 2D(\nabla f)^2$$

Where D is the diffusion coefficient.

The scalar dissipation varies along the axis of the flamelet and for the geometry at issue it can be related to strain rate for the position where f is stoichiometric:

$$\chi_{st} = \frac{a_s \exp\{-2[\operatorname{erfc}^{-1}(2f_{st})]^2\}}{\pi}$$

a_s is the strain rate and is given by $a_s = \frac{v}{2d}$. Where v is relative speed of the fuel and oxidizer jets, d is the distance between the jet nozzles, and erfc^{-1} is the inverse complementary error function.

Scalar dissipation allows to quantify the departure from equilibrium. In fact, diffusive fluxes are a function of space, thus of mixture fraction, as the flame is strained the width of the reaction zone diminishes and the gradient of f at stoichiometric position increases. This parameter represents the inverse of characteristic diffusion time (s^{-1}). For $\chi_{st} \rightarrow 0$ the chemistry tends to equilibrium. High values of the scalar dissipation correspond to high gradients and diffusion occurs in brief time. If it reaches a critical value the flamelet quenches.

The steady laminar flamelet model is suited to predict chemical non-equilibrium due to aerodynamic straining of the flame by the turbulence. The

chemistry, however, is assumed to respond rapidly to this strain, so as the strain relaxes to zero, the chemistry tends to equilibrium.

However, at the outlet of many combustors the strain is small and the steady flamelet model predict all species, including slow-formation species like NO_x , to be near equilibrium, which is often inaccurate. The cause of this inaccuracy is the disparity between the flamelet time-scale, which is the inverse of the scalar dissipation and the slow-forming species time-scale. In fact the Steady Laminar Flamelet model does not follow the path of particles in slow reactions so another model is needed: the Unsteady Flamelet model.

In this way fluxes of particles are seen as flamelets which cross the flow field on statistically different paths. The model processes an unsteady marker probability equation on a steady-state, converged flow field.

The transport equation for the unsteady flamelet marker probability I is

$$\frac{\partial}{\partial t}(\rho I) + \nabla \cdot (\rho \mathbf{v} I) = \nabla \cdot \left(\frac{\mu_t}{\sigma_t} \nabla I \right)$$

2.4.3 Premixed combustion models

In premixed combustion fuel and oxidizer are mixed at molecular level before entering the combustion chamber. Examples of premixed combustion include aspirated internal combustion engines, lean-premixed gas turbine combustor and gas-leak explosions.

Reactions take place in a flame front that propagate into the unburned reactants and that separate them from the burned combustion products. In fact all these reactions occur at very high temperature and as they follow the Arrhenius law, it is evident that they are extremely fast and the flame front is seen as a discontinuity surface which divides the burned zone from the unburned one.

The thin flame is stretched and contorted by turbulence and this makes really difficult to model this type of combustion.

For subsonic flows, the overall rate of propagation of the turbulent flame ($\frac{dm_b}{dt}$) is determined by both the laminar flame speed S_L [m/s] and the turbulent eddies.

The laminar flame speed refers to a combustion in absence of motion or a laminar motion at very low speed and is determined by the kinetic scheme and the burning rate of the species. Thus, it represents the synthesis of all the detailed chemical kinetics and molecular diffusion processes.

$$\frac{dm_b}{dt} = \rho_u A_L S_L$$

The flame front has a certain thickness indicated with δ_L [m] and it is linked to laminar speed by the following relation:

$$\delta_L = \frac{v}{S_L}$$

It is also possible to define a characteristic time:

$$t_c = \frac{\delta_L}{S_L}$$

This is the time that a particle spends to cross the flame front that is a chemical reaction time.

To capture the laminar flame speed and the flame thickness that is of order of millimetres or smaller, the internal flame structure would need to be resolved, but the resolution required is usually unaffordable.

For this reason the best solution is the obtained by the experimentation: air and fuel enter in a transparent tube at a given speed, by reacting a flame front

will be visible through the tube, if the flame front is steady, the entering reagents speed will represent S_L .

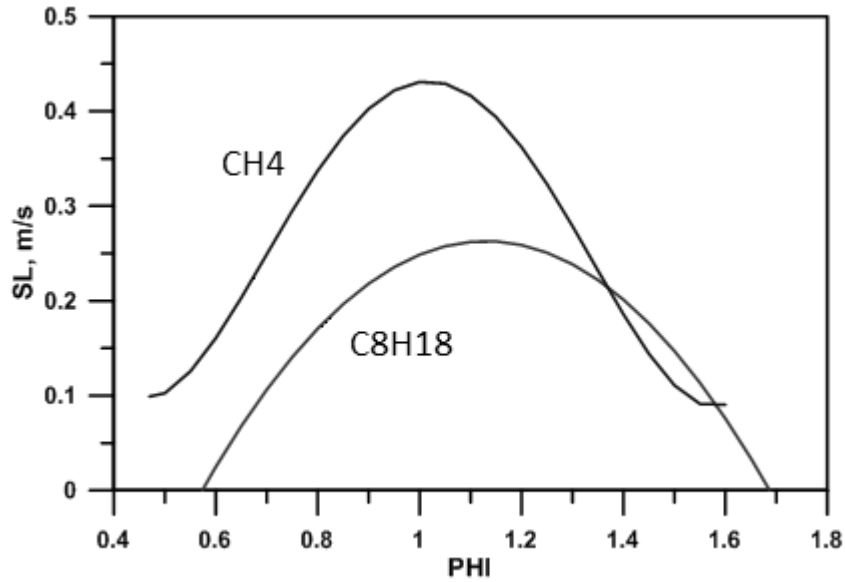


Fig. 2.10: Laminar flame speed for two different hydrocarbons [71].

The laminar flame speed is a function of the equivalent ratio φ and in particular it reaches a maximum near stoichiometric mixture.

Moreover S_L depends on the fuel, temperature and pressure:

$$S_{L0} = 0.2632 - 0.8472(\varphi - 1.13)^2$$

Beside S_{L0} is the flame speed at ambient temperature and atmospheric pressure. For different operating condition:

$$S_L = S_{L0} \left(\frac{T}{T_0}\right)^{\alpha_s} \left(\frac{p}{p_0}\right)^{\beta_s} (1 - cx_r^{\delta_s})$$

- $\alpha_s = 2.18 - 0.8(\varphi - 1)$
- $\beta_s = -0.16 + 0.22(\varphi - 1)$
- $c = 2.1$
- $\delta_s = 0.77$
- x_r is the percentage of inert in unburned mixture

Moreover, the flame considered in the tube is planar, which means that it an “unstretched flame”. Actually, the flame propagates spherically and a “stretch” effect must be taken to account.

$$k = \frac{1}{A_L} \frac{dA_L}{dt} = \frac{2}{r} \frac{dr}{dt}$$

With A_L , it is denoted the laminar area over the time.

In some cases the stretch coefficient k tends to enhance the laminar speed but in other cases it can have the opposite effect. This is determined by another parameter which is characterised experimentally and is called Markstein length L_M .

$$S_{L,s} = S_{L,u} - kL_M$$

The other phenomenon that influences the propagation is the turbulence, its effect is to wrinkle the propagating laminar flame sheet increasing the area and in turn effective flame speed. The large eddies wrinkle and corrugate the front, while the eddies smaller than the flame thickness may penetrate it and modify the laminar structure.

To understand the influence of turbulence in the combustion, it is necessary to compare the scales of length, velocity and time of the two phenomena. This is how the Borghi diagram works, basing on the ratio of these quantities, identifies different zones which correspond to different combustion regimes.

As shown in Figure 2.11 the various zones are delimited by non-dimensional parameters. Apart from the Reynolds number, the most important are the Damköhler number and the Karlovitz number; the first compares the characteristic time of macrovortices and combustion, the second compares the characteristic time of combustion and microvortices.

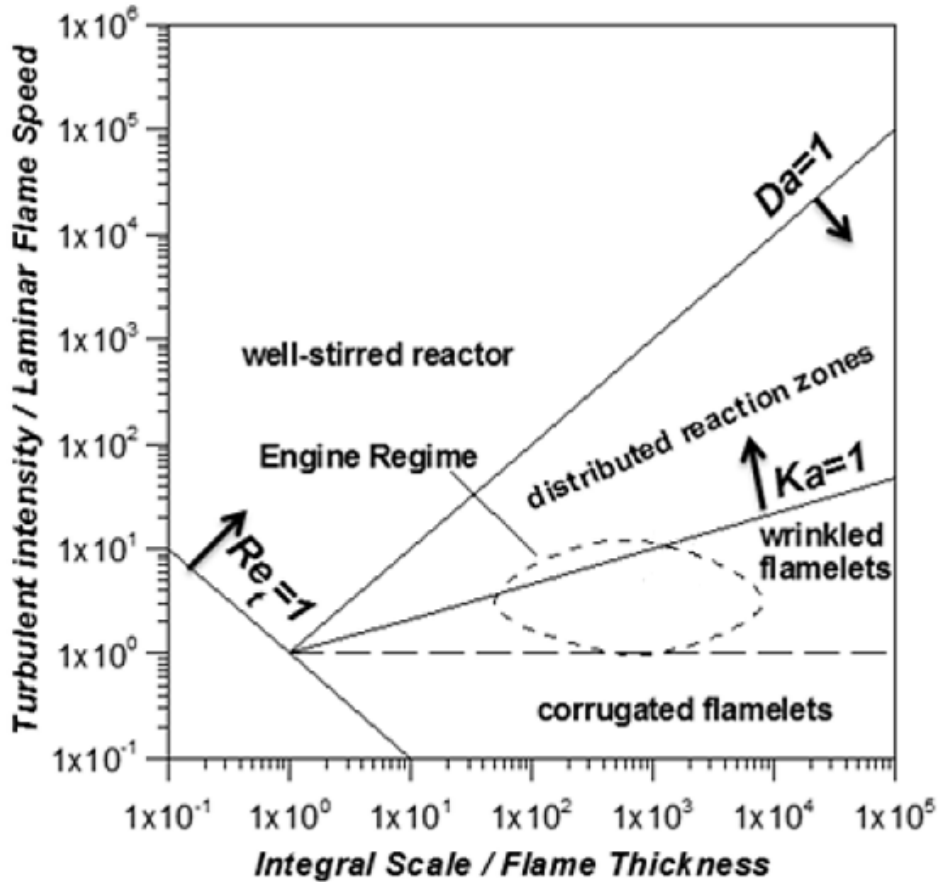


Fig. 2.11: Borghi diagram [71].

$$Da = \frac{t_t}{t_c} = \frac{L_I}{u'} \cdot \frac{S_L}{\delta_L}$$

$$Ka = \frac{t_c}{t_\eta} = \frac{\delta_L}{S_L} \cdot \frac{\nu}{\eta^2} = \frac{\delta_L}{S_L} \cdot \frac{\delta_L S_L}{\eta^2} = \left(\frac{\delta_L}{\eta}\right)^2$$

- For $Re_t < 1$ the combustion is laminar.
- In the strip where $\frac{u'}{S_L} < 1$, turbulence has no effect on combustion, possibly it wrinkles lightly the flame front.
- The triangle delimited by $\frac{u'}{S_L} = 1$ and $Ka = 1$ is the wrinkled flamelet zone, the front thickness is smaller than the smaller eddy, this means that the microvortices cannot penetrate into the flame.
- In the zone where $Ka > 1$ and $Da > 1$ chemistry is altered by turbulence. It is called “distributed reaction zone” because

microvortices can enter into the reaction zone and macrovortices can break the flame front generating separated combustion zones.

- For $Da < 1$ larger eddy enters the flame which disappears, this implies a homogeneous reactor and the combustion occurs diffusely throughout the volume without a real propagation mechanism.

To take account of all that combustion speed is written in a different way:

$$\left(\frac{dm_b}{dt}\right)_T = \rho_u A_T S_L = \rho_u A_L S_T$$

Due to difficulties to assess the turbulent flame speed, combustion is seen as a turbulent flame front which propagates locally at laminar speed.

At least the term A_T is evaluated with the assistance of an important tool which is fractal geometry.

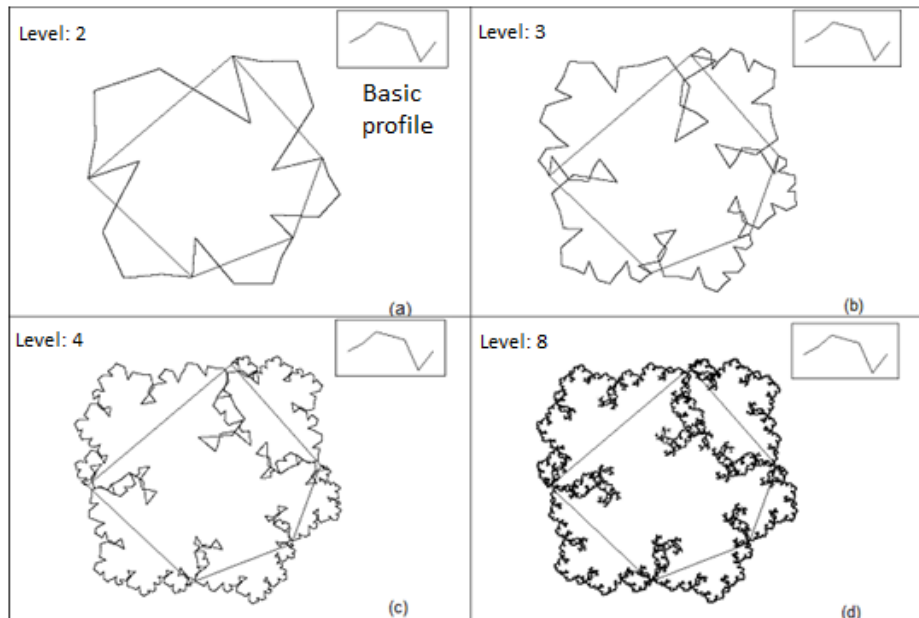


Fig. 2.12: Example of fractal geometry [71].

Fractal geometry allows to calculate the reaction area's increase A_T due to turbulence compared to the average value of A_L .

$$A_T = \left(\frac{A_T}{A_L}\right) A_L$$

However an important premixed combustion model implemented in CFD codes is based on Zimont's work, applicable when $Ka < 1$, it involves the solution of a transport equation for reaction progress variable and the closure equation is based on the definition of turbulent flame speed.

$$\frac{\partial}{\partial t}(\rho c) + \nabla \cdot (\rho v c) = \nabla \cdot \left(\frac{\mu_t}{S_c} \nabla c\right) + \rho S_c$$

c is the mean reaction progress variable and S_c is the reaction progress source term [s^{-1}].

The progress variable is defined as a normalized sum of the product species:

$$c = \frac{\sum_{i=1}^n Y_i}{\sum_{i=1}^n Y_{i,eq}}$$

Where n is the number of products, Y_i is the mass fraction of i th product species and $Y_{i,eq}$ is the equilibrium mass fraction of i th product species.

Then:

- $c = 0$ for unburned mixture
- $c = 1$ for burned mixture

The mean reaction rate is given by:

$$\rho S_c = \rho_u S_T |\nabla c|$$

The Zimont turbulent flame speed closure is computed using the following correlation:

$$S_T = B u' \left(\frac{\tau_t}{\tau_c}\right)^{1/4}$$

Where B is a constant, u' is the root-mean-square velocity, τ_t is the turbulence time scale and τ_c is the chemical time scale.

2.5 Flame Models: G-equation

The flame model used in this thesis is the G-equation model, which is capable to track the position and then the propagation of fully developed, premixed or partially premixed, turbulent flames [72]. However, the flame is initiated by the source of ignition (e.g. spark), the ignition-kernel is formed but its structure is typically smaller than the average grid size. For this reason, the flame front is first described by the Discrete Particle Ignition Kernel Flame model that assumes a spherical-shaped kernel whose surface is marked by Lagrangian particles, the density of the surface is obtained from the number density of these particles in each computational cell. Assuming the temperature inside the kernel to be uniform, the kernel growth rate is:

$$\frac{dr_k}{dt} = \frac{\rho_u}{\rho_k} (S_{plasma} + S_T)$$

Where r_k is the kernel radius, ρ_u and ρ_k are respectively the density of the local unburnt gas and the density inside the kernel region. The plasma velocity S_{plasma} depends on the energy discharged during the spark.

As the flame structure grows bigger than a characteristic flow length scale the calculation switches from the Kernel model to the turbulent G-equation model occurs. The transition is controlled by a comparison of the kernel radius with a critical size that is proportional to the locally averaged turbulence integral length scale:

$$r_k \geq C_{m1} \cdot l = C_{m1} \cdot 0.16 \frac{k^{3/2}}{\varepsilon}$$

Where C_{m1} is a model constant with a typical value equal to 2.0.

The flame propagation can be also induced by the autoignition kinetics. In this case a temperature criterion is used: computational cells with temperatures greater than the critical temperature become ignition sites.

The G-equation model consists of the Favre-averaged mean equation and its variance.

$$\frac{\partial \tilde{G}}{\partial t} + (\tilde{\mathbf{u}} - \mathbf{u}_{vertex}) \cdot \nabla \tilde{G} = \frac{\bar{\rho}_u}{\bar{\rho}_b} S_T^0 |\nabla \tilde{G}| - D_T \tilde{\kappa} |\nabla \tilde{G}|$$

$$\frac{\partial \tilde{G}''^2}{\partial t} + \tilde{\mathbf{u}} \cdot \nabla \tilde{G}''^2 = \nabla_{\parallel} \cdot \left(\frac{\bar{\rho}_u}{\bar{\rho}_b} D_T \nabla_{\parallel} \tilde{G}''^2 \right) + 2D_T (\nabla \tilde{G})^2 - c_s \frac{\tilde{\epsilon}}{\bar{k}} \tilde{G}''^2$$

Where ∇_{\parallel} denotes the tangential gradient operator, \mathbf{u} is the fluid velocity, \mathbf{u}_{vertex} is the velocity of the moving vertex, ρ_u and ρ_b are respectively, the average densities of the unburned and burned mixtures, D_T is the turbulent diffusivity, κ is the Favre mean flame front curvature and c_s is a model constant.

The prediction of the turbulent burning velocity is obtained by the scaling of laminar flame speed; indeed, it is an intrinsic property of a premixed fuel/air for a given unburned temperature, pressure, and composition (species mass fractions). It is possible to specify the laminar flame speed via a simple ‘‘power law formulation’’:

$$S_L^0 = S_{L,ref}^0 \left(\frac{T_u}{T_{u,ref}} \right)^{\alpha} \left(\frac{p}{p_{ref}} \right)^{\beta} F_{dil}$$

Where the subscript *ref* means the reference condition (typically at 298 K and 1 atm) and the subscript 0 is referred to a planar and unstretched flame. F_{dil} takes in account the diluent effect. The exponents α and β describe the temperature and pressure dependencies.

The reference flame speed can be calculated using two formulas. The first one is defined by Metghalchi [73]:

$$S_{L,ref}^0 = B_m + B_\phi(\phi - \phi_m)^2$$

However, for very lean or very rich mixture can give negative flame speeds, on the contrary the second one by Gülder [74] has always not negative solution:

$$S_{L,ref}^0 = \omega\phi^\eta \exp(-\xi(\phi - \sigma)^2)$$

The coefficients B_m , B_ϕ , ϕ_m and ω , η , ξ and σ respectively in the Metghalchi and Gülder correlations depend on the selected fuel.

This model provides a complete description of a premixed turbulent flame-front propagation together with the Reynolds-averaged Navier-Stokes equations.

2.6 Liquid Jet Atomisation and Breakup models

In order to increase the surface/volume ratio of the fuel, it is necessary to disrupt the liquid jet introduced in the combustion chamber. Actually, the injection phase is extremely complex since it is characterised by a series of different phenomena such as atomisation, vaporisation and distribution of parcels, that contribute to a more efficient heat exchange between fuel and air with a consequent faster vaporisation, then a shorter ignition delay and a reduction of pollution. For instance, it is important to prevent the combustion of big drops still at liquid state, since they are the main cause of smoke in the exhaust gas.

A fundamental parameter used to compare the forces that promote and oppose to the droplets break-up is the Weber number:

$$We = \frac{\rho_g u_r^2 D}{\sigma}$$

Indeed, the numerator represents the aerodynamic forces that tend to disrupt the liquid jet while the denominator presents the surface tension as stabilising force. The break-up of the droplet occurs as soon as a critical value of the Weber number is reached.

In this paragraph well-established models used for the simulation of spray evolution and its interaction with air, are illustrated [75].

2.6.1 TAB Model

The model presented in [76] is based on the Taylor's analogy of the droplet distortion to an oscillating spring-mass system:

$$m\ddot{x} = F - kx - d\dot{x}$$

The external force acting on the mass, the restoring force of the spring and the damping force are respectively analogous to the gas aerodynamic force, the liquid surface tension force and the liquid force, as show in the following:

$$\frac{F}{m} = C_F \frac{\rho_g u^2}{\rho_l r}; \quad \frac{k}{m} = C_k \frac{\sigma}{\rho_l r^3}; \quad \frac{d}{m} = C_d \frac{\mu_l}{\rho_l r^2}$$

$$\ddot{x} = \frac{C_F \rho_g u^2}{C_b \rho_l r^2} - \frac{C_d \sigma}{\rho_l r^3} x - \frac{C_k \mu_l}{\rho_l r^2} \dot{x}$$

The damping time is expressed as:

$$\frac{1}{t_d} = \frac{C_d \mu_l}{2 \rho_l r^2}$$

The function becomes:

$$x(t) = \frac{C_F}{C_k C_b} We + e^{(-t/t_d)} \left[\left(x_0 - \frac{C_F}{C_k C_b} We \right) \cos \omega t + \frac{1}{\omega} \left(\dot{x}_0 + \frac{x_0 - \frac{C_F}{C_k C_b} We}{t_d} \right) \sin \omega t \right]$$

C_F , C_k and C_b are dimensionless constants, determined by comparing experimental and theoretical results. For example, in shock tube experiments

the critical Weber number for break-up was found to be $We_{crit} \cong 6$, $t_d \cong \infty$ and $x_0 = \dot{x}_0 = 0$, then:

$$x(t) = \frac{C_F}{C_k C_b} We(1 - \cos \omega t)$$

The model predict break-up only if $x > 1$, which occurs if:

$$2 \frac{C_F}{C_k C_b} We > 1$$

Hence, the model gives the experimental result for:

$$\frac{C_k C_b}{C_F} = 2We_{crit} = 12$$

2.6.2 WAVE Model

The Wave model assumes that aerodynamic forces provoke unstable wave on the surfaces of the jet [77]. The liquid jet is injected in the shape of blobs with an initial radius a then broken into smaller droplets of radius r following the law of variation:

$$\frac{da}{dt} = -(a - r)/\tau$$

$$r = B_0 \Lambda$$

Where τ is the break-up time:

$$\tau = \frac{3.72 B_1 a}{\Lambda \Omega}$$

Λ is the wavelength of the most unstable wave disturbance and Ω is the maximum wave growth rate:

$$\Lambda = 9.02r \frac{(1 + 0.45Z^{0.5})(1 + 0.4T^{0.7})}{(1 + 0.87We^{1.67})^{0.6}}$$

$$\Omega = \frac{(0.34 + 0.38We^{1.5})}{(1 + Z)(1 + 1.4T^{0.6})} \sqrt{\frac{\sigma}{(\rho_l r^3)}}$$

Z is the Ohnesorge number: $Z = \frac{\sqrt{We}}{Re}$

T is the Taylor number: $T = Z \cdot We^{0.5}$

Usually a calibration of the two constants B_0 and B_1 is necessary for the fitting of the numerical results with experimental ones. In literature a value of $B_0 = 0.61$ is most common [78, 79], while for B_1 a range from 1.7 to 30 is acceptable [80].

2.6.3 KHRT Model

The Kelvin-Helmholtz (KH) model is based on the Wave model [78] and is used to predict the initial break-up of the intact liquid core or the injected blobs. The Rayleigh-Taylor (RT) model is used combined with the KH model to describe the secondary break-up of the droplets. The RT model predicts the development of the instabilities on the surface of droplet that grow until a characteristic time is reached and the break-up happens.

The droplet acceleration and the break-up time are:

$$a = \frac{3}{8} C_D \frac{\rho_g u_r^2}{\rho_l r}; \quad \tau_{RT} = \frac{C_\tau}{K_{RT}}$$

Usually it assumed $C_\tau = 1$. Also:

$$\Lambda_{RT} = 2\pi C_{RT}/K_{RT}$$

$$\Omega_{RT} = \sqrt{\frac{2}{3\sqrt{3}\sigma} \frac{|g_t(\rho_l - \rho_g)|^{3/2}}{\rho_l + \rho_g}}$$

C_D , C_{RT} and K_{RT} are constants.

The new droplet radius is:

$$r_c = \pi C_{RT}/K_{RT}$$

2.7 Combustion features and problems

In the previous paragraphs different models were outlined for the different combustion regimes. If focusing on the Dual Fuel configuration studied in this thesis, the primary fuel is natural gas that is introduced into the intake manifold with air in order to mix perfectly and to obtain the conditions for a premixed combustion while the little amount of diesel oil injected as source of ignition burns in the same way as any other diesel engine such as in a diffusive, non-premixed flame.

For each of the two distinct types of combustion, the process is extremely complex, characterised by different phenomena that can even influence each other. Experimental activity provides useful validation tests for numerical investigation. By observing the different phenomena, it is possible to formulate important correlations that reproduce in the best way the real behaviour of all the elements involved in this process. In particular, these correlations are used in the numerical analysis that allows a deep investigation of each issue relating and unrelating from the others, and that, in turn, can be useful to experimental tests to identify the most interesting cases. Clearly, the more the models are detailed, the more the costs in terms of computational efforts are expensive.

Premixed combustion develops following a mechanism of flame propagation from any identified ignition point. Diffusive combustion is basically turbulence - controlled, since it is reasonable to assume that, as already said, the reaction takes place as soon as the reactants reach the correct autoignition conditions. Furthermore, direct injection in a diesel engine requires proper models for the prediction of jet distribution and vaporisation to be added to the set of equations for the CFD problem solution. For these reasons, it is easy to understand that DF simulations are characterised by a higher degree of complexity, since models for each of the above mentioned phenomena and

for the two fuels must be implemented and used in the code with a consequent increase of computational efforts. Also, the various phenomena can have a different impact depending on the operating conditions. As a matter of fact, great attention must be paid to the natural gas processes, since it usually burns in lean mixtures with air when employed in dual fuel applications. Therefore, a flame front cannot be always generated and propagated correctly throughout the combustion chamber. Consequently, the model that theoretically is the most suitable for conventional natural gas combustions, could be practice inadequate for the description of this particular process. Furthermore, the diesel vapour burning modifies the methane – air premixed ratio, because it subtracts a fraction of oxygen necessary to the combustion development of NG. However, the inability to sustain the flame front propagation is compensated by the wide spreading of diesel oil that allows the mixture ignition to occur in many points of the combustion chamber. Of course, this implies the need of a correct prediction of the ignition of both fuel, which can be described through empirical correlations or detailed sets of chemical reactions. In the first case, after a certain delay evaluated by correlations, fuel starts to burn as soon as the autoignition conditions are reached; this mechanism is suitable for the diesel oil ignition. Using detailed kinetic schemes implies that “low temperature reactions” are firstly activated, so describing the early ignition phases. The fastest oxidation reactions develop only once the activation temperature is reached

Based on the above considerations, the main challenge for a exhaustive numerical model of dual fuel combustion is the choice of the kinetic scheme and the related oxidation mechanism. In literature a lot of mechanism can be found for the two distinct fuels. but it is not possible to simply merge them together; indeed, the presence of one fuel can likely influence the reaction development of the other one. It may be possible that one fuel is present in

the kinetic scheme of the other one as an intermediate species. Nevertheless, this does not ensure a proper modelling of the combustion development of the secondary fuel.

Moreover, every commonly used fuel (diesel oil, gasoline, natural gas...) consists of a mixture of species but generally, when the composition is not specified, a surrogate of a single compound is used. In addition, a great number of intermediate species is involved in the long chain of reactions. With the aim to keep the time of calculations acceptable, usually reduced kinetic schemes are implemented in the codes by merging more reactions in a limited number of steps, and modifying the constants of the model in order to meet the timing of the whole process. Sometimes, this practice is due to the computational limits of the solver that is not capable to deal with more reactions at once.

It is important to highlight that another limit can be imposed by the code used to perform calculations. Although a model that is capable to simulate the dual fuel combustion may exist, it is not sure that is available among the commercial solver options.

Finally, another important issue that affects the difficulty of the calculations regards the dimensions and features of the mesh grid. Depending on the number and the shape of the cells, the code resolves the equations for each cell and with a certain degree of accuracy. Furthermore, the numerical study of reciprocating engines is also complicated by the necessity of a dynamic mesh. Indeed, the volume variation and the valve opening period dictated by the cyclic operation of this type of engine requires a continuous change of the domain geometry and consequently the mesh grid. For these reasons, alongside the study of dual fuel diesel engines supplied with NG, parallel investigations were carried out by the author of this thesis on systems which work under steady conditions, such as the micro gas turbines, as reported in

section 3.1. In fact, air and fuel continuously flow inside the combustion chamber within a stationary domain, so that no dynamic mesh is needed. Therefore, all the computational efforts can be addressed to the utilisation of more detailed kinetics schemes and combustion models.

Chapter 3

PRELIMINARY EXPERIENCE

In the present chapter the parallel studies led by the author on micro gas turbines and the previous experiences of the researchers of the University of Naples on the computational fluid dynamics and on the combustion kinetic of Dual Fuel technology that framed this thesis are illustrated.

3.1 Micro gas turbine

Micro gas turbines (MGT) are gas turbines with power rating ranging from a few kW and 100 kW. The adjective “micro” is due to the total redesign of the machines’ architecture with respect to standard gas turbines as a consequence of the downsizing. Indeed, the rotating parts present radial flows, a centrifugal compressor and a centripetal turbine (turbocharger) while the combustor usually has a reverse flow annular configuration in order to reduce the dimensions of the whole implant. This last component is the object of the investigation.

As already said, the steady operating conditions of this type of system allow to focus on the testing of more complex kinetic schemes, fuel compositions and combustion models. Therefore, in the present paragraph the study carried out on a combustor of a micro gas turbines with a nominal power output of 30 kW is illustrated.

The reference case was simulated with the natural gas, the study of the 30kW gas turbines was focused on the utilisation of hydrogen enriched NG, that seems an appealing solution to DF problems due to its positive stabilising effect on lean natural gas flame despite the well-known risk of flashback [81, 82, 83, 84].

The first geometry is based on the Capstone C30 [85]. The base-rating data are reported in Table 3.1.

Tab. 3.1: Base-rating data of Capstone C30.

Fuel flow rate [kg/s]	0.0026
Fuel energy rate [kW]	115.4
Fuel Heat rate [kJ/kWh]	14,208
Recovered Heat from exhaust [kW]	51.33
Fuel Energy Utilisation factor	0.695
Overall Electric efficiency	26.05%
CO ₂ [kg/h] (kg/kWh)	24.37 (0.812)

Starting from sketches available in literature [86] a CAD geometry that includes the external liner, the internal liner and the injector, was rebuilt by the authors through a reverse – engineering process by means of CATIA V5R17 (Figure 3.1). Actually, due to periodicity of the component it was possible to carry out the study only on a third of the domain, i.e., a 120° sector, so that both computational effort and computational time were drastically reduced.

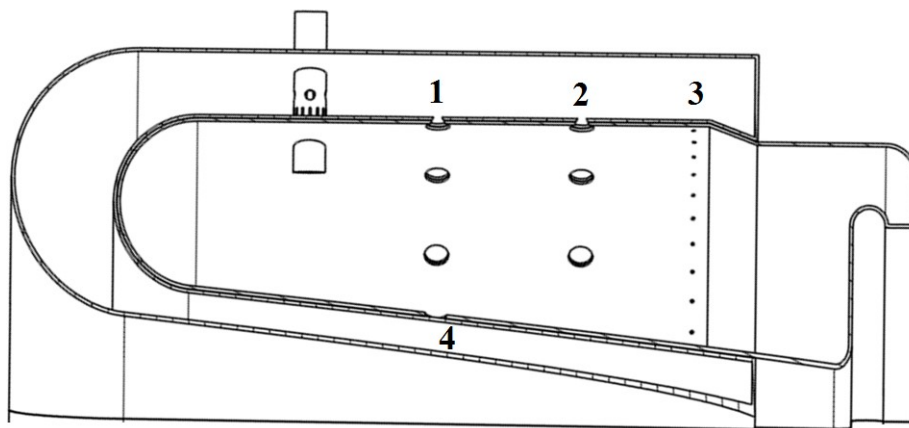


Fig. 3.1: Combustor section made with CATIA.

Air from the recuperator passes through the external liner, a small part of this air enters the injector via premix holes and swirl slots, while the main fraction enters the combustor core across holes located along the internal liner. Then the burned gases leave the combustor through a radial outflow to the turbine.

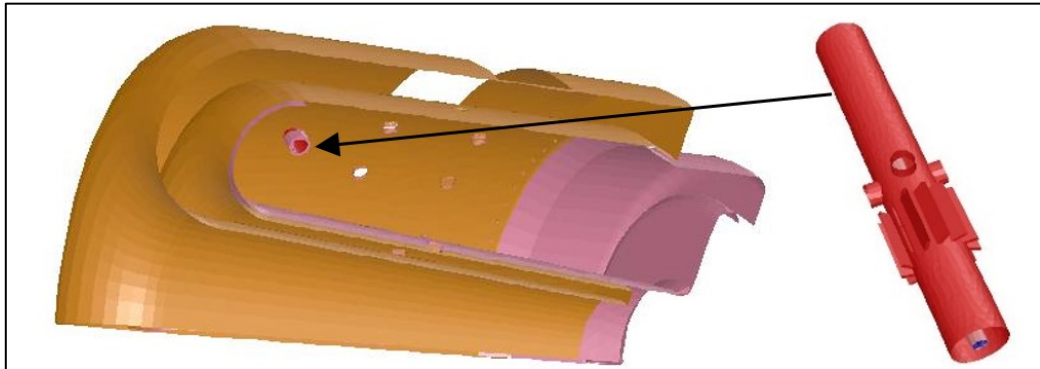


Fig. 3.2: Computational domain.

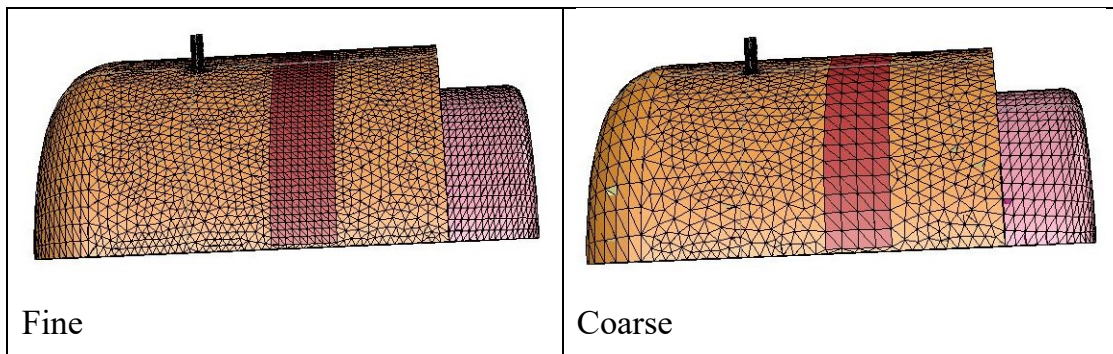


Fig. 3.3: Fine and coarse mesh.

Actually, the fluid domains which correspond to the volumes enclosed by the wall of the various parts, were obtained by filling all the casings: injector, internal core, external liner and all their holes and interstices as shown in Figure 3.2. The same Figure 3.2 provide a detailed description of the injector (on the right) and then of the air-fuel mixture formation through the premixing holes and vertical swirling slots before the fuel enters the combustor core. The swirl effect is ensured by deviating the slots from radial direction. However, the main focus of the study is the central pilot line. In standard operation it injects the fuel directly into the core when the MGT is

operating at part loads, usually below 70%, but the authors' proposal is to exploit it to be an alternate option for hydrogen injection.

Moreover, two meshes, whose data are reported in Table 3.2, were created to operate a sensitivity analysis (Figure 3.3).

Tab. 3.2: Details of the computational meshes.

Domain	Pilot	Premix	Liner	Core
Fine	1,350	33,000	130,000	240,000
Coarse	800	24,000	55,000	44,000

As demonstrated in paper [82] the coarse grid was considered as able to provide a fair approximation of more refined results with a reduced computational effort.

Regarding to the chemical kinetics, the authors have selected the methane three-step oxidation mechanism by Novosselov and Malte [87]. Such a scheme is completed, as well known, by a 5-equation set for the thermal and prompt NO formation (Table 3.3).

The scheme reported in Table 3.4 describes the oxidation mechanism of the other hydrocarbons present in Natural Gas (NG).

In addition, all the test cases involving hydrogen contents have been simulated with the Jachimowski reduced scheme [88]. Such a scheme includes the Zel'dovich reactions [89] in order to describe the oxidation process of hydrogen together with a correct model of the nitrogen chemistry in combustion (Table 3.5).

The CFD analysis was performed with the ANSYS-FLUENT solver where all the reaction schemes in Tables 3.3, 3.4 and 3.5 were implemented, and the EDC based method was adopted.

Tab. 3.3: Novosselov and Malte mechanism [87].

$CH_4 + \frac{3}{2}O_2 \rightarrow CO + 2H_2O$ $R_1 = 10^{13.354-0.004628p}[CH_4]^{1.3-0.01148p}[O_2]^{0.01426}[CO]^{0.1987}$ $\exp\left(-\frac{182342648 + 2.2398 \times 10^6 p}{RT}\right)$
$CO + \frac{1}{2}O_2 \rightarrow CO_2$ $R_2 = 10^{14.338+0.1091p}[CO]^{1.359-0.0109p}[H_2O]^{0.0912+0.0909p}[O_2]^{0.891+0.0127p}$ $\exp\left(-\frac{186216972 + 6.2438 \times 10^5 p}{RT}\right)$
$CO_2 \rightarrow CO + \frac{1}{2}O_2$ $R_3 = 10^{15.8144-0.07163p}[CO_2]$ $\exp\left(-\frac{5.3979 \times 10^8 - 2.7795 \times 10^6 p}{RT}\right)$
$N_2 + O_2 \rightarrow 2NO$ $R_4 = 10^{14.122+0.0376p}[CO]^{0.8888-0.0006p}[O_2]^{1.1805+0.0344p}$ $\exp\left(-\frac{388662872 + 1.0526 \times 10^6 p}{RT}\right)$
$N_2 + O_2 \rightarrow 2NO$ $R_5 = 10^{29.8327-4.7822 \log_{10}(p)}[CO]^{2.7911-0.04880p}[O_2]^{2.4613}$ $\exp\left(-\frac{509357210 + 5.8589 \times 10^6 p}{RT}\right)$
$N_2 + O_2 \rightarrow 2NO$ $R_6 = 10^{14.592}[N_2][H_2O]^{0.5}[O_2]^{0.25}T^{-0.7}\exp\left(-\frac{574979612}{RT}\right)$
$N_2 + O_2 \rightarrow 2NO$ $R_7 = 10^{10.317}[N_2][O_2]\exp\left(-\frac{439486354}{RT}\right)$
$N_2 + O_2 \rightarrow 2NO$ $R_8 = 10^{14.967}[N_2][O_2]^{0.5}T^{-0.5}\exp\left(-\frac{572826286}{RT}\right)$

Tab. 3.4: Hydrocarbons mechanism.

$C_2H_6 + \frac{7}{2}O_2 \rightarrow 2CO_2 + 3H_2O$ $R_9 = 6.186 \times 10^9 [C_2H_6]^{0.1} [O_2]^{1.65} \exp\left(-\frac{1.256 \times 10^8}{RT}\right)$
$C_3H_8 + \frac{7}{2}O_2 \rightarrow 3CO_2 + 4H_2O$ $R_{10} = 5.62 \times 10^9 [C_3H_8]^{0.1} [O_2]^{1.65} \exp\left(-\frac{1.256 \times 10^8}{RT}\right)$
$C_4H_{10} + \frac{13}{2}O_2 \rightarrow 4CO_2 + 5H_2O$ $R_{11} = 4.161 \times 10^9 [C_4H_{10}]^{0.15} [O_2]^{1.6} \exp\left(-\frac{1.256 \times 10^8}{RT}\right)$

A first comparison between the base-rating and off-design conditions is necessary to assess the behaviour of the flow mixing when the fuel is introduced in the combustion chamber from the premixer and from the pilot. In Table 3.6 the boundary conditions for the reference cases (NG Operation) are listed for the two load levels.

The methane reaction rates displayed in Figure 3.4 outlines the different combustion evolution in the two cases: at full load the ignition begins near the injector outlet due to the fuel/air premixing; at part load the unmixed fuel reaches the maximum value of the reaction rate farther from the injector, giving rise to different temperature distributions. This means that the employment of the pilot line for hydrogen supply simultaneously to the premixer one for the NG seems effective in order to avoid the early ignition and flashback problems of the latter fuel.

Five test cases were examined (Table 3.7). Cases #2 and #3 compared two different kinetic schemes when the hydrogen supply is set to 10% which is considered the upper limit to avoid flashback. However, cases #4 and #5 are used as demonstration of the validity of the solution proposed.

Tab. 3.5: Jachimowski and Zeldovich mechanisms.

$H + OH + M = H_2O + M$ $R_1 = 2.21 \times 10^{16} [H][OH] T^{-2}$
$H + H + M = H_2 + M$ $R_2 = 7.3 \times 10^{11} [H][H] T^{-1}$
$H_2 + O_2 = OH + OH$ $R_3 = 1.7 \times 10^{10} [H_2][O_2] \exp\left(-\frac{2.0083 \times 10^8}{RT}\right)$
$H + O_2 = OH + O$ $R_4 = 1.2 \times 10^{14} [H][O_2] T^{-0.91} \exp\left(-\frac{6.9086 \times 10^7}{RT}\right)$
$OH + H_2 = H_2O + H$ $R_5 = 2.2 \times 10^{10} [OH][H_2] \exp\left(-\frac{2.1548 \times 10^7}{RT}\right)$
$O + H_2 = OH + H$ $R_6 = 50.6 [O][H_2] T^{2.67} \exp\left(-\frac{2.6317 \times 10^7}{RT}\right)$
$OH + OH = H_2O + O$ $R_7 = 6.3 \times 10^9 [OH][OH] \exp\left(-\frac{4560560}{RT}\right)$
$N + N + M = N_2 + M$ $R_8 = 2.8 \times 10^{11} [N][N] T^{-0.8}$
$O + O + M = O_2 + M$ $R_9 = 1.1 \times 10^{11} [O][O] T^{-1}$
$N + O_2 = NO + O$ $R_{10} = 6400000 \times [N][O_2] T^1 \exp\left(-\frac{2.6359 \times 10^7}{RT}\right)$
$N + NO = N_2 + O$ $R_{11} = 1.6 \times 10^{10} [N][NO]$
$N + OH = NO + H$ $R_{12} = 6.3 \times 10^8 [N][OH] T^{0.5}$

Tab. 3.6 Boundary condition data for the combustion simulation

	Base Rating	70% Load
Combustor Inlet Temperature (K)	870	883
Combustor Outlet Pressure (bar)	3.20	2.62
Fuel mass flow rate (kg/s)	0.00292	0.00183
Oxidant mass flow rate (kg/s)	0.306	0.270
Overall equivalence ratio	0.143	0.102

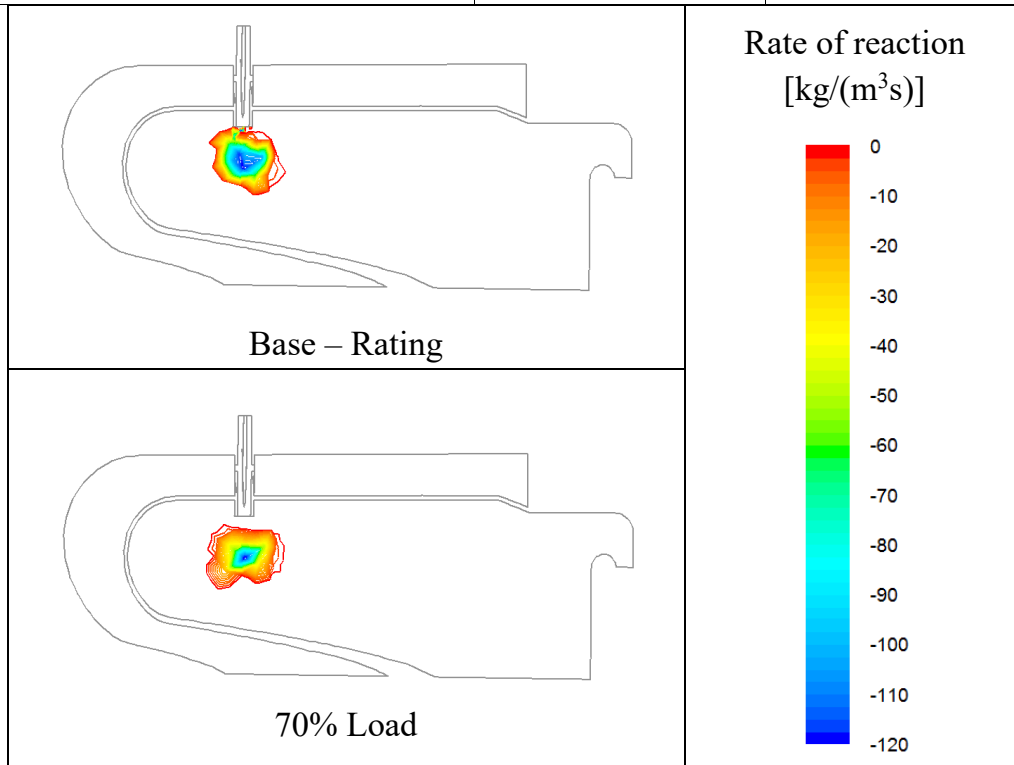


Fig. 3.4 Comparison of methane reaction rates at base-rating and part-load.

Tab. 3.7: Test cases

Case #1	Base - Rating, Natural Gas from premixer
Case #2	90% NG from premixer - 10% H ₂ from pilot (Nitric Oxides from Novosellov and Malte scheme)
Case #3	90% NG from premixer - 10% H ₂ from pilot (Nitric Oxides from Jachimowski scheme)
Case #4	75% NG from premixer - 25% H ₂ from pilot (Nitric Oxides from Jachimowski scheme)
Case #5	75% NG- 25% H ₂ mixture from premixer (Nitric Oxides from Jachimowski scheme)

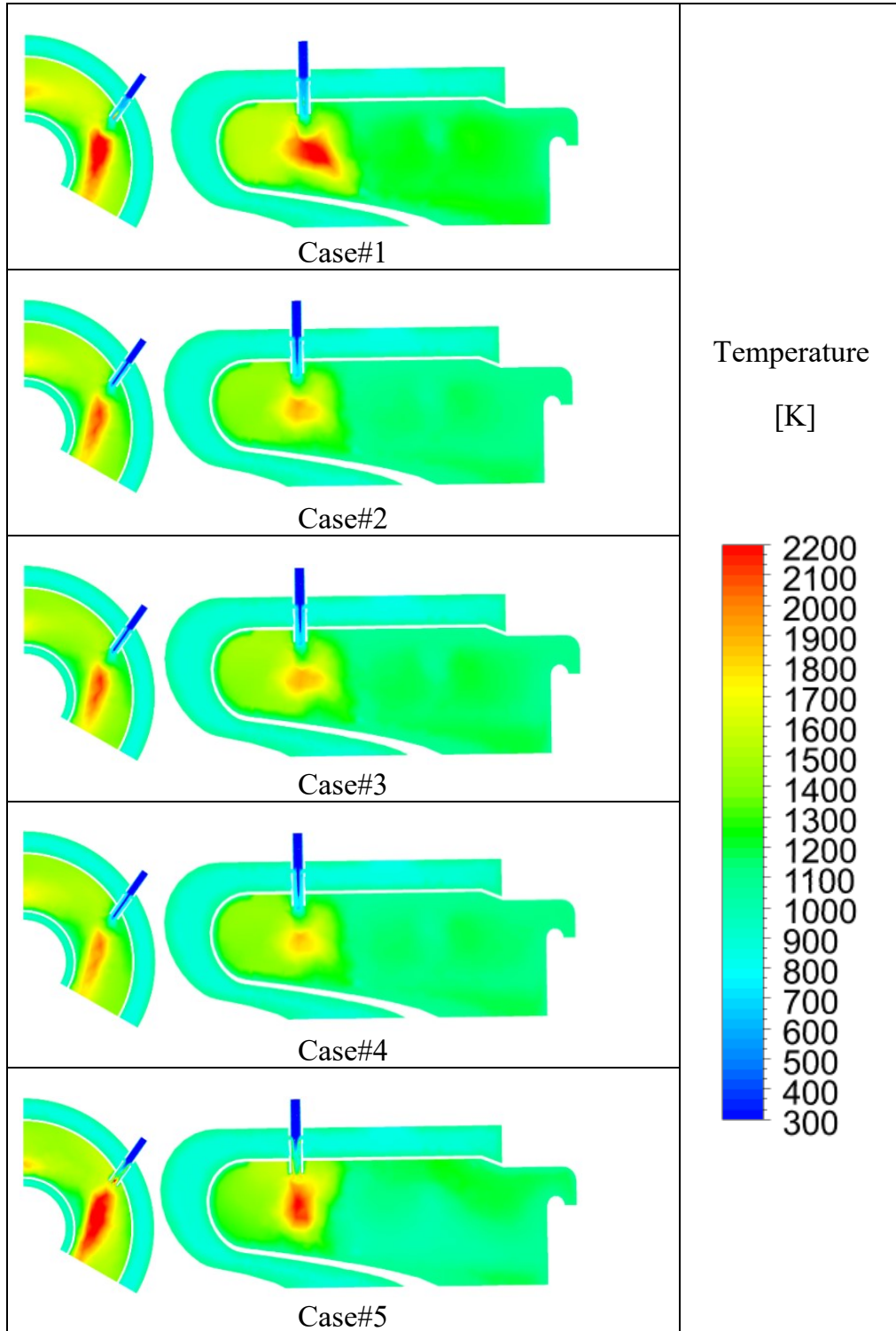


Fig. 3.5 Temperature distributions in the combustor.

The temperature distributions in Figure 3.5 also put into evidence that the combustor behaviour approaches the typical one of a RQL combustor. This effect is mainly due to the poor concentration of air inside the primary region

of the core. The air flow delivery from the secondary and dilution holes produces a typical quick mixing with the combustion products with a consequent steep decrease in temperature. The combustion completion takes place, therefore, under lean conditions and the nitric oxide formation is strongly decelerated.

Tab. 3.8 Volume averaged and outlet properties from CFD.

Case	T _{max} [K]	T _{out} [K]	NO [ppm]	CO [ppm]	Burned CH ₄ [%]	Burned H ₂ [%]
#1	2567	1206	5.07	462	99.86	--
#2	2274	1159	3.82	841	99.60	99.99
#3	2296	1178	5.38	1153	99.80	99.99
#4	2140	1178	5.88	836	99.63	99.87
#5	2717	1153	8.01	728	99.79	99.99

From the results in Table 3.8, it is noted that in all the cases the value of the NO calculated are close to that provided by the manufacturer, meaning that the kinetic mechanisms can well describe the chemistry of the process. In cases #2 and #3, with the 10% of H₂ from pilot, the maximum temperature and, consequently, the NO values decrease. On the other hand, despite the lower peak of temperature in the primary zone in case #4 presents higher values of NO amount since hydrogen has the higher flame temperature. Furthermore, case #5 highlight the highest temperature levels and NO emissions due to the intake of hydrogen in the premixing duct which leads to an unusual combustion. Such a phenomenon is highlighted in the Figure 3.6 where a comparison between the H₂ reaction rate distributions in a larger picture of the injector plane is shown. In the case #5, as expected, the ignition starts in the premixing line. Therefore, the proposed supply solution appears to be effective for the combined use of hydrogen and natural gas in order to avoid a pre-ignition inside the premixing line and gives the possibility of reaching higher H₂/NG ratios. Moreover, the results in Table 3.8 put into evidence that a nearly complete oxidation of both methane and hydrogen.

Nevertheless, the same Table 3.8 indicates that non-negligible amounts of carbon monoxide are produced by the several combustion regimes. Such amounts are generally increased in all cases with hydrogen, so that a slight decrease in combustion efficiency should be taken into account.

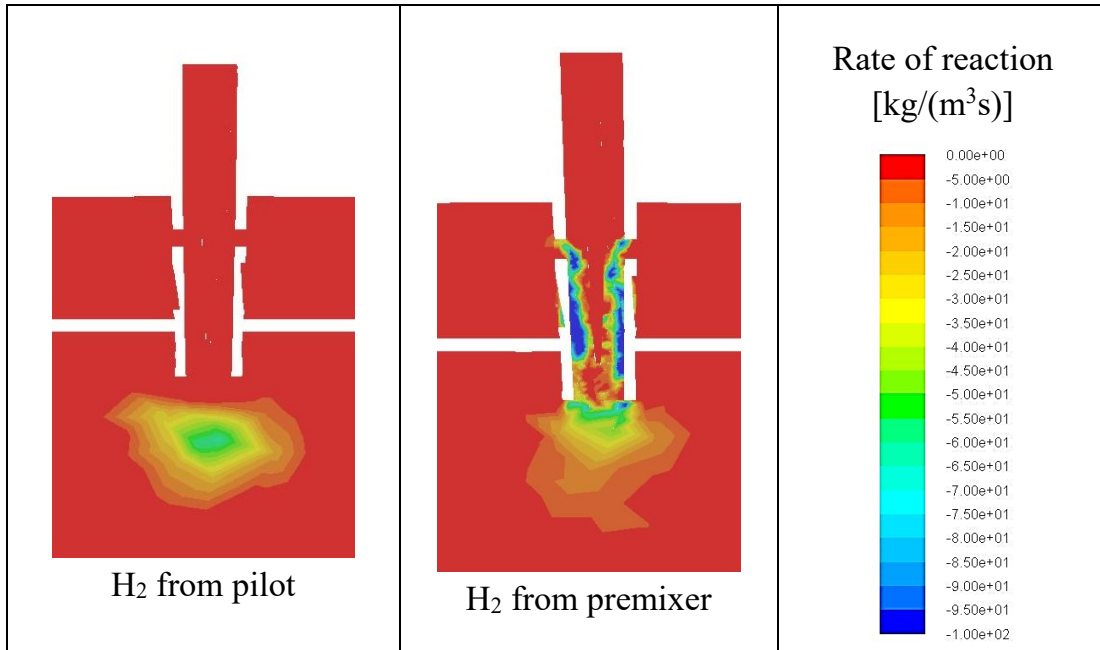


Fig. 3.6 Comparison between the reaction rate of H₂ when injected from the pilot or the premixer.

Tab. 3.9 Maximum reaction rates.

Case	CH ₄ oxidation rate [kg/(m ³ s)]	H ₂ oxidation rate [kg/(m ³ s)]
#2	5.82	28.49
#3	12.77	27.92
#4	14.28	23.46
#5	30.77	38.13

Finally, in Table 3.9 the reaction rates for CH₄ and H₂ are compared. As it is possible to notice, in all cases the maximum reaction rate for hydrogen is higher than the rate for methane. Also, Figure 3.7 evidences that the zones of higher methane consumption are located in correspondence of the zone of higher reaction rates of hydrogen. This means that hydrogen represents a sort

of pilot for the ignition of methane, reproducing the same behaviour of diesel vapour in Dual Fuel combustion.

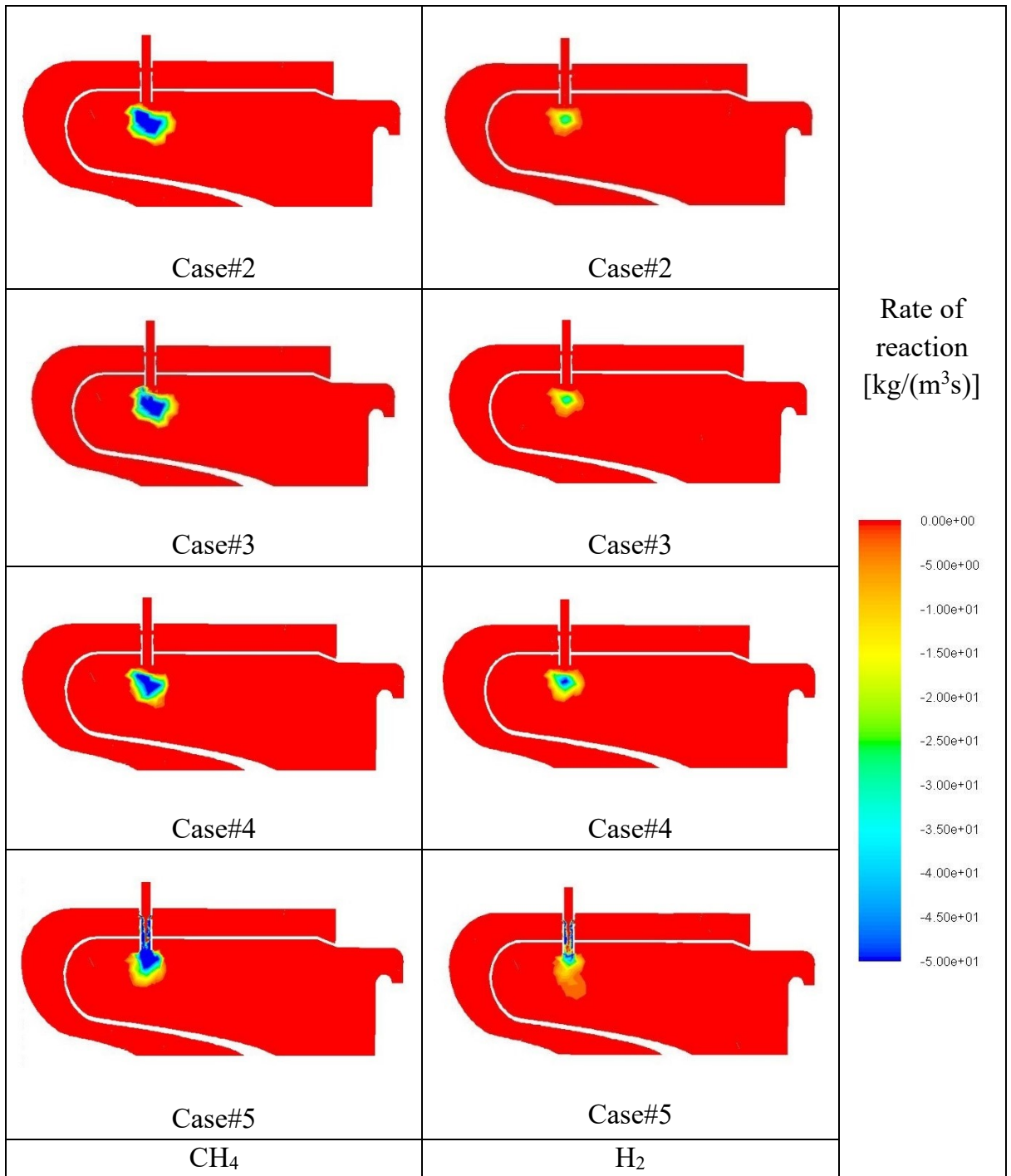


Fig. 3.7 CH₄ and H₂ rate of reaction distributions in the combustor (blue regions designate the maximum intensity).

Another important experience is reported in paper [84], where the Eddy Dissipation Concept, which is reliable in the treatment of multiple reactions,

is compared with flamelet-PDF based approach. The mixture fraction theory, as widely illustrated in Chapter 2, can be applied to non-premixed and partially premixed flames where a strong dependence on convection and diffusion caused by turbulence is observed. Once mixed, the chemistry can be modelled as being in chemical equilibrium (CE), near chemical equilibrium with the Steady Laminar Flamelet (SLF) or far from it with the Unsteady Laminar Flamelet model. The kinetic mechanisms of Novoselov and Jachimowski (Tables 3.3, 3.4 and 3.5) are used, respectively for the hydrocarbons oxidation, and for the complex hydrogen kinetics. In order to evaluate the quality of the results, the reference case was also simulated with the well-established GRIMECH mechanisms consisting of 53 species and 325 reactions, since it includes detailed kinetics for both hydrocarbons and hydrogen.

In Table 3.10 the test cases with the relative model and configuration are listed, the simulations were performed in accordance with the same boundary conditions reported in Table 3.6 for the full load.

Tab. 3.10: Test cases.

Case	Model	Fuel
#4	EDC	NG
#5	EDC (GRIMECH)	NG
#6	SLF	NG
#7	CE	NG
#8	SLF	75%NG + 25%H ₂ Premixed
#9	CE	75%NG + 25%H ₂ Separated fuel streams

It is important to highlight that the use of the CE model was necessary because it is the only model in ANSYS-FLUENT that allows two distinct fuel streams, with two different compositions to be set. Actually, before

utilising hydrogen, first attempts with these models have been carried out by suppling the MGT combustor with natural gas only.

Tab. 3.11: Volume averaged and outlet properties from CFD.

Case	T _{max} [K]	T _{out} [K]	NO [ppm]	CO [ppm]	Burned CH ₄ [%]	Burned H ₂ [%]
#4	2567	1206	5.07	462	99.88	--
#5	2458.6	1263	38	1602	99.88	--
#6	2475.8	1116	417	9.3e-2	77.62	--
#7	2504.6	1093.7	163	7.6e-10	70.47	--
#8	2543	1086	276	0.63	68.79	62.79
#9	2540	1129.8	607	1.36	83.31	83.31

From Table 3.11 it is possible to see that in cases with EDC model combustion is highly efficient and NO_x emissions comply with the manufacturer's data. Even if the cases with the PPC models present lower temperature at outlet, a higher value of NO_x has been calculated; however, CO concentrations are near to zero but in the two cases with hydrogen, CH₄ is not able to oxide completely maybe due to the presence of hydrogen itself.

Figure 3.8 shows the temperature's levels; case #4 presents higher values while case #5 is characterised by a wider zone at high temperature. It is important to notice that cases #6 and #7, both employing the pdf tables but with either the flamelet or the chemical equilibrium approach, do not present differences. For this reason, it is possible to try a comparison between two modes of injecting H₂ in the combustor. The only PPC model that allows utilisation of two different fuel streams is the CE, so in case #8 25% of hydrogen is mixed with the NG in the premix line, while in case #9 the same amount of hydrogen is injected separately from the pilot line.

This time, the early hydrogen ignition occurs in both cases #8 and #9. In the former as already proven in [82] this behaviour was expected, while for case #9 it can be explained by two different reasons: the first one is related to the CE model, apparently even without the high reactivity of hydrogen, natural

gas can reach the condition of chemical equilibrium; the second one is that only the 75% of mass fuel is injected in the premix so it is possible that there is more air that can oxidise the fuel.

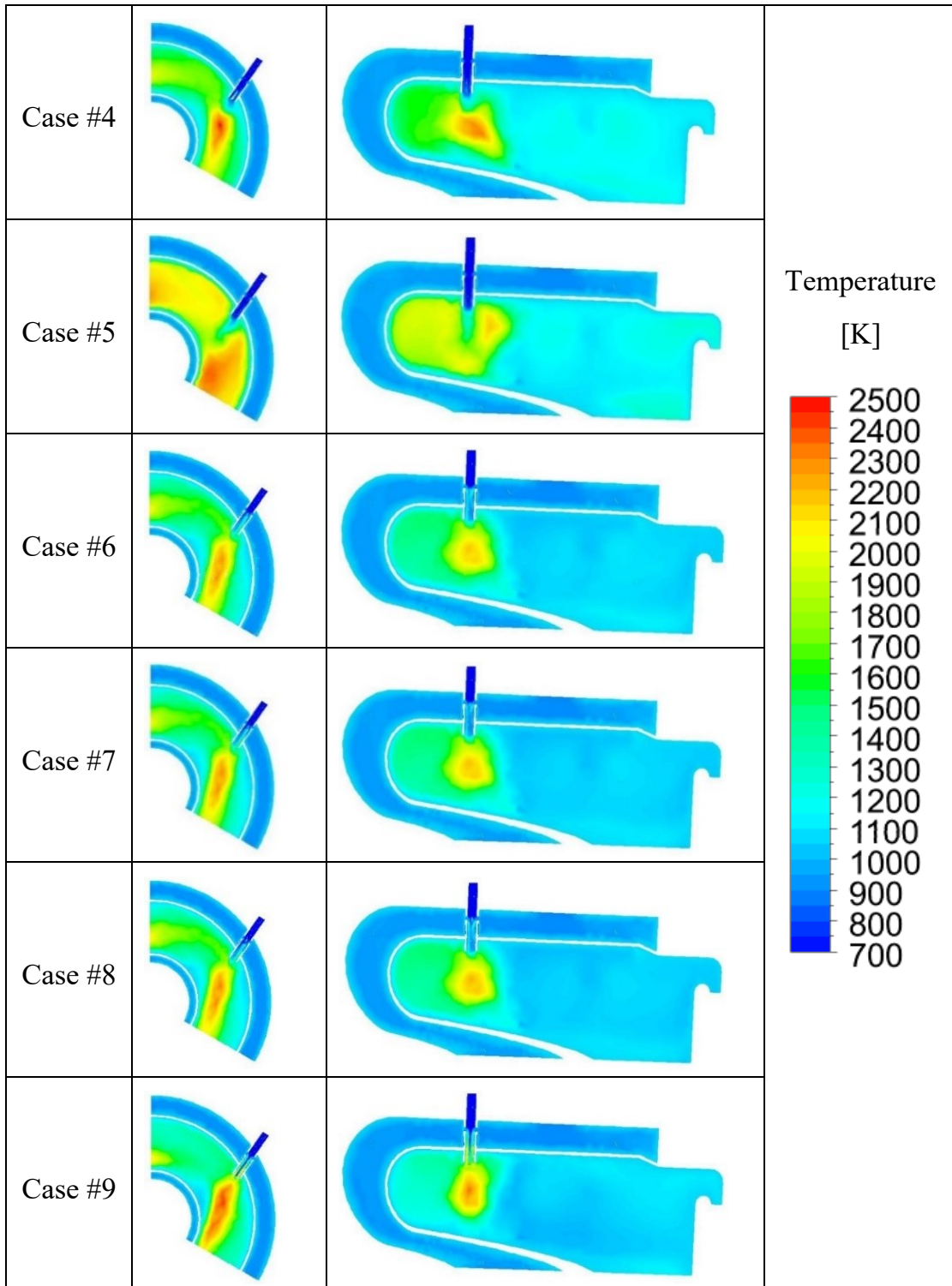


Fig. 3.8: Temperature distributions.

3.2 Dual Fuel diesel engines

Previous to the studies directly involving the Ph. D candidate, the Dual Fuel technology has represented the object of investigation of a research group in the University of Naples “Federico II”. In the last decade, it has collected a series of results that represent the basis for this thesis. To better understand the evolution of the work carried out by the author, an overview of the previous findings is reported in this section.

The first studies [57, 58, 59] were focused on the evaluation of the CFD potential to predict the main features of combustion and pollutant formation of a common rail diesel engine supplied with natural gas and diesel oil, under different conditions induced by different choices of the operating parameters and fuel ratio. Indeed, the calculations were compared with experimental data obtained on a light duty direct injection diesel engine at steady state test bench whose characteristics are outlined in Table 3.12:

Tab. 3.12: Characteristics of the engine used in the experimental activity.

Engine	1.9 Multijet
Type	4 stroke CI
Number of cylinders	4
Valves/cylinder	2
Bore [mm]	82
Stroke [mm]	90.4
Cylinder volume displacement [cm ³]	480
Maximum power [kW]	88
Maximum torque [Nm]	255 @ 2,000 rpm
Compression ratio	18:1

The experimental activity was carried out at Istituto Motori (CNR) on a diesel engine fuelled by either diesel oil (full diesel operation, FD) or natural

gas ignited by a pilot diesel injection (dual fuel operation, DF). In FD mode, the engine does not require any structural modification and it is able to operate with pure diesel oil, since volumetric compression ratio and injection system of the original diesel engine are unchanged.

The properties of the natural gas used are displayed in Table 3.13.

Tab. 3.13: Fuel properties.

Methane [% vol]	85.44
Ethane [% vol]	8.38
Propane [% vol]	1.71
Butane [% vol]	0.47
α_{st}	15.73
LVH [MJ/kg]	45.83
ρ [kg/Std ^m 3]	0.83

An engine condition (i.e. 2,000 rpm/100 Nm) was tested varying diesel oil quantity from FD to DF up to 90% of diesel replacement with NG. In Table 3.14 the injection timing and the amount of fuel are listed for each experimental operating condition.

Tab. 3.14: Experimental operating conditions.

Test case	Pilot		Main		Fuel [mg/cycle]
	SOI [c.a.]	EOI [c.a.]	SOI [c.a.]	EOI [c.a.]	
Full Diesel	341.5	345	362.5	375.5	20.792
CH ₄ =28%	342	345.5	362.5	372	14.552
CH ₄ =50%	342	345.5	363	374	9.851
CH ₄ =72%	342	345.5	362.5	372.5	4.582
CH ₄ =90%	342	345.5	362.5	371.5	1.009

The natural gas amount was increased acting on gas injection time, while simultaneously the diesel mass flow rate was reduced acting only on the

injection pressure, leaving the injection advance and the pilot and the main duration unchanged with respect to the FD mode. In this way, the liquid fuel injection conditions have been the same in FD and DF operation, since the test points have been set at the same injection advance both in FD and DF mode.

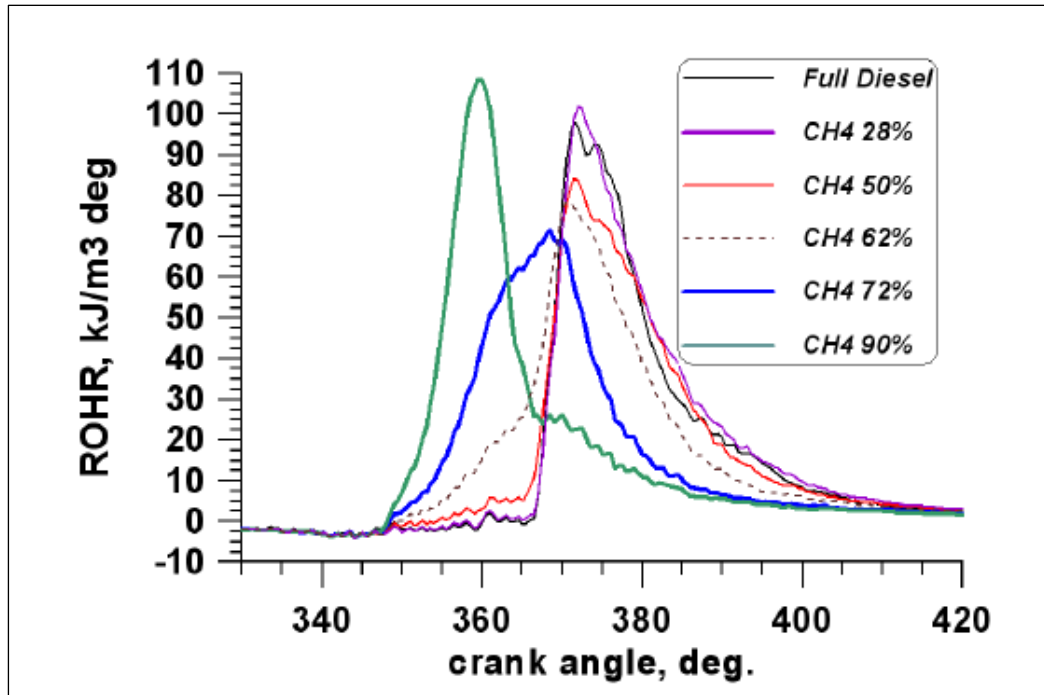


Fig. 3.9: Experimental Rate of Heat Releases by varying the NG ratio.

In Figure 3.9 the rate of heat release is plotted for a better understanding of combustion development by varying natural gas ratio. These operating conditions are characterised by high THC emissions and low efficiency. On the other hand, at high power output the combustion conditions achieve a relevant improvement but, since there is at least one ignition start point for each diesel injector hole, the combustion speed can become so high as to induce knocking, despite of the high methane octane number (130). This behaviour causes difficulties for an effective control of the DF combustion.

In the $\text{CH}_4 = 90\%$ case the start of natural gas ignition is anticipated with a sudden slope causing a formation of NO_x certainly greater (Figure 3.10) while the CO contents decrease (Figure 3.11).

The experimental activity was used as a validating tool for the evaluation of the numerical calculations' potential. It should be highlighted that the authors' approach to the study of the dual fuel diesel engine, in this first phase, was different from the classical numerical-experimental matching. Indeed, according with the experimental tests, some numerical results obtained in similar operating conditions were analysed although some key aspects differ considerably.

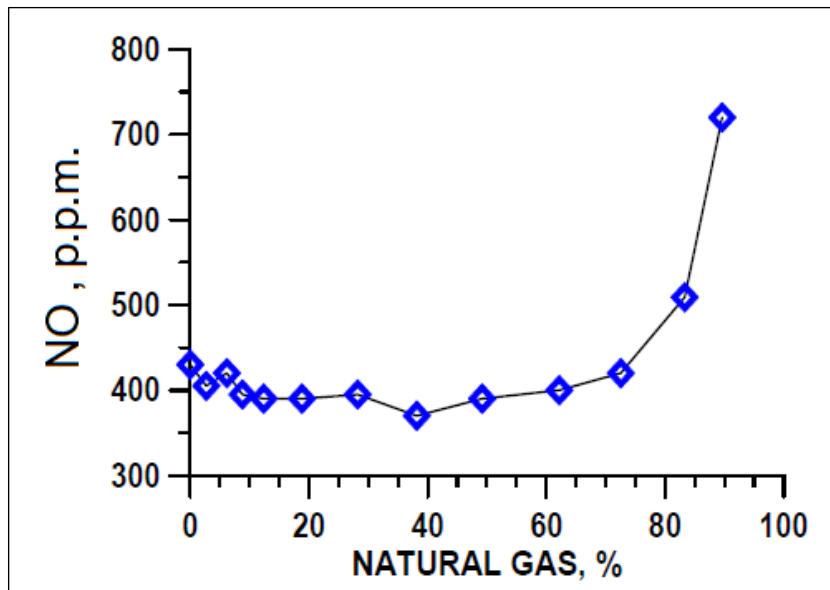


Fig. 3.10: Experimental mass fraction of NO.

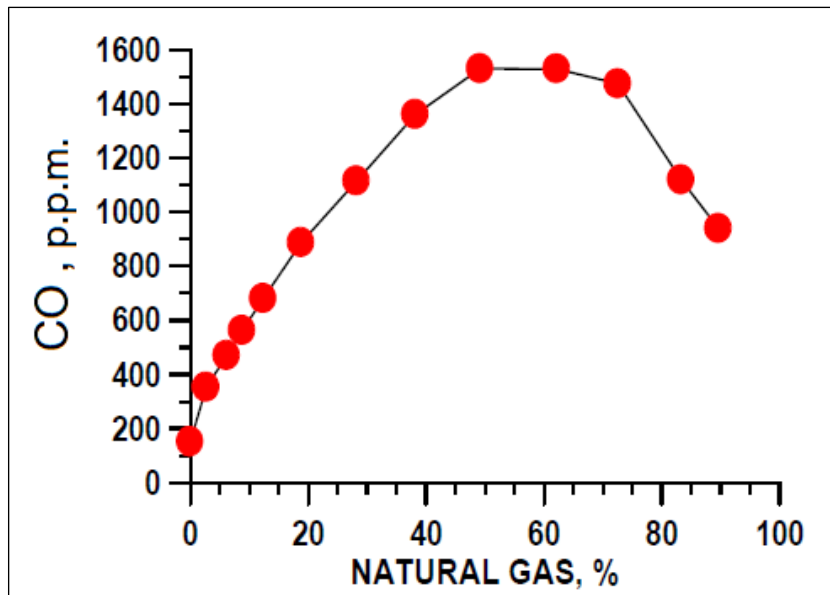


Fig. 3.11: Experimental mass fraction of CO.

Since, a mesh grid of the actual engine geometry was not available, the calculations were carried out on a different geometry which, as reported in Table 3.15, has almost the same cylinder displacement but different volumetric pressure ratio and external duct shape. In addition, the cylinder considered for the CFD is a four-valve one, while the engine at the test bed has only two valves per cylinder.

Tab. 3.15: Characteristics of the engine used in the numerical activity.

Engine	3.0 Multijet
Type	4 stroke CI
Number of cylinders	6
Valves/cylinder	4
Bore [mm]	84
Stroke [mm]	90
Cylinder volume displacement [cm ³]	499
Compression ratio	16:1

The cylinder and duct structured dynamic mesh (Figure 3.12) was obtained by using the ANSYS-ICEM CFD meshing tool. The multi-block structured Cartesian grid was set up as a result of the mesh generation consistent with the valve geometry. The grid size independence was reached with a mesh of 104,000 cells, the cylinder and bowl volume discretization being of nearly 58,000 and 5000 cells respectively. It is worth-noting that such a reduced mesh size produced, however, a fair convergence of the results if compared with those obtained with more refined grids, also due to the well-known robustness of the KIVA3-V solver: this allowed the development of multiple numerical cases in a reasonable computational time.

In order to examine the dual fuel combustion process in-cylinder and to explore, as stated above, the potential, especially in terms of emissions, of this new technology the CFD solver KIVA-3V was adopted.

Prior to proceeding with the CFD computations, preliminary investigations were carried out to determine the correct setting of the atomisation models for characterising the liquid spray pattern inside the cylinder.

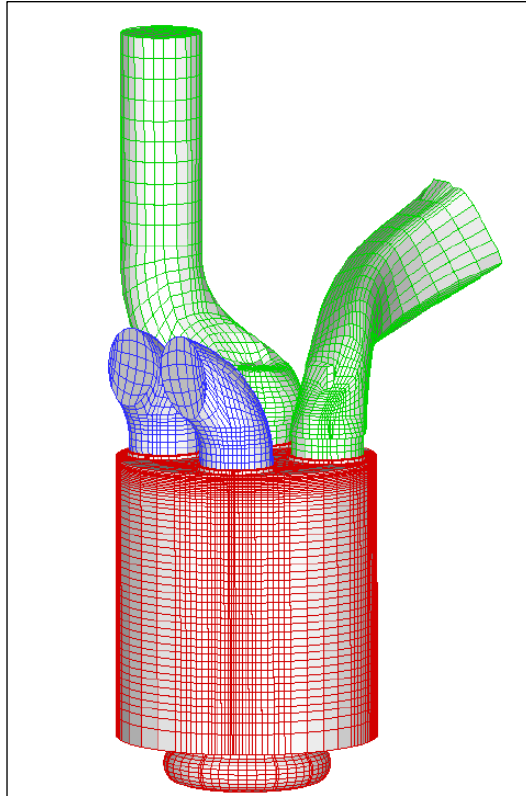


Fig. 3.12: Computational domain.

Three atomisation models were analysed for the selection of the most appropriate to determine the correct setting of the atomisation models for characterising the liquid spray pattern inside the cylinder: the TAB model, the WAVE model and the KHRT model. The WAVE model appeared to match better the experimental data with a B_1 constant set in the 5 – 7 range. The Finite rate – Eddy dissipation approach is employed for the assessment of the oxidation of the two fuels through the kinetic mechanism illustrated in Table 3.18 [90]. The self-ignition of diesel fuel is governed by the Stringer relationships [91]; while two empirical correlations for the auto-ignition delay time of methane are used: the first one was generated by Spadaccini et al. [92] whose validity is limited to temperatures of 1,300 K and above, and the second one by Li and Williams [93] for the low temperatures defined as

less than 1,300 K. The combustion simulation is completed by a system of chemical kinetic equations for the mechanism of thermal nitric oxide formation [89]. However, the computation of the ignition delay is activated by starting from an auto-ignition threshold that was set at 1,100K.

Tab. 3.16: Kinetic mechanism [90].

$1. C_{12}H_{26} + 37/2 O_2 \rightarrow 12CO_2 + 13H_2O$ $R_{f1} = 3.0 \times 10^{11} [C_{12}H_{26}]^{0.25} [O_2]^{1.5} \exp\left(-\frac{15,780}{T}\right)$ $R_{b1} = 0$
$2. CH_4 + 3/2 O_2 \rightarrow CO + 2H_2O$ $R_{f2} = 10^{15.220} [CH_4]^{1.460} [O_2]^{0.5217} \exp\left(-\frac{20,643}{T}\right)$ $R_{b2} = 0$
$3. CO + 1/2 O_2 \rightarrow CO_2$ $R_{f3} = 10^{14.902} [CO]^{1.6904} [O_2]^{1.570} \exp\left(-\frac{11,613}{T}\right)$ $R_{b3} = 10^{14.349} [CO_2]^{1.0} \exp\left(-\frac{62,281}{T}\right)$

Unlike the experimental tests, where the diesel oil injection consists of a pilot and a main injection, in the numerical simulations only a main injection was set for both FD and DF cases. Moreover, the fuel injection timing was determined in order to produce, in all cases, the auto-ignition at approximately the same crank angle.

The results of the CFD computations reported in Table 3.17, show that all cases are characterised by almost the same level of indicated mean effective pressure (IMEP) with a slight decrease for increasing NG rates and a consequent decay in thermal efficiency.

Tab. 3.17: Numerical results.

CH ₄ [%]	IMEP [bar]	T _{out} at EVO [K]	CO ₂ at EVO [%]	CO ₂ Index [kg/kWh]
0	6.77	1093	10.14	0.750
28	6.49	1022	9.95	0.765
50	6.77	1036	9.27	0.686
72	6.61	1275	8.28	0.625
90	6.03	1243	7.95	0.658

On the opposite, the enhancement of the outlet temperature implies a different response of the turbocharging system when the engine is operating in dual fuel mode. Most important is the reduction of CO₂ content and CO₂ index when increasing the CH₄ rate which demonstrate the effective benefit attainable from the dual fuel concept adoption.

The pressure cycles, displayed in Figure 3.13, refer to the most significant cases. It is possible to notice that, by increasing the methane rate, the shape of the pressure cycles and the peak pressure positions and levels change, due to a different combustion development. The distributions in a bowl meridional section in Figure 3.14 also confirm that the methane combustion in the 90% case induces higher temperature peaks in proximity of TDC with respect to the 50% case because of a sudden growing to a full combustion immediately after the pilot injection start.

The Figure 3.15 shows the NO distribution at the same crank angle and the highest concentration is present in the 90% case, as expected.

The comparison of numerical and experimental results outlined in Figure 3.16, evidences that a good agreement can be found in terms of in-cylinder pressures. The enhanced peaks at the highest values of methane (or NG) contents confirms that an optimization of the injection timing is necessary to ensure a regular combustion development.

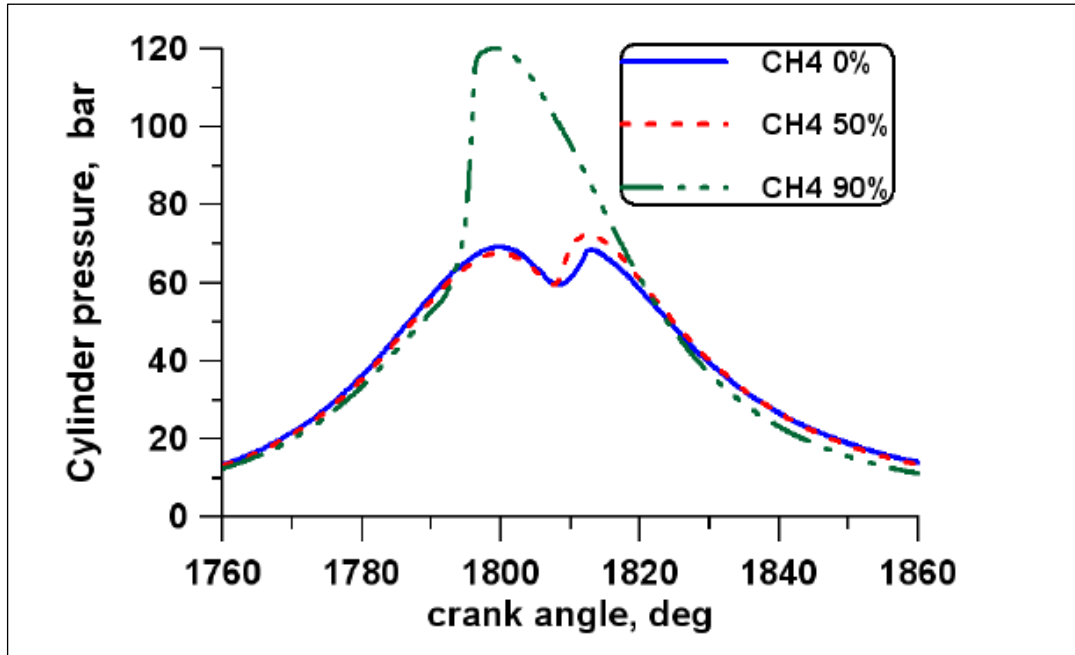


Fig. 3.13: In-cylinder pressure in FD and DF mode at different NG rates.

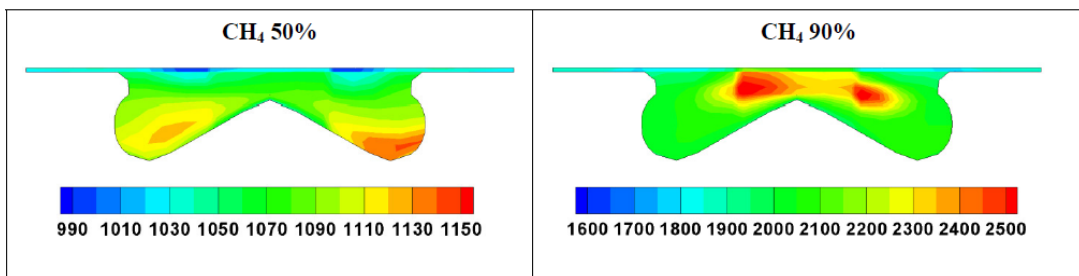


Fig. 3.14: Temperature distributions [K] for different CH₄ ratios at TDC.

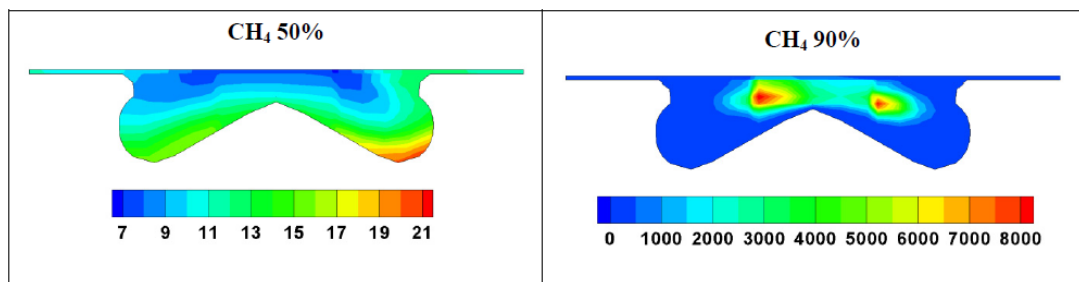


Fig. 3.15: NO distributions [ppm] for different CH₄ ratios at TDC.

In particular, for low methane ratio (i.e. up to 50%) the pressure cycle presents a double peak that is due to the delayed timing of the main injection of the diesel oil, which is, then, the real responsible of the ignition of the methane-air mixture ignition.

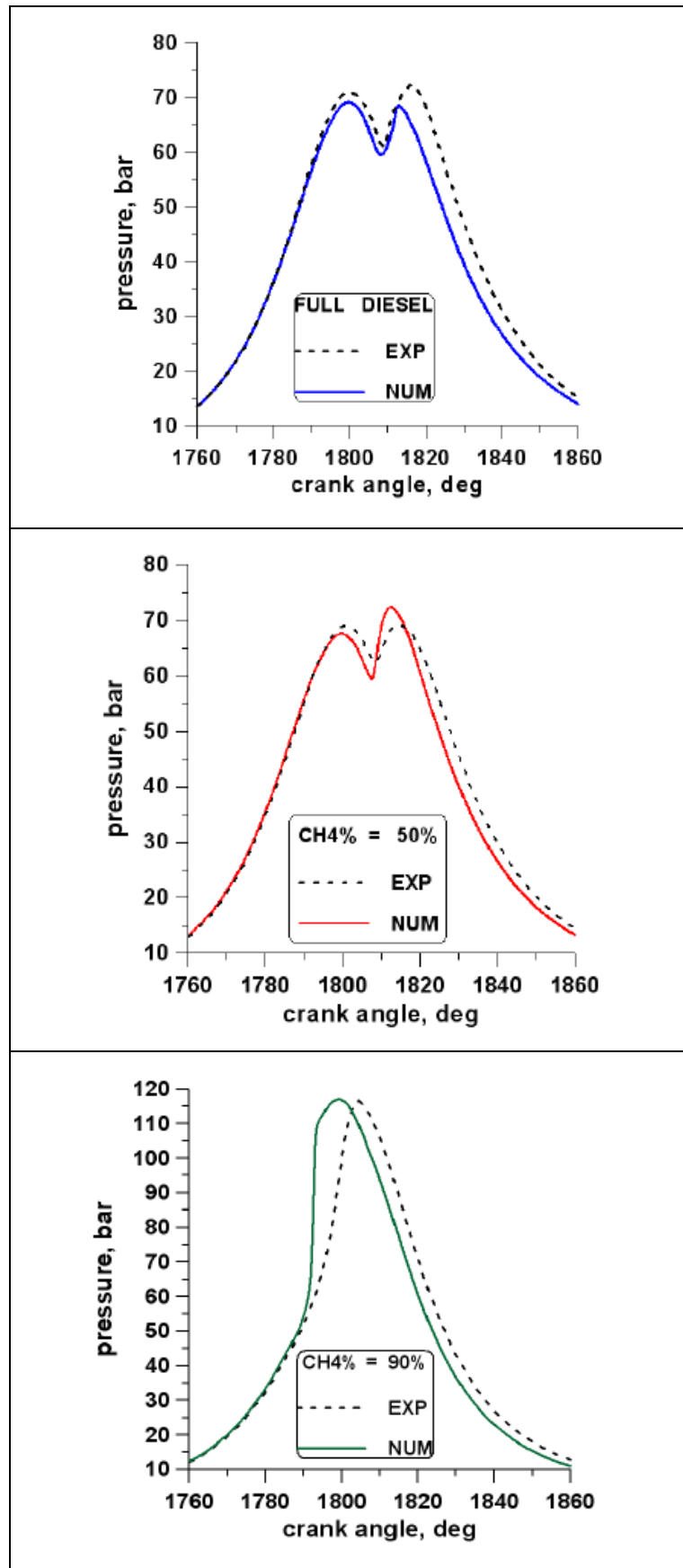


Fig. 3.16: Comparison of pressure cycles at different CH₄ rates.

On the contrary, at $\text{CH}_4 = 90\%$, it is evident that the mixture ignition occurs after the pilot injection but before the main injection and in advance with respect to the TDC. This explains the single peak and the steeper pressure rise that can even lead to knock.

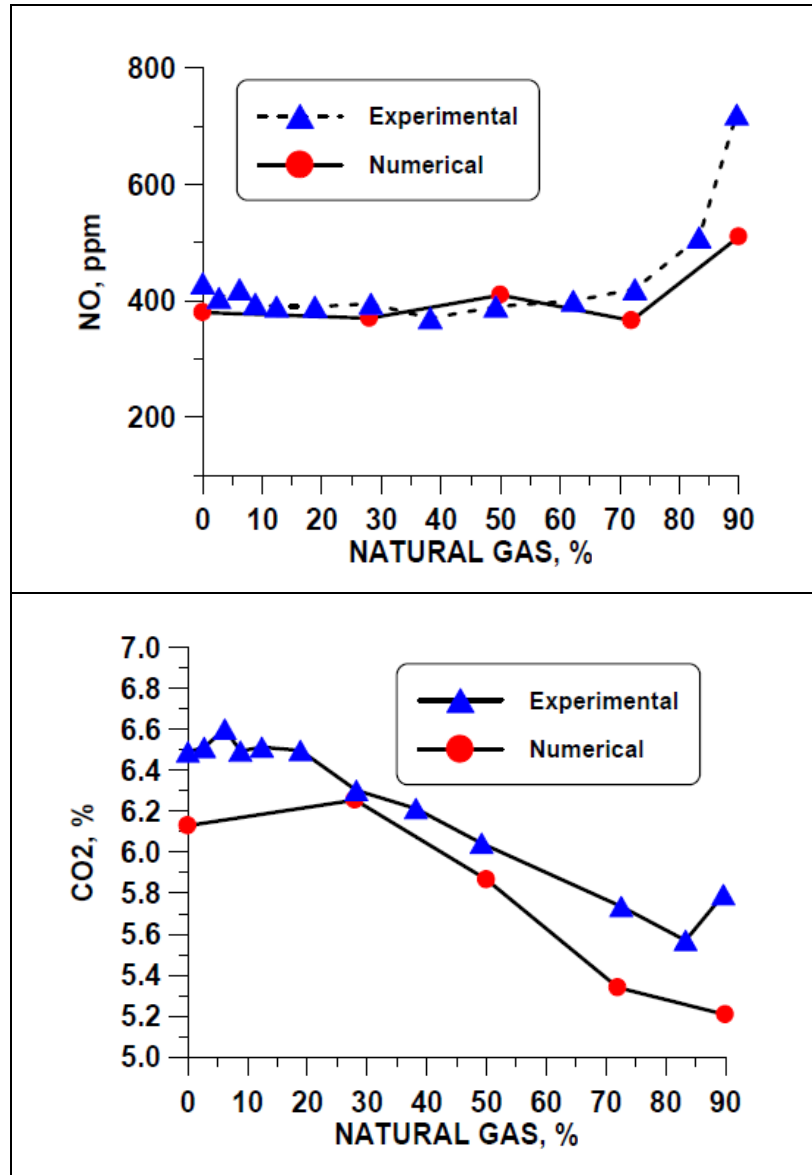


Fig. 3.17: Comparison of experimental and numerical NO and CO₂ fractions. Finally, by examining the CO₂ and NO levels in Figure 3.17, the experimental and numerical levels trends show a reasonable accordance in terms of variation of these species with the NG contents. Both numerical and experimental results suggest an increase of NO for the higher ratios of CH₄,

while a slight decrease in the CO₂ fraction is obtained because of the diminished H/C ratio in the fuel blend. It is worth-noting that the typical trade-off between these noxious species can be observed up to nearly 40 – 50% of methane rate. Beyond such limits, a simultaneous reduction in both pollutants occurs as a consequence of the increased air/fuel ratios together with the variations in the injection setup of the diesel fuel, like previously discussed. NG rate at 70 – 90% levels lead to conditions close to knocking and to a relevant increase of nitric oxides.

Such results point out that the CFD based activity is able to predict the engine response to different rates of natural gas independently of the actual engine geometry. However, in papers [60, 61] the authors discussed the results of a numerical study on a domain that precisely reproduces the geometry of the actual engine whose characteristics are listed in Table 3.14. In particular, based on a new set of experimental tests the effect of different injection timings on performance and pollutant fractions were analysed. Two data sets were originated, one in FD and the other one in the DF operation with the same boundary conditions (i.e. air mass flow rate, injection advance etc.) for two different loads (50 and 100 Nm) at 2,000 rpm. In each test case the only difference between FD and DF mode is the decreased amount of diesel fuel, achieved by a reduction of the main injection duration, and compensated by the injection of the gaseous fuel in the intake manifold to keep the same engine torque. For each engine operating condition, several diesel injection timings were tested. In particular, they were modified from extremely advanced to largely delayed injections, with respect to the optimal value adopted in full diesel condition. In the investigated test cases, the amount of diesel oil was fixed at a minimum value (less than 20%), at given load and speed, by varying the injection timing (Table 3.18). As a consequence, the natural gas amount was automatically regulated and its measured value was kept almost constant, i.e. nearly the 80% of the total fuel at 100 Nm and

about 75% at 50 Nm. The composition of the natural gas used during the experimental activity is the same as already reported in Table 3.13.

Tab. 3.18: Testing operating conditions.

Test case	Start of Pilot BTDC	Pilot duration [CAD]	Main duration [CAD]	Rail Pressure [bar]
FD 100 Nm	17	3.0	8.0	810
	23	3.0	8.7	793
	27	3.0	8.0	775
	32	3.0	8.7	795
FD 50 Nm	15	3.2	8.0	591
	20	3.0	8.1	568
	26	3.6	8.0	565
	29	3.9	7.5	565
DF 100 Nm 80% NG	17	3.0	5.0	815
	23	3.0	4.6	810
	27	3.0	4.1	809
	33	3.0	4.0	809
DF 50 Nm 75 % NG	16	4.0	5.1	626
	22	3.6	5.5	626
	27	3.1	5.0	625
	31	3.7	4.7	624

In Figure 3.18 the trend of the measured emissions in FD and DF are compared. In Figure 3.18 the experimental NO trends show a reduced amount of the NO emissions in the dual fuel mode operations, compared with the full diesel one, especially at part load operation. Also, the values decrease for lower injection advances due to a milder combustion. The CO and HC emissions (Figures 3.18.b and c), as expected, present an opposite trend with respect to the NO one, and the values in the dual fuel mode at 50 Nm are higher due to a not complete combustion. Moreover, in Figure 3.18.c the emission of HC in full diesel are not reported because they are considered negligible if compared with the levels of the dual fuel cases for all injection advances.

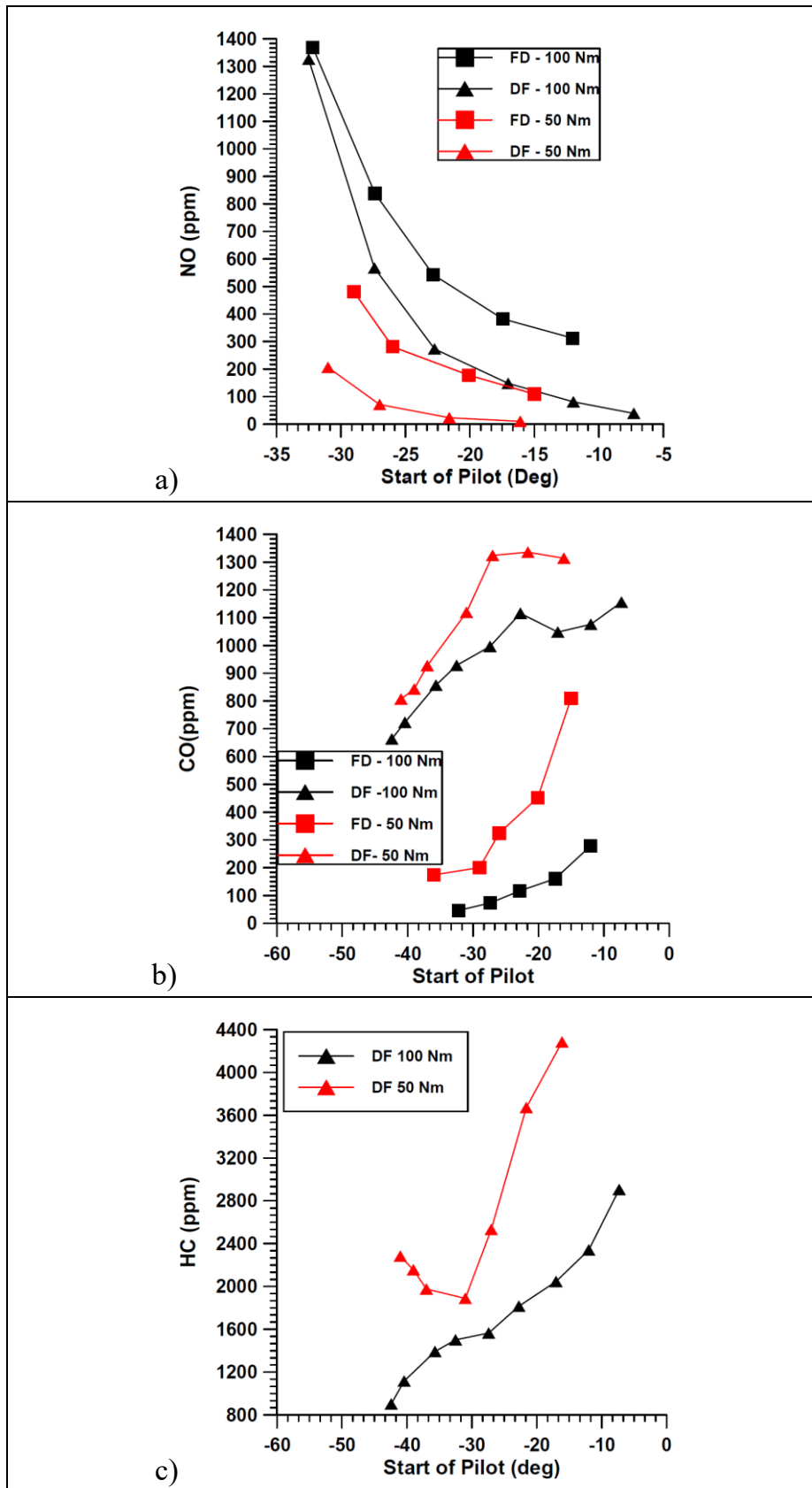


Fig. 3.18: Comparison of experimental a) NO, b) CO and c) HC in FD and DF mode for the two load level.

Tab. 3.19 Engine efficiency and CO₂ emissions.

Test case	Start of Pilot BTDC	CO ₂ [%]	Brake Efficiency	EICO ₂ [g/kWh]
FD 100 Nm	17	6.0	34.3	484.8
	23	6.1	37.3	465.6
	27	6.0	37.3	464.7
	32	6.2	36.8	480.3
FD 50 Nm	15	3.9	28.7	571.1
	20	3.8	30.7	519.2
	26	3.8	31.8	515.0
	29	3.8	31.7	518.0
DF 100 Nm 80% NG	17	5.0	33.8	376.1
	23	5.0	33.8	374.7
	27	5.2	34.7	375.0
	33	5.4	35.3	383.2
DF 50 Nm 75 % NG	16	3.4	21.2	462.0
	22	3.3	21.9	454.1
	27	3.3	22.8	482.1
	31	3.4	27.7	431.9

The incomplete combustion typical of DF operation induces a general decrease in the engine efficiency, especially at 50 Nm, as illustrated in Table 3.19. However, despite the efficiency reduction, not only the CO₂ contents in the exhausts but also the CO₂ emission index decreases in the case of dual fuel mode for both loads, so confirming the validity of this fuel supply system. Generally, the delayed cases present a smooth combustion but with a not really complete oxidation and then a lower combustion effectiveness that affects the engine efficiency. On the other hand, an advanced diesel injection improves the mixing between diesel oil and NG/air mixture in the combustion chamber, allowing a better mixture homogeneity and therefore a more efficient combustion development also with very lean mixtures. In Figure 3.19 the experimental pressure cycles for the most advanced injection timing are displayed for the two loads both in full diesel and dual fuel mode.

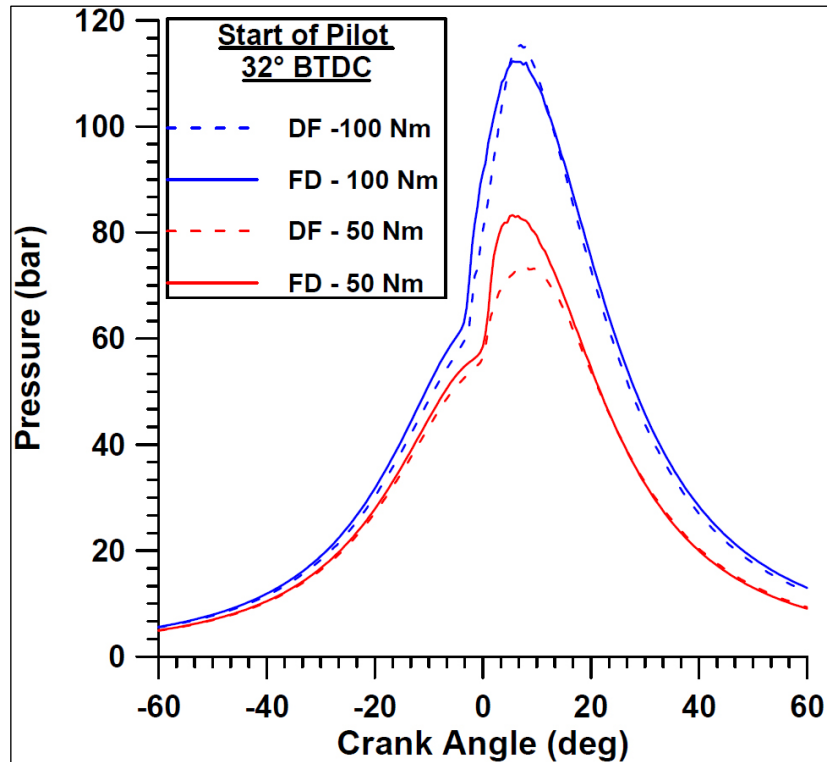


Fig. 3.19 Comparison of pressure cycles for FD and DF operation.

In accordance with the experimental test cases, 3D simulations were performed by using the CFD ANSYS-FLUENT code. Once achieved a satisfactory confidence level of the numerical activities, the aim of the computational calculations was to search an optimized strategy to reduce emissions and to avoid undesirable phenomena.

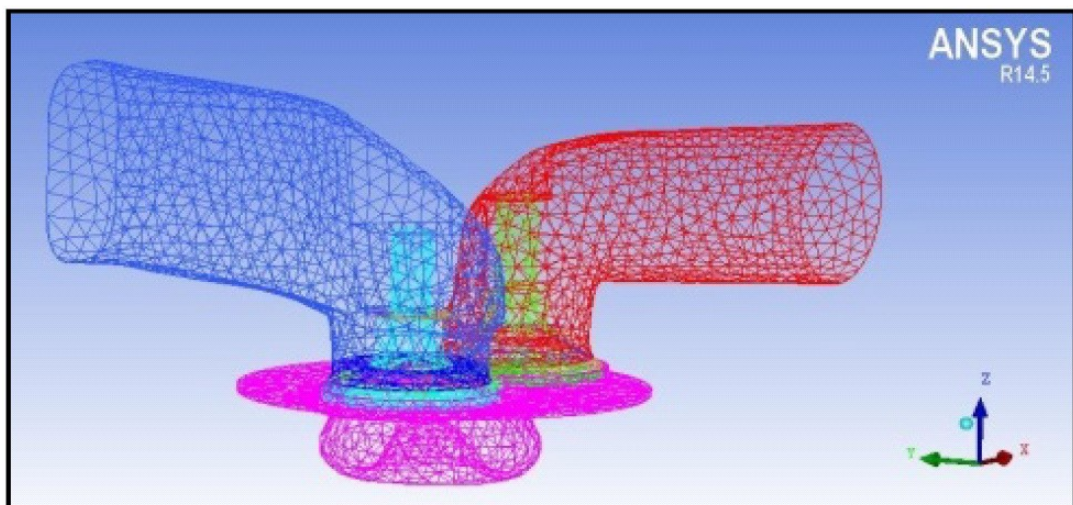


Fig. 3.20: Computational domain and unstructured mesh.

As already anticipated, the computational domain reproduces the geometry of the actual engine (Figure 3.20). It includes the inlet and exhaust ducts and open valve period. The cylinder and duct block-unstructured mesh was obtained by means of the ANSYS meshing tool. The cylinder mesh size is of about 600,000 cells at BDC and of 300,000 calls at TDC, while the bowl one is of 84,000 cells.

The boundary conditions require the assignment of the inlet pressure and temperature data and of the exhaust pressure. Such data were derived from the experimental measurements at the intake and the exhaust manifolds. The turbulent flow motion through the external ducts and inside the cylinder is approached by a realizable $k-\varepsilon$, two-equation, model, while the diesel oil atomisation is described by the Wave model. The Hardenberg & Hase correlation was used to reproduce the combustion delay for the diesel fuel.

The combustion model relies on the Finite Rate – Eddy Dissipation scheme with four reactions: the first three for the methane oxidation [87] and the last one for the diesel oil oxidation as listed in Table 3.20:

Tab. 3.20: Kinetic mechanism.

1. $CH_4 + 3/2 O_2 \rightarrow CO + 2H_2O$
$R_1 = 10^{13.354-0.004628p} [CH_4]^{1.3-0.01148p} [O_2]^{0.01426} [CO]^{0.1987} e^{-\frac{21932+269.4p}{T}}$
2. $CO + 1/2 O_2 \rightarrow CO_2$
$R_2 = 10^{14.338-0.1091p} [CO]^{1.359-0.0109p} [H_2O]^{0.0912+0.0909p} [O_2]^{0.891+0.0127p} e^{-\frac{21398+71.1p}{T}}$
3. $CO_2 \rightarrow CO + 1/2 O_2$
$R_3 = 10^{15.8114+0.07163p} [CO_2] e^{-\frac{649258-334.31p}{T}}$
4. $C_{10}H_{22} + 31/2 O_2 \rightarrow 10CO_2 + 11H_2O$
$R_4 = 2.587 \times 10^9 [C_{10}H_{22}]^{0.25} [O_2]^{1.5} e^{-\frac{15106}{T}}$

The numerical test cases refer to three operating conditions that have been experimentally tested, namely:

- A 100 Nm load with a SOP advance of 17 crank angle degrees.
- A 100 Nm load with a SOP advance of 32.5 crank angle degrees.
- A 50 Nm load with a SOP advance of 31 crank angle degrees.

Looking at the comparison of the experimental and numerical pressure cycles in Figures 3.21 and 3.22, a fair agreement of the numerical results with the experimental data is obtained.

As a matter of fact, the comparison of the reaction rates under dual fuel conditions in Figure 3.23 highlights that at higher loads the methane combustion starts just after the pilot injection with a moderate intensity and it exhibits a sudden steep rise as a consequence of the main injection of the diesel oil. If considering a different injection timing (Figure 3.24) a completely different combustion pattern can be observed. Actually, delaying the start of pilot by 15 crank angle degrees (i.e., SOP = 17° BTDC) induces a much smoother methane oxidation. Furthermore, methane combustion clearly appears to be triggered by the pilot injection while no significant effect is exerted by the combustion of the main diesel oil injection.

Figure 3.25 confirms that an engine load reduction, with the same injection timing, leads to a considerable decrease in nitric oxides, while both the unburned methane and the carbon monoxide are present with higher mass fractions. It is also of interest to observe that the NO level attains a stable level at nearly 30° ATDC, so that the growth in the nitric oxide appears to be strictly related to the steep increase in the methane oxidation in accordance with the reaction rates in Figure 3.23.

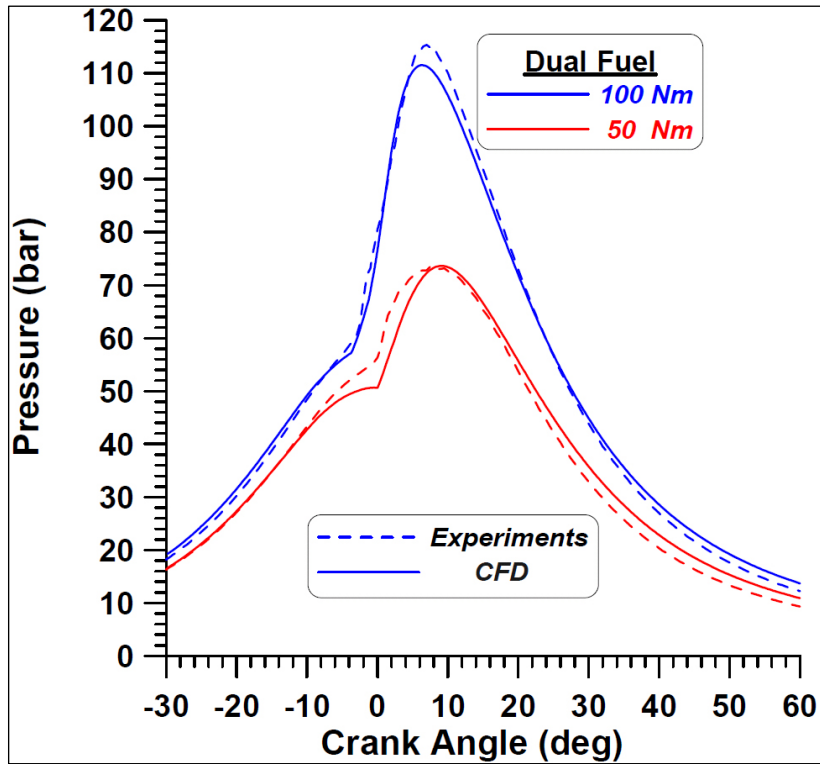


Fig. 3.21: Comparison of experimental and numerical pressure cycles (SOP = 32.5 BTDC).

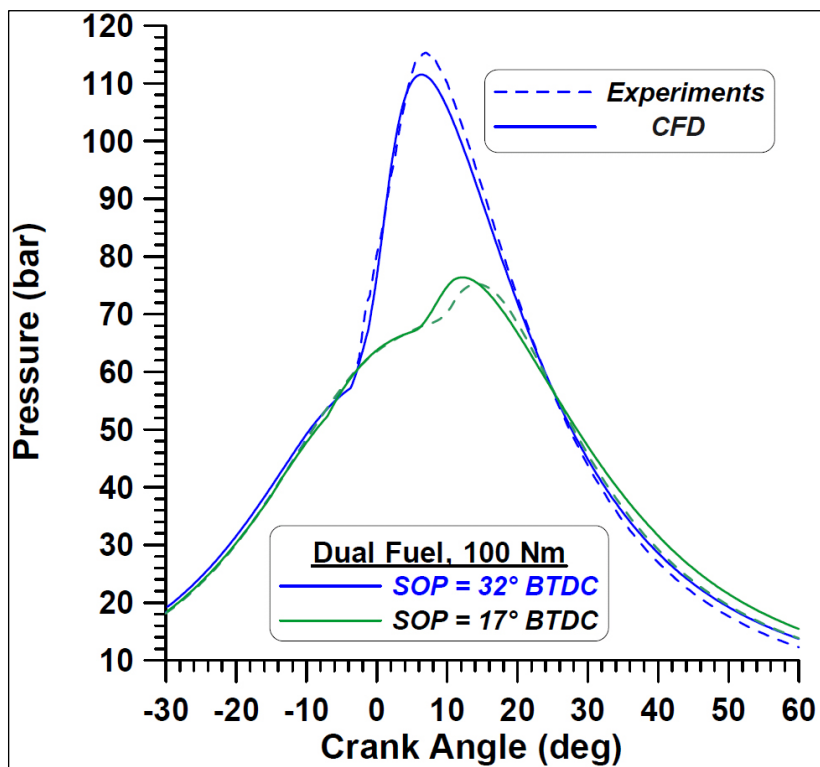


Fig. 3.22: Comparison of experimental and numerical pressure cycles at different injection timings.

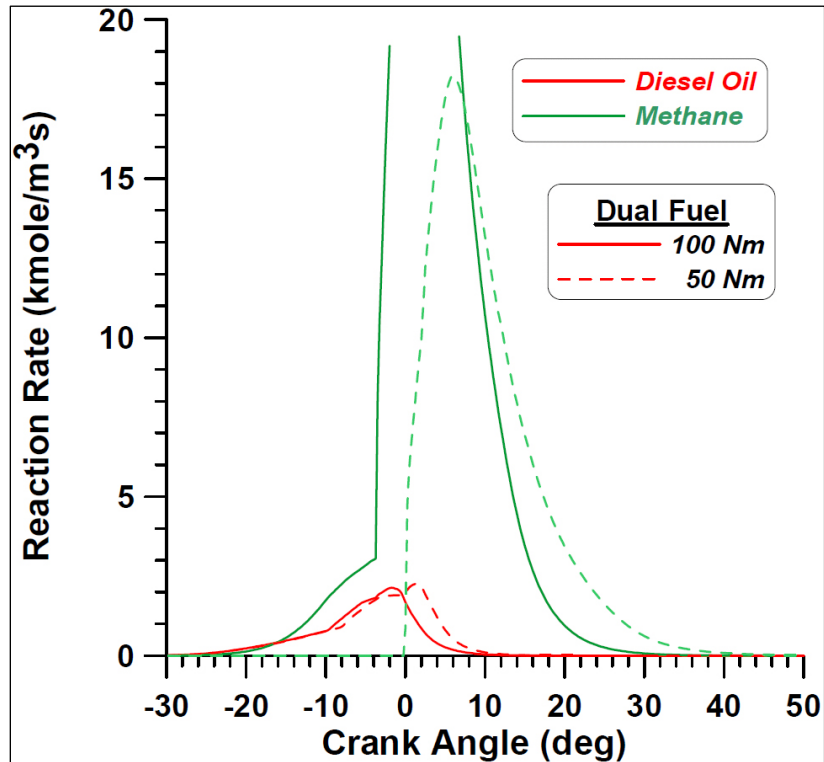


Fig. 3.23: Reaction rates of diesel fuel and methane at different engine loads (SOP = 32.5° BTDC).

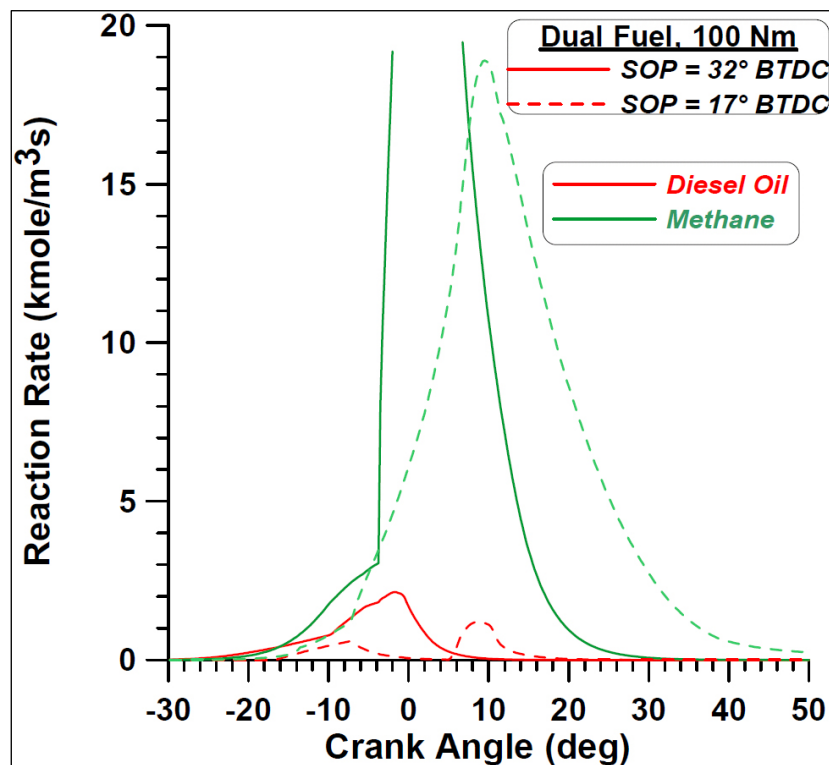


Fig. 3.24: Reaction rates of diesel fuel and methane for different injection timings (100 Nm load).

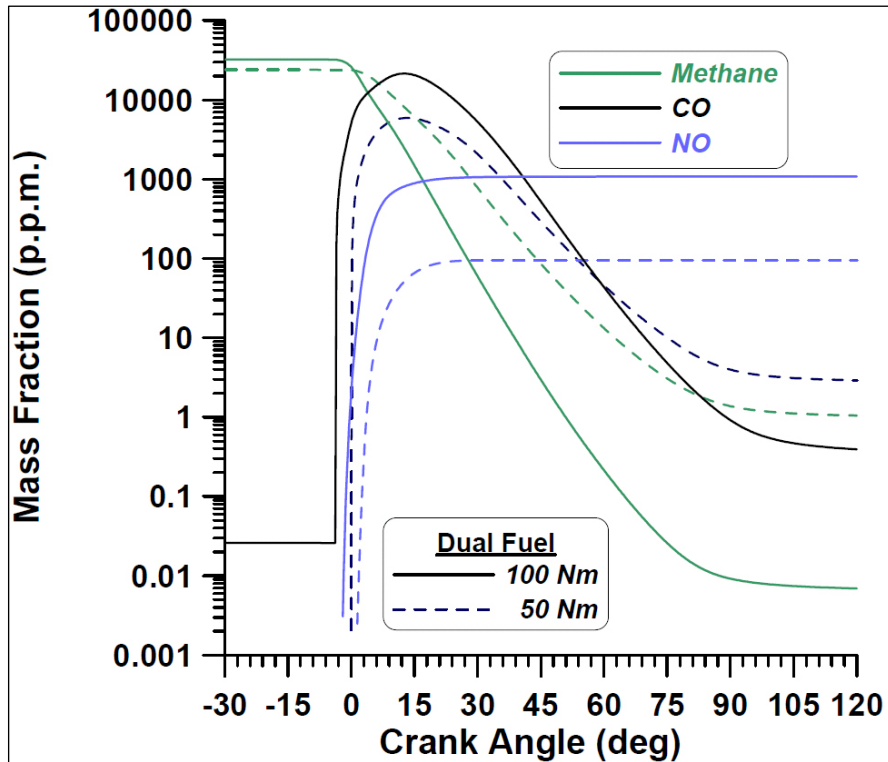


Fig. 3.25: Pollutant formation and methane consumption at different engine loads (SOP = 32.5°-31° BTDC).

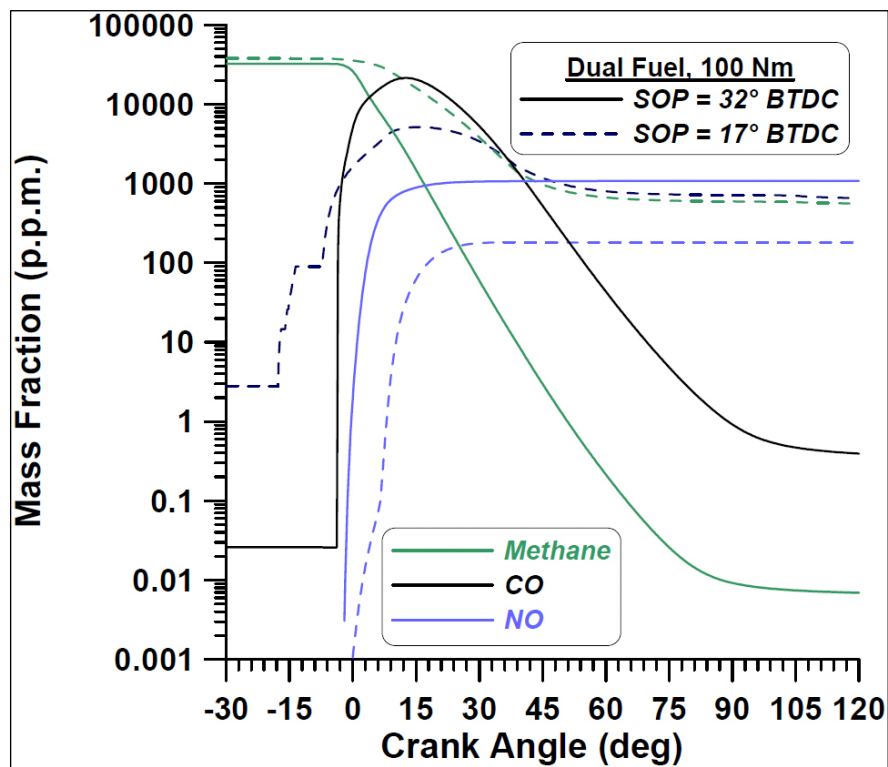


Fig. 3.26: Pollutant formation and methane consumption for different injection timings (100 Nm load).

Figure 3.26 highlights that advancing the start of injection (SOI) a more efficient combustion is achieved with lower values of products of incomplete combustion such as CH_4 and CO . This is due to the higher pressure (Figure 3.22) and consequently, higher temperature reached. On the other hand, this implies a greater formation of nitric oxides.

Moreover, when shifting from full diesel to dual fuel mode, the increases in unburned methane and carbon monoxide emissions, appear to be not so relevant in the case of a large injection advance (of nearly 32°) but they attain unacceptable levels if operating the engine with a lower injection advance, of 17° BTDC.

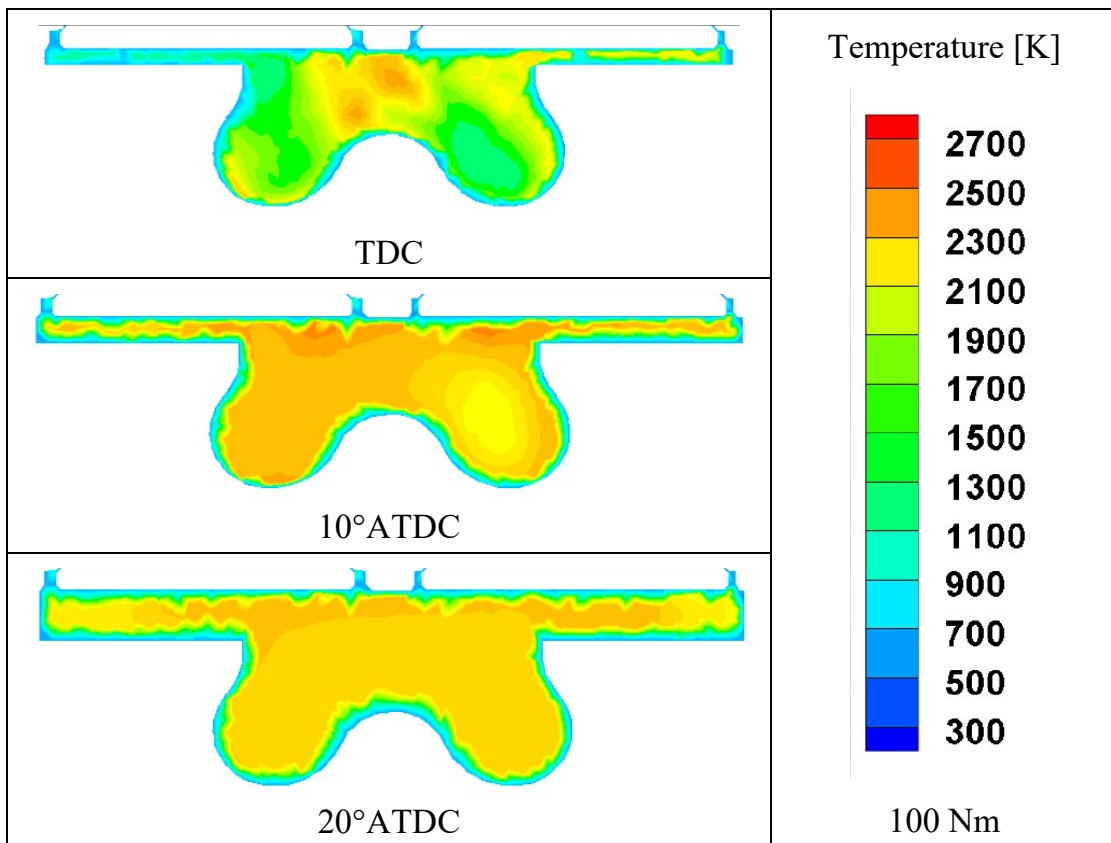


Fig. 3.27: In-cylinder temperature distributions at 100 Nm load, Dual Fuel (SOP = 32.5° BTDC).

Actually, at 100 Nm load with advanced SOP, a quite uniform temperature distribution is observed after 10° ATDC. This can be intended as a consequence of the steep combustion development that was observed in

Figure 3.23. On the contrary, at 50 Nm the temperature pattern is more irregular, probably due to the major difficulties in the flame front propagation throughout the methane-air mixture.

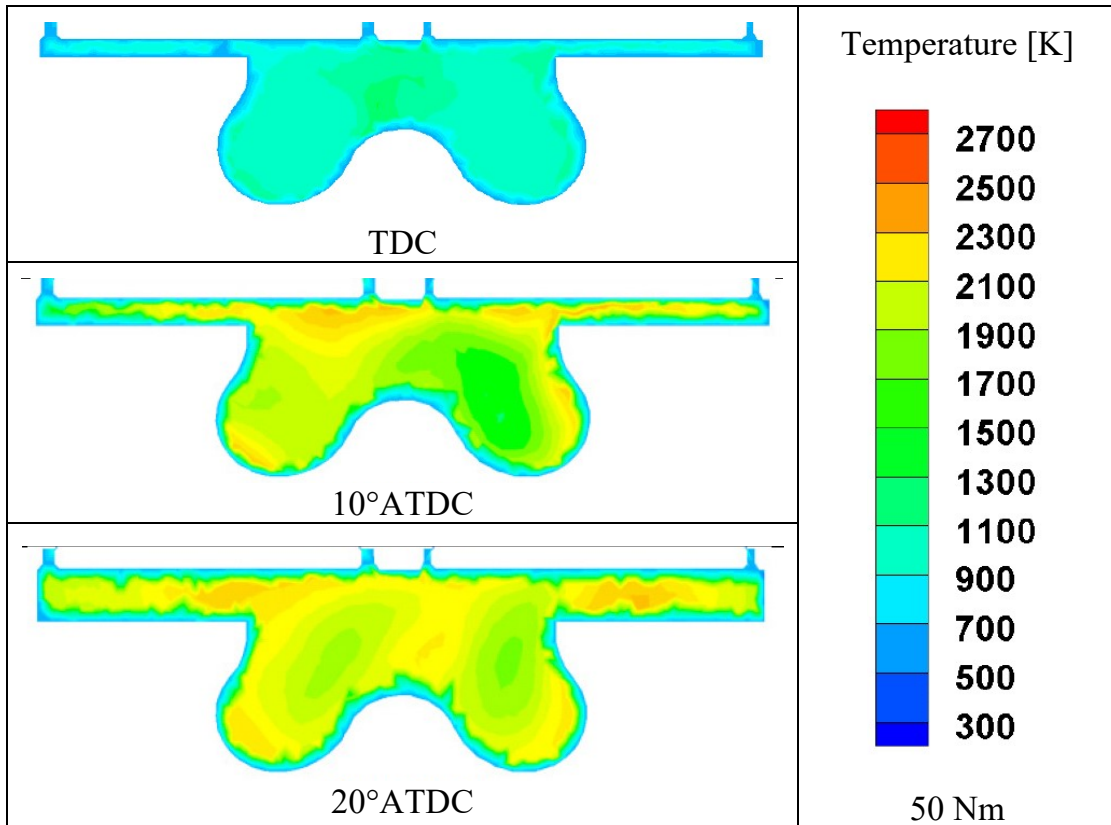


Fig. 3.28: In-cylinder temperature distributions at 50 Nm load, Dual Fuel (SOP = 31° BTDC).

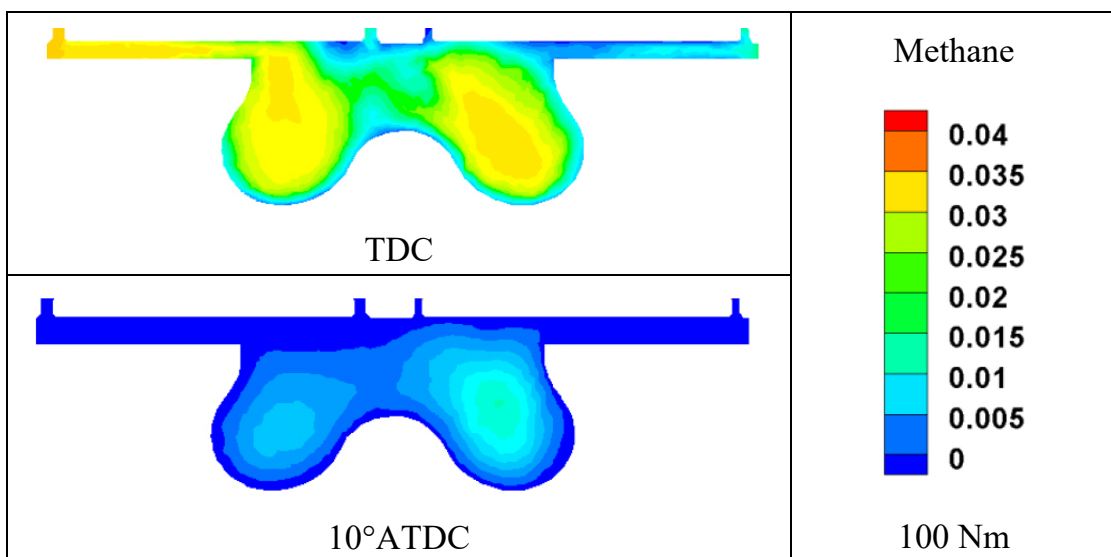


Fig. 3.29: In-cylinder distributions of methane mass fraction at 100 Nm load, Dual Fuel (SOP = 32.5 BTDC).

Figure 3.29 evidences that, at the higher load, the fuel consumption is almost completed at 10° ATDC and the unburned methane contents are practically negligible, as already shown in Figure 3.25.

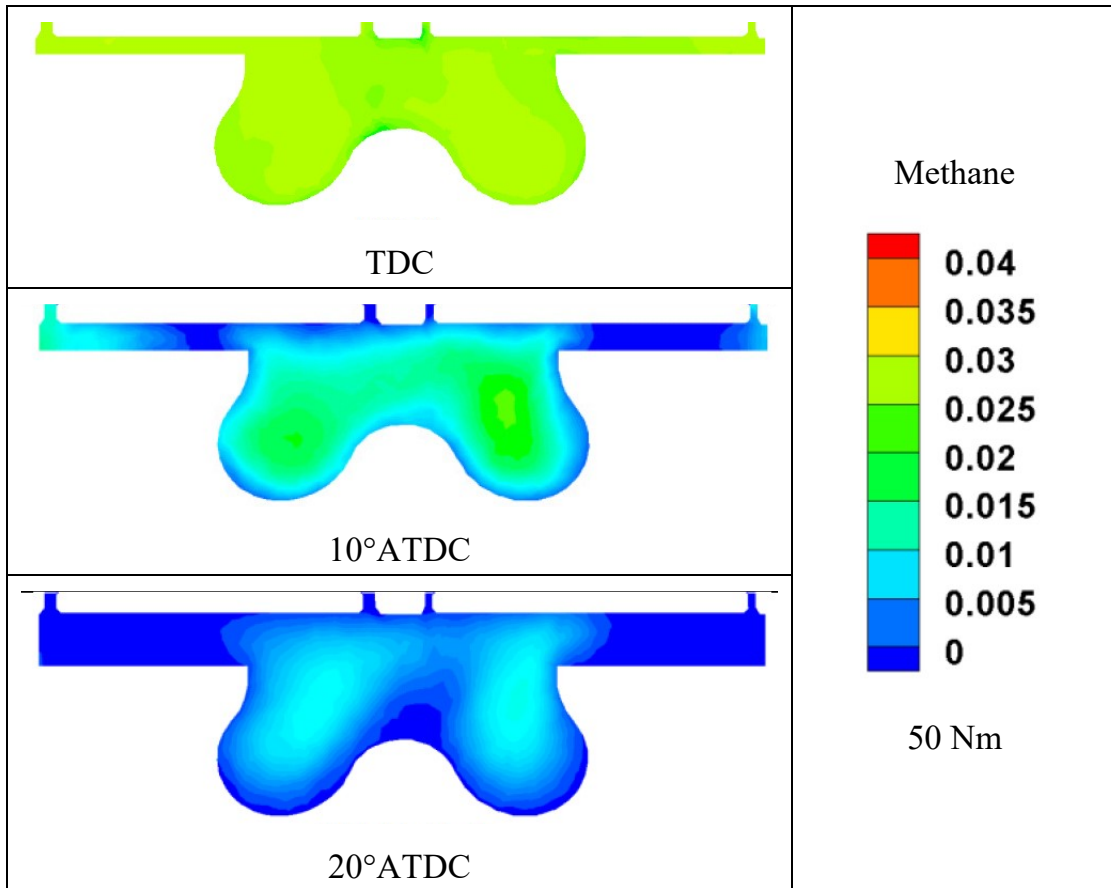


Fig. 3.30: In-cylinder distributions of methane mass fraction at 50 Nm load, Dual Fuel (SOP = 32.5° BTDC).

Figure 3.30 confirms that by reducing the engine load, a slower consumption of methane is achieved at 10 crank angle degrees, because of the lower reaction rate already outlined in Figure 3.23. Finally, retarding the start of pilot injection (i.e., 17° BTDC), the difficulties in the methane combustion development appear to be more evident. Indeed, in Figure 3.31 it is clearly shown that in the squish zone of the chamber non-negligible methane contents are still detected and this explains the increased levels of unburned species displayed in the previous Figure 3.26.

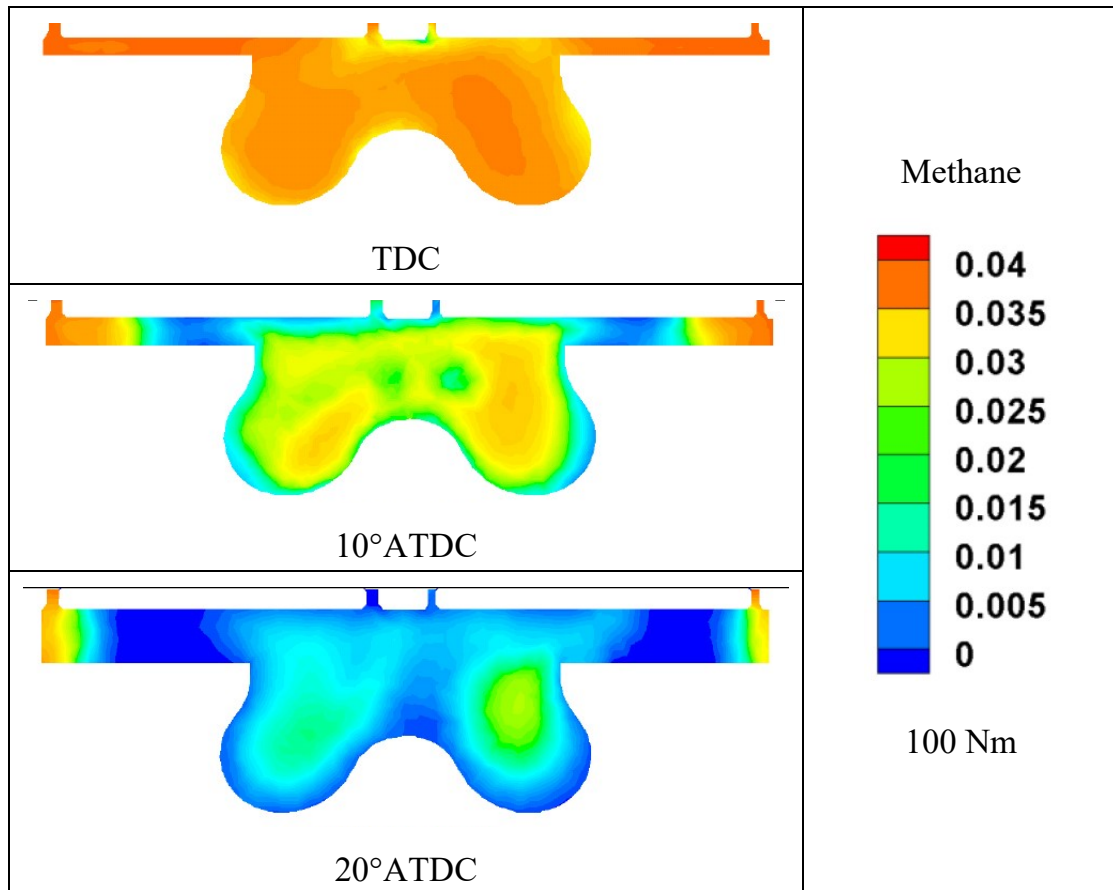


Fig. 3.31: In-cylinder distributions of methane mass fraction at 100 Nm load, dual fuel (SOP = 17 BTDC).

Chapter 4

LIGHT DUTY ENGINE

Based on the experimental activity illustrated in the previous chapter [60, 61], in this section an integrated numerical methodology between a one-dimensional and a three-dimensional code is developed with the aim to predict the behaviour of a light duty engine by varying injection advance in full diesel and dual fuel modes [94].

4.1 Methodology

The phenomena that occur in the cylinder are very complex and strongly depend on the boundary conditions imposed at the cylinder control system. Usually, the reduced experimental test cases available do not allow an overall view of the engine behaviour in the different operating conditions, therefore by combining the results of one-dimensional and three-dimensional models, it is possible to carry out correlations in order to extend the range of functioning.

In particular, starting from experimental test cases carried out at a test bench at Istituto Motori and reported in the previous chapter [60, 61] in Table 3.18, a proper calibration of numerical models has been implemented in order to reach a quite good fitting between experimental and numerical results. Then, the results obtained from 3D simulations provide to the 1D model the information necessary to build correlations between parameters that characterise the development of combustion (start, duration and heat release peak position) on an extended range. In this way, in turn, once the most interesting cases are identified, the same correlations provide the boundary conditions to CFD simulations to deeper investigate the in-cylinder processes such as the in-cylinder fuel vapour, temperature, burning rate distributions.

The reason behind this procedure is due to the advantages of one-dimensional codes that allow to perform fast calculations and to simulate the whole engine, not only the combustion inside the cylinder but including the turbocharger, the intake and exhaust systems and other control devices. On the other hand, the 3D calculation requires several consecutive cycles to achieve convergence and therefore long computational times. However, only the CFD analysis allows to better understand the mechanisms which govern the combustion phenomenon inside the cylinder.

The calculations have been referred to a light duty direct injection diesel engine whose specifications are reported in Table 3.15. The reason of the use of a different geometry from the one used in the experimental activity was due to the necessity to study an engine with features compliant with more modern engines.

4.2 One-dimensional Model

The solution of the commercial code is based on one-dimensional fluid dynamics for the ducts and zero-dimensional in-cylinder calculation. Detailed modelling of individual components is included to specify the phenomena in the singular components. In this way the software can recreate the behaviour of the whole engine. The first step is to give general information of the engine as engine type (SI or CI) number of strokes, number of cylinders and valve and of course the dimensions of the cylinder (Table 4.1, the same as Table 3.15). The building of the engine is made by adding the various components and linking each other on a canvas (Figure 4.1). Some objects are designed and utilised for a specific purpose such as the cylinder and the turbocharger, while other objects like the air filter and the muffler can be obtained by the combination of pipes and junctions.

Tab. 4.1: Engine specifications.

Engine	1.9 Multijet
Type	4 stroke CI
Number of cylinders	4
Valves/cylinder	2
Bore [mm]	82
Stroke [mm]	90.4
Cylinder volume displacement [cm ³]	480
Maximum power [kW]	88
Maximum torque [Nm]	255 @ 2,000 rpm
Compression ratio	18:1

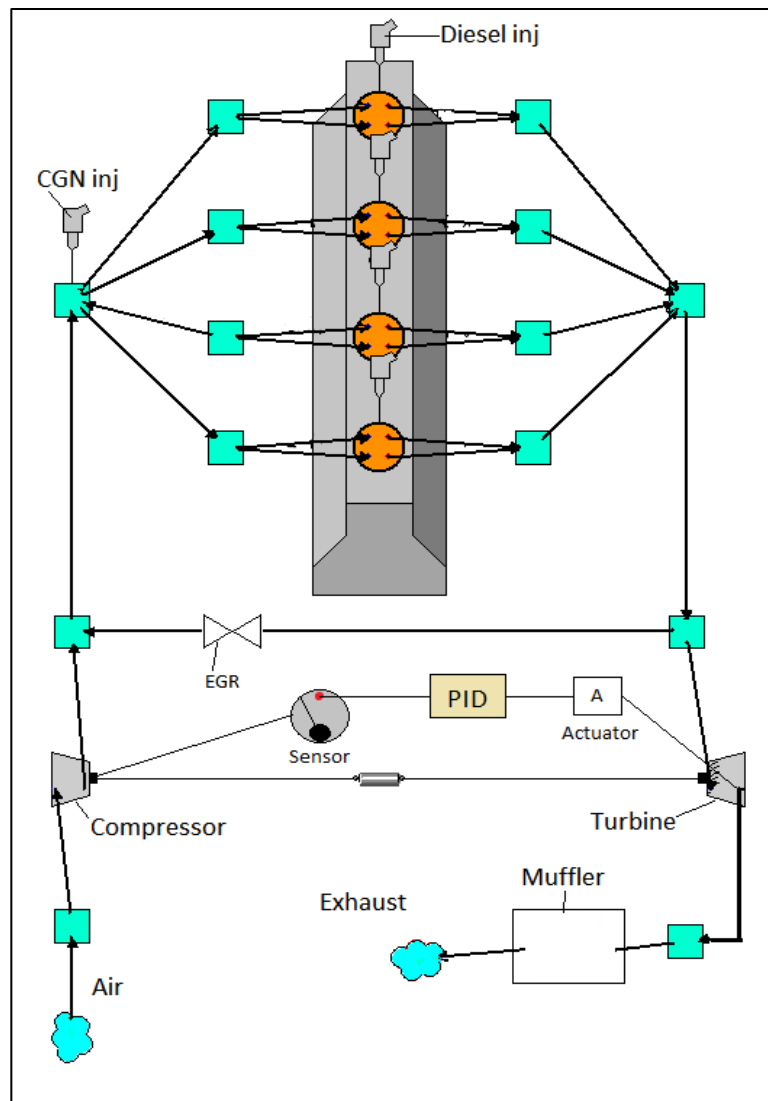


Fig. 4.1: Engine scheme.

The engine is a turbocharged four cylinders, four strokes and four valves per cylinder, there is also an EGR valve which in this study is kept constantly closed. Also, a PID controlled is put on the vane opening of the Variable Geometry Turbine in order to obtain a fixed boost pressure while a sensor is linked to the compressor exit as feedback of the pressure ratio. The NG injector is located before the different intake pipes that lead to each cylinder since it constantly injects a certain amount of gas (expressed in kg/h). Instead, a diesel injector is dedicated for each cylinder since diesel oil is directly in the chamber, the nozzle injects a fixed mass (mg) each cycle and the law of injection is composed of a pilot and a main.

The Annand model is set to describe the heat transfer between the colder cylinder walls and the hot gas:

$$Q = h_c A (T_g - T_w)$$

The first term represents the heat exchanged by convection, A is the surface of heat exchange, T_g and T_w are respectively the temperature of the hot gas and cold walls, the focus of this correlation is the coefficient h_c that is related to the engine parameters:

$$Nu = \left(\frac{h_c b}{k} \right) = a \left(\frac{\rho \bar{S}_p b}{\mu} \right)^d$$

Where Nu is the Nusselt number, b is the bore, k is thermal conductivity, a is a constant in a range between 0.35 and 0.7, ρ is the density of the gas, \bar{S}_p is mean piston speed, μ is the dynamic viscosity and d is constant equal to 0.7.

For the combustion model the multi-Component Wiebe function is used to describe the process. It is a composition of different single Wiebe function, each of them estimates the mass fraction burned. The single Wiebe function is expressed as:

$$x_b = \left\{ 1 - \exp \left[-a \left(\frac{\theta - \theta_0}{\Delta\theta} \right)^{m+1} \right] \right\}$$

a is a constant related to the combustion duration $\Delta\theta$, and m is the form factor. The function indicates that the mass fraction burned profile grow from zero (θ_0) and tends to one, and the difference between the crank angles of the start and the end of the combustion is the duration of the combustion.

In the full diesel mode two Wiebe curves have to be defines, the first for the pilot and the second for the main while in dual fuel mode a third curve is added for the NG combustion. For the three (or two) combustions the fitting for the Wiebe correlation is made by assigning the three crank angles at which three determined percentage in mass are burned, in particular the three percentages are 0.5%, 50% and 98% that identify respectively the start, the peak and the end of the burning law.

The released heat is obtained from the instantaneous burned mass fraction via the following correlation:

$$\frac{dQ_{ss}}{d\theta} \Delta\theta = m_b k_i \frac{dx_b}{d\theta} \Delta\theta$$

For the data fitting of the Wiebe functions the three crank angles that identify the law of fuel burning are obtained from CFD results.

4.3 Three-dimensional Model

CFD simulations have been referred to a light duty direct injection diesel engine, whose geometry and mesh are reported in Figure 4.2. The cylinder and bowl discretization is of 535,000 and 46,000 cells, respectively. The computational domain includes the intake and exhaust ducts and the valve profiles, in order to evaluate the mass exchange processes

The computational simulations were performed mean the three-dimensional ANSYS-FLUENT code. Combustion is modelled with the Finite rate – Eddy Dissipation model and a kinetic mechanism made of four reactions (Table 4.2).

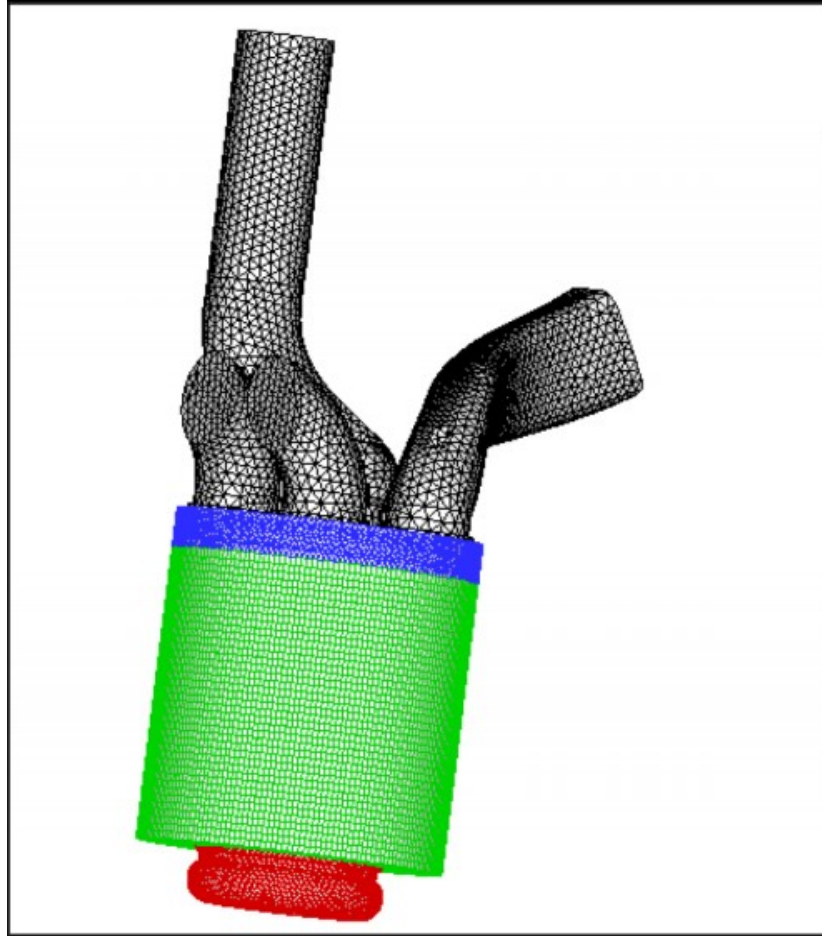


Fig. 4.2: Mesh of the cylinder, intake and exhaust ducts.

Tab. 4.2: Kinetic mechanism [87].

1. $CH_4 + 3/2 O_2 \rightarrow CO + 2H_2O$
$R_1 = 10^{13.354-0.004628p} [CH_4]^{1.3-0.01148p} [O_2]^{0.01426} [CO]^{0.1987} e^{-\frac{21932+269.4p}{T}}$
2. $CO + 1/2 O_2 \rightarrow CO_2$
$R_2 = 10^{14.338-0.1091p} [CO]^{1.359-0.0109p} [H_2O]^{0.0912+0.0909p} [O_2]^{0.891+0.0127p} e^{-\frac{21398+71.1p}{T}}$
3. $CO_2 \rightarrow CO + 1/2 O_2$
$R_3 = 10^{15.8114+0.07163p} [CO_2] e^{-\frac{649258-334.31p}{T}}$
4. $C_{10}H_{22} + 31/2 O_2 \rightarrow 10CO_2 + 11H_2O$
$R_4 = 2.587 \times 10^9 [C_{10}H_{22}]^{0.25} [O_2]^{1.5} e^{-\frac{15106}{T}}$

Natural gas is represented by 100% of methane, its oxidation is described by a two-step mechanism, the first reaction converts CH₄ in CO that is consequently oxidized in CO₂ in second reaction. The third reaction takes into account the dissociation of the CO₂ into CO. Finally, reaction 4 describes the complete oxidation of diesel oil which consider C₁₀H₂₂ as surrogate, it is the default reaction for diesel oil in FLUENT.

In order to simulate the ignition delay, the Hardenberg and Hase correlation is used:

$$\tau_{id} = \left(\frac{C_1 + 0.22\bar{S}_p}{6N} \right) \exp \left[E_a \left(\frac{1}{RT} - \frac{1}{17,190} \right) + \left(\frac{21.2}{p - 12.4} \right)^{e_p} \right]$$

Where τ_{id} is the expressed in seconds, C_1 is a constant equal to 0.36, N is the engine speed expressed in rpm, E_a is the effective activation energy and e_p is the pressure exponent equal to 0.63. The turbulent flow motion through the external ducts and inside the cylinder is approached by a realizable k- ϵ model while the diesel oil atomisation is described by the Wave model illustrated in Chapter 2, the injection system presents six holes and the mean injection velocity is set to 400 m/s; finally the nitric oxides oxidation formation model is the one by Zel'dovich [89].

4.4 Test Cases

All the numerical test cases refer to the engine operating with an overall equivalence ratio of 0.75, for the Dual Fuel cases the NG/air equivalence ratio is equal to 0.62 and an energy supply from natural gas of 80%.

The tests cases simulated in the numerical activity relating to experimental data (Table 3.18) are listed in Table 4.3.

The test cases are characterised by the same operating condition and same amount of liquid fuel injected but a different injection advance of pilot and

main jets and a fixed dwell angle, i.e. the angular shift between pilot and main injection starts.

It is important to highlight that the start of injection can provoke significant effects on the combustion development and the emission production.

Tab. 4.3: Test cases.

FULL DIESEL	Pilot Injection		Main Injection	
Injected Mass	1 mg		20.7 mg	
Test Cases	Start	Duration	Start	Duration
Case 1	8° BTDC	3°	14° ATDC	8°
Case 2	12° BTDC	3°	10° ATDC	8°
Case 3	17° BTDC	3°	5° ATDC	8°
Case 4	22° BTDC	3°	TCD	8°
Case 5	27° BTDC	3°	5° BTDC	8°
Case 6	32° BTDC	3°	10° BTDC	8°
DUAL FUEL	Pilot Injection		Main Injection	
Injected Mass	1 mg		2.8 mg	
Test Cases	Start	Duration	Start	Duration
Case 7	12° BTDC	3°	5° ATDC	5°
Case 8	17° BTDC	3°	TDC	5°
Case 9	27° BTDC	3°	10° BTDC	5°

For the full diesel simulations four cases (1, 2, 4 and 6) have been used for the construction of the correlations which should be able to predict the development of the combustion. Then cases 3 and 5 are used as a proof of validation of these correlations. Instead, for the dual fuel mode cases the correlations are found for the three cases performed (7, 8 and 9).

4.5 Full Diesel Results

As already said full diesel cases 1, 2, 4 and 6 were performed with the three-dimensional code, the results in terms of fuel oxidation rate (Figure 4.3) are used to calibrate the one-dimensional model. In particular, for the pilot and main injections respectively the start, the peak position and the end of combustion obtained from CFD calculations are assigned in the Wiebe function. Figure 4.4 shows the calibration of the fuel burning rates of the CFD and 1D calculations for the case 2 (SOP -12°): the combustion timing corresponds in both models. A first validation is made through a comparison of pressure curves which confirm that the 1D dimensional model can reproduce the 3D results (Figures 4.5 to 4.8). Based on these outcomes, three correlations for pilot and three correlations for the main injection (start, peak and end of combustion) have been obtained by using second order polynomial curves, as shown in Figures 4.9 and 4.10.

At this point, cases 3 and 5 have been performed by the two codes but the start, the peak and the end of combustion for the 1D model are provided by the correlations previously obtained. Figures 4.11 and 4.12 demonstrate that the use of these correlations allows to simulate new cases by varying the injection timing in the 1D with greatly reduced computational time and to provide the boundary conditions to realise a CFD calculation for the estimation of emissions and engine performances.

In Figure 4.13 the temperature distributions at 20° ATDC are reported for three cases (2, 3 and 5). Of course the combustion development is completely different: for the case 2 the first flame nuclei are detected near fuel jets; in case 3 the combustion is in the middle of the process, high temperatures, due to ignition, are more distributed in the chamber; in case 5 the combustion is at the final stage.

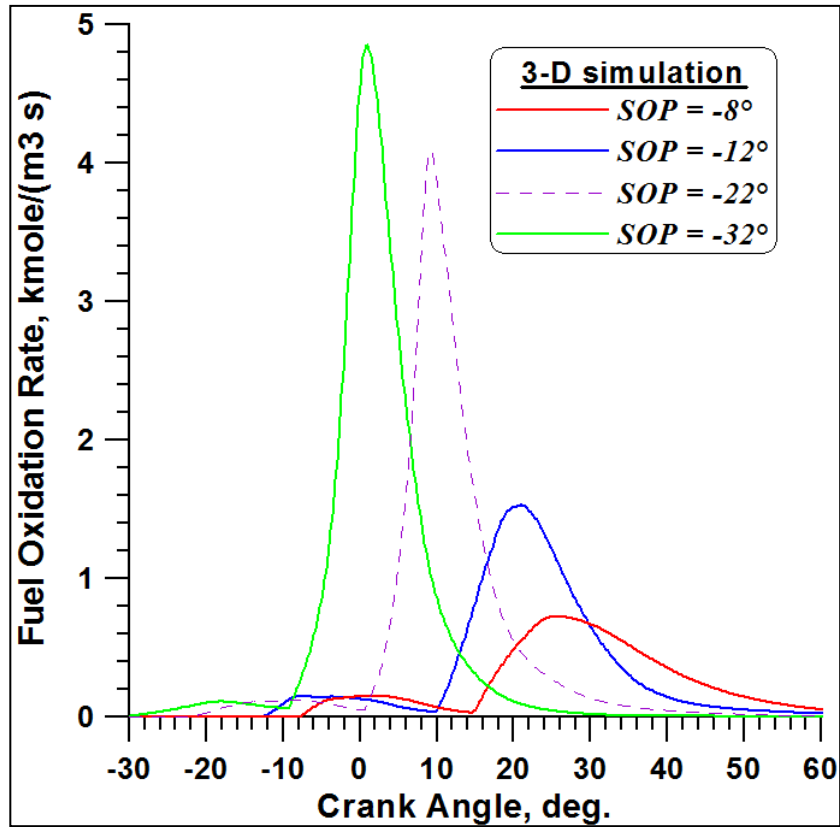


Fig. 4.3: Diesel oil vapour oxidation rates for different SOP in FD mode.

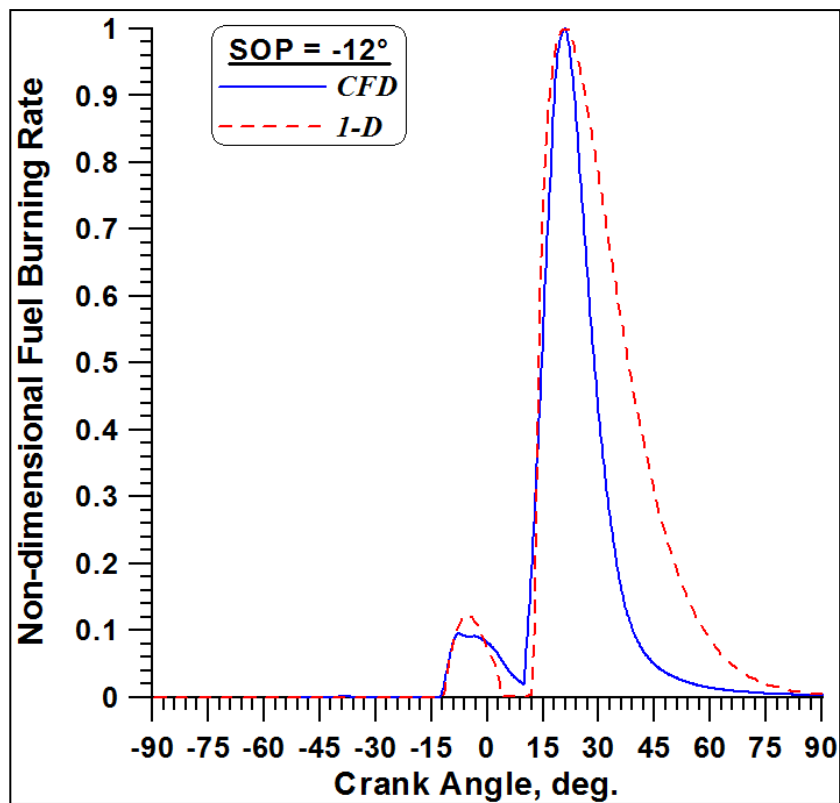


Fig. 4.4: Comparison of FBR c by the CFD and 1D models in FD mode.

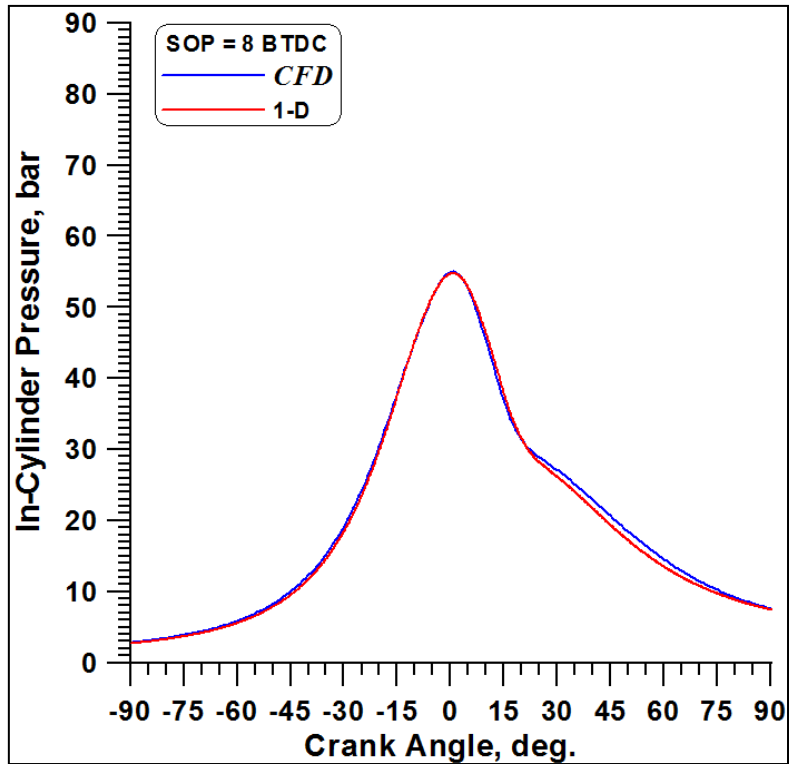


Fig. 4.5: In-cylinder pressure by the CFD and 1D models (SOP=8° BTDC) in FD mode.

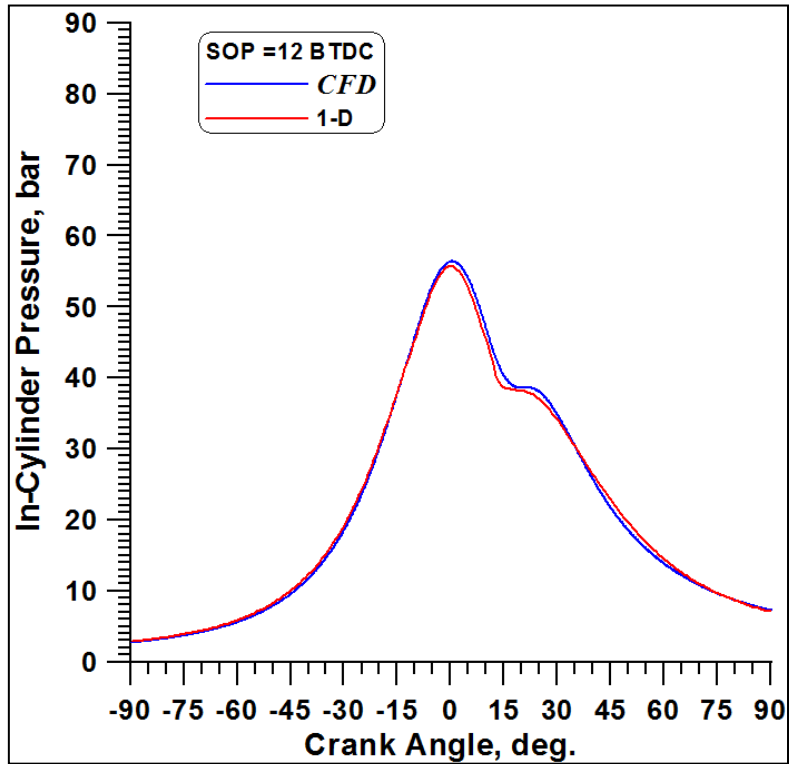


Fig. 4.6: In-cylinder pressure by the CFD and 1D models (SOP=12° BTDC) in FD mode.

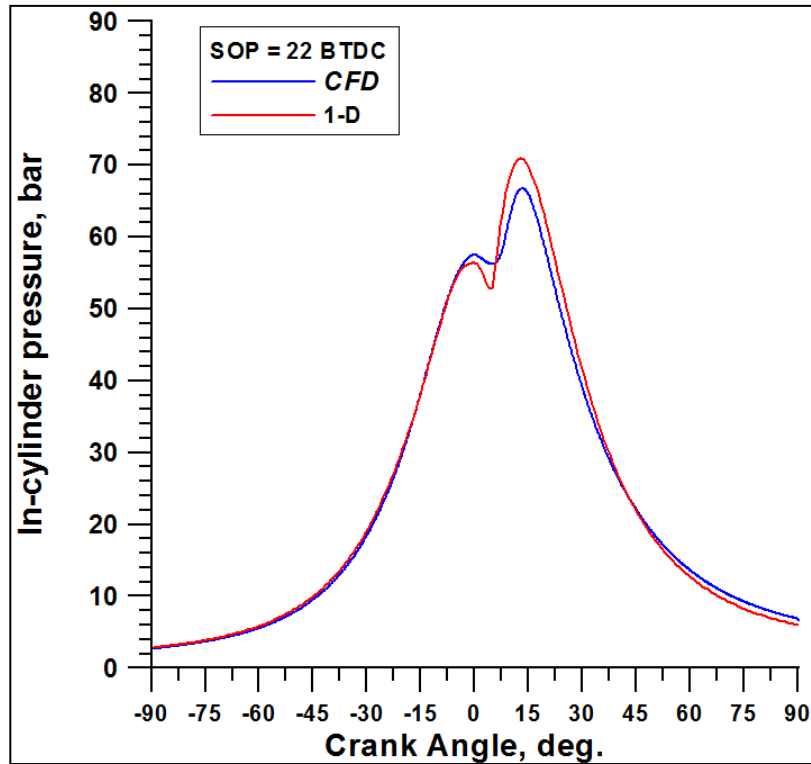


Fig. 4.7: In-cylinder pressure by the CFD and 1D models (SOP=22° BTDC) in FD mode.

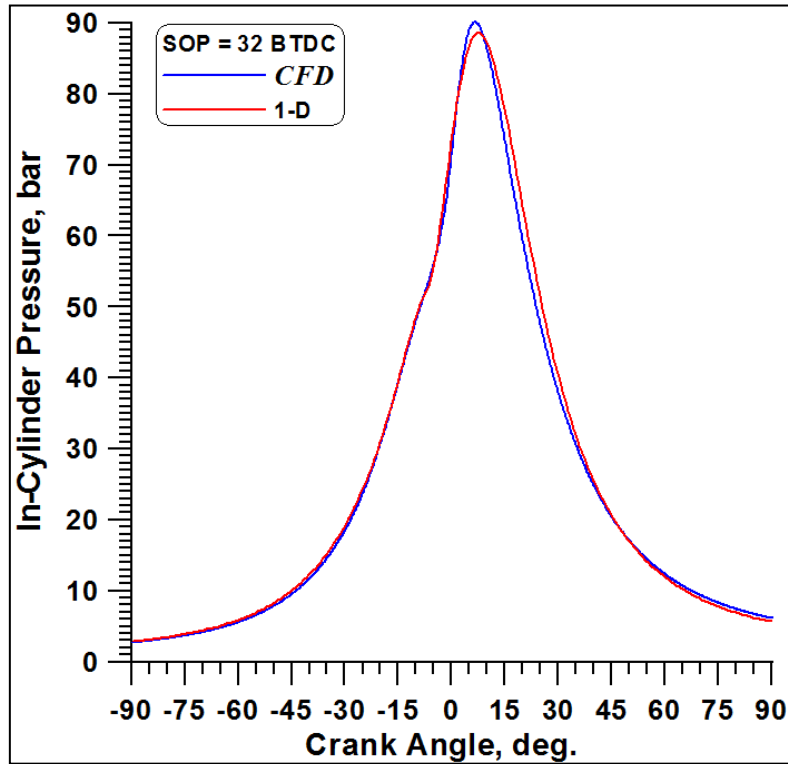


Fig. 4.8: In-cylinder pressure by the CFD and 1D models (SOP=32° BTDC) in FD mode.

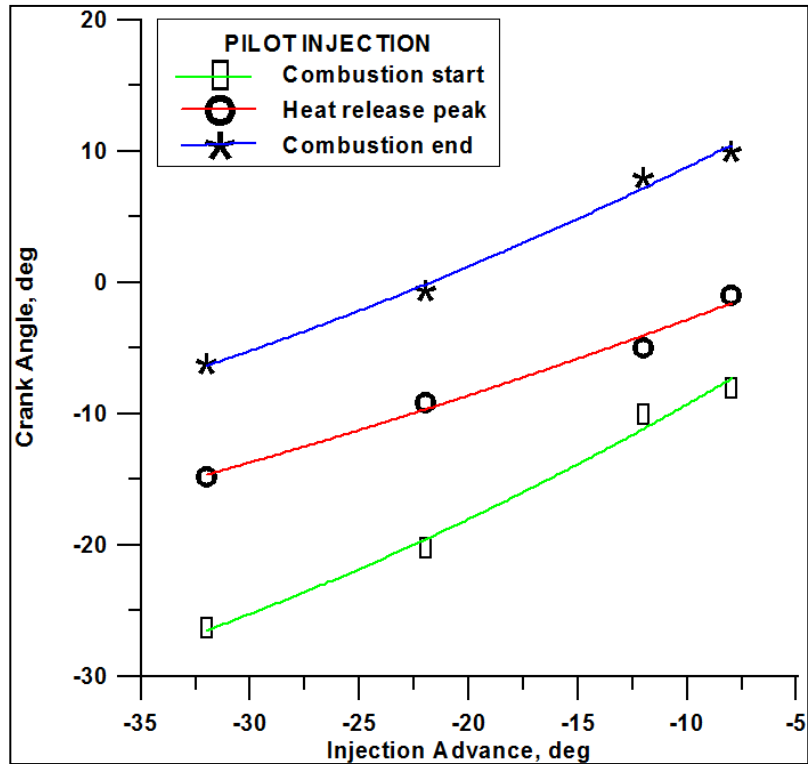


Fig. 4.9: Correlation curves of Wiebe model after pilot injection in FD mode.

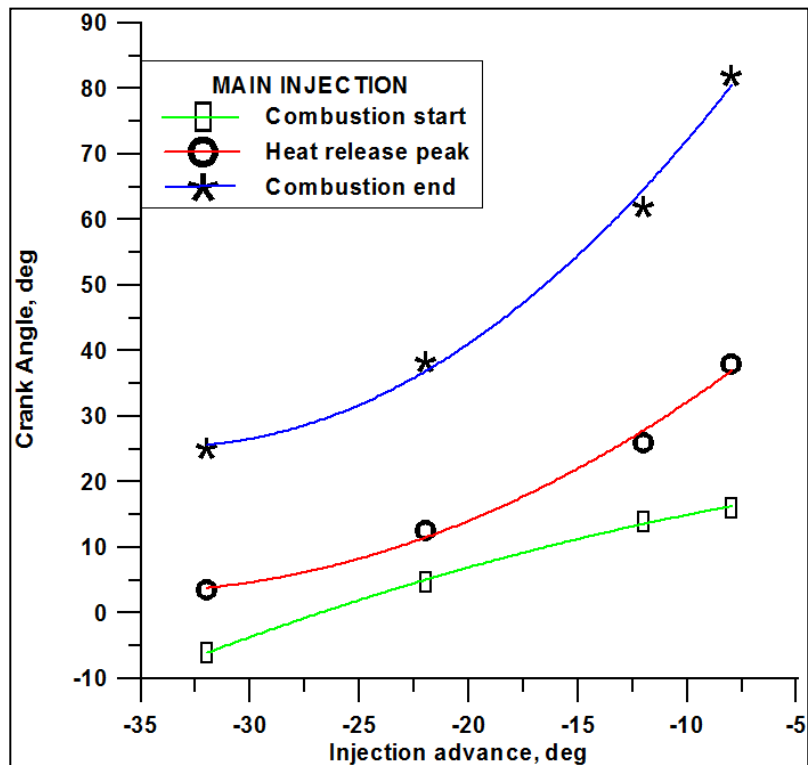


Fig. 4.10: Correlation curves of Wiebe model after main injection in FD mode.

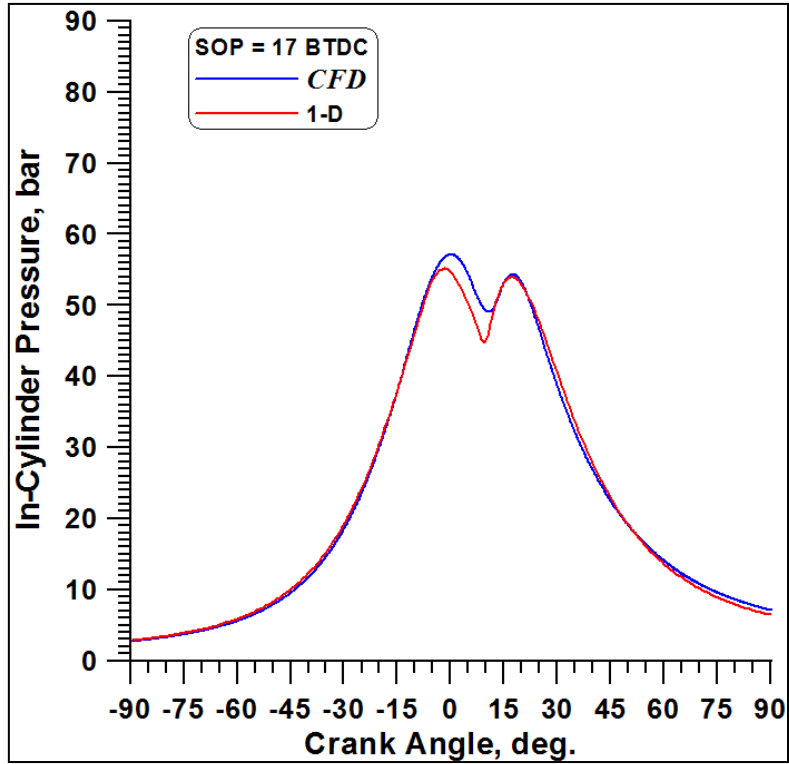


Fig. 4.11: In-cylinder pressure by the CFD and 1D models (SOP=17° BTDC) in FD mode.

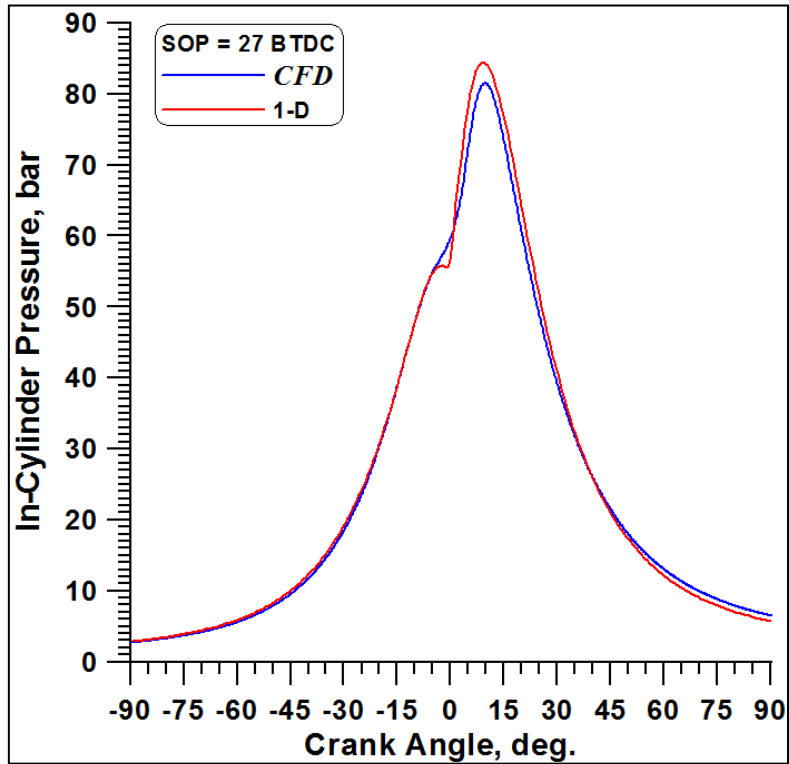


Fig. 4.12: In-cylinder pressure by the CFD and 1D models (SOP=27° BTDC) in FD mode.

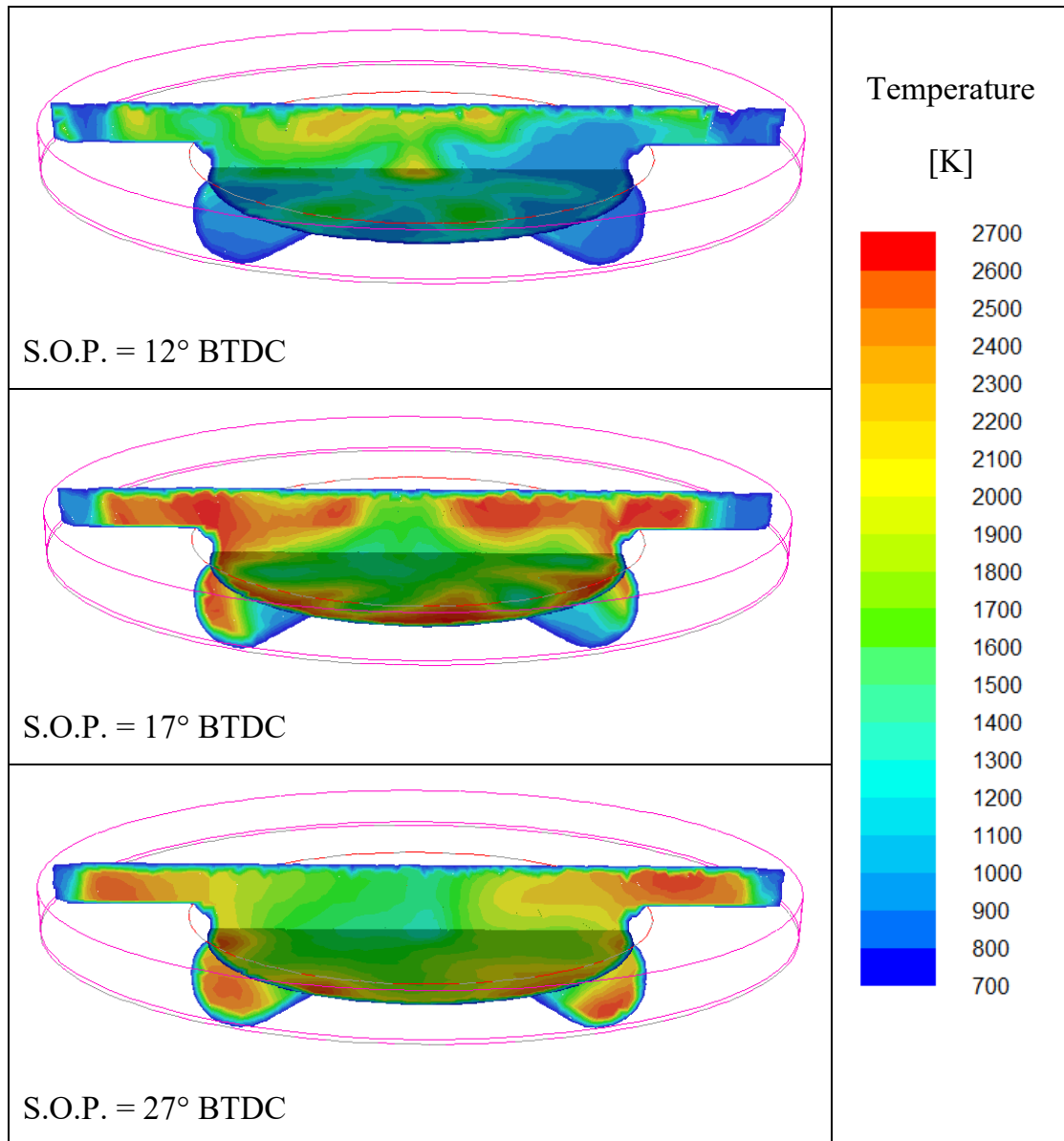


Fig. 4.13: Temperature distributions for different injection timings at 20° ATDC.

4.6 Dual Fuel Results

As shown in Table 4.2 for dual fuel cases only three starts of injection have been selected, i.e. cases 2, 3 and 5. However, the only difference is the reduced duration of the main injection in order to reduce the liquid fuel amount since about of 80% of energy is now provided by the natural gas introduced in the inlet manifold.

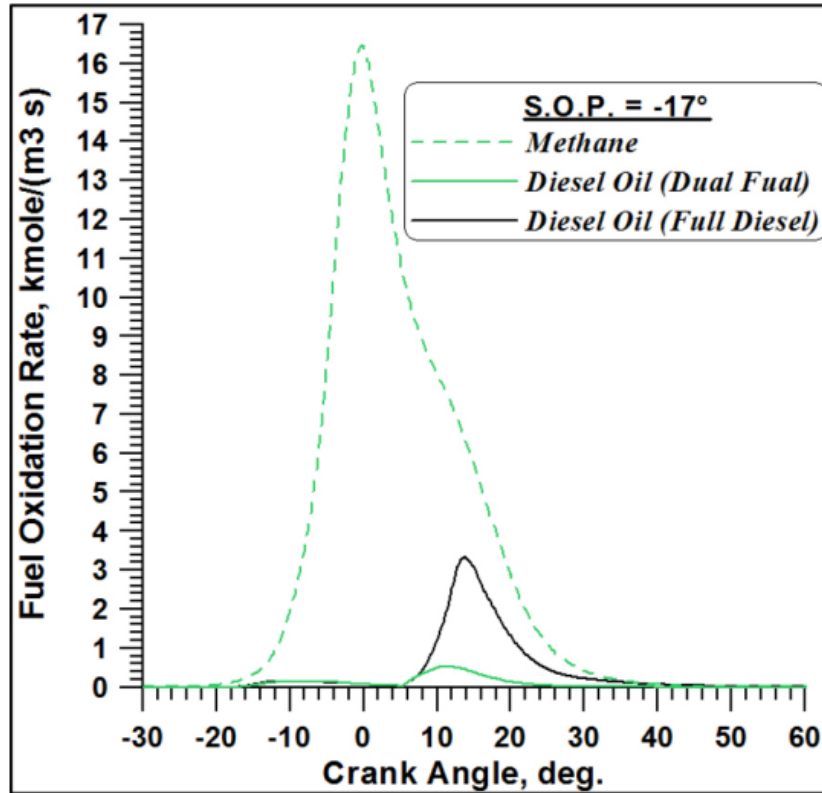


Fig. 4.14: Comparison of fuel oxidation rates for FD and DF operation.

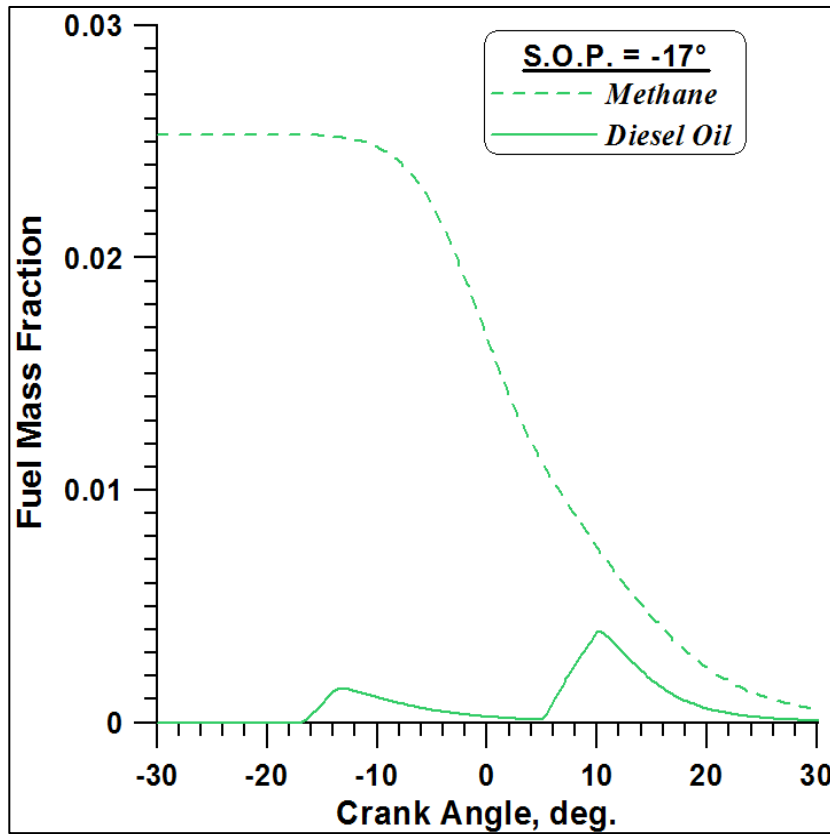


Fig. 4.15: Fuel mass fractions of diesel oil and NG in DF mode.

The role of the pilot and main injection of the diesel fuel is the ignition of the natural gas/air mixture and the activation of multiple flame fronts that accelerate the natural gas oxidation. This is confirmed by Figure 4.14, The higher and anticipated peak of curve for NG is due to a fast ignition of gas mixture after the pilot injection.

Actually, the most relevant increase in the slope of the methane oxidation rate can be detected after the ignition of the diesel fuel from the pilot injection. Also, the main diesel oil ignition appears to be helpful exclusively to accelerate the combustion of methane as stated before. Moreover, Figure 4.15 confirms that the deep decrease in methane mass fraction occurs at nearly 7° BTDC, so 10° later than the start of pilot injection. Finally, it is important to notice that the pressure curve in dual fuel mode is more similar to the trend of a spark ignition than a diesel engine (Figure 4.16).

Following the same procedure used for the full diesel operation, the three cases were firstly simulated with CFD code. Figure 4.17 illustrated the three methane oxidation rates while in Figure 4.18 the calibration of the fuel burning rates of 1D model Wiebe functions for pilot, main and methane combustion starting from the 3D results is reported. In Figures 4.19 to 4.20 the comparison between the 3D and 1D pressure curves demonstrate that the one-dimensional model is again capable to fairly reproduce the CFD results. Also, as expected, the pressure peak increases with the SOP value.

In order build the Wiebe correlations, the same method used for full diesel cases is used, second order polynomial curves are used for the fitting of the combustion parameters as illustrated in Figure 4.22.

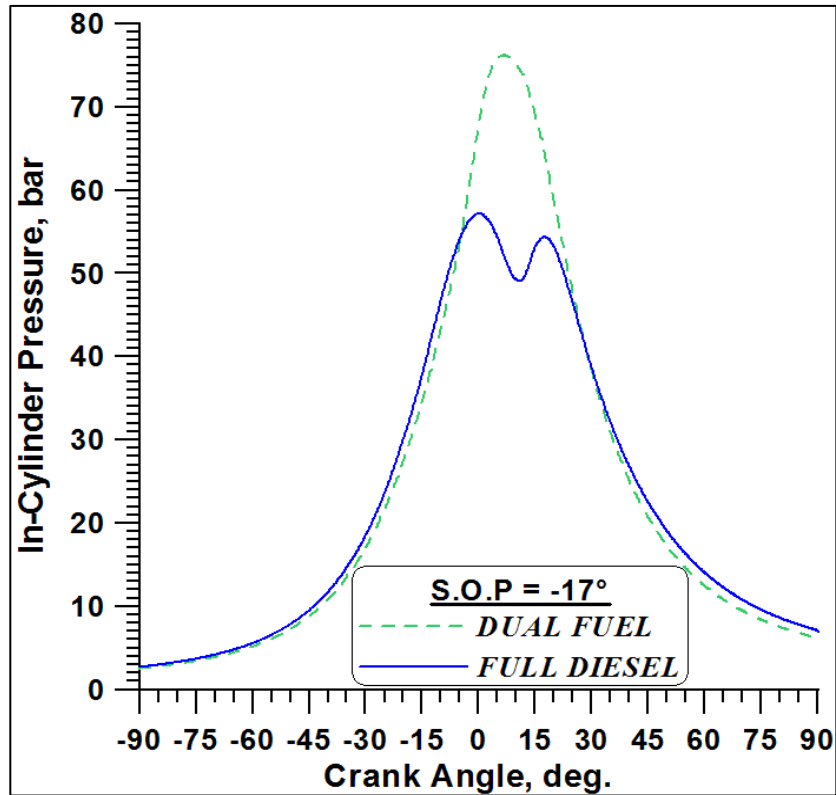


Fig. 4.16: Comparison of in-cylinder pressure by CFD for FD and DF.

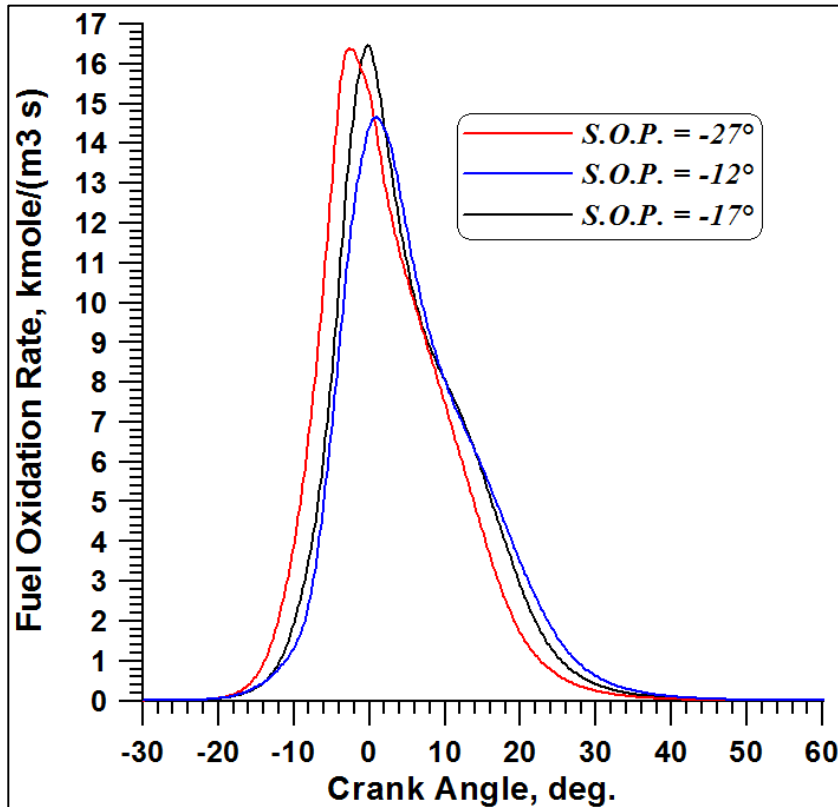


Fig. 4.17: CFD methane oxidation rates for different injection advances.

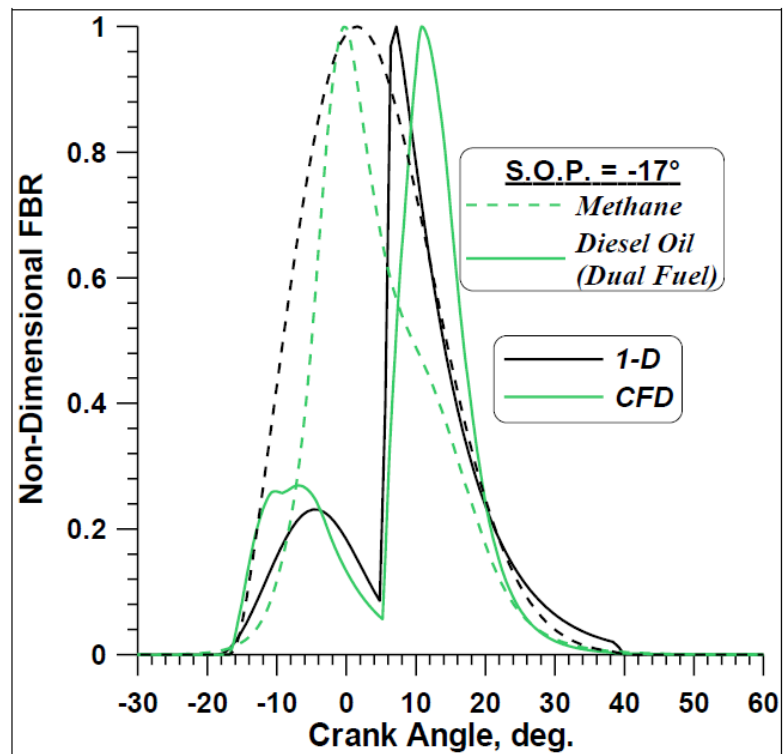


Fig. 4.18: Calibration of fuel burning rates computed by the CFD and 1D model for SOP=17° BTDC in DF mode.

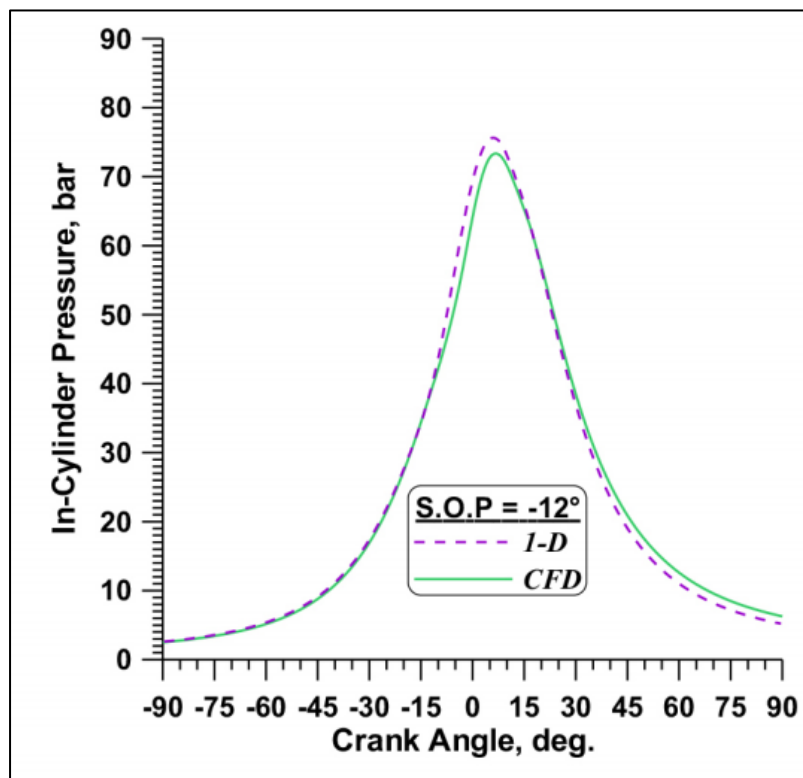


Fig. 4.19: In-cylinder pressure by the CFD and 1D models (SOP=12° BTDC) in DF mode.

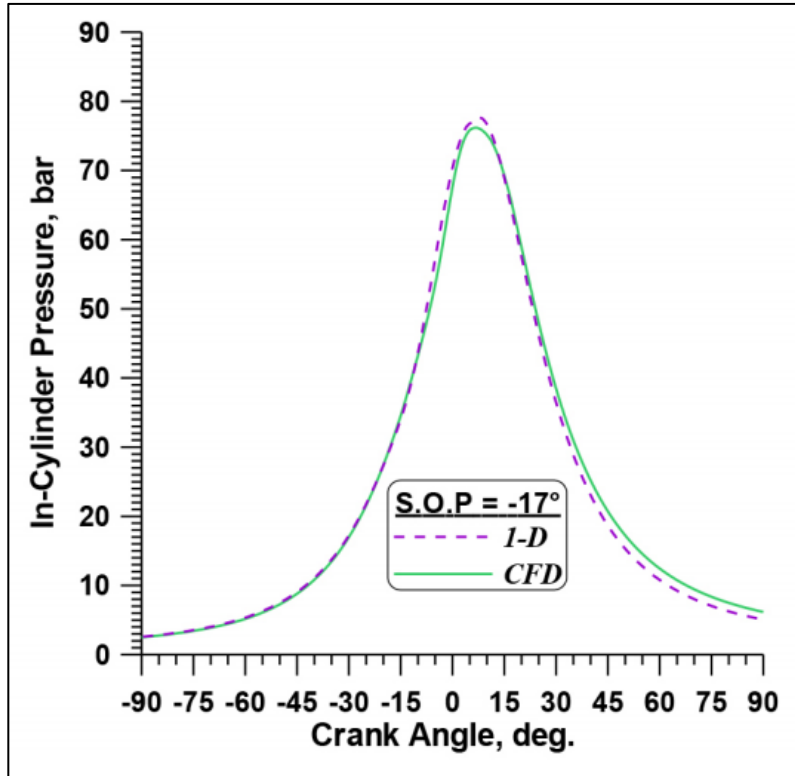


Fig. 4.20: In-cylinder pressure by the CFD and 1D models (SOP=17° BTDC) in DF mode.

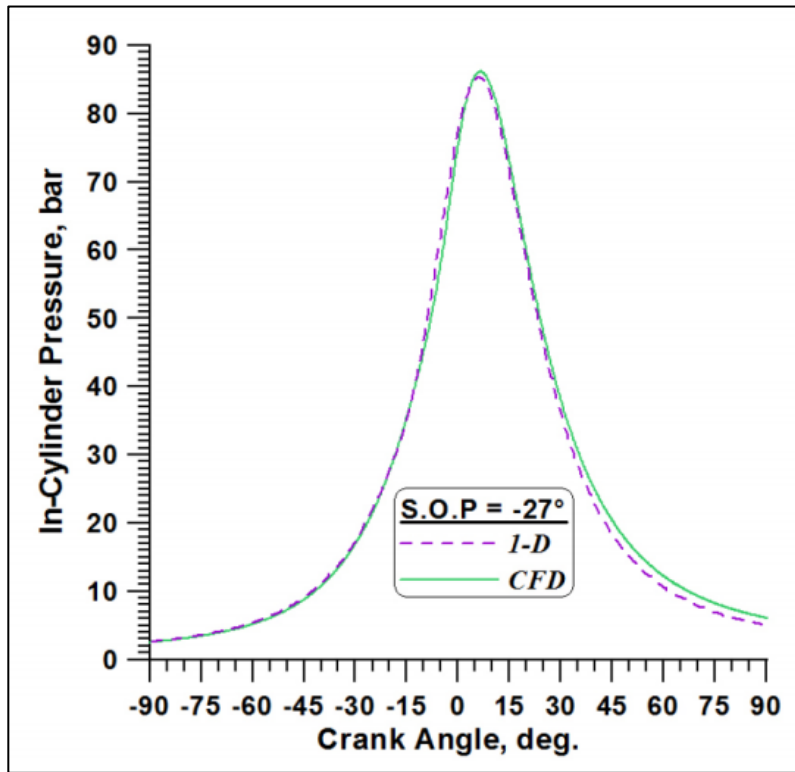


Fig. 4.21: In-cylinder pressure by the CFD and 1D models (SOP=27° BTDC) in DF mode.

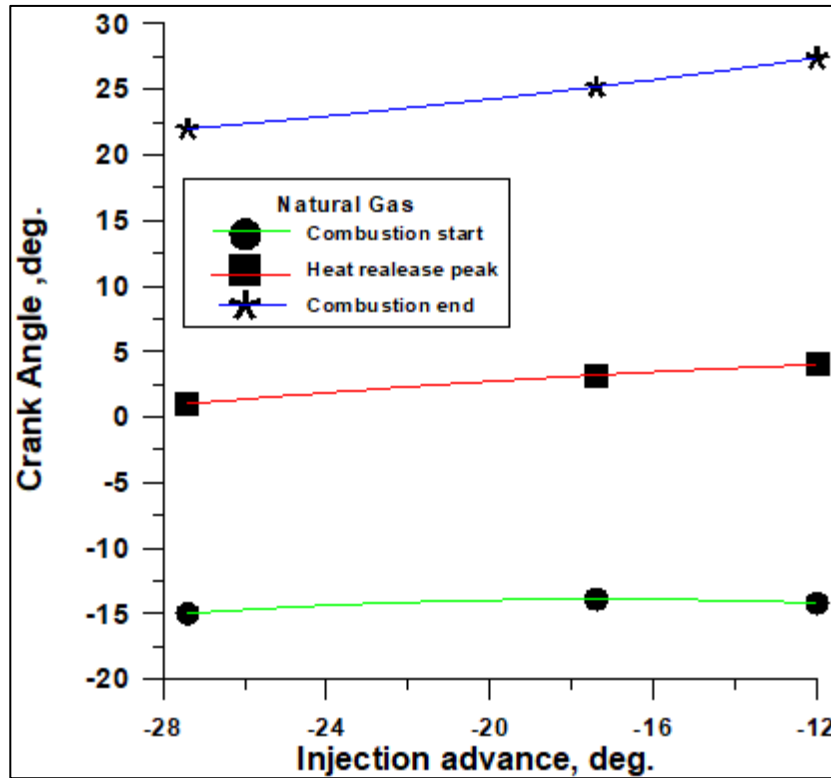


Fig. 4.22: Correlation curves of Wiebe model for natural gas in DF mode.

In Figure 4.23 the Methane and Diesel Fuel Vapour mass fractions and reaction rates distributions for case 7 (S.O.P = 12° BTDC) are shown at 20° ATDC. The higher intensity of reaction for diesel oil correspond to the zone where the methane is rapidly consumed, this confirms that the role of the diesel fuel combustion is to allow a faster consumption of the gaseous fuel.

Figure 4.24 illustrates the temperature contours at 20° ATDC for the three test cases: compared to full diesel mode (Figure 4.13) where the high temperatures due to ignition appear near the walls of the chamber, in dual fuel mode the presence of NG/air mixing produces an homogeneous distribution in all the zones since the combustion is rapid as already demonstrated by Figures 4.14 and 4.17.

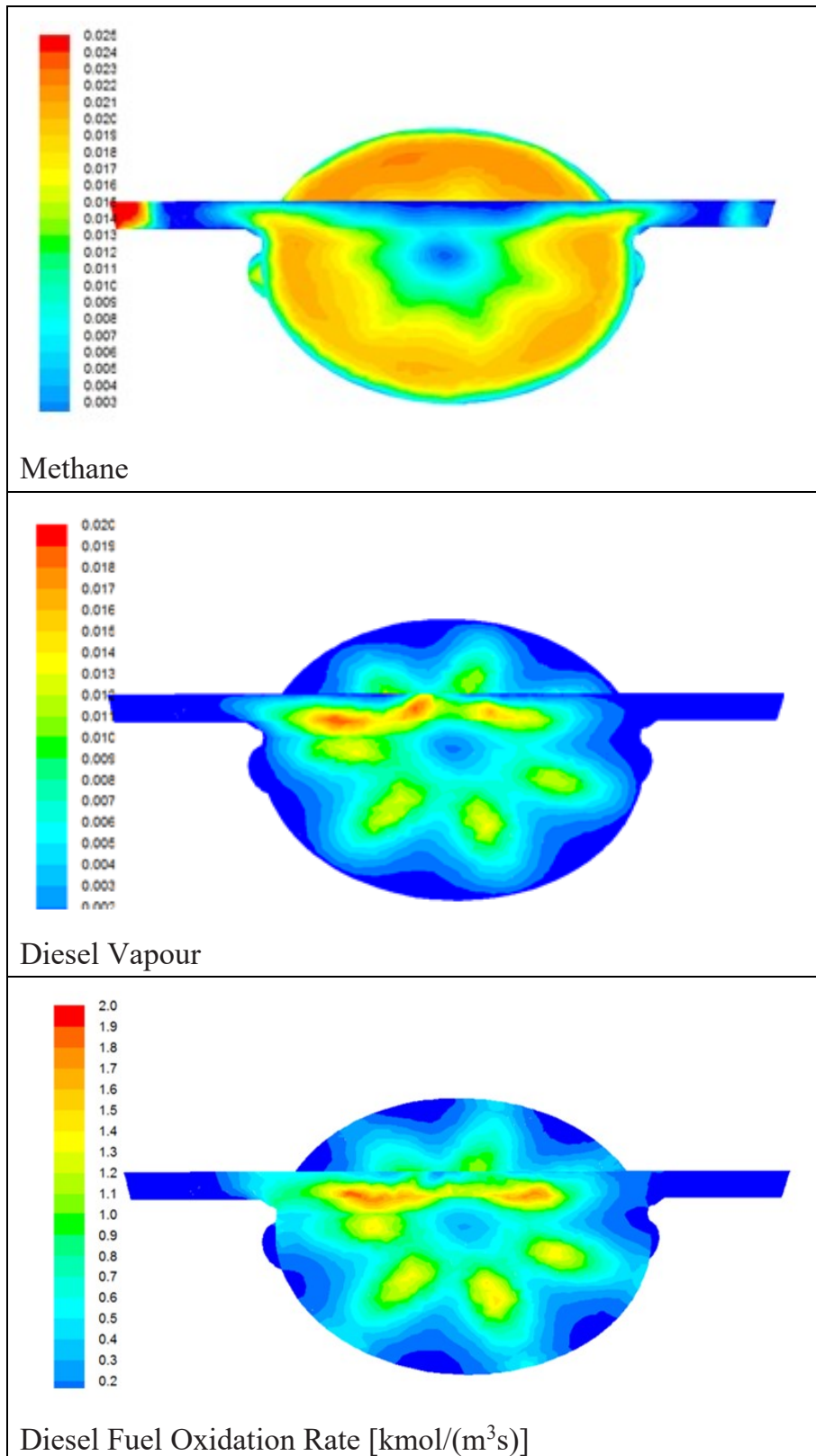


Fig. 4.23: Methane, diesel fuel vapour mass fractions and reaction rates distributions (SOP=12° BTDC) at 20° ATDC in DF mode.

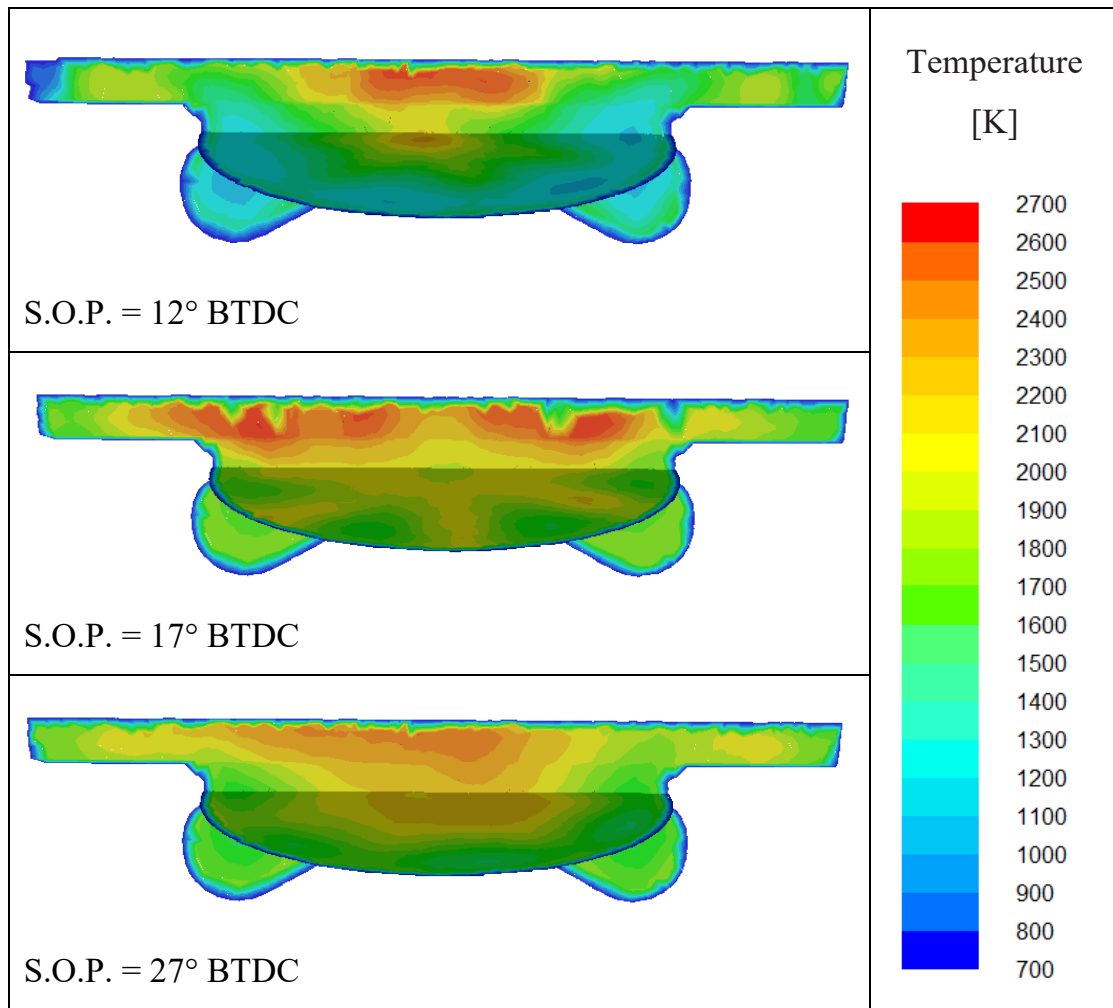


Fig. 4.24: Temperature distributions for different injection timings at 20° ATDC in DF mode.

Figures 4.25 and 4.26 report the NO and CO emissions. The low nitric oxides emissions in case 7 confirm the results of the fuel burning rate trend in Figure 4.17 where the less anticipated injection implied a lower peak of combustion.

It is important to highlight that the correlations calculated for the one-dimensional models allow the prediction of the engine performances in a wide and continuous range of operating conditions.

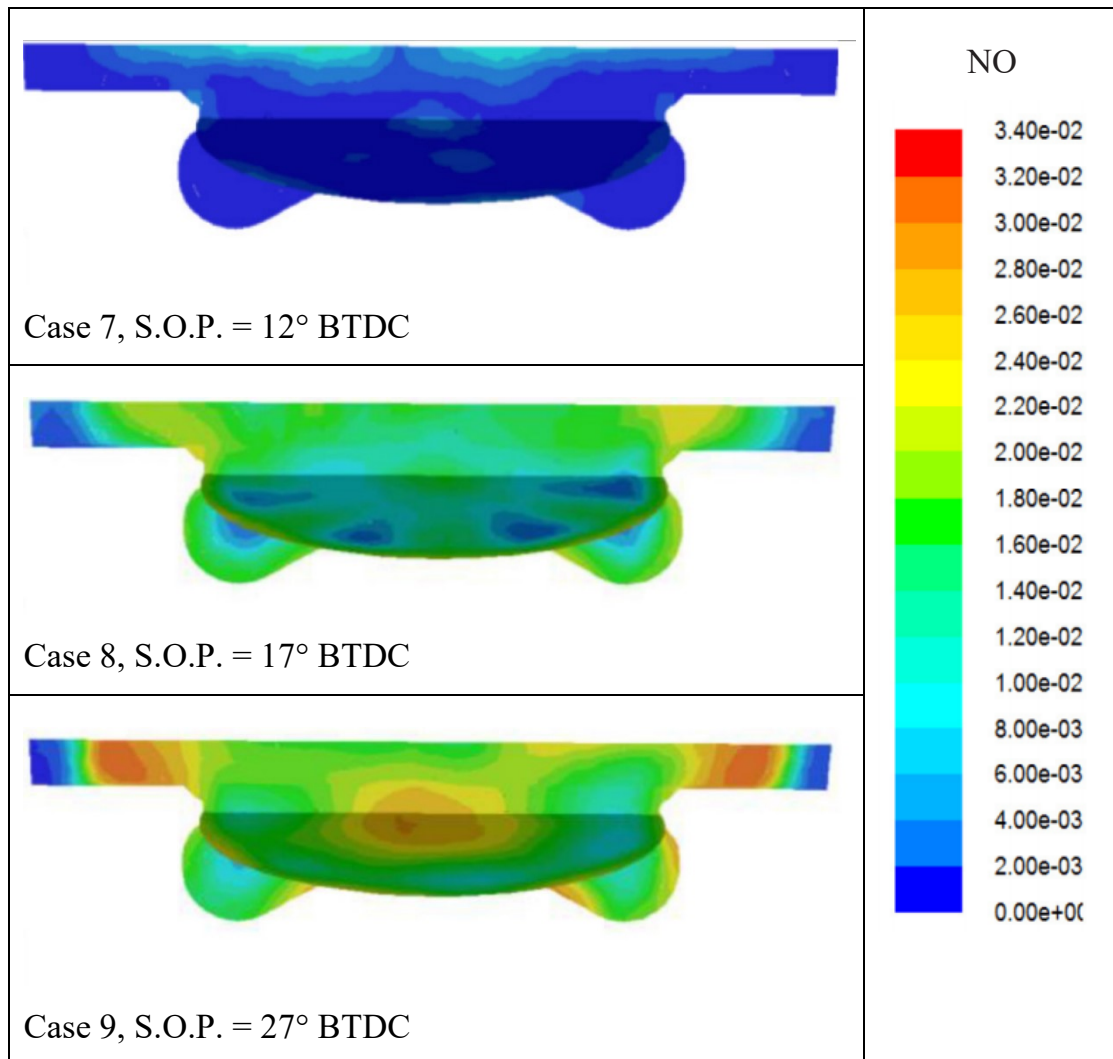


Fig. 4.25: NO mass fraction distributions for different injection timings at 20° ATDC in DF mode.

Figure 4.27 shows a comparison between the trends of the indicated mean effective pressures for the examined cases in full diesel and dual fuel mode, in FD mode the IMEP decreases significantly with a reduction of the injection advance while in DF mode, despite the slight increase it can be considered almost constant. For this reason, in dual fuel mode a right choice of SOP can be suggested as a function of the only reduction of the pollutants.

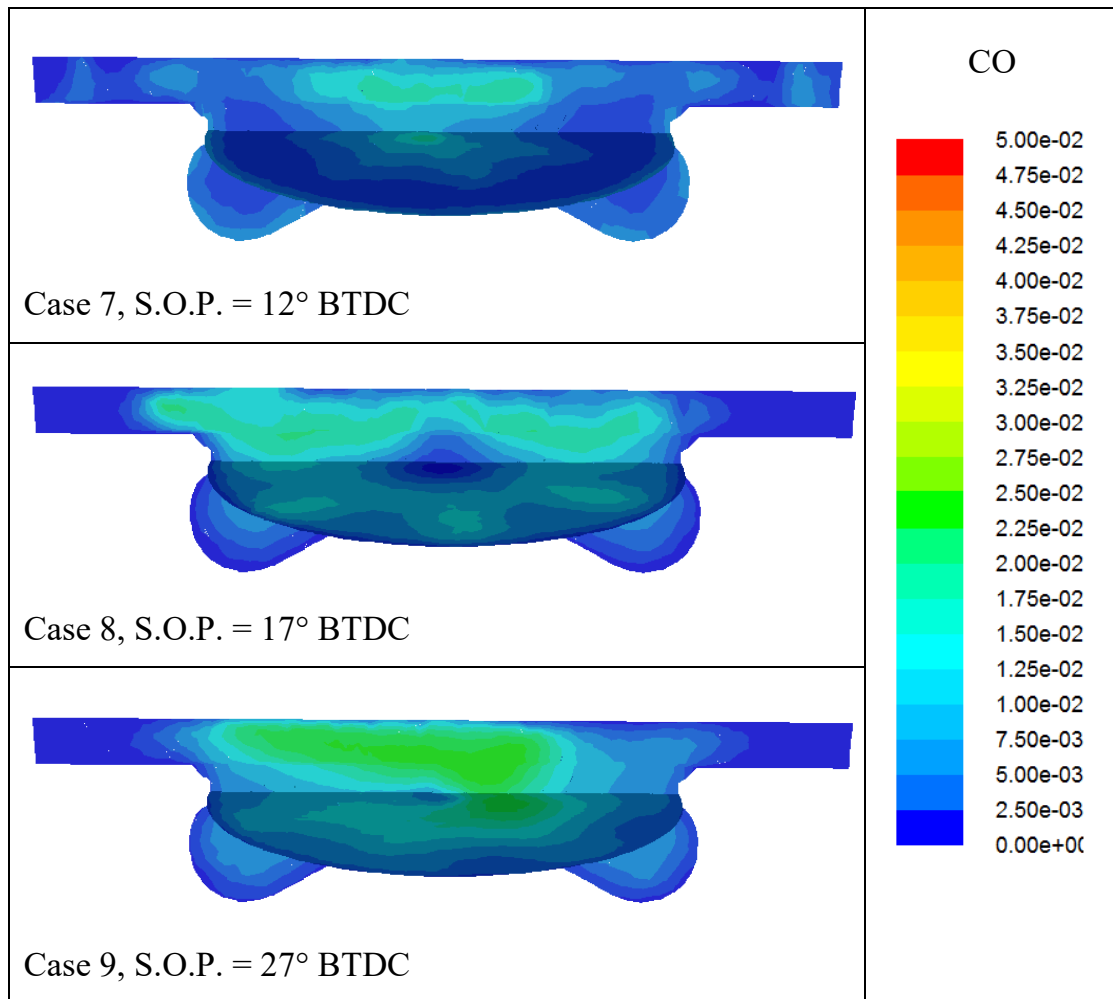


Fig. 4.26: CO mass fraction distributions for different injection timings at 20° ATDC in DF mode.

However, the most important result, as shown in Figure 4.28, is that the CO₂ emission index in DF mode is always lower with respect to FD mode demonstrating that this technology can be an effective mean to reduce the carbon dioxides emissions. Furthermore, the nearly constant trend suggests the independence of the emission level of CO₂ from the injection advance.

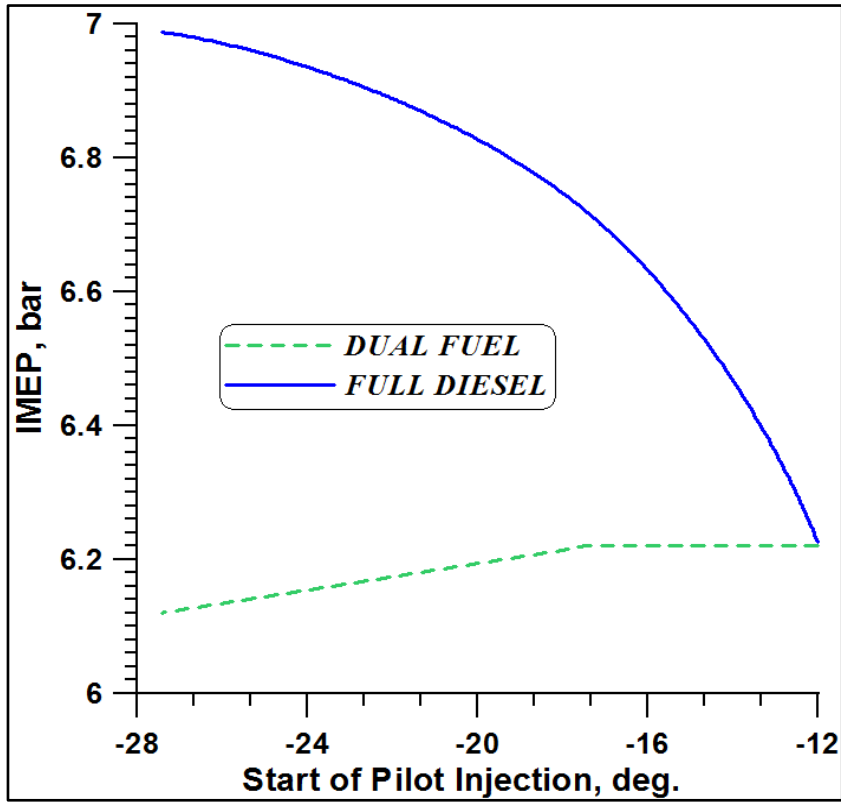


Fig. 4.27: IMEP calculated by 1D model for FD and DF modes.

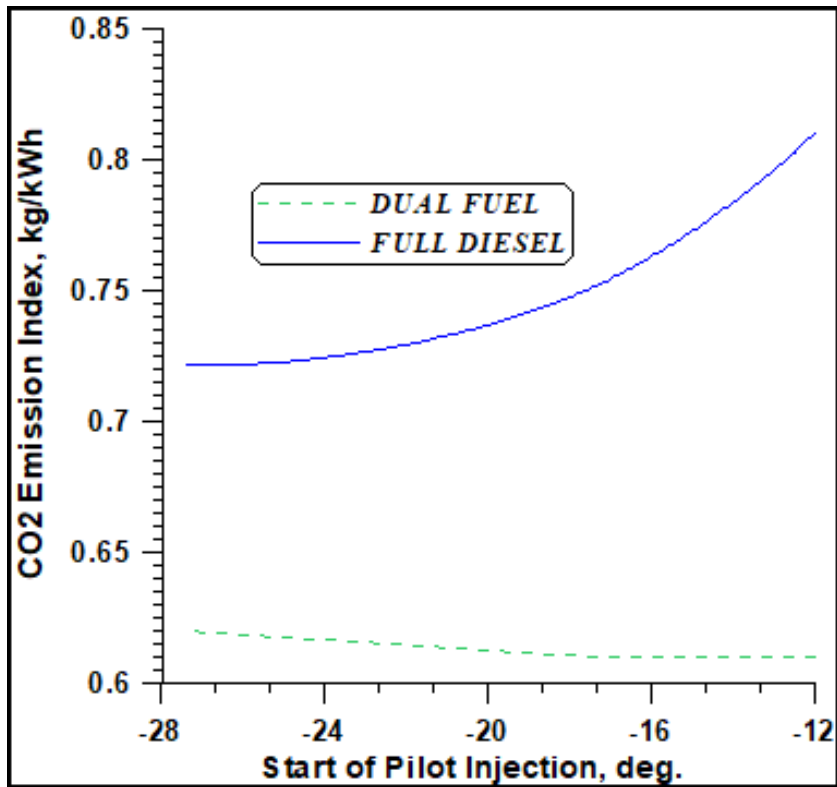


Fig. 4.28: CO₂ emissions calculated by 1D model for FD and DF modes.

Chapter 5

OPTICALLY ACCESSIBLE ENGINE

In this chapter simulations and results based on the experimental activity carried out at Istituto Motori on an optically accessible single cylinder research engine [95] and published in papers [96, 97] are illustrated. It is necessary to highlight that the aim of this research is different from the previous chapter, the object of the investigation is a research engine that allows to directly observe the phenomena that occur inside the cylinder, therefore the attention is mainly focused on the fundamental features of the combustion rather than on engine performance. In this specific case, the different test cases are not characterised by a diesel substitution but by increased methane addition. The purpose is to analyse the effect of the methane presence on the combustion, rather than the variations in combustion development for a given fuel energy input. As a matter of fact, the data set includes some information on in-cylinder distributions (i.e. OH) that can represent a significant test case for the CFD analysis.

5.1 Experimental results

The aim of the experimental campaign was to visualise the combustion development in terms of species concentration, especially for OH radical that is considered to be a significant signal of the combustion rate intensity and location. In the current paragraph an overview of the experimental setup and results is given in order to better understand the methodology used and results obtained from the numerical calculations.

In order to make the research engine under consideration optically accessible, a modification of the combustion bowl was necessary. In particular, the lower part was substituted with a quartz window, as shown in Figures 5.1 and 5.2.

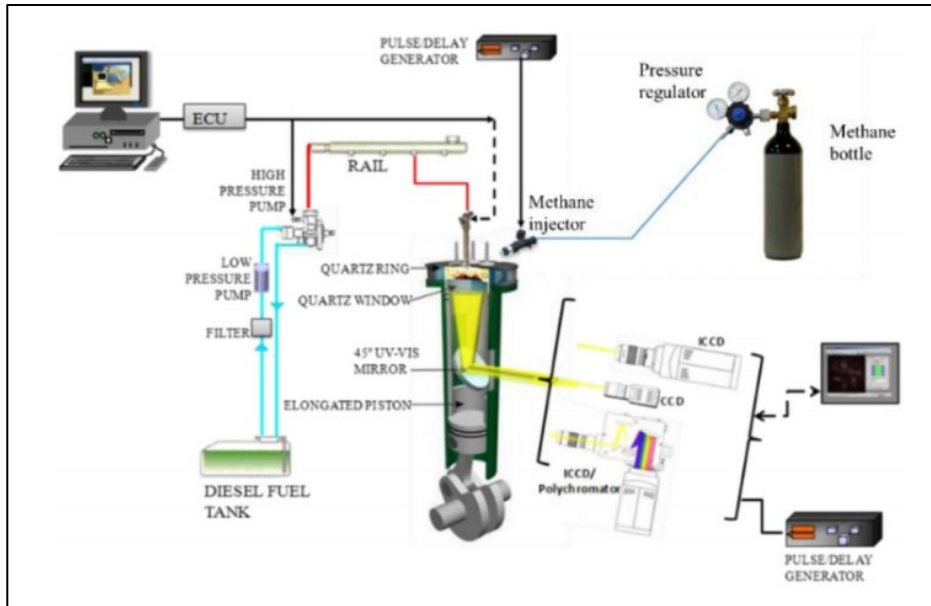


Fig. 5.1: Optical single cylinder engine experimental setup.

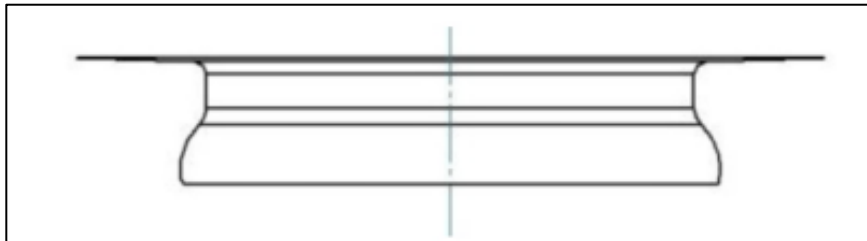


Fig. 5.2: Modified geometry of the combustion chamber.

The engine is equipped with a Common Rail injection system of a the four-cylinder standard engine. The engine specifications are reported in Table 5.1.

Tab. 5.1: Engine specifications.

Engine type	4-stroke, single cylinder, 4 valves
Bore [mm]	85
Stroke [mm]	92
Cylinder vol. displ. [cm ³]	522
Combustion bowl volume [cm ³]	19.7
Vol. compression ratio	16.5:1

The investigation of the spatial distribution and temporal evolution of the UV-VIS emission light of the typical combustion species was made through spectroscopic measurements recorded with an ICCD camera. Data were detected with the spectrograph placed at two central working wavelengths: 350 and 500 nm. In particular, the OH spatial distribution was investigated by means of a band pass filter at 310 nm wavelength [98]. The exposure time of images and spectra detected was of 55 μ s, that at engine speed of 1500 rpm, corresponds to 0.5° deg. More details and specifications can be found in [95].

Tab. 5.2: Injection systems specifications

Diesel Injection system	Common rail
Number of holes	7
Cone angle of fuel jet axis	148°
Hole diameter [mm]	0.141
Methane Injection system	PFI
Number of holes	1
Maximum injection pressure [bar]	5

Tab. 5.3: Engine operating conditions.

Engine speed [rpm]	1500	1500	1500	1500	1500	1500	1500
Methane flow rate [mg/str]	0.0	0.1	0.86	1.32	1.57	1.88	2.14
Diesel SOI	-3	-3	-3	-3	-3	-3	-3
Diesel inj. duration [μ s]	450	450	450	450	450	450	450
Diesel flow rate [mg/str]	8.9	8.9	8.9	8.9	8.9	8.9	8.9
P_{in} [bar]	1.27	1.27	1.27	1.27	1.27	1.27	1.27
T_{in} [°C]	52	50	50	50	50	49	49
T_{out} [°C]	72	77	80	95	107	115	128
Air flow rate [kg/s]	35.4	34.8	34.6	34.4	34.2	33.7	33.4
Premixed ratio	0	1	10	15	17	20	22

In Table 5.2 the injection systems specifications are reported. Since the methane is port fuel injected to mix with air into the intake manifold, the injection pressure can be low.

The engine operating conditions and thus experimental test cases are listed in Table 5.3.

The different test cases are characterised by the same engine speed and same amount of diesel fuel, which means start and duration of injection, while the amount of methane is increased to vary the premixed ratio (RP) value that indicates the percentage ratio of energy input due to methane and is expressed as follows.

$$RP = \frac{(m_p LHV_p)}{(m_p LHV_p + m_d LHV_d)} \times 100$$

Where m_p and m_d are the mass flow rate of premixed fuel (methane) and directly injected fuel (diesel), respectively, LHV_p and LHV_d their lower heating values. Therefore, the RP is equal to zero in full diesel and greater than zero in dual fuel mode. The experimental purpose was to investigate the diesel combustion and emissions when only a poor amount of methane was added to air in order to identify regions where the combustion is not efficient. However, it is important to highlight that the premixed ratio of the examined test cases is significantly low and far from the usual load levels for a diesel engine, but it is important to take into account that the presence of a quartz window imposes limits on the amount of fuel that can burn inside the chamber.

In Figure 5.3 the in-cylinder pressures are displayed for only three test cases: RP = 0, 15 and 22%, since these three test cases have been used for the numerical simulations.

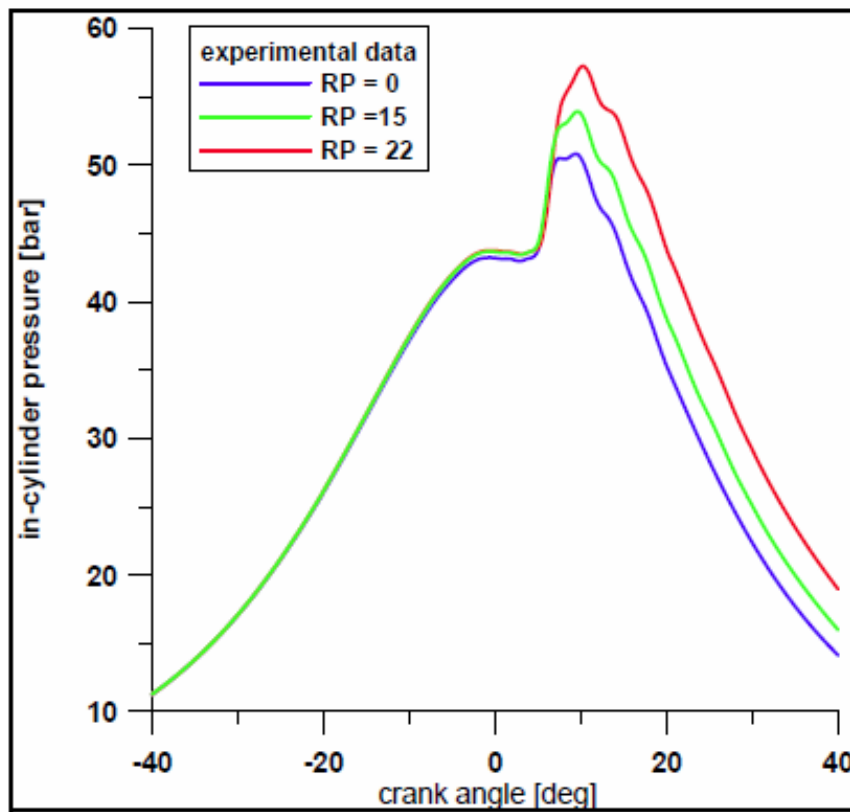


Fig. 5.3: In-cylinder pressure for three values of RP parameter.

The increase in methane amount implies a higher pressure peak and a wider expansion phase curve.

In Figure 5.4.a the brake specific emissions of the total unburned hydrocarbons (THC), CH_4 , CO and NO_x are reported, by varying the premixed ratio. The THCs increase dramatically in dual fuel mode, they mainly consist of CH_4 , this is due to the low levels of the premixed ratio that do not allow an efficient ignition of the premixed mixture. Also, CO and NO_x are favoured by higher premixed ratio, the former are due to the incomplete oxidation of the premixed methane already indicated by the unburned hydrocarbons; while the latter are promoted by the higher temperatures caused by the methane combustion, although the oxygen concentration is reduced by the presence of the gaseous fuel in the intake charge.

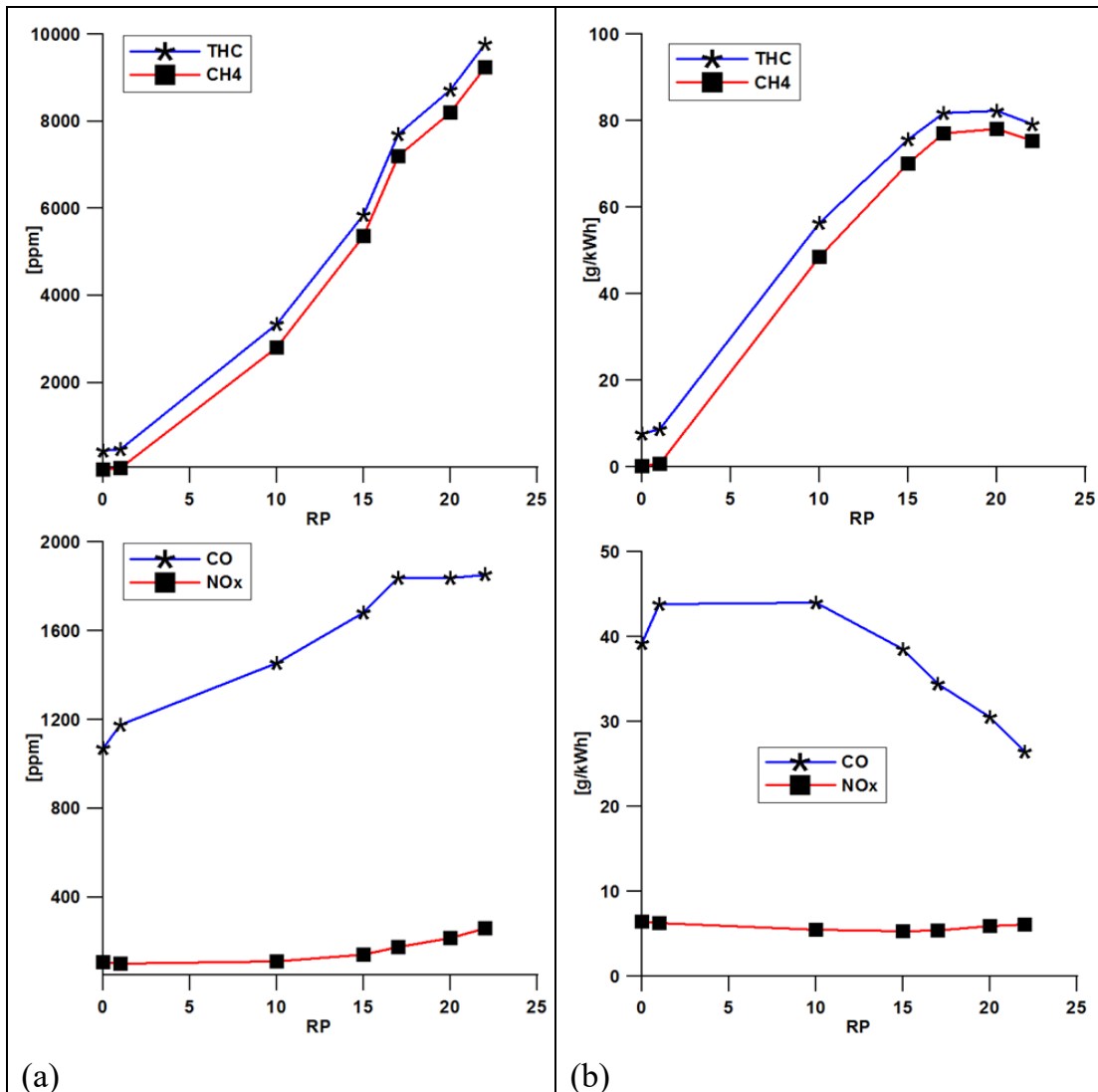


Fig. 5.4 Pollutants emissions with RP expressed in a) ppm and b) in g/kWh.

The same species trends are reported in g/kWh in Figure 5.4.b. Indeed, an enhancement of RP influences also the engine power output and it is interesting to assess how the emissions are related to the indicated power that obviously increases with the total amount of fuel introduced, as noted in Figure 5.5. The THC and CH₄ specific emissions still increase but from RP=17 their trends are inverted since the increase in indicated power is predominant. Moreover, the CO specific emissions decrease with premixed ratio higher than 10 and the nitric oxides result almost constant.

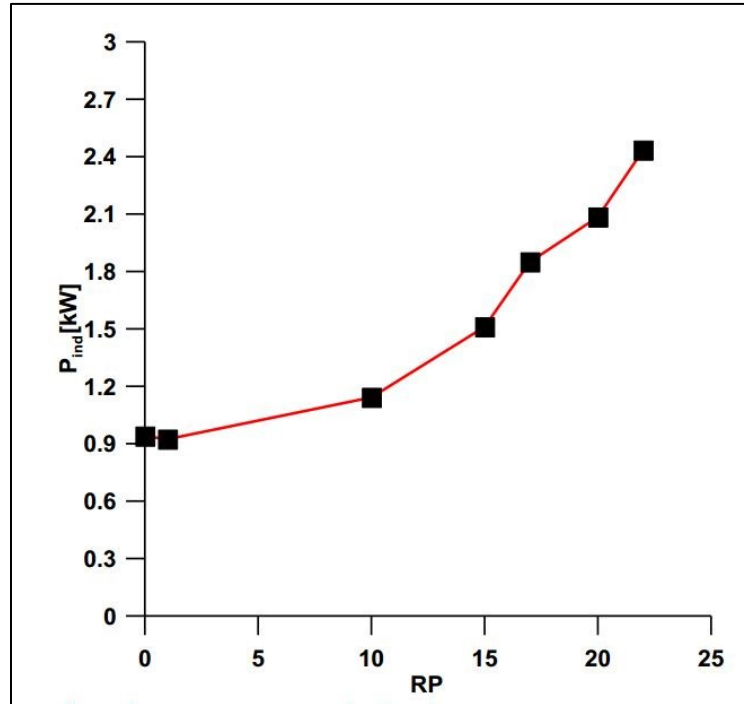


Fig. 5.5: Indicated power versus premixed ratio.

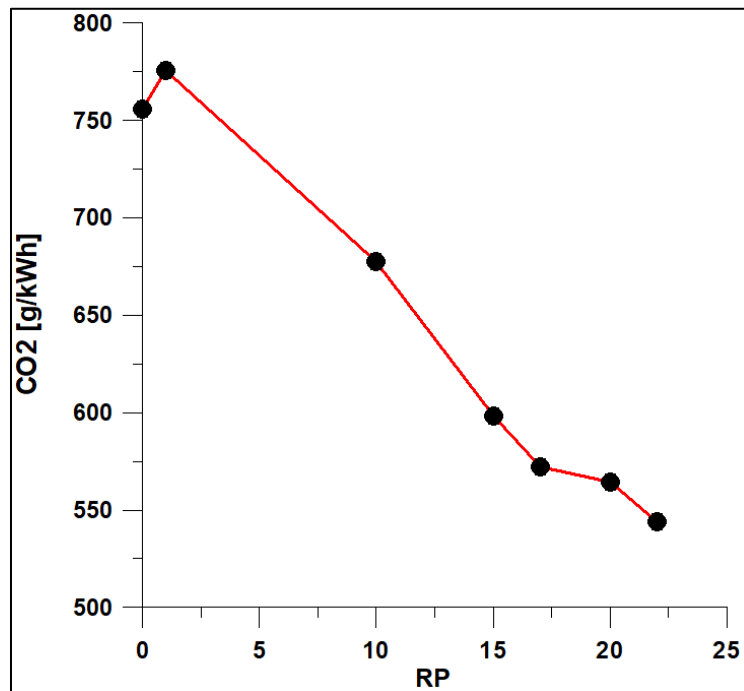


Fig. 5.6: CO₂ emission index versus premixed ratio.

Finally, the CO₂ emission index decreases, due to the combined effect of the reduced carbon ratio in the fuel and the power increase.

Confirming that dual fuel strategy can effectively reduce the emissions of this greenhouse gas.

Finally, in Figure 5.7 the hydroxyl radical images for RP=0 and 22 at different crank angles show the combustion development.

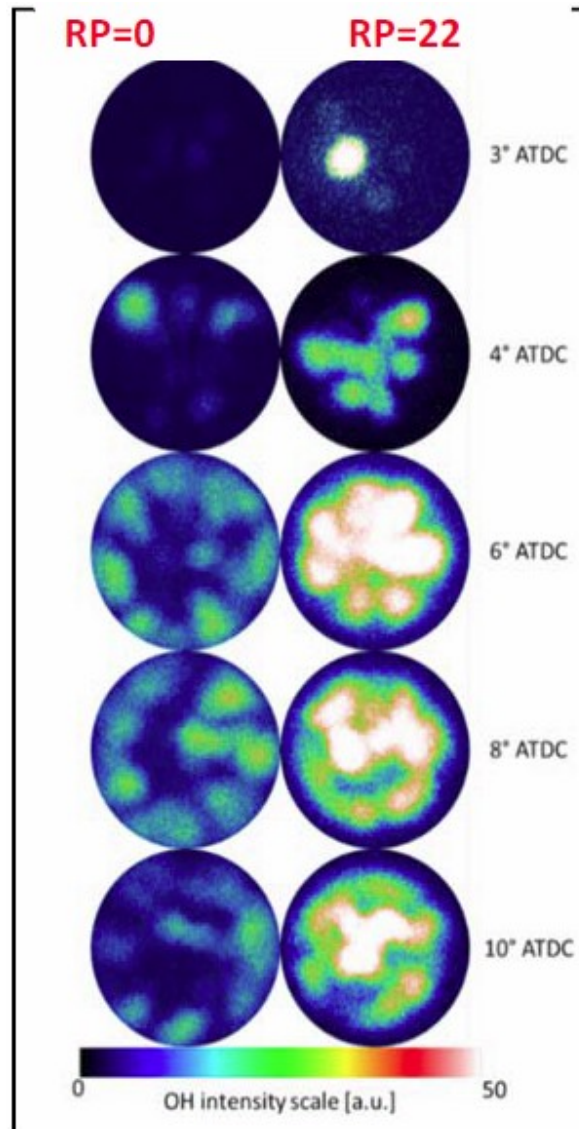


Fig. 5.7: OH images at several crank angles during the premixed combustion for RP 0 and 22 [95].

As already said, the OH radical is considered as one of the most important indices of premixed combustion since it is an intermediate species in the combustion process. For RP=0 (full diesel) the spatial and temporal distribution of OH follows mainly the tip of the jets. In fact, the small amount of diesel, once reached the walls of the bowl, vaporises and burns in a premixed way. On the contrary, the presence of OH radical is also detected in the middle of the chamber due to the front flame moving from the bowl wall

towards the centre in a methane/air charge. Therefore, in dual fuel combustion reactions occur with a more homogenous distribution in the whole bowl with respect to diesel mode.

5.2 Methodology

As said above, the available experimental tests were carried out on a research, optically accessible cylinder that required relevant changes in the bowl geometry. Due to the lack of a mesh grid that reproduced the real geometry, the CFD analysis presented in this chapter aimed to reproduce the same tests in an in-cylinder domain with the same baseline geometrical features but with a bowl shape more consistent with those usually adopted for automotive application, proving the transferability of the experimental results to real diesel engines and providing more detailed information on the dual fuel combustion. However, in Chapter 7 a further improvement was made with the reproduction of the exact bowl geometry and with the deep investigation of the crevices issue that considerably affects this research engine.

The CFD calculations were performed with the KIVA-3V solver on the computational domain in Figure 5.8. The meshed domain was obtained by using the ANSYS-ICEM meshing tool and it consists of 104,000 cells (approximately 58,000 cells for the cylinder and 5,000 cells for the bowl), including the external ducts and the valve lift laws.

The model utilised to describe the combustion process is the Finite Rate – Eddy Dissipation approach. This model seems to be the most suitable to describe the combustion development because as previously highlighted these test cases are characterised by an extremely low equivalence ratio that fall outside the flammability limits of methane, so preventing the propagation of a flame front.

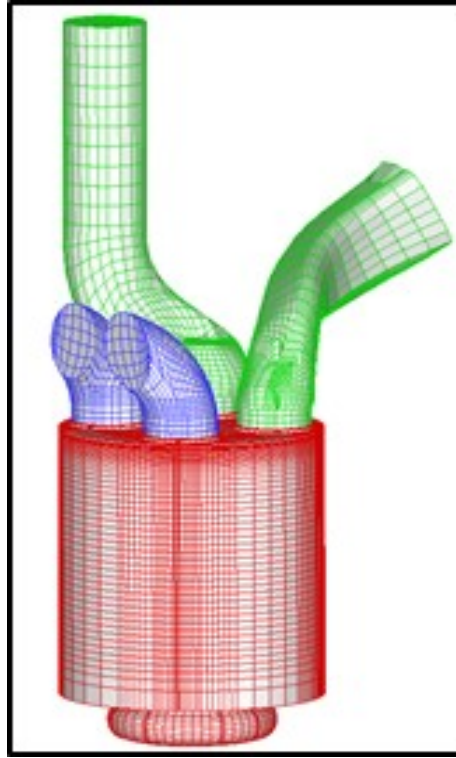


Fig. 5.8: Computational domain for KIVA code.

Tab. 5.4: First kinetic mechanism [90].

$1. C_{12}H_{26} + 37/2 O_2 \rightarrow 12CO_2 + 13H_2O$ $R_{f1} = A \times 10^{11} [C_{12}H_{26}]^{0.25} [O_2]^{1.5} \exp\left(-\frac{15,780}{T}\right)$ $R_{b1} = 0$
$2. CH_4 + 3/2 O_2 \rightarrow CO + 2H_2O$ $R_{f2} = 10^{15.220} [CH_4]^{1.460} [O_2]^{0.5217} \exp\left(-\frac{20,643}{T}\right)$ $R_{b2} = 0$
$3. CO + 1/2 O_2 \rightarrow CO_2$ $R_{f3} = 10^{14.902} [CO]^{1.6904} [O_2]^{1.570} \exp\left(-\frac{11,613}{T}\right)$ $R_{b3} = 10^{14.349} [CO_2]^{1.0} \exp\left(-\frac{62,281}{T}\right)$

Diesel oil and natural gas are represented by dodecane ($C_{12}H_{26}$) and CH_4 , respectively (Table 5.4); in the first studies one reaction converts dodecane

directly into CO₂ following the standard reaction included in the KIVA-3V, while the two-step mechanism is used for the oxidation of methane [90]. For reaction 3 the backward reaction rate indicates that the dissociation of CO₂ into CO is also considered.

Nevertheless, this approach requires a proper calibration of the constant affecting the kinetics (constant A in the first Arrhenius correlation reported in the first reaction of Table 5.4), and the turbulent mixing rate as well for both diesel oil and methane (constant C in the Magnussen and Hjertager correlation).

$$R_t = C \frac{\varepsilon}{k} \cdot \min(Y_R, Y_P) \quad (5.2)$$

In addition, in Table 5.5 six equilibrium reaction present in the model are listed.

Tab. 5.5: Equilibrium reactions.

e.1	$H_2 \leftrightarrow 2H$
e.2	$O_2 \leftrightarrow 2O$
e.3	$N_2 \leftrightarrow 2N$
e.4	$O_2 + H_2 \leftrightarrow 2OH$
e.5	$O_2 + H_2O \leftrightarrow 4OH$
e.6	$O_2 + 2CO \leftrightarrow 2CO_2$

The primary fuel (NG) is mixed with air only in one of the two inlet ducts and introduced into the cylinder while a pilot diesel injection allows the ignition of the NG-air mixture.

The WAVE model was again chosen for the atomisation and evolution of the diesel spray with a B_1 delay time constant equal to 1.73. Instead the self-ignition delay of diesel fuel is governed by the Assanis relationship [99]:

$$\tau_{ID} = 2.4\phi^{-0.2}\bar{p}^{-1.02} \exp\left(\frac{E_a}{R_u\bar{T}}\right)$$

On the other hand, the self-ignition delay time of methane is controlled by two correlation depending on the temperature level. The first one was generated by Spadaccini et al. [92] and is valid above 1,300 K:

$$\tau = 2.21 \times 10^{-14} [O_2]^{-1.05} [CH_4]^{0.33} \exp\left(\frac{22,659}{T}\right)$$

For temperature below 1,300 K the correlation by Li and Williams [93] is introduced:

$$\tau = \frac{2.6 \times 10^{-15} [O_2]^{-4/3} [CH_4]^{1/3}}{T^{-0.92}} \exp\left(\frac{-13,180}{T}\right)$$

In the combustion simulation, also a system of chemical kinetic equations is included for the mechanism of thermal nitric oxide formation [89].

The kinetic mechanism listed in Table 5.4 consists of only 3 reactions. However, the complexity of the dual fuel combustion, due to the presence of two fuels with different characteristics requires an improvement of the chemical model in order to better understand the combustion process. Moreover, a more detailed mechanism gives the possibility to release from the empirical self-ignition correlation for methane. Therefore, the Li and Williams [100] kinetic scheme was successively implemented in the KIVA-3V. Diesel combustion is still described by a one-step reaction and the Assanis self-ignition delay correlation. The overall reaction mechanism consists of the 18 species reported in Table 5.6 and the 12 reactions in Table 5.7.

Tab. 5.6: Detailed Species present in the mechanism.

1	DF2	7	H ₂	13	HO ₂
2	O ₂	8	O	14	CH ₃
3	N ₂	9	N	15	H ₂ O ₂
4	CO ₂	10	OH	16	CH ₂ O
5	H ₂ O	11	CO	17	CHO
6	H	12	NO	18	CH ₄

Tab. 5.7: Reaction mechanism.

RR1	$C_{12}H_{26} + 37/2 O_2 \rightarrow 12CO_2 + 13H_2O$
RR2	$CO + 1/2 O_2 \leftrightarrow CO_2$
RR3	$CH_4 + O_2 \rightarrow HO_2 + CH_3$
RR4	$CH_4 + HO_2 \rightarrow H_2O_2 + CH_3$
RR5	$CH_4 + OH \rightarrow H_2O + CH_3$
RR6	$CH_3 + O_2 \rightarrow CH_2O + OH$
RR7	$CH_2O + OH \rightarrow CHO + H_2O$
RR8	$CHO + O_2 \rightarrow CO + HO_2$
RR9	$CHO + M \rightarrow CO + H + M$
RR10	$H + O_2 + M \rightarrow HO_2 + M$
RR11	$H_2O_2 \rightarrow 2OH + M$
RR12	$CH_4 + 3/2 O_2 \rightarrow CO + 2H_2O$

In particular, the Li and Williams mechanism introduces 5 new species (13 to 17 in Table 5.6) and 9 reactions (RR3 to RR11 in Table 2) for the autoignition of methane. The introduction of these new reactions implies the reduction of the six equilibrium equations to only two (e.2 and e.3).

Li and Williams state in their paper that the mechanism proposed is suitable to describe the early phases of methane oxidation, so that it is able to predict the methane ignition induced by the diesel fuel combustion for temperatures between 1,000 K and 2,000 K, pressure between 1 bar and 150 bar, and equivalence ratios between 0.4 and 3. Actually, they presented a detailed mechanism consisting of 127 reactions and 31 species. However, below 1,300 K the concentrations of most of the species are negligible and the reduced scheme made of 9 reactions can be applied. The temperature and

pressure ranges of this mechanism are consistent with those typical of a high compression ratio. On the contrary, the methane-air equivalence ratio can be lower at reduced engine loads. However, higher local equivalence ratios are expected because of the oxygen consumption that derives from the earlier diesel fuel combustion.

In Table 5.7 reaction 12, which represents the oxidation of methane to carbon monoxide, is still present but it is activated when the cell temperature is above 1,300 K. While the oxidation is completed by reaction 2 that refers to the association and dissociation of CO_2 in CO . The thermal NO_x prediction is still described by the Zel'dovich mechanism.

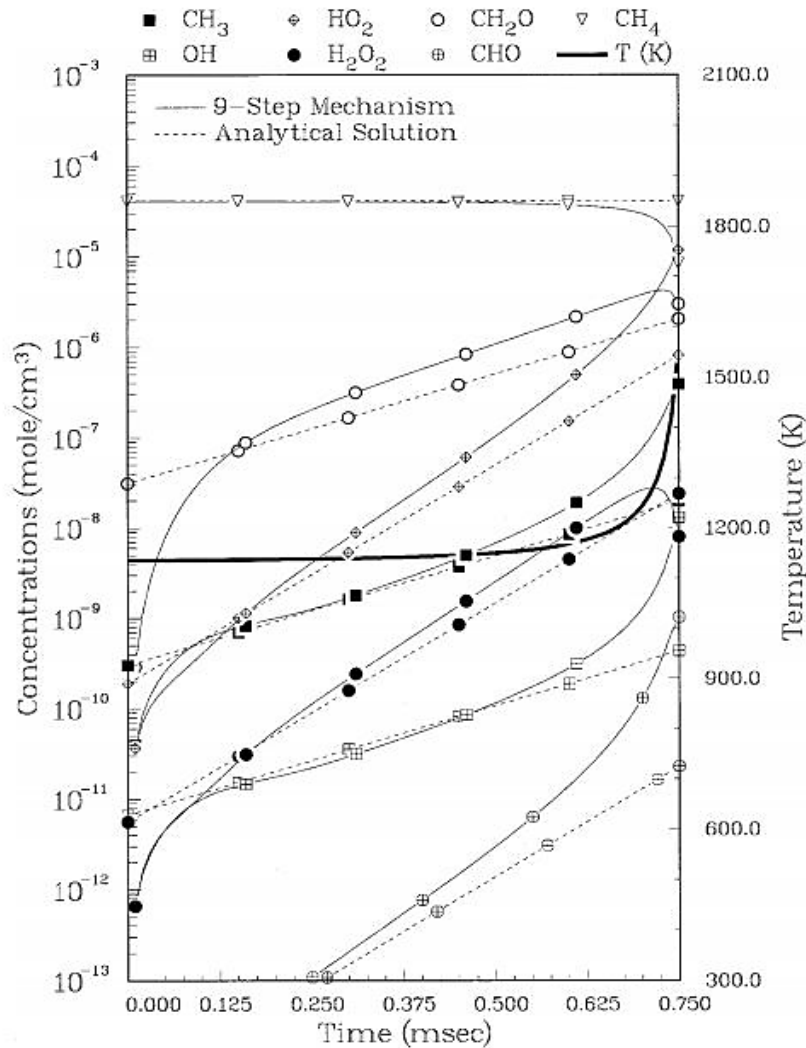


Fig. 5.9: Temperature calculated by Li and Williams in [100].

Preliminarily, Li and Williams calculated the temperature trend for a mixture at 1,136 K, 100 bar and an equivalence ratio of 0.4 (Figure 5.9), then the reaction scheme was tested in CHEMKIN using a closed homogenous reactor under the same condition showing a good agreement with their results (Figure 5.10).

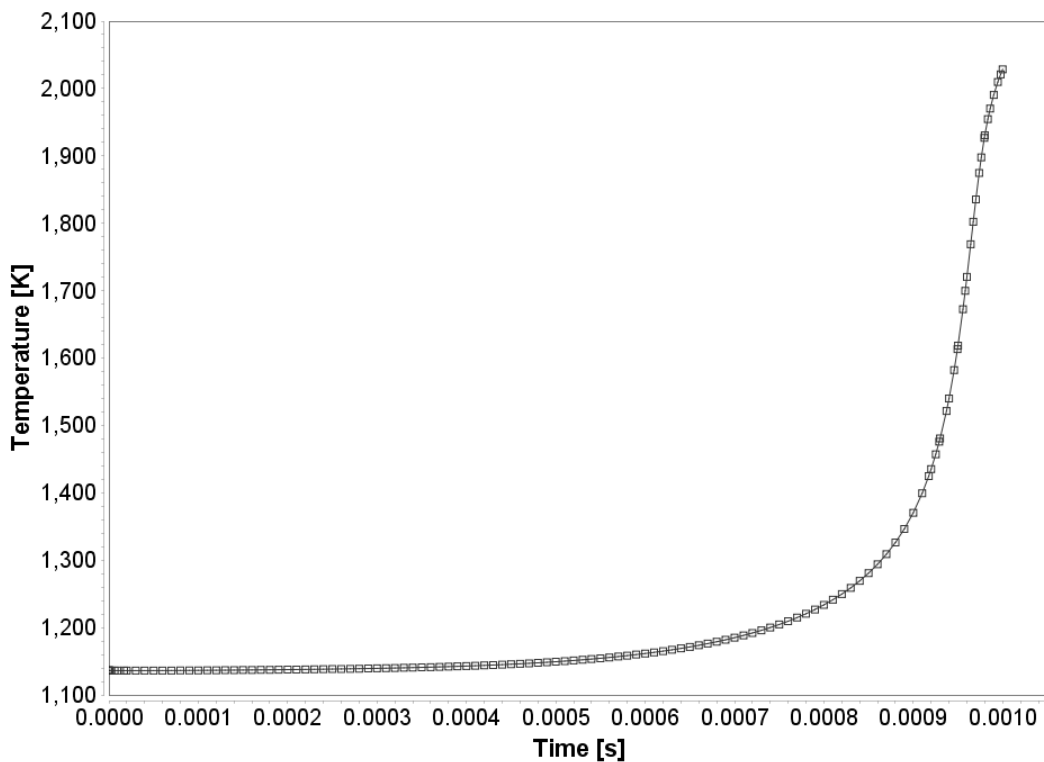


Fig. 5.10: CHEMKIN results.

Combustion is again simulated with the Finite rate – Eddy dissipation model for the same reasons previously mentioned but, since methane is premixed with air, for reactions from 3 to 12, only the kinetic rate is considered. In Table 5.8 the values of constants in the Arrhenius correlation for each reaction are listed.

Finally, the atomisation model used is still the WAVE model, after a proper calibration the values of $B_0 = 0.61$ and $B_1 = 7$ are set for the two model constants.

Tab. 5.8: Values of A, n and T_a [100].

Reaction	A [mol, cm ³ , s]	N [-]	T _a [K]
RR1	8.00 x 10 ⁺¹¹	0.0	15,780
RR2	7.9899 x 10 ⁺¹⁴	0.0	11,613
RR3	3.980 x 10 ⁺¹⁰	0.0	28,626
RR4	9.04 x 10 ⁺⁰⁹	0.0	12,401
RR5	1.60 x 10 ⁺⁰⁴	1.83	1,395
RR6	3.30 x 10 ⁺⁰⁸	0.0	4,498
RR7	3.90 x 10 ⁺⁰⁷	0.89	204.5
RR8	3.00 x 10 ⁺⁰⁹	0.0	0.0
RR9	1.86 x 10 ⁺⁰⁹	-1.0	8,552
RR10	6.76 x 10 ⁺¹⁶	-1.4	0.0
RR11	1.20 x 10 ⁺¹⁴	0.0	22,901
RR12	1.6596 x 10 ⁺¹⁵	0.0	20,643

5.3 Case study

From the experimental test case only three RP values were chosen to be reproduced with the two-step mechanism for methane, i.e. RP = 0, 15 and 22. Instead, for the implementation of the Li and Williams kinetic mechanism the RP =10, 15 and 22 were chosen. In addition, an arbitrary fourth case with a premixed ratio closer to that of a real engine (RP=80%) has been added and performed only numerically. The first three cases aimed to analyse the dual fuel combustion, but the role of the diesel oil is clearly predominant. On the other hand, in the RP=80% case the amount of methane allows the methane/air ratio to fall inside the flammability limits and different combustion behaviour is expected.

Tab. 5.9 Operating conditions in the computational cases

RP [%]	0	10	15	22	80
Thermal Power (fuel LHV) [kW]	4.78	5.32	5.6	6.125	23.53
IMEP [bar]	1.4	1.8	2.3	3.75	13.16
Trapped Air Mass [mg/cycle]	786	769	764	742	673
Injected diesel oil [mg/cycle]	8.9	8.9	8.9	8.9	8.9
Trapped Methane Mass [mg/cycle]	0	0.86	1.32	2.14	30
Methane mass fraction	0	0.00112	0.00172	0.00287	0.03885
Air/Fuel Ratio	88.39	78.78	74.80	67.23	19.08
Fuel/Air Equivalence Ratio	0.164	0.187	0.199	0.24	0.871
Methane/Air Equivalence Ratio	0	0.0193	0.0298	0.0497	0.6968

For all cases with RP up to 22%, the fuel thermal power and the indicated mean effective pressure levels listed in Table 5.9 are considerably lower than those atypical of mean or full loads. The same Table displays the values of air and fuel masses considered in each calculation. The boundary conditions such as pressure and temperature at the inflow of the duct and the injection timing are derived by experimental test reported in Table 5.3. According to the experimental procedure, the injection timing is fixed, the single injection starts at 3.3° BTDC and has a duration of 4.5 crank angle degrees, that means that the amount of diesel oil injected is the same for all the cases. Hence, the additional energy supply is provided exclusively by methane.

In order to achieve an adequate level of periodic convergence each case was performed for multiple engine cycles. Figure 5.11 shows the in-cylinder pressure by KIVA-3V solver for three subsequent cycles. The first cycle differs significantly from the other and cannot be considered reliable. After at least three cycles the calculation provide what is considered as the final solution. Therefore, all the results discussed in the following refer to the third computed cycle.

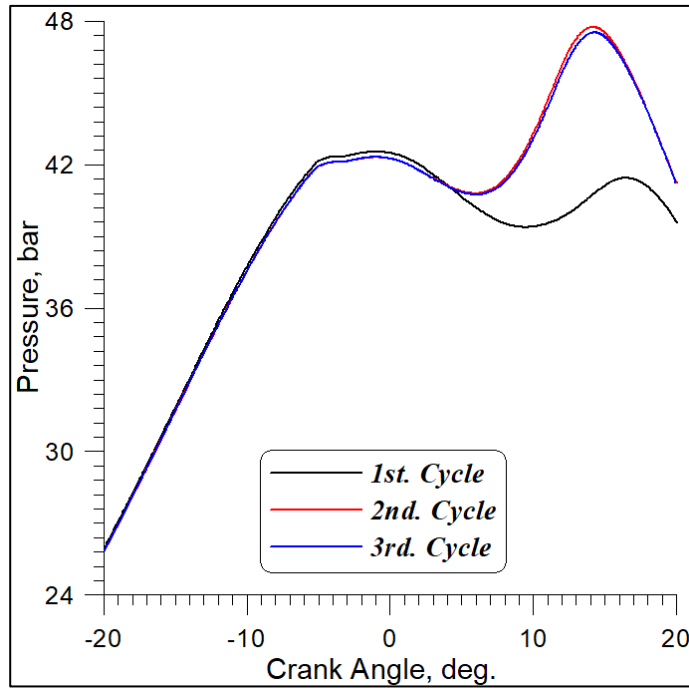


Fig. 5.11: Example of convergence history of the computed in-cylinder pressure to the periodic regime.

5.4 Two-step mechanism results

In this section, the results obtained with the two-step mechanism for methane oxidation are illustrated. Since the scheme consists of few reactions, the reliability of the ignition delay correlations employed for diesel vapour and methane influences the quality of the results. The turbulence-chemistry interaction is governed by the C constant in equation (5.2) for the reactant mixing rate. A proper calibration of this parameter was necessary for the prediction of both diesel oil and methane combustion development (Table 5.10).

Tab. 5.10: Constants of calibration.

RP	0%	15%	22%
A	36	24	12
C_{diesel}	6	9	27
$C_{methane}$	-	108	108

Firstly, the evolution of the multiphase is illustrated in Figure 5.12. The liquid fuel particles progressively decrease and disappear and in turn the corresponding region is filled with vaporised fuel.

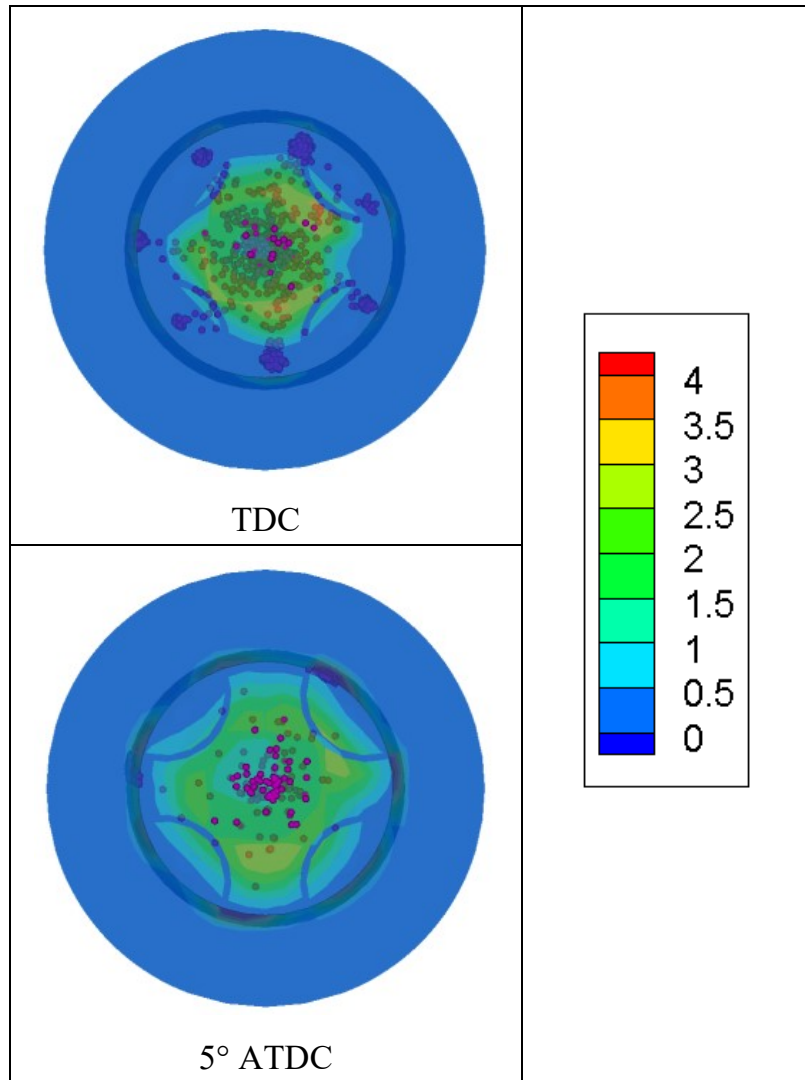


Fig. 5.12 Particle jets and diesel vapor mass fraction (%) contours (RP=22).

In Figures from 5.13 to 5.15 the comparison of numerical and experimental in-cylinder mean pressure is illustrated for the three test cases considered. As it can be observed, the typical features such as start of pressure rise, rise and peak appear to be correctly detected. In Figure 5.16, also the numerical temperature trend (for case RP=22) reproduce properly the experimental one.

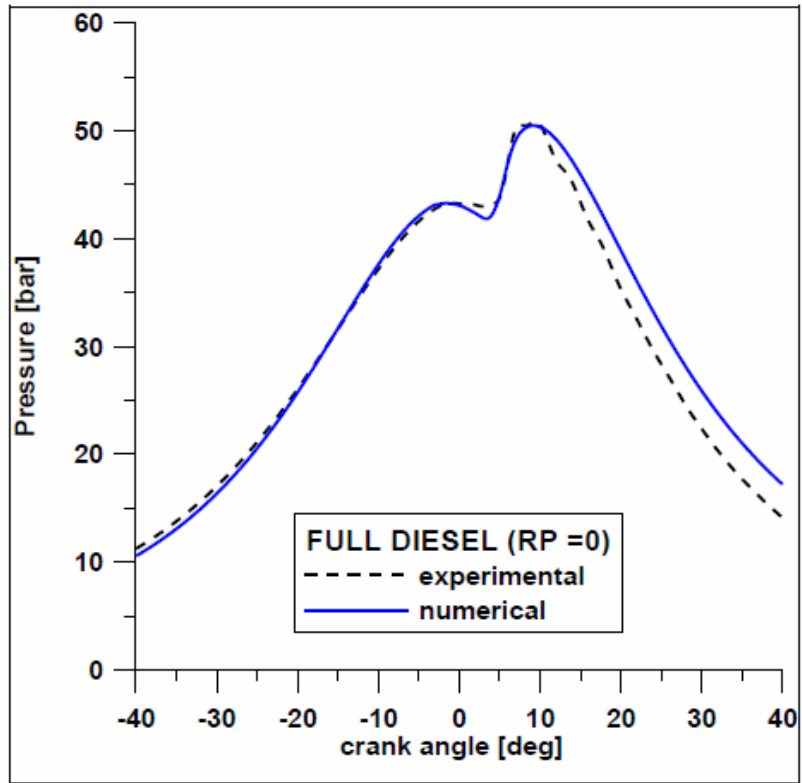


Fig. 5.13: In cylinder pressure for RP=0.

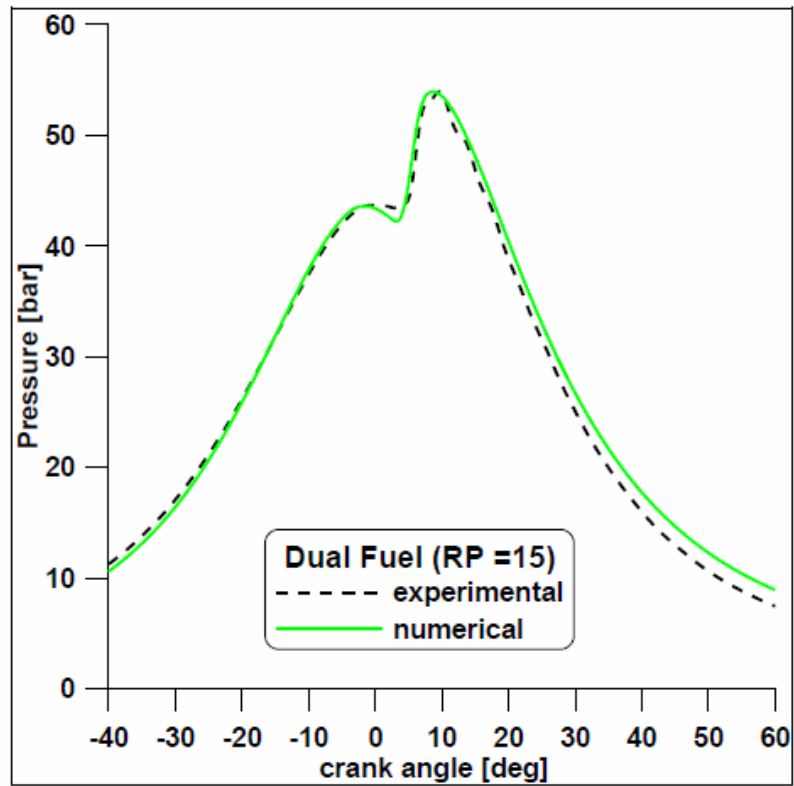


Fig. 5.14: In cylinder pressure for RP =15.

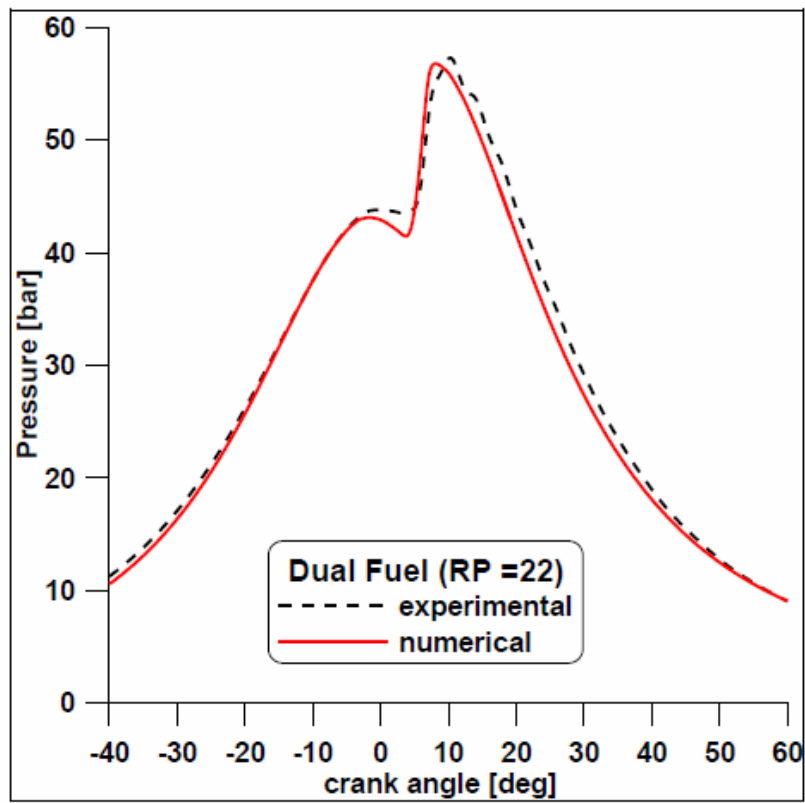


Fig. 5.15: In cylinder pressure for RP =22.

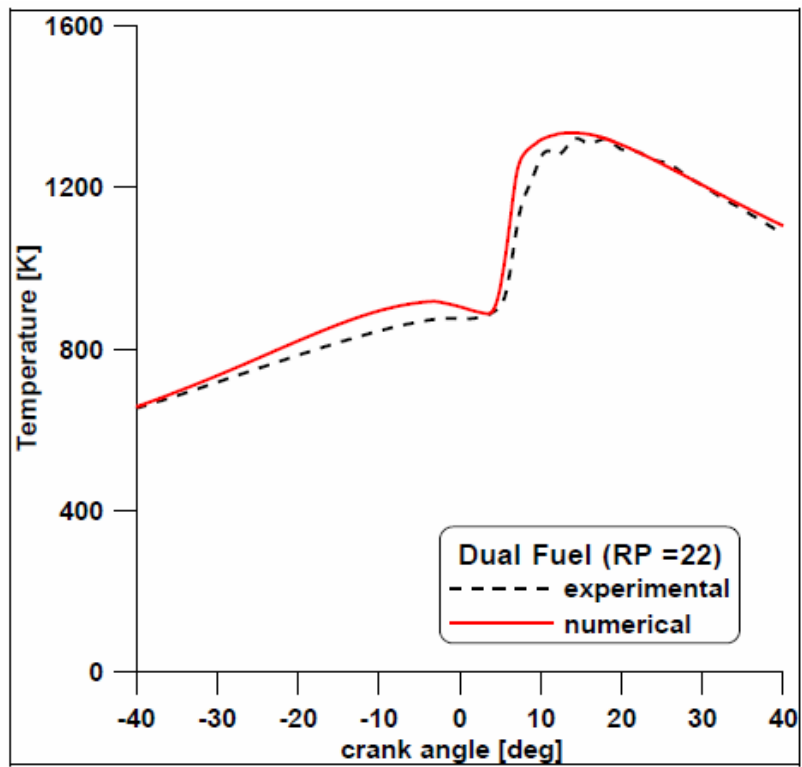


Fig. 5.16: In cylinder temperature for RP=22.

More detailed information is obtained from the computed and experimental fuel burning rate comparison for the case RP=15% reported in Figure 5.17. The activation of the combustion is shifted by 2.5 crank angle degrees, but steep rise is reproduced with a fair accuracy. However, the maximum results are anticipated with respect to the experimental measurement. Finally, the combustion durations appear to be comparable.

Figure 5.19 compares the kinetic and the turbulent reaction rates during the combustion evolution. Only in the early phase the kinetic rate results lower than the turbulent one. For the remaining duration, diesel fuel combustion is governed by the mixing-controlled mechanism. In addition, Figures 5.20 and 5.21 show the kinetic and turbulent rates for each case examined and the latter is always lower than the former one by one order of magnitude. This confirms that the diesel combustion is mainly controlled by turbulent effects.

Moreover, the decreasing level of kinetic rates for higher methane contents in Figure 5.20 is due to the lower oxygen availability caused by methane presence and combustion. On the other hand, during dual fuel operation changes in the flow field and temperature throughout the combustion chamber are induced and consequently the methane oxidation increases the turbulent combustion rates of the diesel fuel. Such an effect results in significant variations in the local Reynolds number and, therefore, variable values of the C constant in the Magnussen and Hjertager equation are to be determined. A proper calibration of this constant suggested increasing value (ranging from 6 to 12) for increasing levels of the premixed ratio. In this way a satisfactory fitting of the pressure curves is achieved.

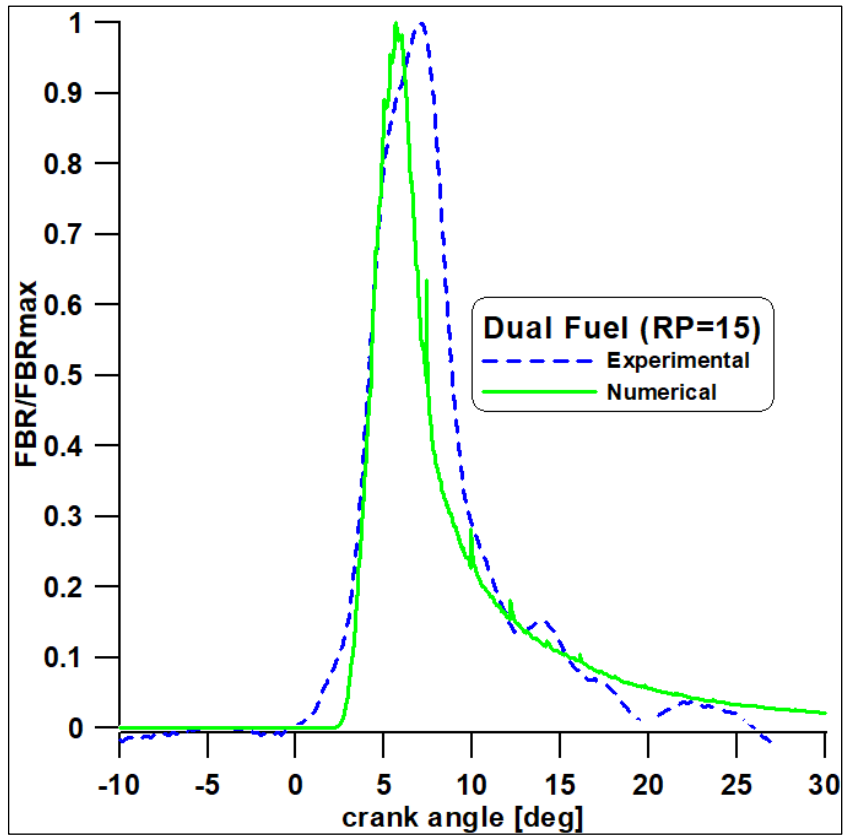


Fig. 5.17: Experimental and numerical fuel burning rates for RP=15.

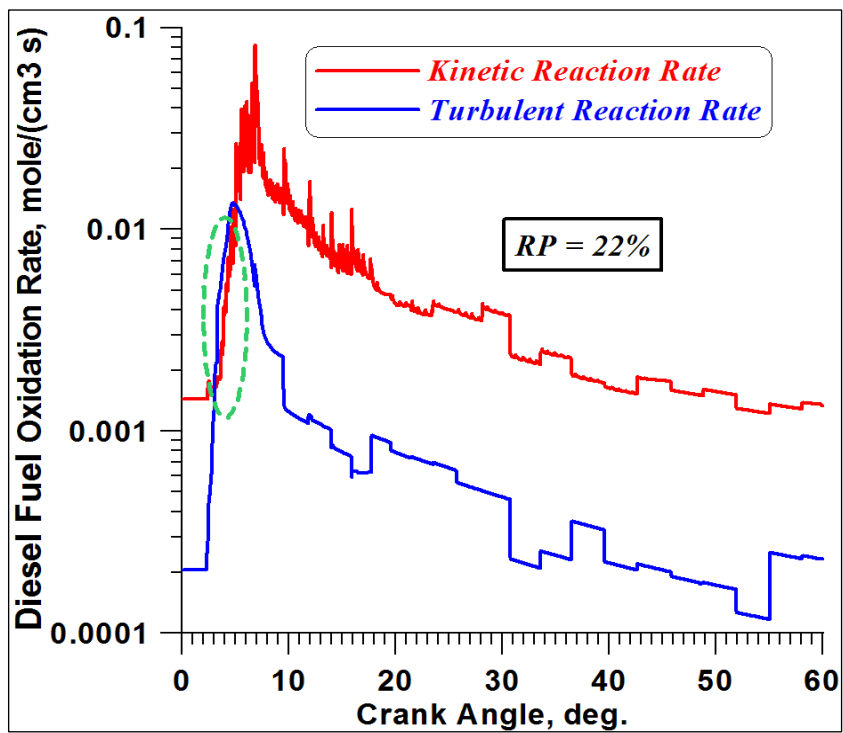


Fig. 5.18: Experimental and numerical fuel burning rates for RP=15.

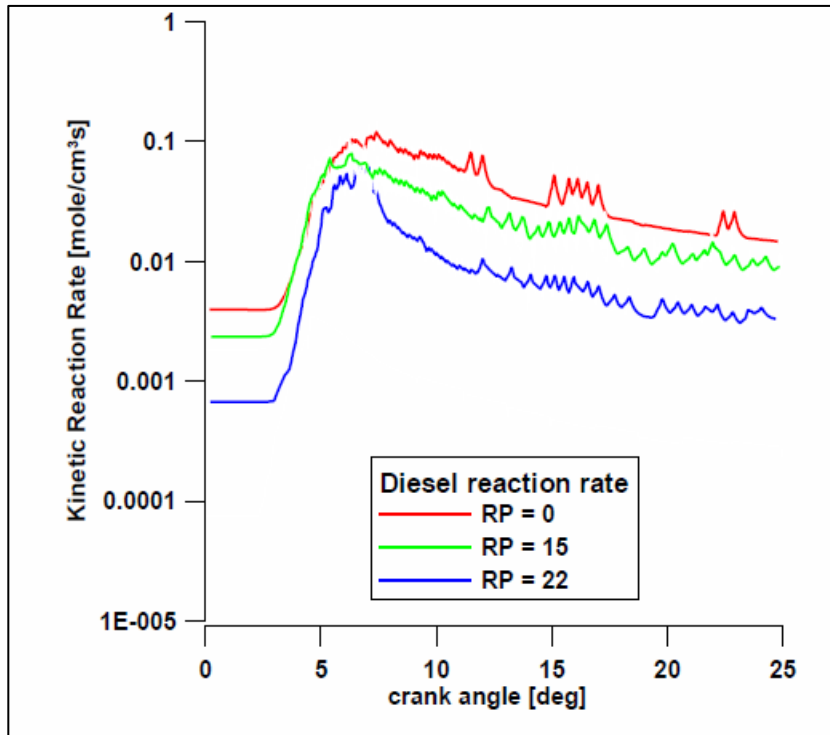


Fig. 5.19: Comparison of kinetic reaction rates for the three cases examined

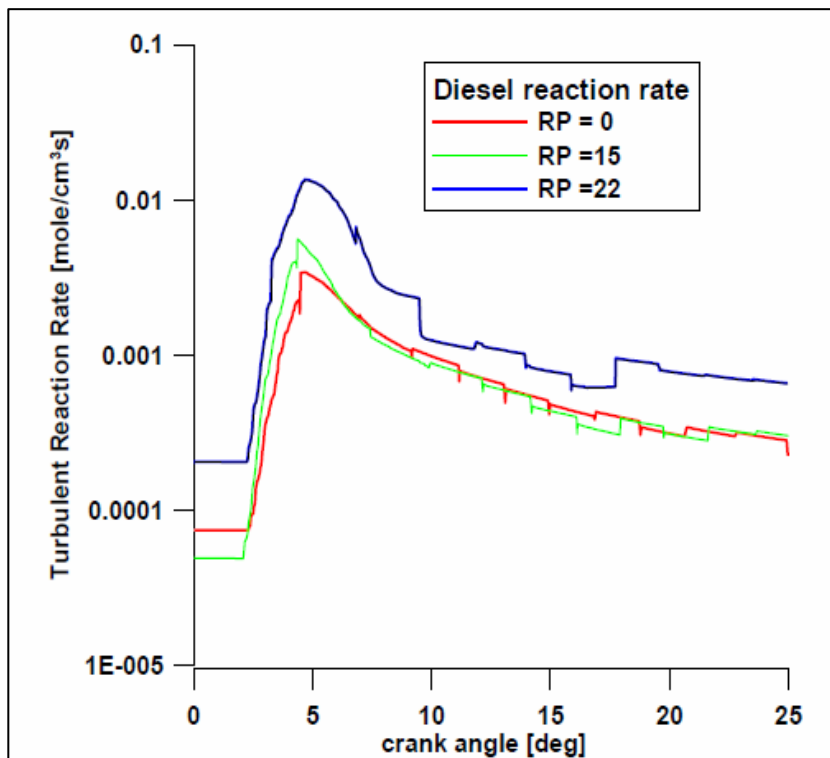


Fig. 5.20: Comparison of turbulent reaction rates for the three cases examined.

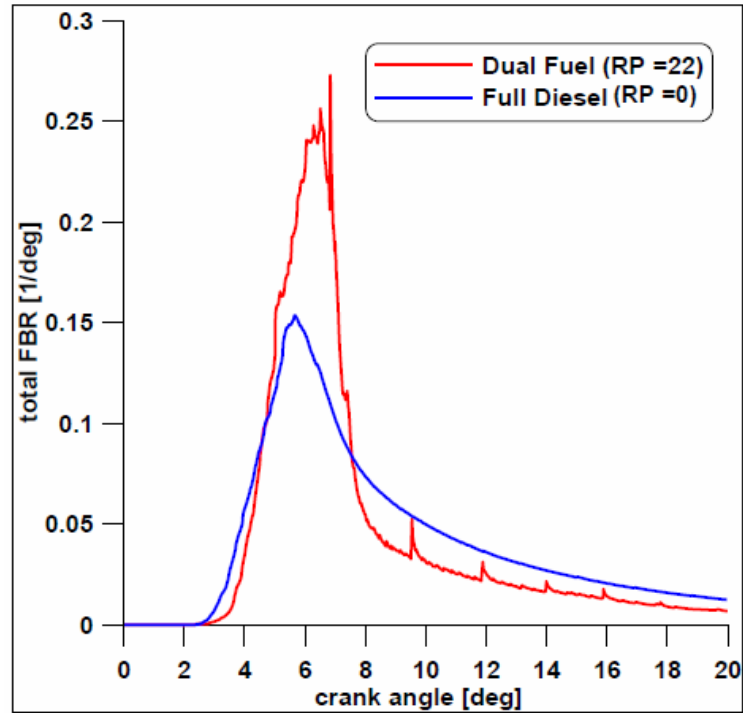


Fig. 5.21: FBR trend for the full diesel and dual fuel (RP=22) case.

In Figure 5.21 the total FBR trends are illustrated for full diesel and dual fuel (RP=22) cases. As expected, the addition of methane in the intake manifold varies the physical and transport properties of the introduced mixture such as the partial pressure of oxygen, retarding the pre-ignition reaction activity and hence enhancing the duration of the delay. Moreover, diesel vapour burns in a shorter time, while the dual fuel combustion presents a longer duration and a smoother behaviour. However, it should be taken into account that also the heat exchange properties can be affected by the presence of methane in the mixture.

For RP=22, the fuel burned fraction and the FBR of natural gas and diesel oil are shown in Figures 5.22 and 5.23 respectively. Differently from diesel vapour, methane does not complete the combustion. As previously highlighted, the equivalence ratio of methane is outside the flammability limits of this fuels, then a not efficient flame propagation is expected for these test cases. This result is in agreement with the unburned species in the

exhausts illustrated in the experimental results, which are characterised by a greater amount of THC (Figure 5.4.a).

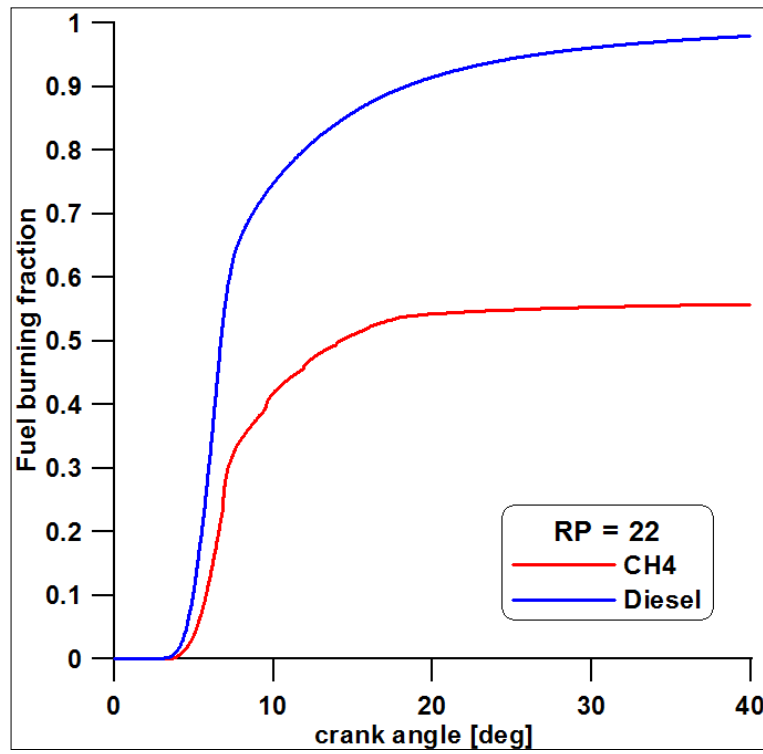


Fig. 5.22: Fuel burning fraction for diesel oil and natural gas.

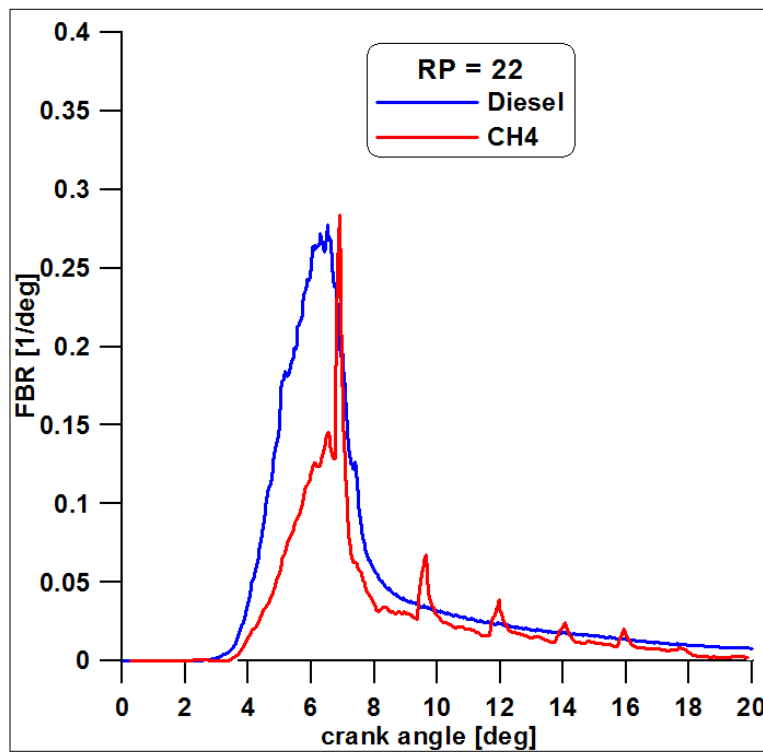


Fig. 5.23: FBR for diesel oil and natural gas (RP =22).

For this reason, both Figures evidence that CH₄ combustion must be activated and sustained by the diesel ignition.

In Figures 5.24 and 5.25, temperature distributions inside the bowl are plotted for the three cases in an axial and in a transversal plane, respectively. Both Figures highlight wider zones at high temperature when the methane amount is increased.

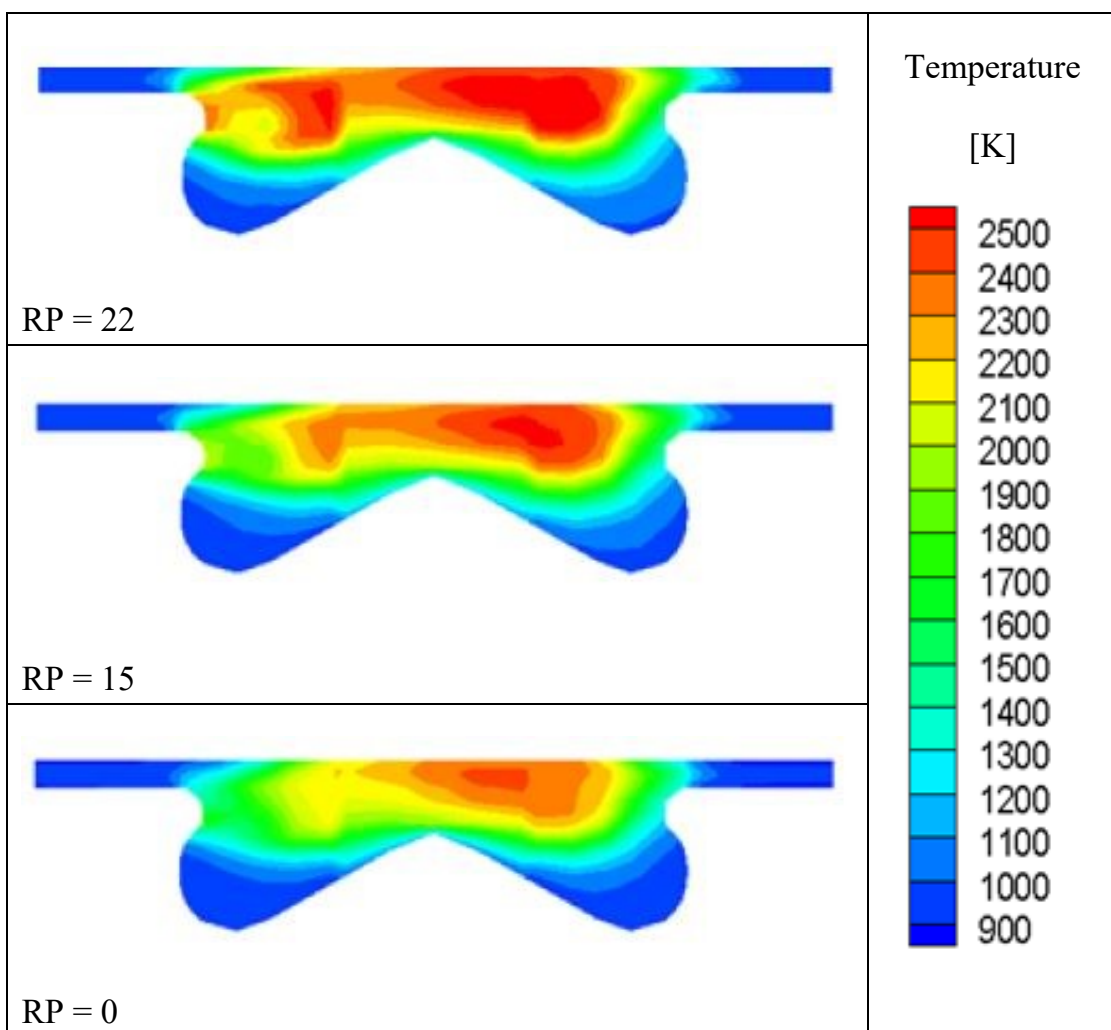


Fig. 5.24: In-bowl temperature distribution in a meridional plane at 10° ATDC.

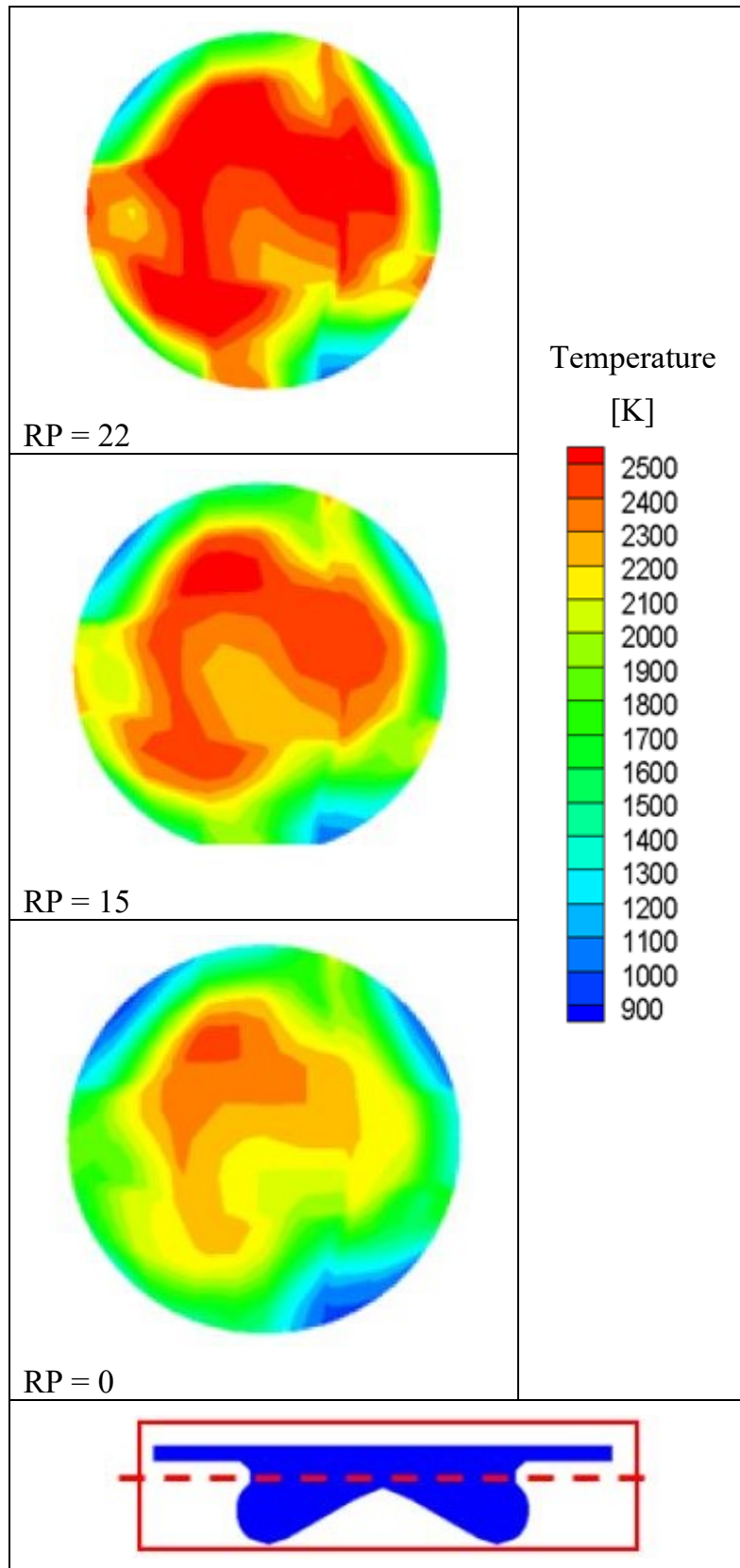


Fig. 5.25: In-bowl temperature distribution in a cross plane at 10° ATDC.

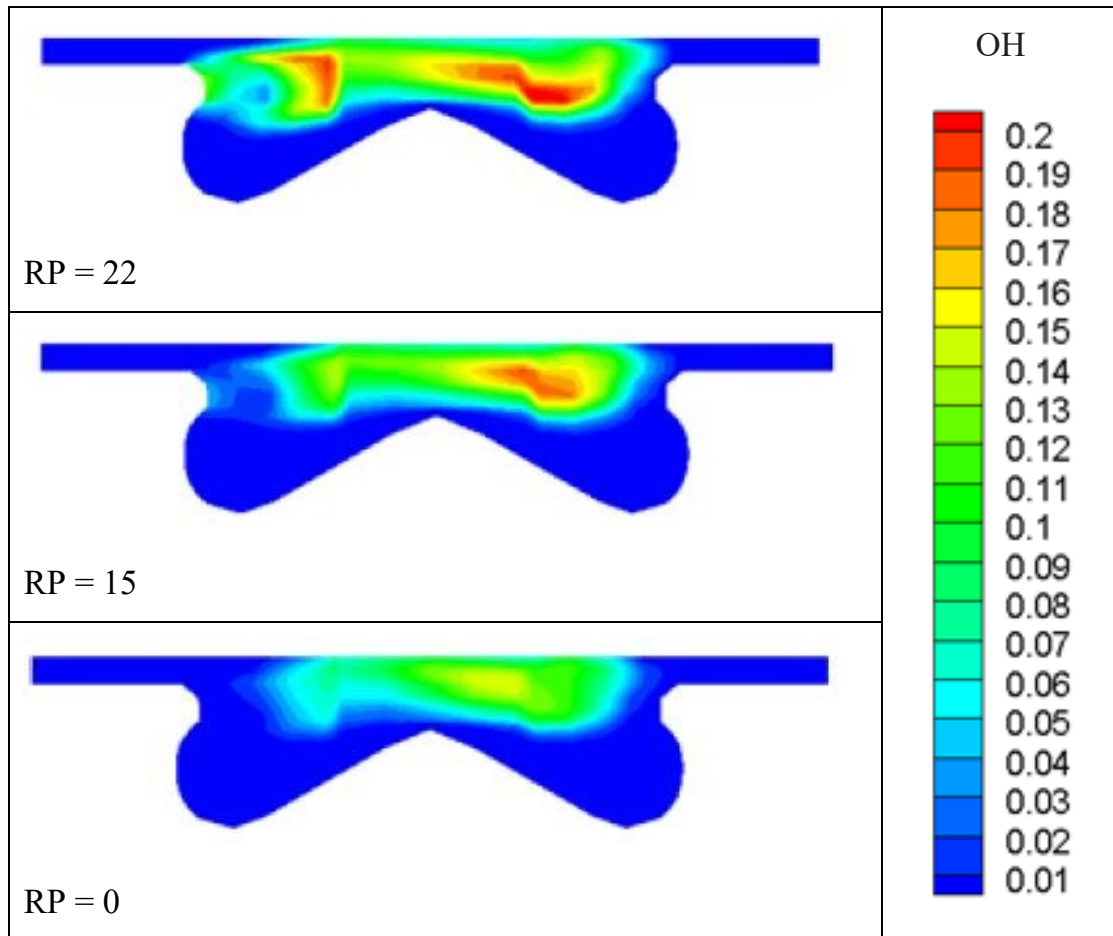


Fig. 5.26. In-bowl OH distribution in meridional plane at 10° ATDC.

The OH distributions reported in Figures 5.26 and 5.27 are coherent with the temperature contours. Indeed, the high oxidation rate intensity detected by the OH production implies the corresponding region at high temperature.

In Figure 5.28 a qualitative comparison between the numerical and experimental distribution for case RP=22 demonstrates that the CFD simulations have proven to be capable to reproduce the real phenomena that occur inside the cylinder.

Finally, Figure 5.29 shows the NO fraction levels in the exhaust for the three numerical and experimental cases highlighting a good agreement between the trends since both detected an increase of nitric oxides with the increase of the NG amount. Nevertheless, numerical computations tend to overestimate the emissions of this pollutant.

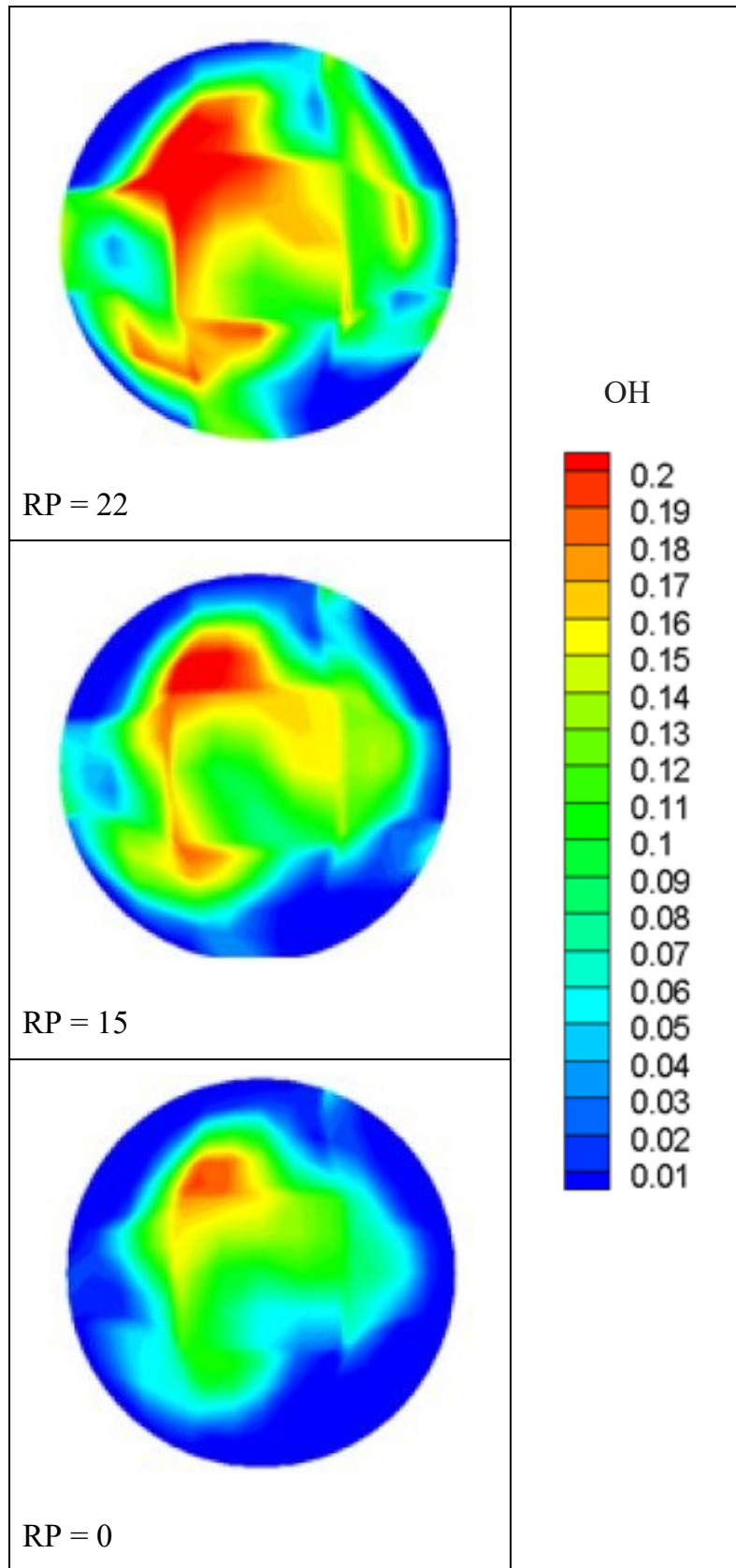


Fig. 5.27: In-bowl OH distribution in a cross plane at 10° ATDC

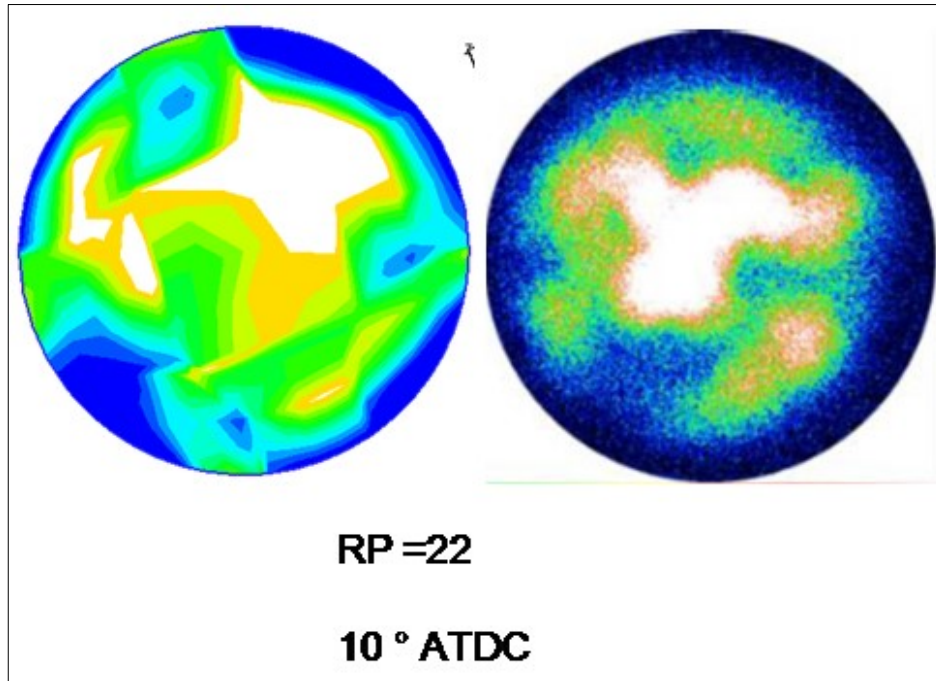


Fig. 5.28: Comparison between numerical and experimental OH traces at 10° ATDC (case RP=22)

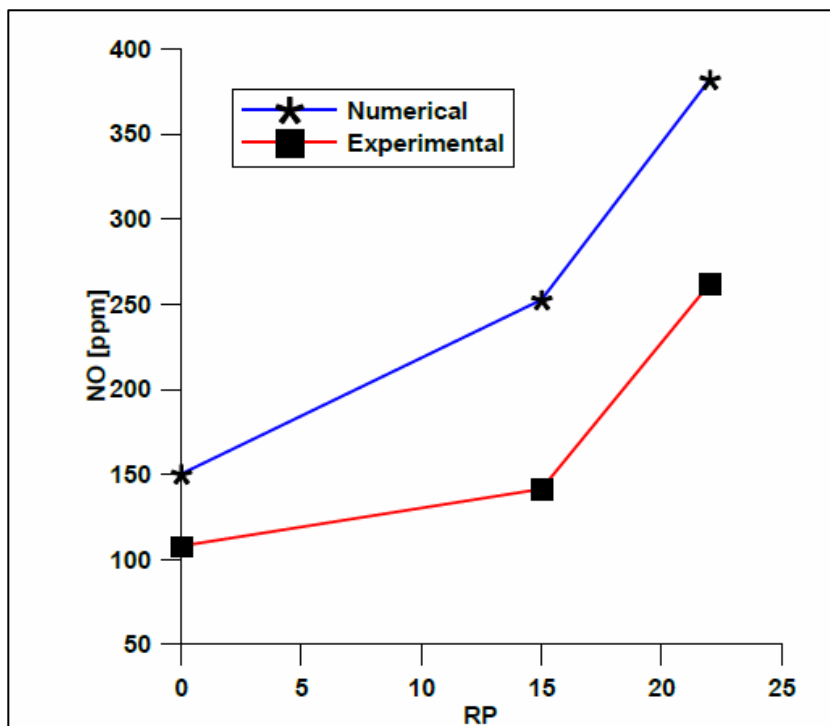


Fig. 5.29: Experimental and numerical NO fractions by varying the RP value.

5.5 Li and Williams mechanism results

As demonstrated in the previous section, results obtained with a simple two-step mechanism are able to reproduce combustion trends provided by the experimental activity. In this paragraph, the same procedure employing the autoignition mechanism for methane presented by Li and Williams is carried out and a comparison with the two-step mechanism is illustrated in order to evidence the differences between the two schemes.

5.5.1 Case $RP = 15\%$

In Figures 5.30 and 5.31 the comparison of the in-cylinder mean pressure and the total fuel burning rate obtained by numerical and experimental tests are plotted. The in-cylinder pressure is fairly reproduced since the numerical growth rate, peak and expansion rate are in agreement with the experimental curve. On the contrary, the numerical FBR presents slight differences such as the start of combustion, which is delayed, and the end of combustion that is less intense than the experimental trend; however the peak is perfectly detected and duration of the combustion is almost the same. In Figure 5.32 it is noticeable that the methane start of combustion is delayed with respect to the diesel one. Again, the incomplete methane oxidation occurs as shown in Figure 5.33.

In Figure 5.34 compares the rates of reaction responsible of diesel oxidation with two of methane. In particular, the RR3 is taken as representative of the Li and Williams mechanism. As it is noted diesel start to burn before methane.

Figure 5.35 confirms the reduced contribution of the heat released by the methane oxidation.

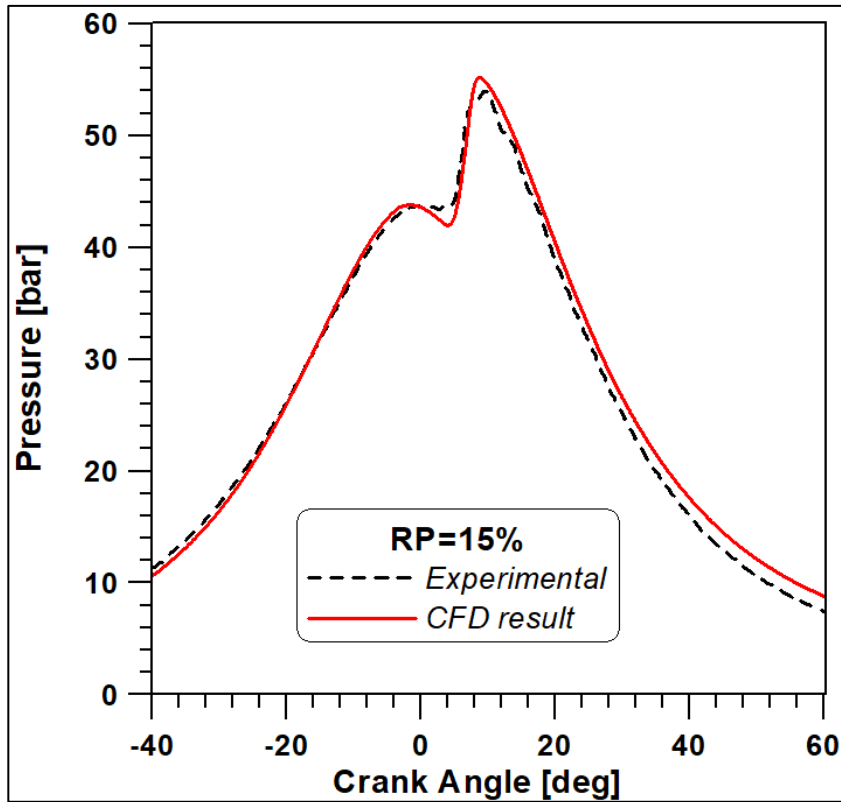


Fig. 5.30: In cylinder pressure for case RP=15%.

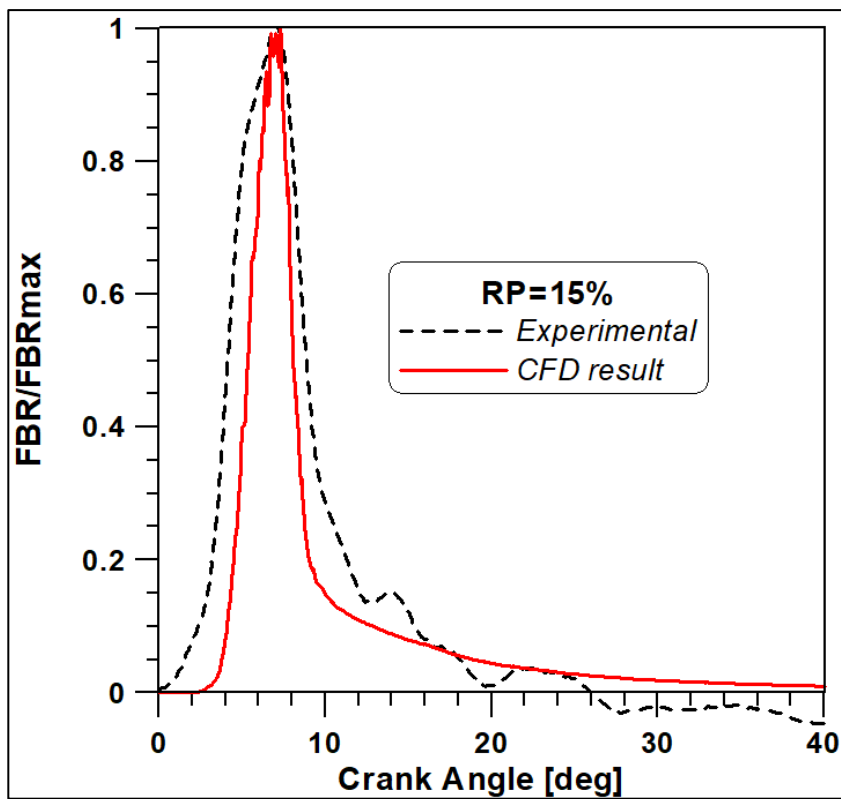


Fig. 5.31: Total fuel burning rates for case RP=15%.

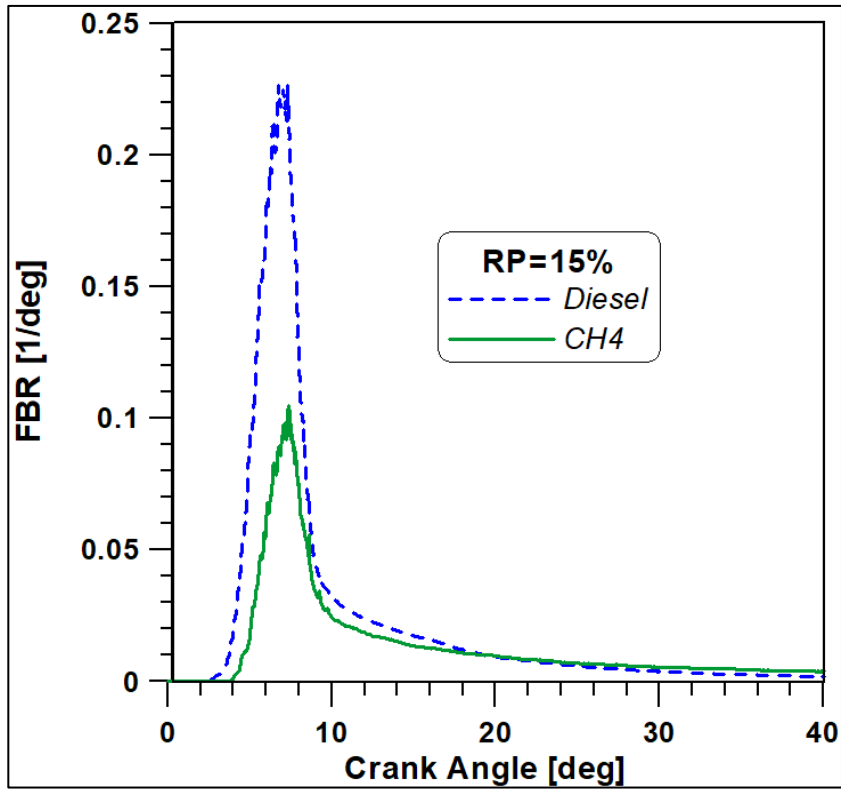


Fig. 5.32: Fuel burning rates for the two fuels.

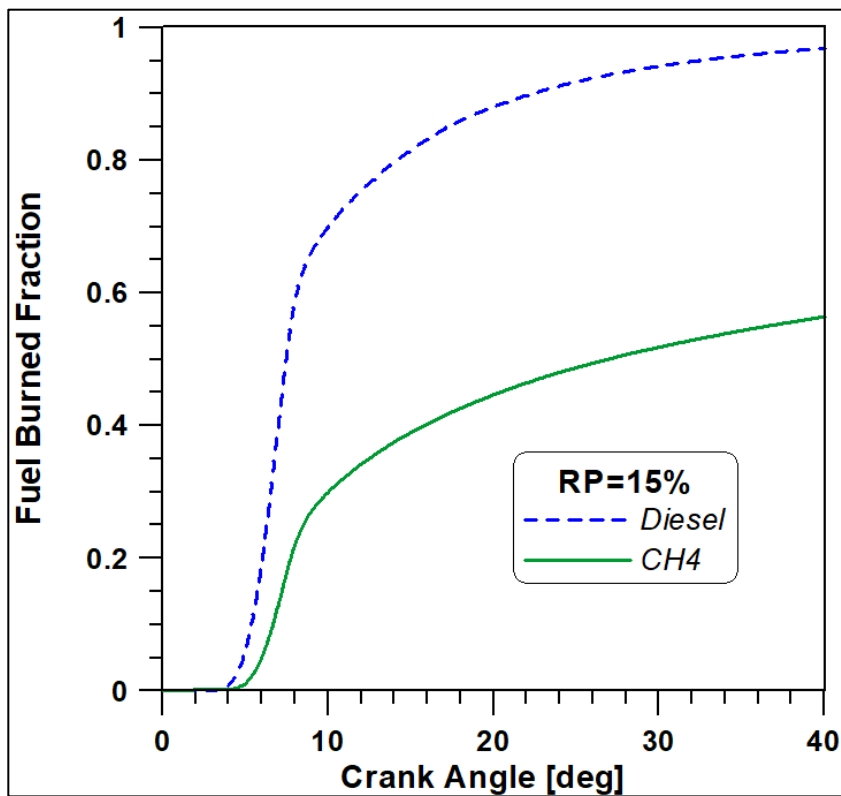


Fig. 5.33: Fuel burnt fraction for the two fuels.

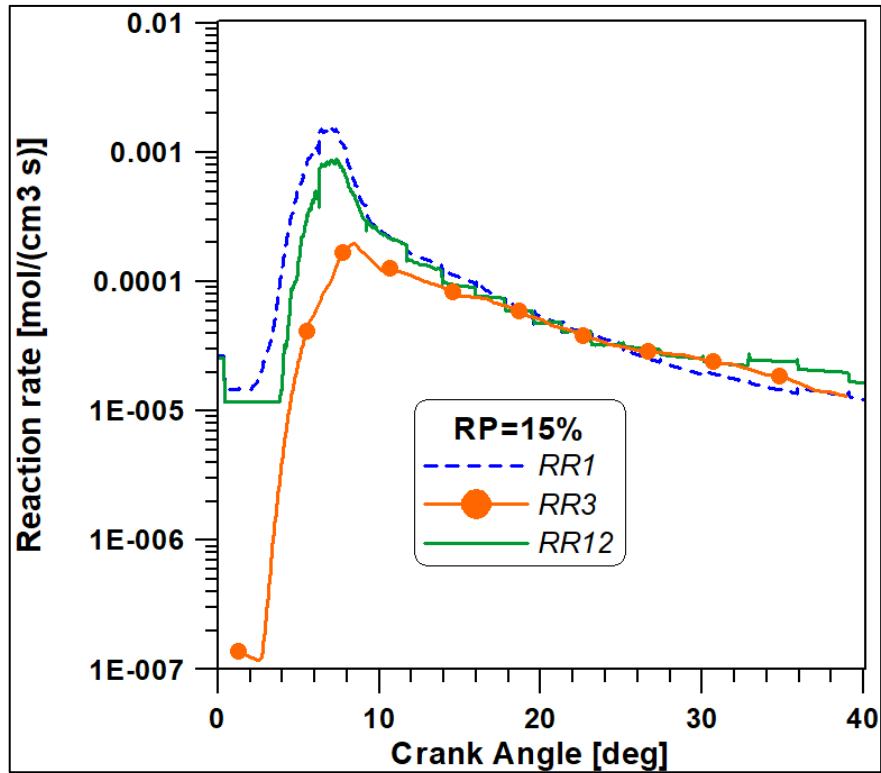


Fig. 5.34: Reaction rates of RR1 (C₁₂H₂₆ oxidation), RR3 (CH₄ conversion in CH₃) and RR12 (CH₄ conversion in CO).

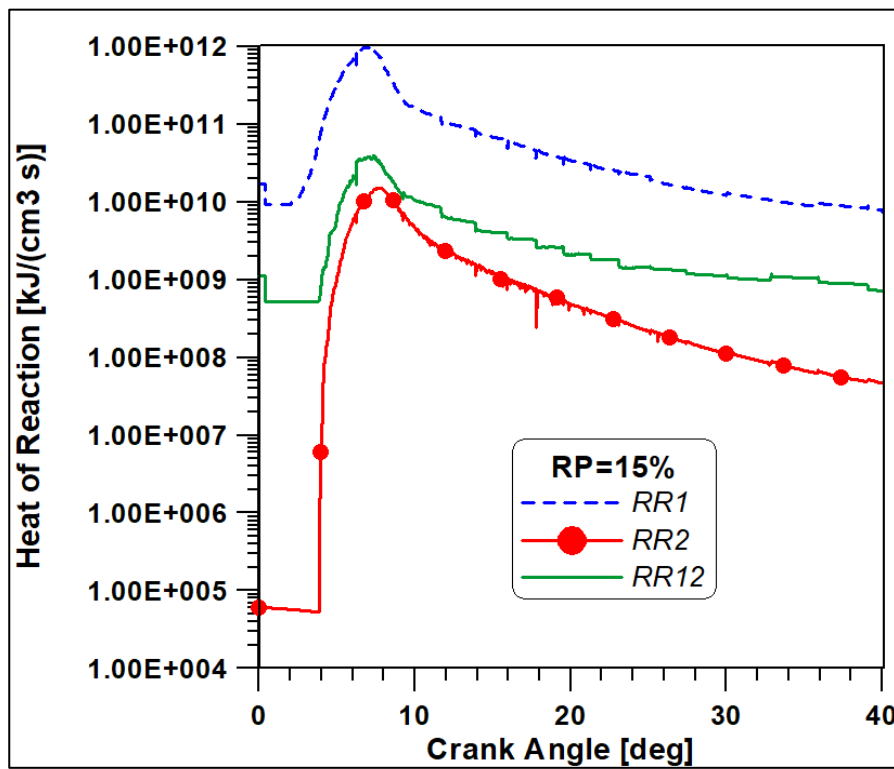


Fig. 5.35: Heat of reaction of RR1, RR2 (CO oxidation in CO₂ and dissociation) and RR12.

5.5.2 Case RP = 22%

The in-cylinder pressure obtained from numerical simulations in good agreement with the experimental one (Figure 5.36). In particular, a perfect accordance is noted for the pressure increasing timing and the growth rate, but the peak position is slightly anticipated, and this induces a lower pressure during the expansion phase.

The comparison between the numerical and experimental volume averaged temperatures (Figure 5.37) is necessary to assess the reliability of the CFD simulations. Indeed, the mesh used slight differs from the geometry of the real engine tested on the bench. However, since the temperature trends present a good agreement, it is possible to affirm that the energy levels obtained are the same.

Temperature appears to be widely stratified during all the combustion process.

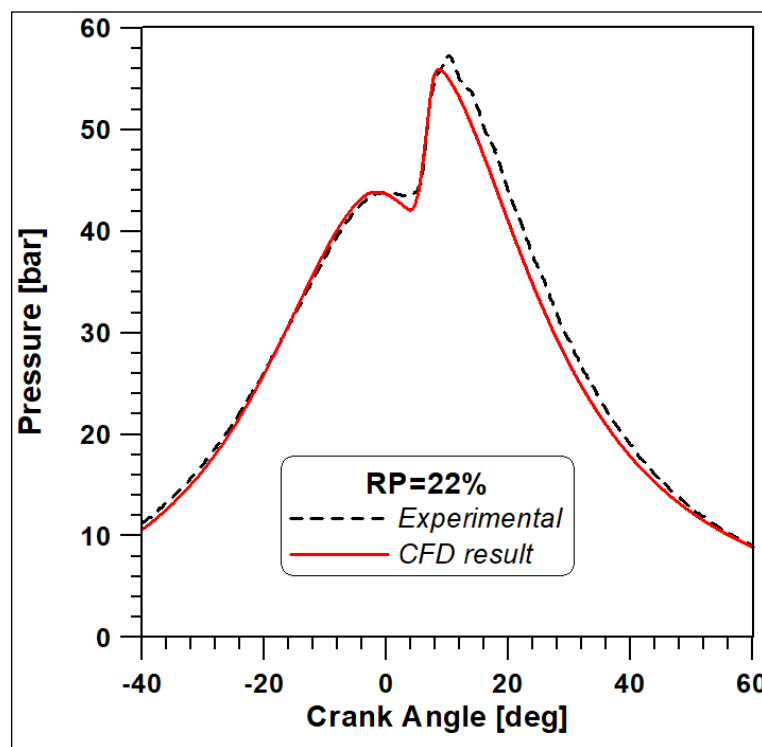


Fig. 5.36: In cylinder pressure for case RP =22%.

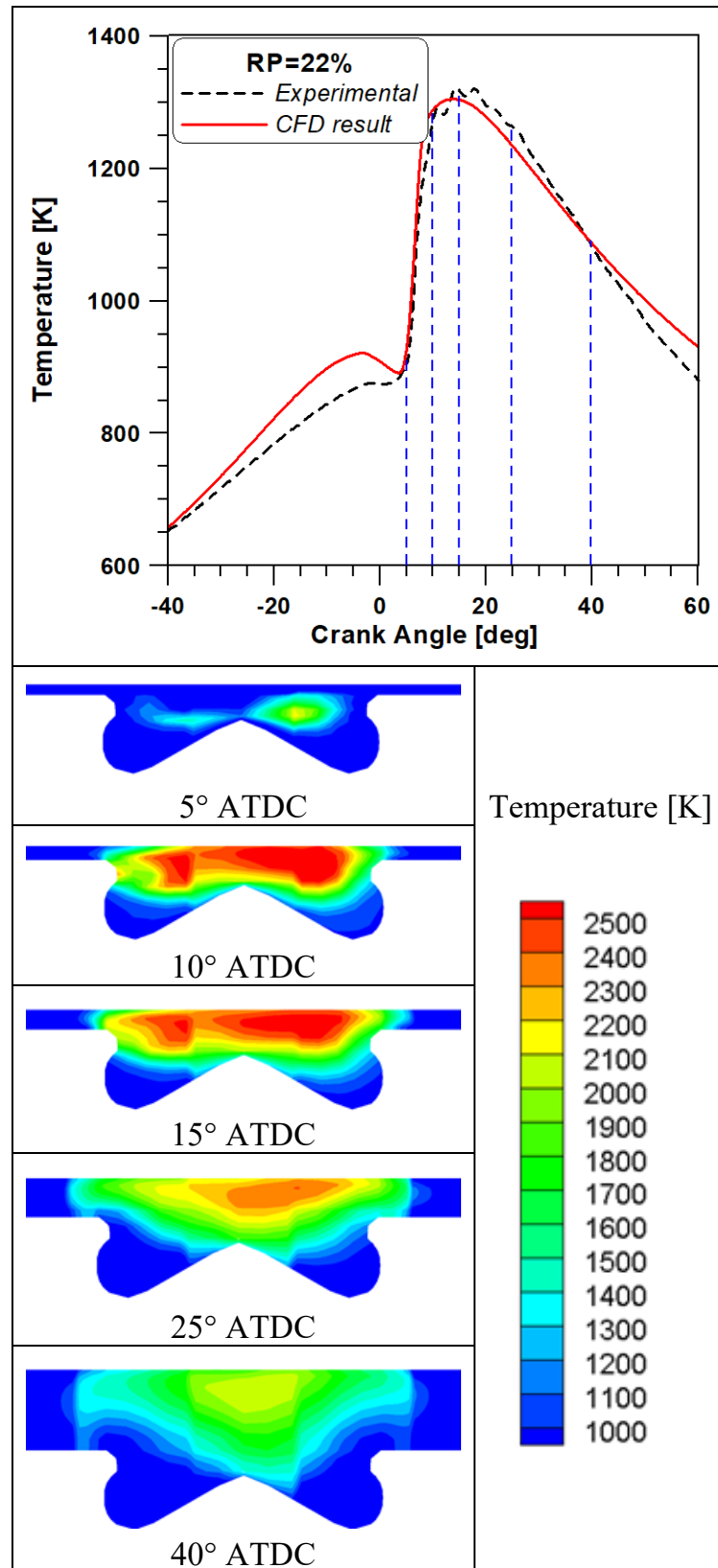


Fig. 5.37: Average in-cylinder temperature and temperature distributions for case RP =22%.

Moreover, Figure 5.37 match the in-cylinder mean temperature with the distribution of the same variable in an axial section at different crank angles. At 5° ATDC temperature begins to increase since the first flame cores are ignited. At 10° and 15° ATDC the peak of temperature is reached and wide zones at high temperature are clearly detected. It is important to highlight that in these zones the greater nitric oxides production is expected.

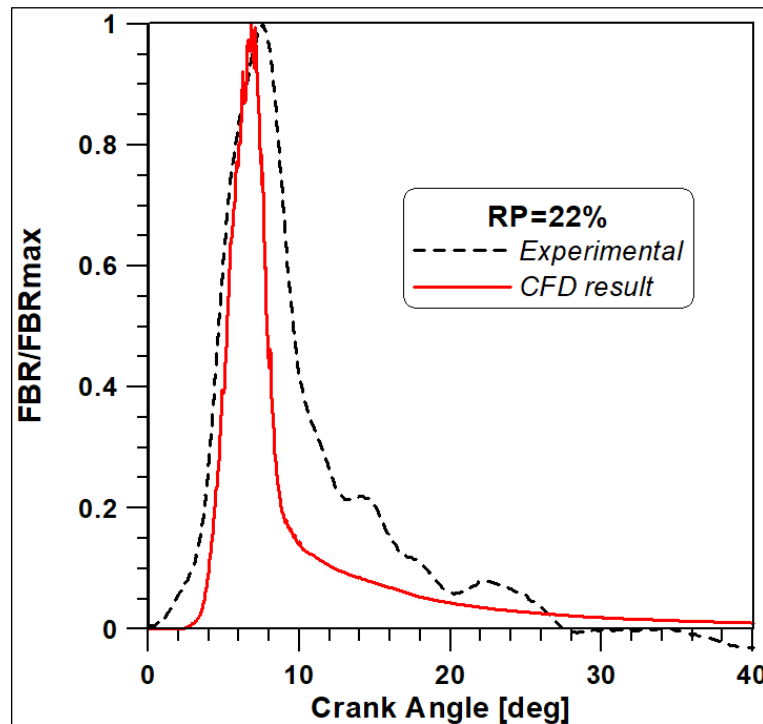


Fig. 5.38: Comparison of experimental and numerical total fuel burning rates.

Figure 5.38 shows differences with respect to the combustion development of methane in the RP=15 case: although the start is again delayed, the peak, is slightly anticipated and the duration is shorter.

In Figure 5.39 the FBR of the two different fuels is reported. Of course, a predominant activity is shown by diesel oil since the reduced amount of ethane injected.

Figure 5.40 evidences, once again the incomplete oxidation of methane which represents the major drawback of this technology.

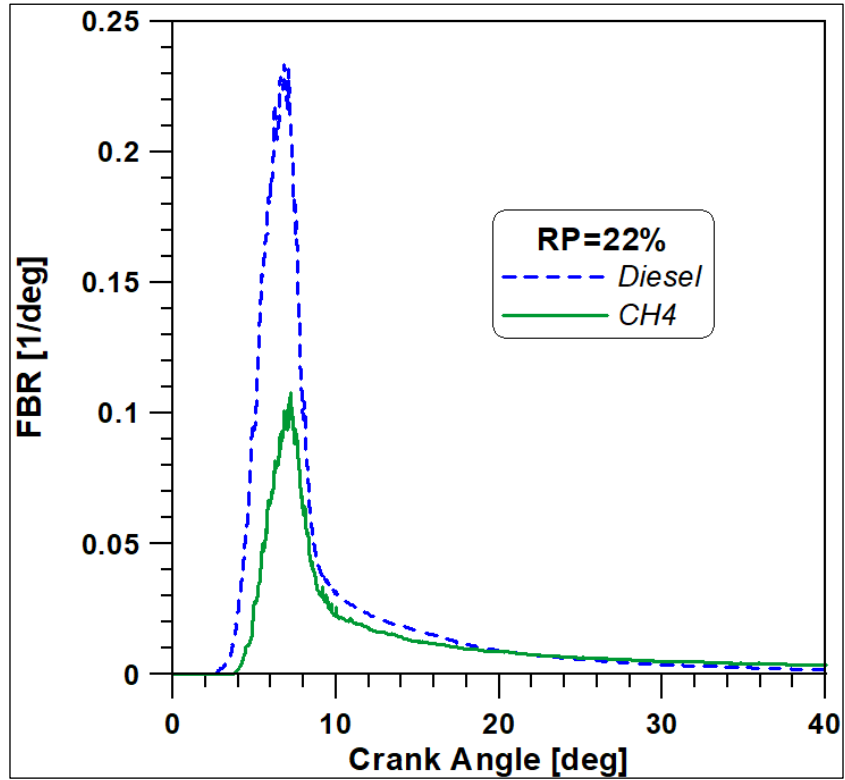


Fig. 5.39: diesel and methane fuel burning rates.

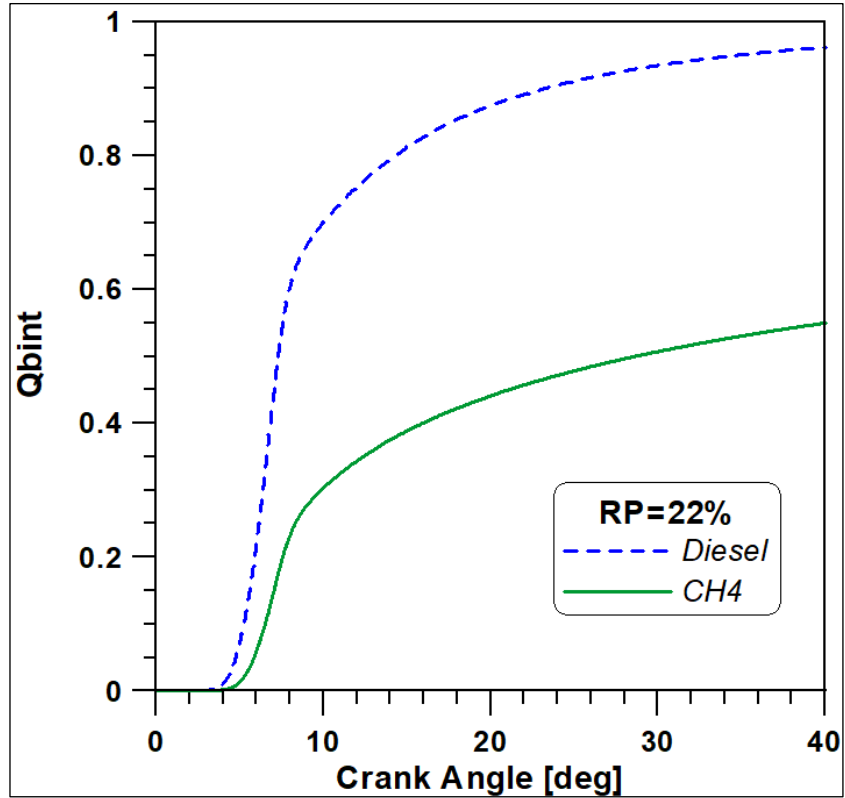


Fig. 5.40: Fuel burning fraction for the two fuels.

Figures 5.41 and 5.42 plot the role of several reactions of the combustion mechanism. Like before, the RR1 describes the diesel vapour combustion, RR12 the complete methane oxidation and RR2 and RR3 are reported as representative of the Li and Williams scheme. The activation of all methane reactions is always delayed with respect to diesel oxidation. Therefore, this mechanism confirms that methane is ignited by diesel oil combustion. Moreover, as an example of the importance of the ignition process, the activation of the RR3 reaction, which occurs at a temperatures below 1300 K and converts methane into an intermediate species, is anticipated with respect to the start of the RR12 reaction, which involves the final methane oxidation. Figure 5.42 points out that the main contribution to overall combustion heat release is provided by the first reaction, i.e., the one involving diesel fuel. Indeed, the thermal power peak of reactions RR3 and RR12 is lower by 1 or 2 orders of magnitude compared with the one from diesel vapour oxidation.

Figure 5.43 displays the evolution of the main and some intermediate species considered in the mechanism. Again, it is demonstrated that the diesel consumption occurs before the decrease in methane contents. Also, the validity of the mechanism is proven by the earlier formation of the intermediate species at lower temperature before the activation of the main methane reaction. The same Figure plots the sequential methane consumption inside the cylinder that reach its maximum rate between 5° and 10° ATDC, as confirmed by the CH₄ trend. After this period, it is noted that methane still present in the squish zone completes the oxidation process while a significant amount of unburned hydrocarbons remains trapped inside the combustion bowl at the later crank angles. It is obvious that the poor methane / air equivalence ratio is not adequate to allow the flame front to reach these zones.

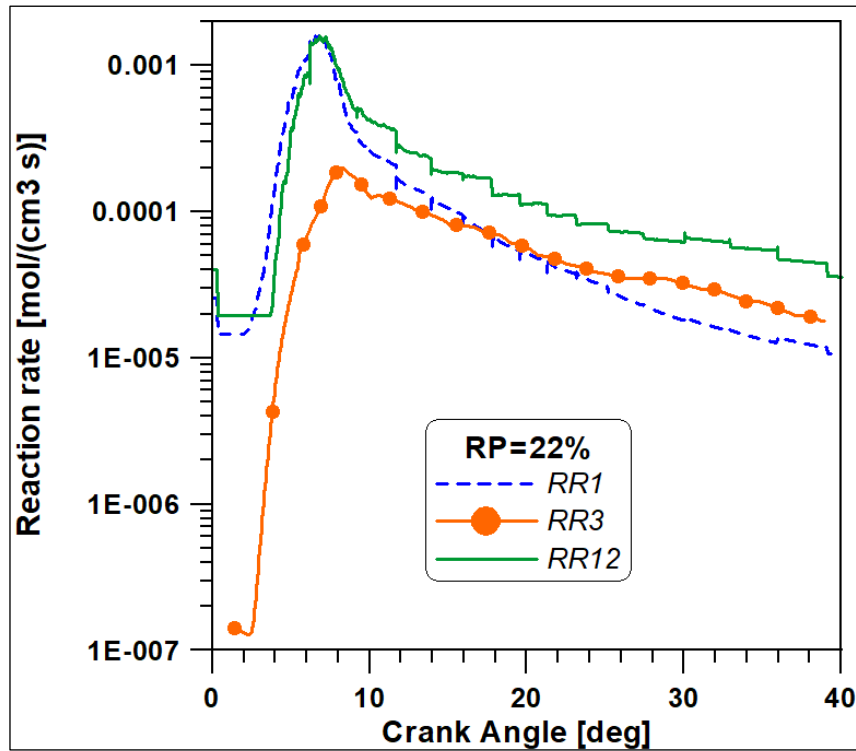


Fig. 5.41: Reaction rates of RR1 (C₁₂H₂₆ oxidation), RR3 (CH₄ conversion in CH₃) and RR12 (CH₄ conversion in CO).

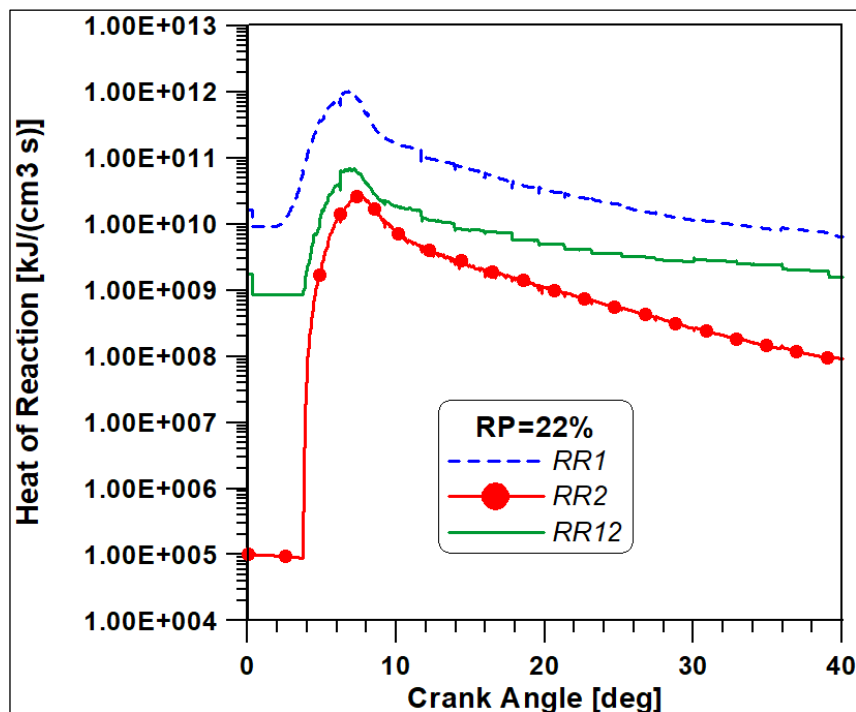


Fig. 5.42: Heat of reaction of RR1, RR2 (CO oxidation in CO₂ and dissociation) and RR12.

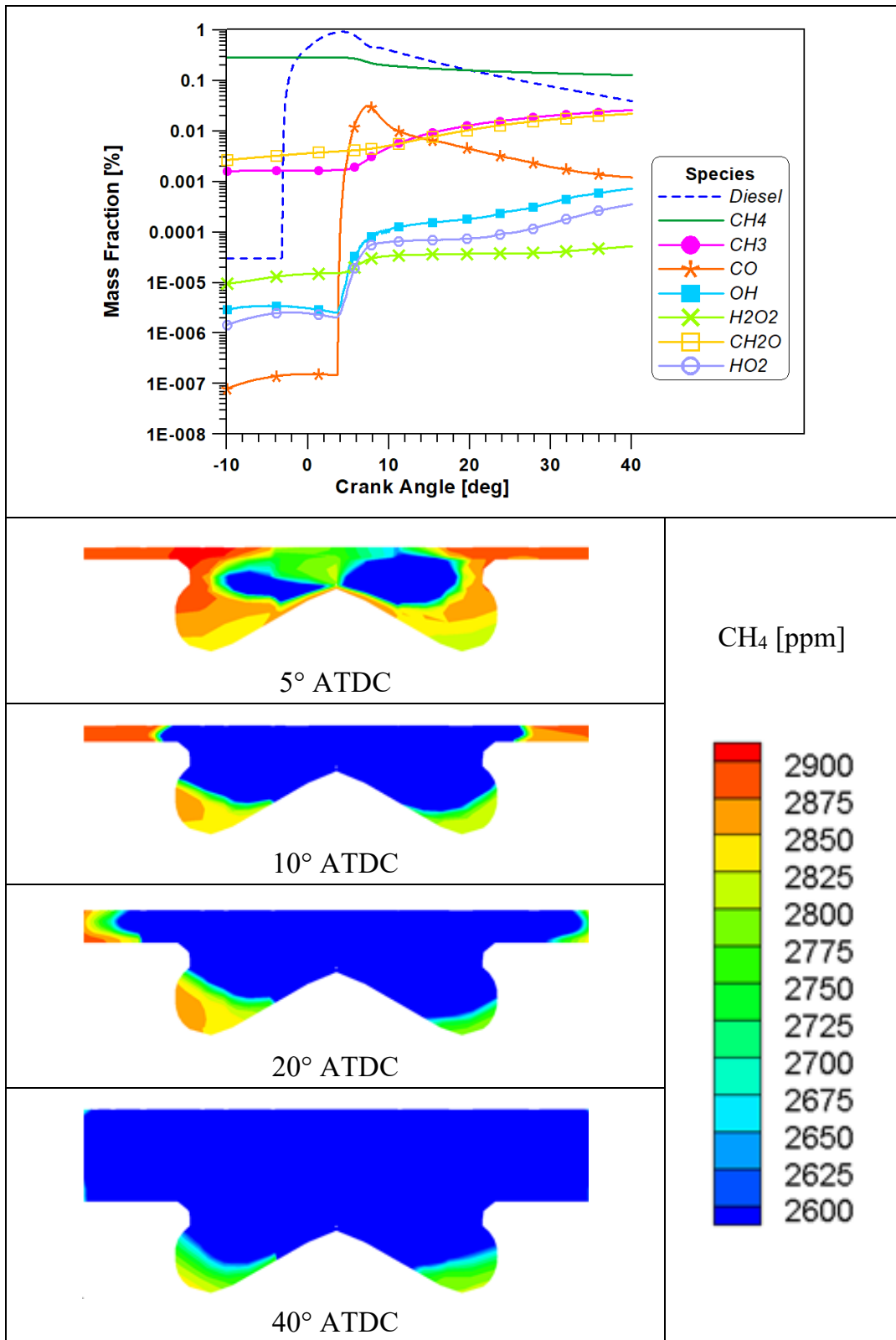


Fig. 5.43: Species evolution and methane distributions at different crank angles.

5.5.3 Comparison RP =10, 15, 22%

A comparison between the three cases with the three values of RP provided by the experimental activity is necessary to understand the effects of methane enhancement in combustion evolution. In each case the contribution of the methane on the overall energy release remains weak, and actually, only slight variations are observed on the mean temperature levels (Figure 5.44). On the other hand, the methane mass fractions displayed in Figure 5.45, highlights a faster consumption rate for the case with the highest premixed ratio (RP=22). Figure 5.46 evidences that after nearly $10^\circ - 12^\circ$ crank angle degrees, the methane burning rate becomes much lower in all cases due to the poor methane/air ratio.

Finally, in Figure 5.47 the NO emissions are shown for the three cases examined and the RP=80% case that is illustrated in the following. As expected, the enhancement of methane supply causes higher local temperature peak due to the increased equivalence ratio. However, as already explained in the experimental result section, the major addition of methane produces an increase in both thermal input and mechanical load. Therefore, higher NO concentrations in the exhausts do not imply the same rise in specific emission (g/kWh).

It should be reminded that all test cases were performed with a fixed injection timing; methane combustion can be affected by the choice of this parameter. A proper optimization of the injection setting could lead to a considerable improvement of combustion behaviour.

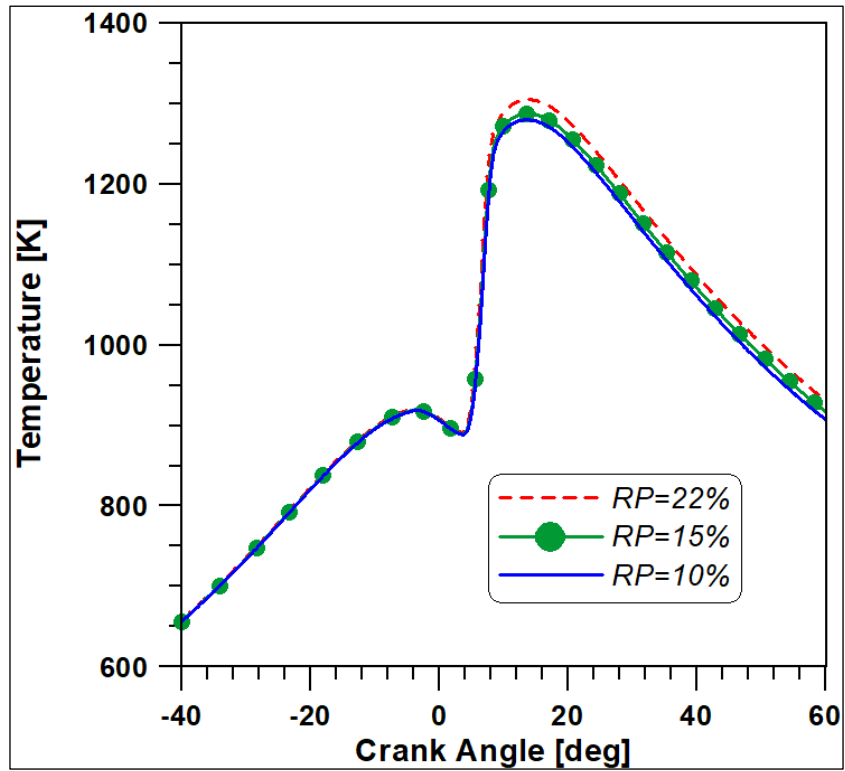


Fig. 5.44: Average in-cylinder temperatures for RP=10, 15 and 22%.

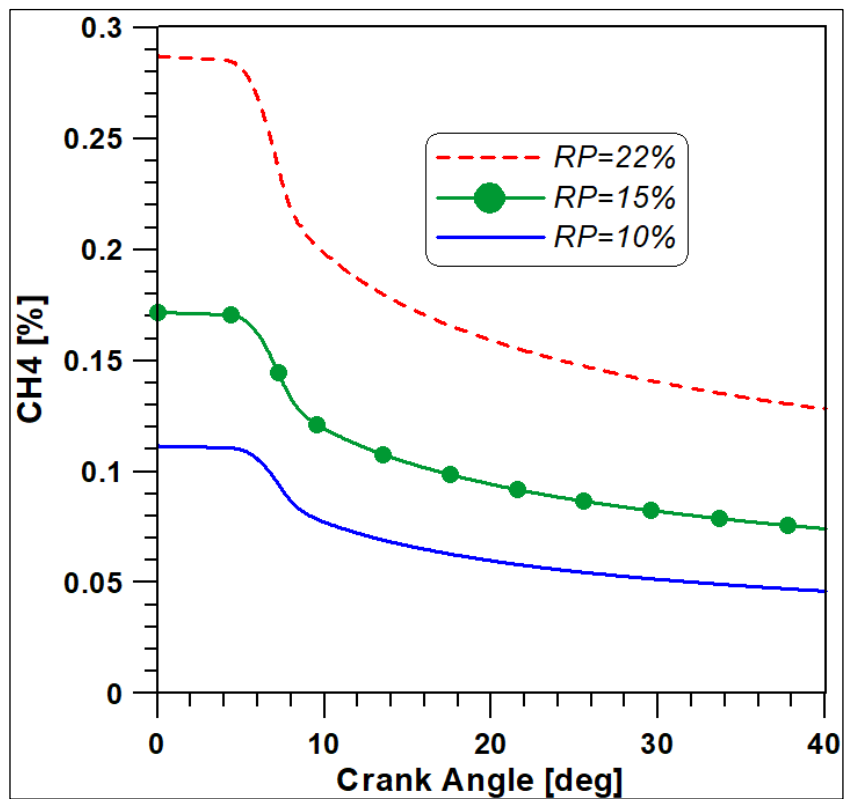


Fig. 5.45: Comparison of methane mass fractions for RP=10, 15 and 22%.

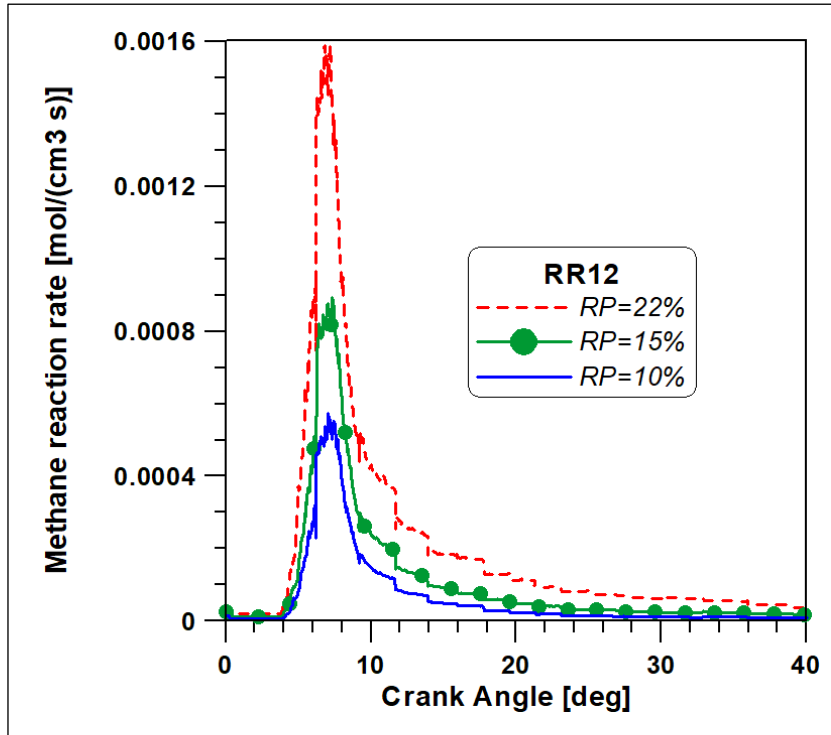


Fig. 5.46: Comparison of methane reaction rates for RP=10, 15 and 22%.

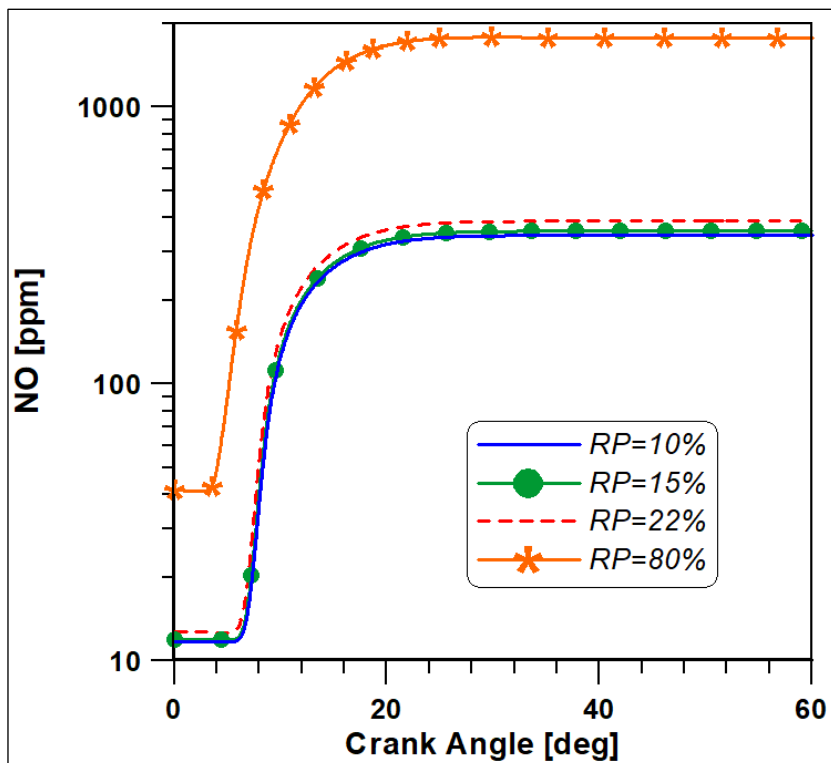


Fig. 5.47 Comparison of NO emissions for RP=10,15 and 22%.

5.5.4 Comparison of Autoignition model vs 2-step model

The comparison between the results obtained with the employment of the Li and Williams model and the two-step mechanism is necessary to assess if an improvement has been achieved for the combustion description. Figure 5.48 does not evidence significant differences in the reproduction of the pressure curve. Recalling Figure 5.38, the FBR peak obtained with the Li and Williams model results anticipated with respect to the experimental one, Figure 5.49 displays an even more anticipated peak for the two-step mechanism and consequently an earlier end of combustion. An important feature highlighted by Figure 5.50 is a smoother methane consumption with the autoignition model that appears to be more realistic, since the low methane-air ratio causes a slow ignition of the premixed charge.

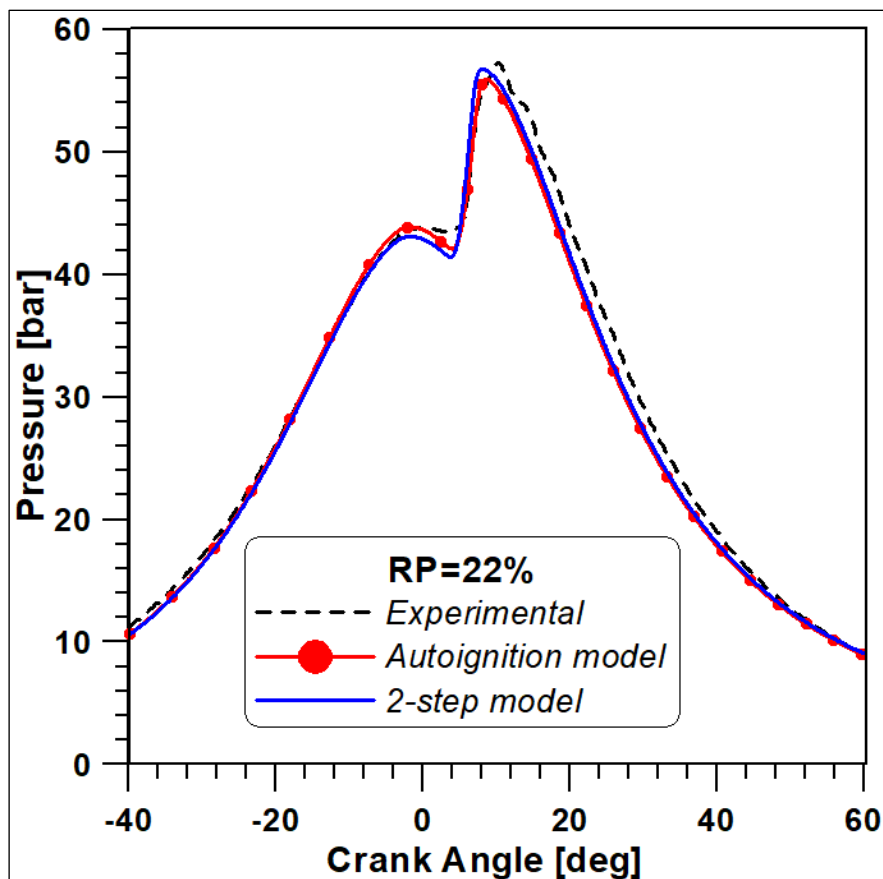


Fig. 5.48: In cylinder pressure for case RP=22%.

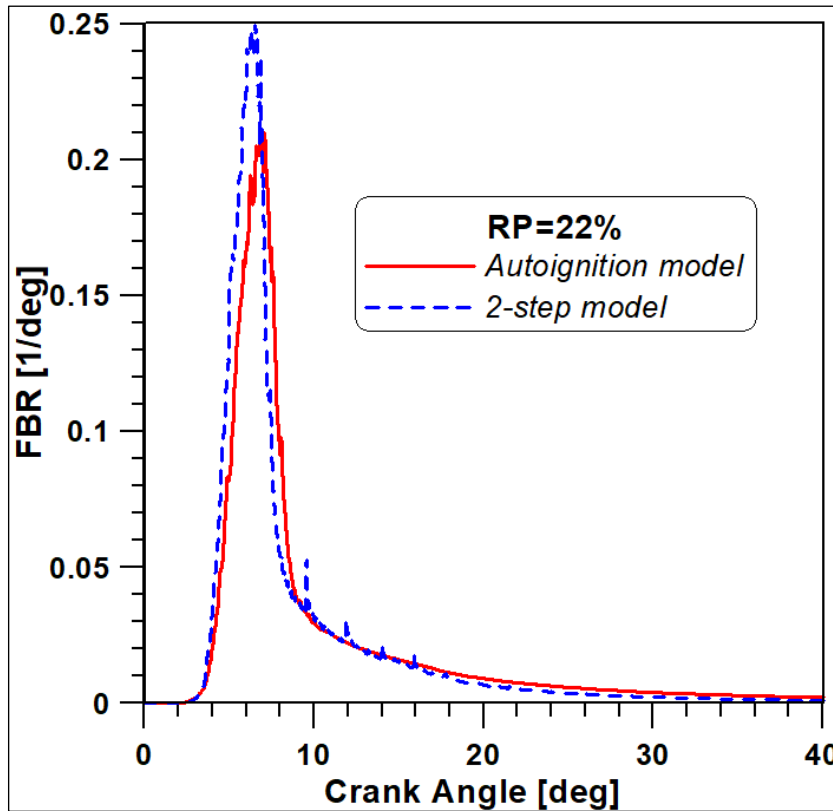


Fig. 5.49: Comparison of total fuel burning rates by different models.

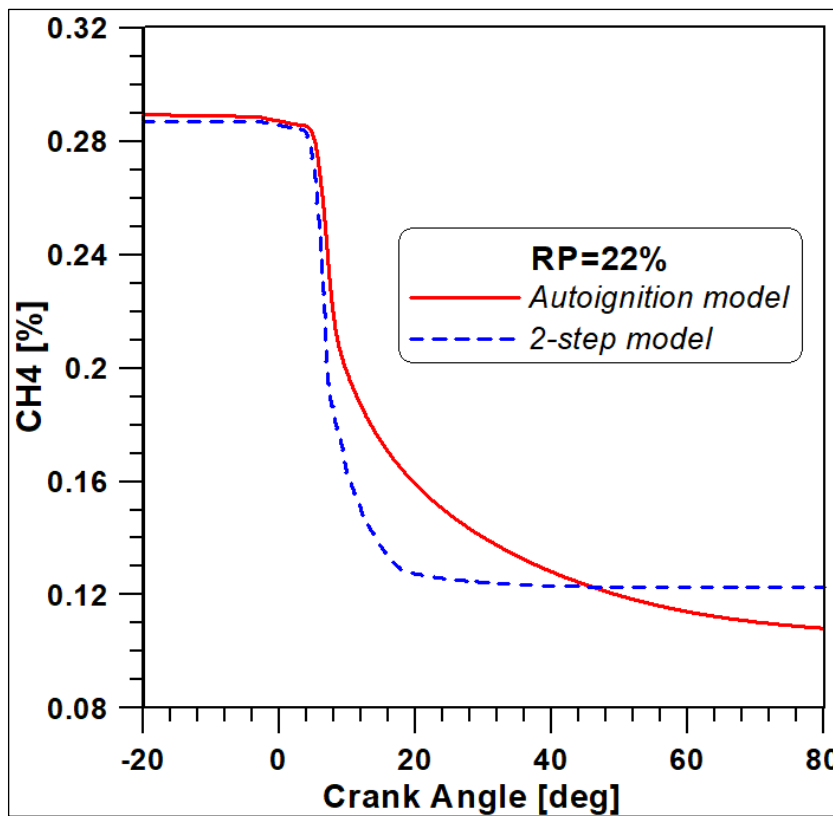


Fig. 5.50: Comparison of total fuel burning rates by different models.

5.5.5 Comparison RP = 80% vs RP = 22%

A great enhancement of methane amount causes an evident increase of pressure and temperature peaks as shown in Figures 5.51 and 5.52. This explains the higher emissions of NO for the RP=80% as already illustrated in Figure 5.47. Differently from the other cases, with an energy input from methane of 80% the mixture falls between the flammability limits of methane and a more efficient combustion is achieved. However, a divergence of pressure and temperature is detected nearly 40° BTDC, this can be due to earlier activation of some reactions in the autoignition mechanism favoured by the higher equivalence ratio. Combustion development is considerably different from the cases previously discussed. Firstly, the over FBR (Figure 5.53) of RP=80% evidences an anticipated start of combustion and longer duration than in the RP=22% case. Figure 5.54 demonstrates that the longer duration is caused by the CH₄ contents. Moreover Figure 5.55 shows that in this case methane burns almost completely at the expense of diesel oil. This can be explained by Figure 5.56 that reports the oxygen consumption. As it is possible to see, oxygen concentration decreases more rapidly in the RP=80% case since the more intense methane oxidation subtracts oxygen to diesel vapour combustion.

Figures 5.57 and 5.58 show that RR12 is predominant with respect to RR1. In particular, even the rate of a reaction in the autoignition mechanism (RR3) results higher than the one of the diesel oxidation.

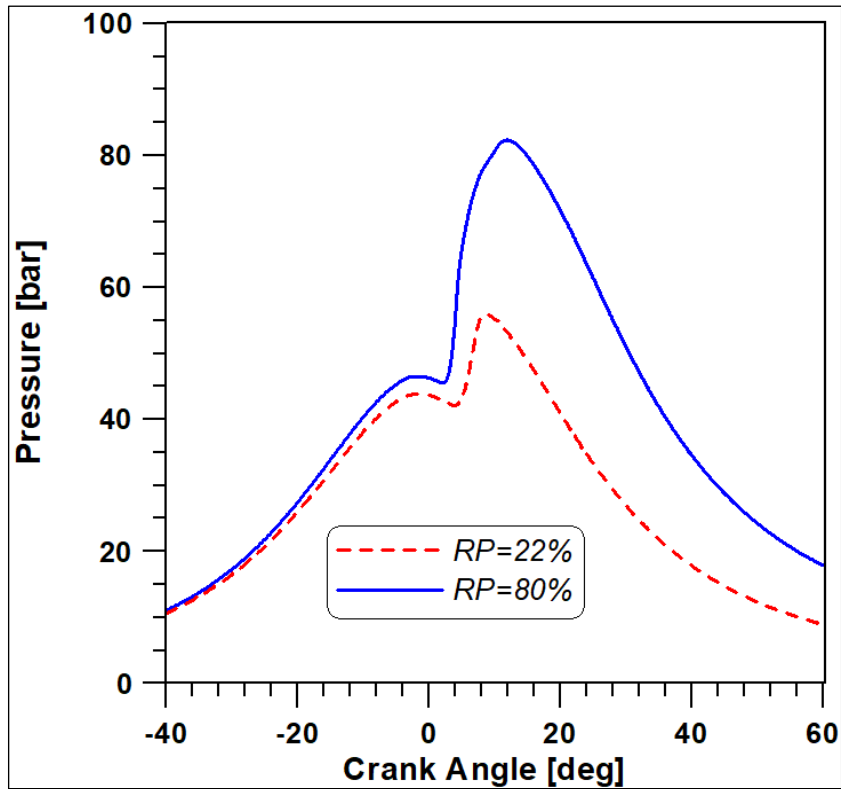


Fig. 5.51: In cylinder pressure for case RP =22 and 80%.

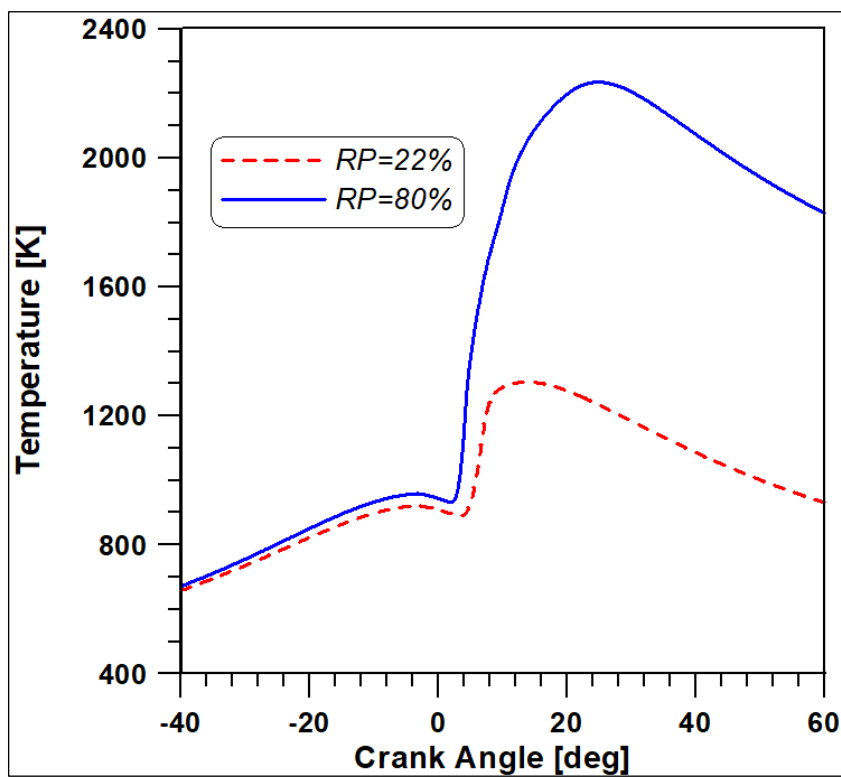


Fig. 5.52: In cylinder temperatures for cases RP=22 and 80%.

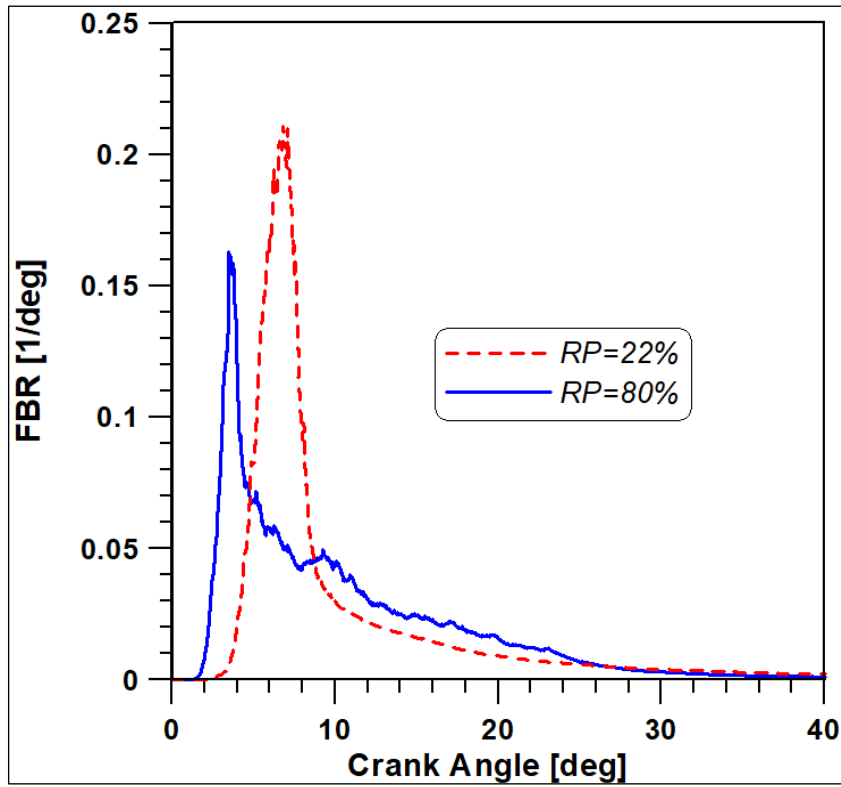


Fig. 5.53: Comparison of total fuel burning rates for cases RP=22 and 80%.

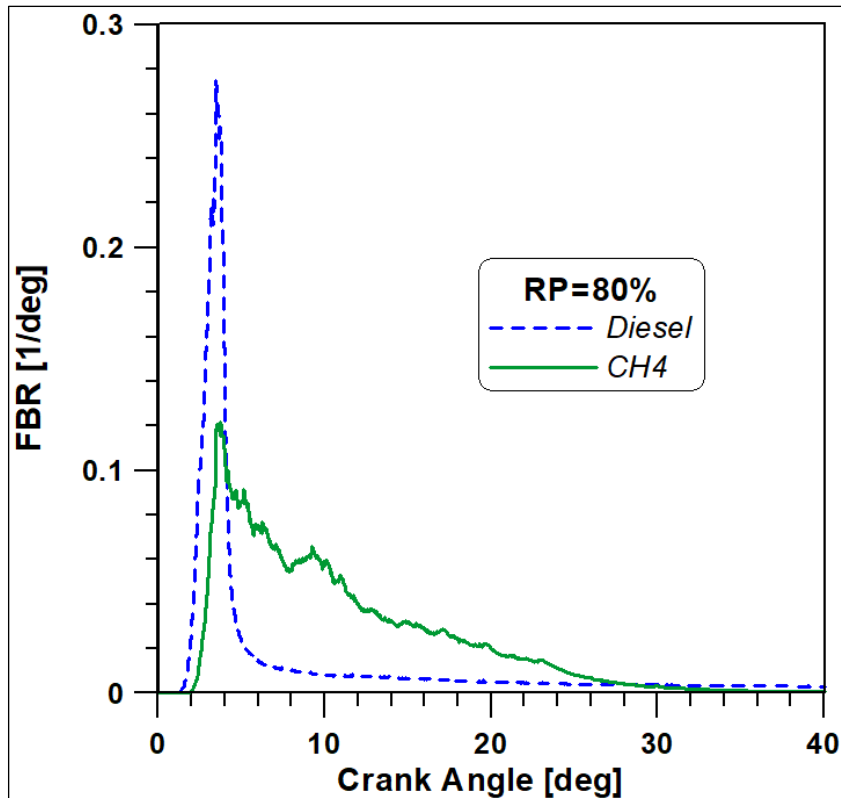


Fig. 5.54: Comparison of diesel and methane fuel burning rates for RP=80%.

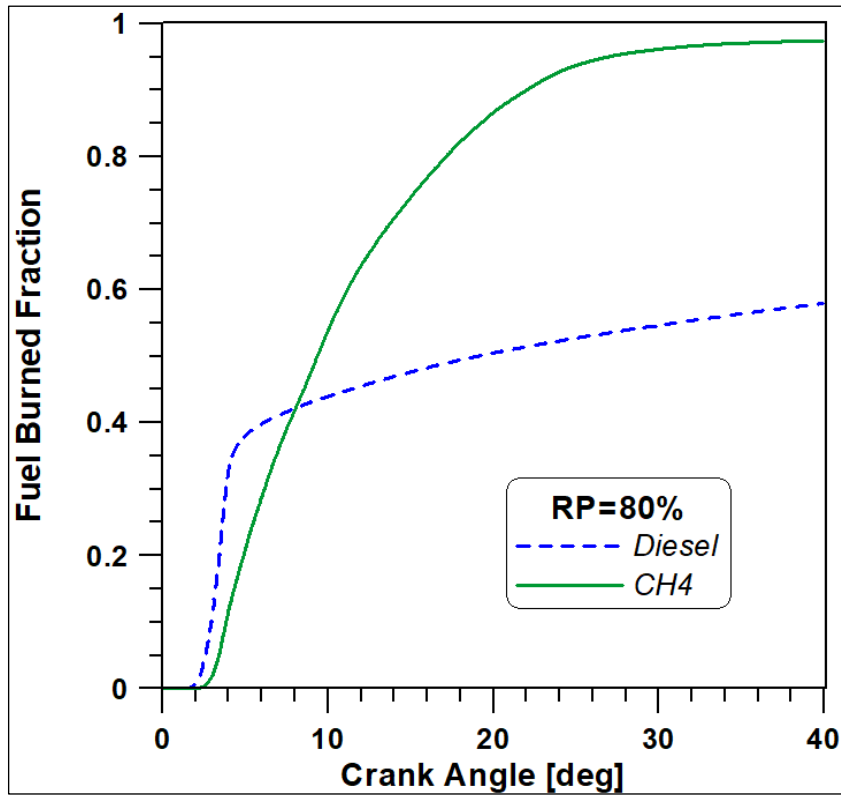


Fig. 5.55: Fuel burning fractions for the two fuels for RP=80%.

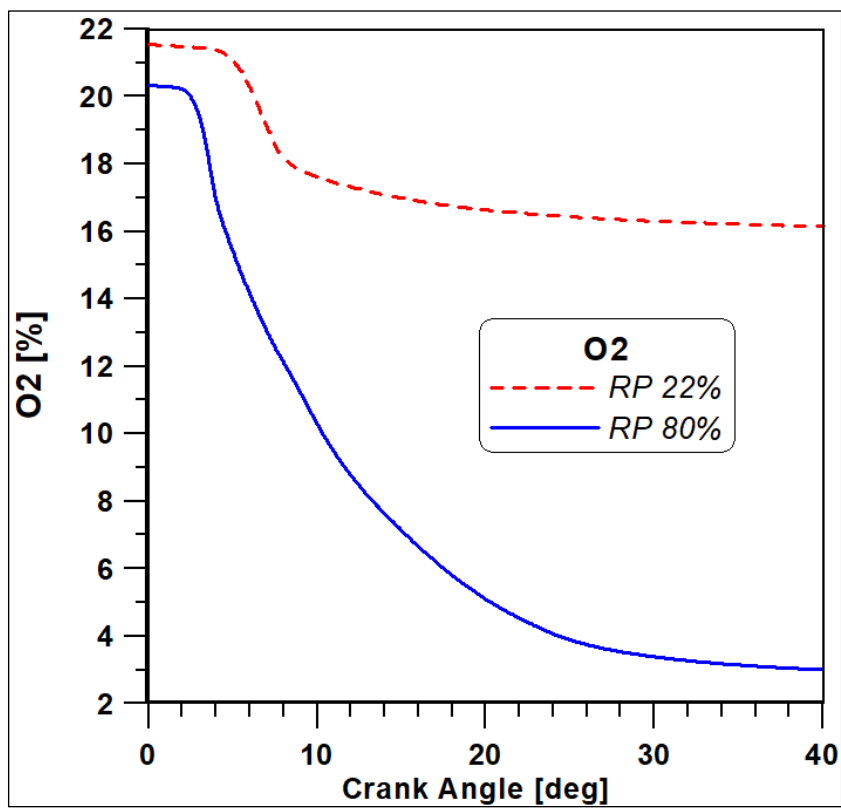


Fig. 5.56: Comparison of oxygen mass fractions for cases RP =22 and 80%.

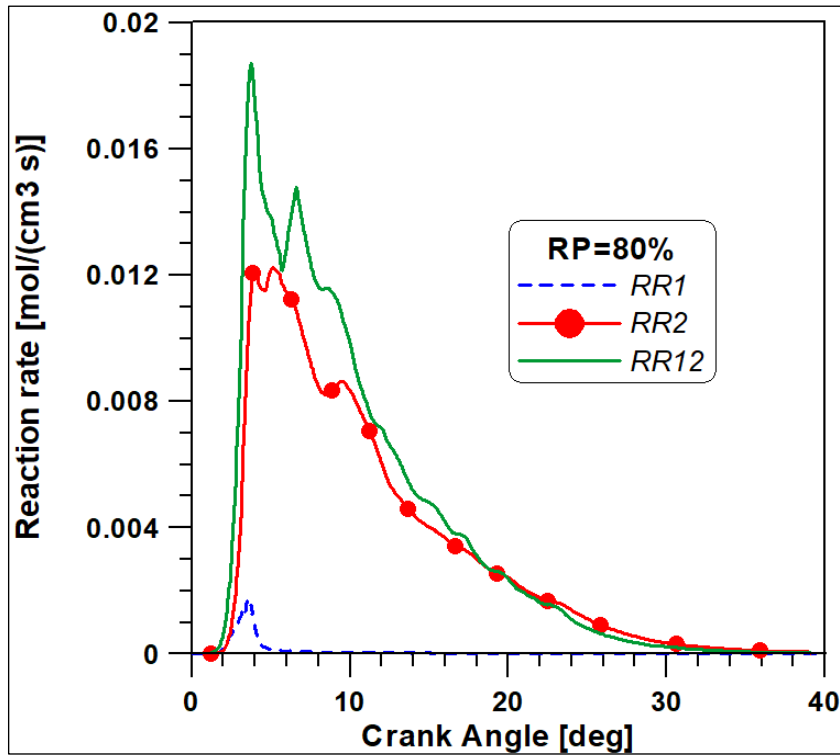


Fig. 5.57: Reaction rates of RR1 (C₁₂H₂₆ oxidation), RR2 (CO oxidation in CO₂ and dissociation) and RR12 (CH₄ conversion in CO) for RP=80%.

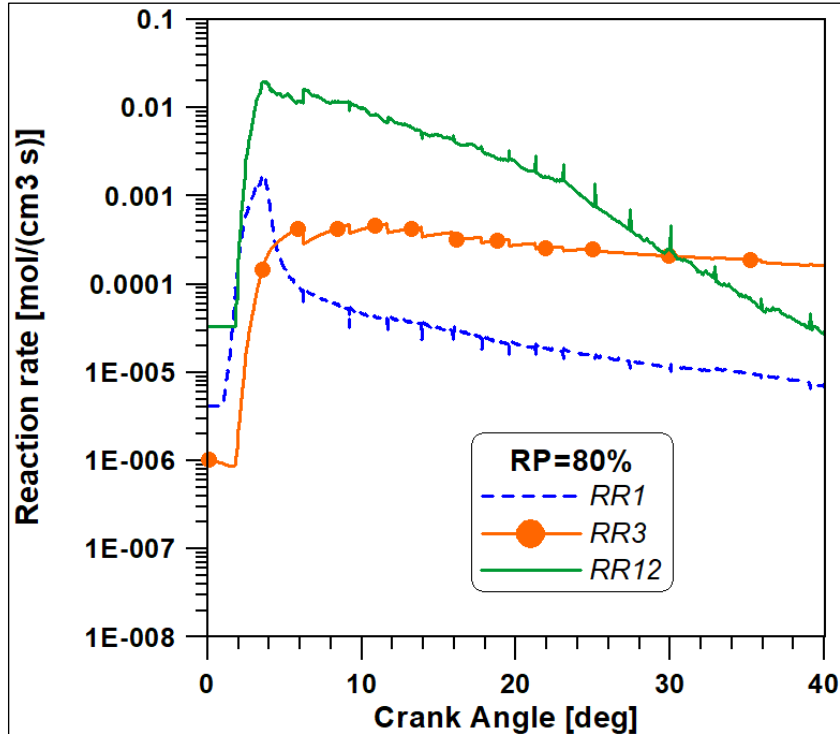


Fig. 5.58: Reaction rates of RR1, RR3 (CH₄ conversion in CH₃) and RR12 for RP=80%.

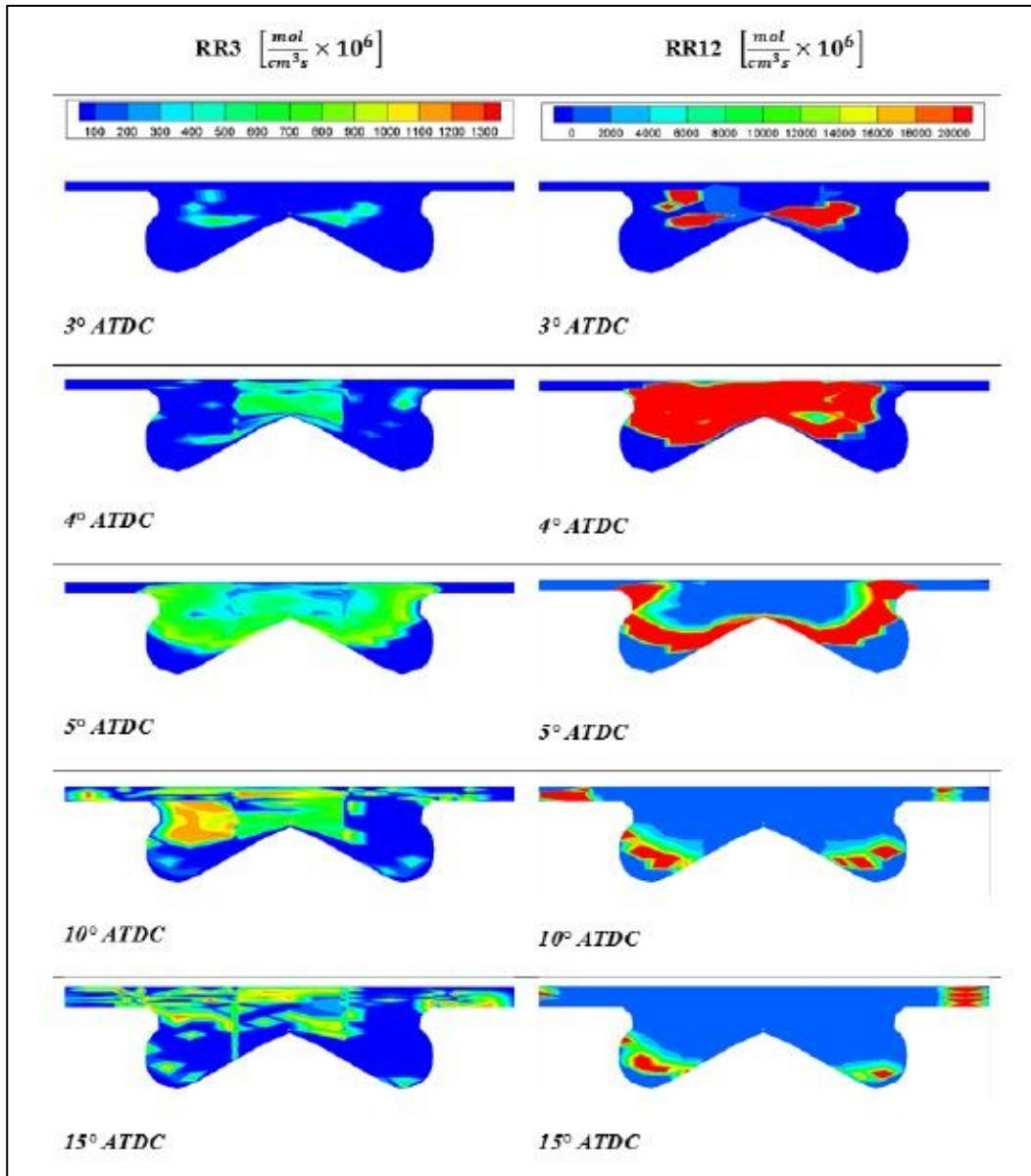


Fig. 5.59: Reaction rate distributions of RR3 and RR12 for RP=80%.

In Figure 5.59 the reaction rates of two reactions involving methane are compared. RR3 and RR12 are activated below and above 1300 K, respectively, the former is taken as representative of the autoignition mechanism and convert CH_4 in CH_3 that is an intermediate species, the latter converts CH_4 in CO . For this reason, the sequential plot of the RR12 reaction rate recalls a flame front propagation through the combustion chamber. As noted at 15° ATDC the end-wall regions of the bowl are already reached by the methane combustion progress in according to Figure 5.55. A real

interaction between the RR3 and RR12 reactions can be only detected in the earliest ignition phases (i.e., within the interval $3^{\circ}\text{BTDC} - 3^{\circ}\text{ATDC}$). Starting from 5° crank angles ATDC, the RR3 reaction presents a more evident scattering with respect to the RR12 progress. Actually, the flame front related to the main methane oxidation seems to proceed in an ordinate way, while the dispersion of the RR3 reaction is probably related to the existence of local zones with lower temperature levels.

Chapter 6

HEAVY DUTY ENGINE

Differently from the previous two engines, in this chapter a 2.0 litre single cylinder Heavy Duty Diesel Engine is examined. It is important to highlight that the dual fuel strategy is more suitable to readapt a heavy-duty engine than a light duty one. More accurate kinetic schemes are introduced for a more reliable development of the numerical test cases. The results illustrated in the following are published in paper [101].

6.1 Experimental Setup

Experimental activity was carried out at Brunel University of London and in Figures 6.1 and 6.2 an image of the test bench situated in the laboratory and the relative scheme are reported.

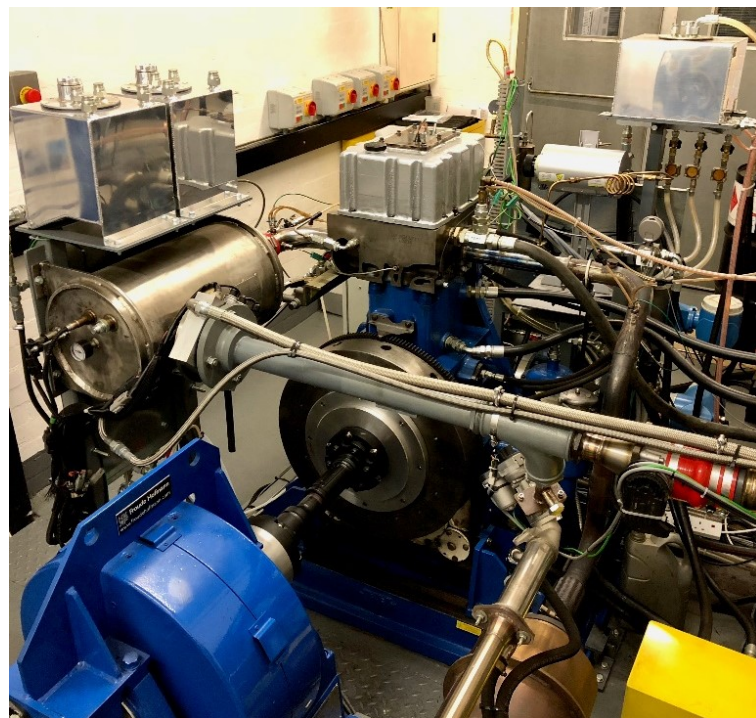


Fig. 6.1: Experimental test bench.

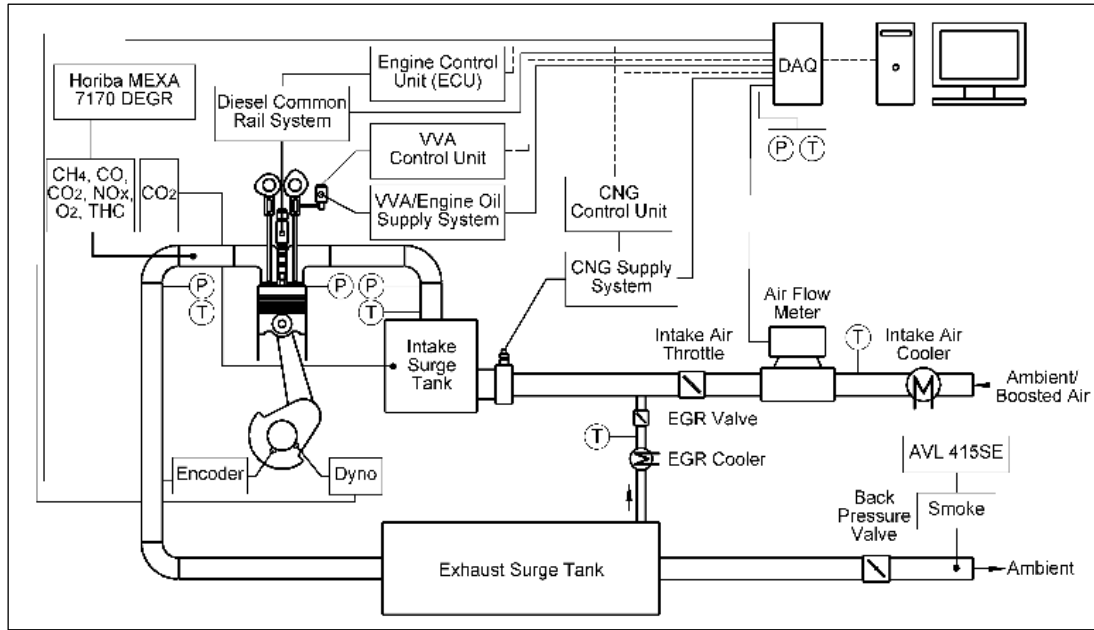


Fig. 6.2: Experimental scheme.

Technical specifications of the single cylinder are listed in Table 6.1.

Tab. 6.1: Single cylinder HD engine specifications.

Displaced volume	2026 cm ³
Stroke	155 mm
Bore	129 mm
Connecting Rod	256 mm
Geometric Compression ratio	16.8
Number of valves	4
Peak in cylinder pressure limit	180 bar
Diesel Injection System	Bosch common rail, 250 – 2200 bar, 8 holes with a diameter of 0.176 mm, included spray angle of 150°
Natural Gas Injection System	G-Volution controller and two Clean Air Power injectors SP-010, injection pressure of 8 bar

Swirl-oriented intake ducts and 4 valves are placed on each cylinder's head like illustrated in Figure 6.3.

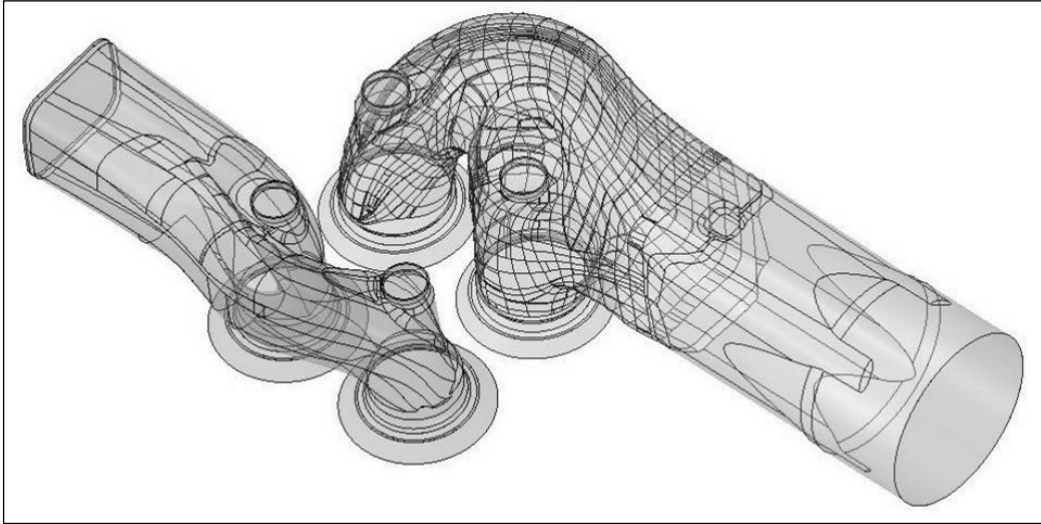


Fig. 6.3: CAD model of the intake (right) and exhaust (left) ports [102].

A high-pressure common rail diesel injection system was controlled via a dedicated engine control unit with the ability to support up to three injections per cycle. By measuring the total fuel supplied to and from the diesel high pressure pump and injector, two Endress+Hauser Promass 83A Coriolis flow meters were used. Natural gas was injected through two port fuel injectors installed upstream of the intake surge tank to facilitate the mixing of the fuel with air. The NG mass flow rate was measured using an Endress+Hauser Proline Promass 80A Coriolis flow meter. An injector driver controls the pulse width of the gas injectors and allowed to run the engine under varying ratios of diesel and NG.

The properties of the diesel oil and natural gas used for the experiments are reported in Table 6.2.

As it is possible to see, the gas selected has a simplified composition containing for the major part methane and only a small quantity of ethane.

Tab. 6.2: Fuels properties.

Property	Diesel	Natural gas
Lower Heating Value [MJ/kg]	42.9	49.8
Stoichiometric air fuel ratio	14.5	17.1
Liquid density (at 1.01 bar and 20°C) [kg/dm ³]	0.827	-
Gas density (at 1.01 bar and 15°C) [kg/m ³]	-	0.708
Methane number (PKI, DNV, GL)	-	87.6
Gas composition (mole fraction) [%]	-	95.0 CH ₄ 5.0 C ₂ H ₆

The concentrations of gaseous emissions (CH₄, CO and NO_x) were measured with a Horiba MEXA-7170 DEGR emissions analyser. While the concentrations of black carbon containing soot, reported on a filter smoke number (FSN) basis, was determined with an AVL 415SE smoke meter.

The in-cylinder pressure was measured by a piezoelectric pressure sensor coupled with a charge amplifier. Intake and exhaust manifold pressures were measured by two water-cooled piezoresistive absolute pressure sensors. K-type thermocouples and pressure gauges were placed to measure temperatures and pressure at relevant locations. The acquisition of the signals was obtained via two data acquisition (DAQ) cards and read thanks to a personal computer that allowed the visualization by an in-house DAQ program and combustion analyser.

Pressure is represented by the average of the maximum pressure variations of 200 cycles of cylinder pressure versus crank angle. Signal noise from the average in-cylinder pressure and heat release rate curves were post-processed using a third order Savitzky-Golay filter with a window size of five data points.

The tests cases and the relative experimental engine conditions are listed in Table 6.3.

Tab. 6.3. Testing conditions for the different engine operating modes.

Load	Low	Medium	High
Engine load (IMEP) [bar]	6	12	18
Percentage of full engine load [%]	25	50	75
Engine speed [rpm]	1200	1200	1200
Diesel Injected Mass [g/cycle]	0.0156	0.0274	0.0421
Diesel Injection pressure [bar]	1000	1300	1600
Diesel Start of injection [CAD]	-5.951	-1.523	6.477
Duration of Diesel injection [deg]	4.77	5.03	5.02
Natural Gas Energy fraction (NG%)	80±1	80±1	80±1
Natural Gas Equivalence ratio [-]	0.375	0.444	0.521
Intake manifold air temperature [°C]	41	42	44
Intake manifold air pressure [bar]	1.25	1.90	2.60
Exhaust manifold pressure [bar]	1.35	2.0	2.7
Exhaust gas recirculation (EGR)	0%	0%	0%

Three different load levels (25%, 50% and 75% of full engine load) were investigated, for a fixed engine speed of 1,200 rpm and a fixed NG energy fraction (80%), defined as the ratio of the energy content of the NG to the total fuel energy supplied. Differently from the research engine studied in the previous chapter, the load levels considered are near to the typical ones of a real engine. These cases were determined after the optimisation of the diesel start of injection, considering as upper bound for calibration a maximum pressure rise rate of 20 bar/CAD. Therefore, the start of injection is retarded with the load increase. Also, the valve opening period is varied by variable valve actuation system. Although the engine is equipped with an EGR system, like shown in Figure 6.2), the testing activity does not include this

strategy in order to minimise the variable for the computational fluid dynamic simulations. All comparisons were carried out for the cases that attained the highest net indicated efficiency while maintaining an engine-out NO_x level of less than 8.0 ± 0.5 g/kWh. This NO_x emissions limit was set in order to meet the Euro VI emissions regulation limit of 0.4 g/kWh using a selective catalyst reduction system with an estimated NO_x conversion efficiency of approximately 95%.

6.2 Experimental Results

A comparison of the different pressure and temperature curves are plotted respectively in Figure 6.4 and 6.5. Significant differences are evidenced starting from the compression curves that reach different pressure levels at the TDC, because the Variable Valve Actuation (VVA) system and the increased boost pressure allow a distinct amount of mixture to enter the cylinder. Also, it is evident the delayed start of injection and then ignition for the increasing load levels.

Figure 6.6 highlights a double-humped heat release rate for case at 25% and 50% of the full load. Likely, diesel vapour starts to burn before the ignition of bulk fuel mass of natural gas occurs. At the lowest engine load of 25%, the diesel heat release spiked and was followed by a slow burning and low levels of heat release of the premixed NG fuel. This was attributed to the relatively low combustion temperatures, which adversely affected the ignition and fuel oxidation process. For the medium load of 50%, the second hump results relatively larger in magnitude. This is primarily a result of the higher amount of NG injected combined with a lower excess of air and higher in-cylinder gas temperatures.

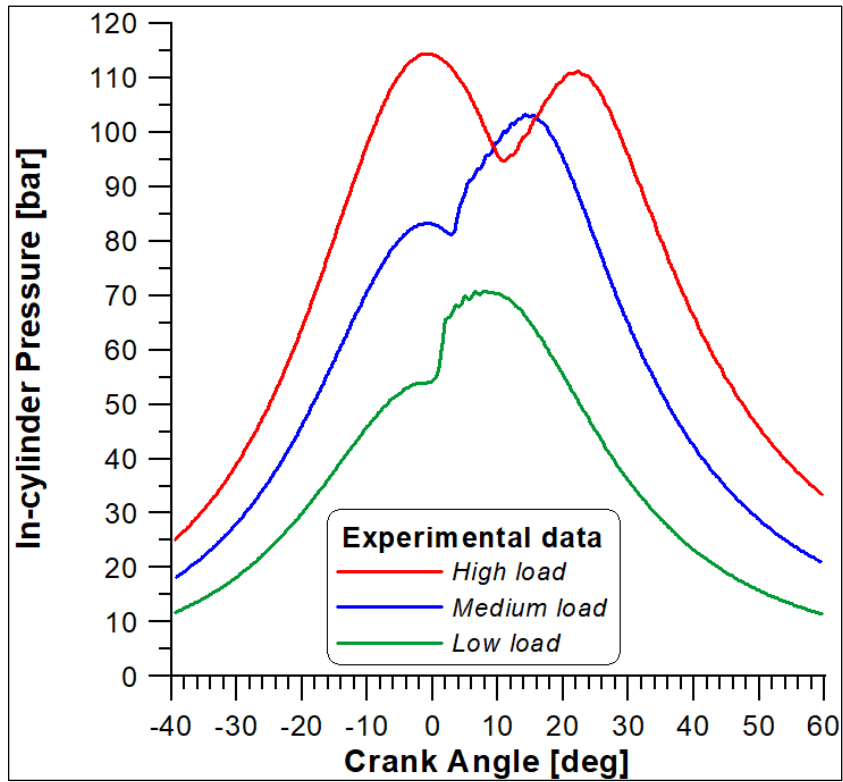


Fig. 6.4: Experimental pressure curves.

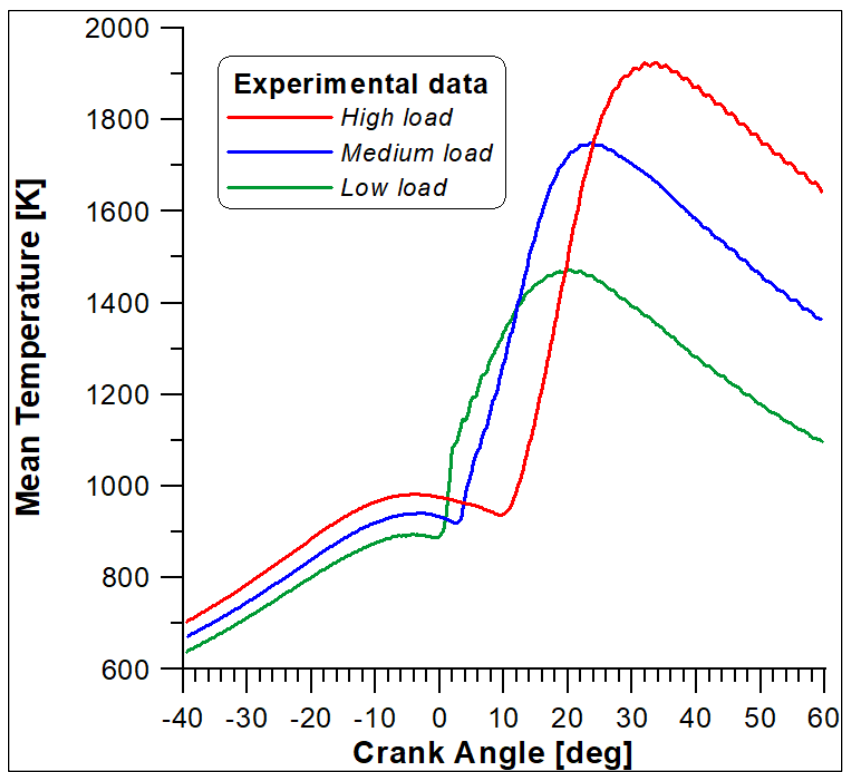


Fig. 6.5: Experimental temperature curves.

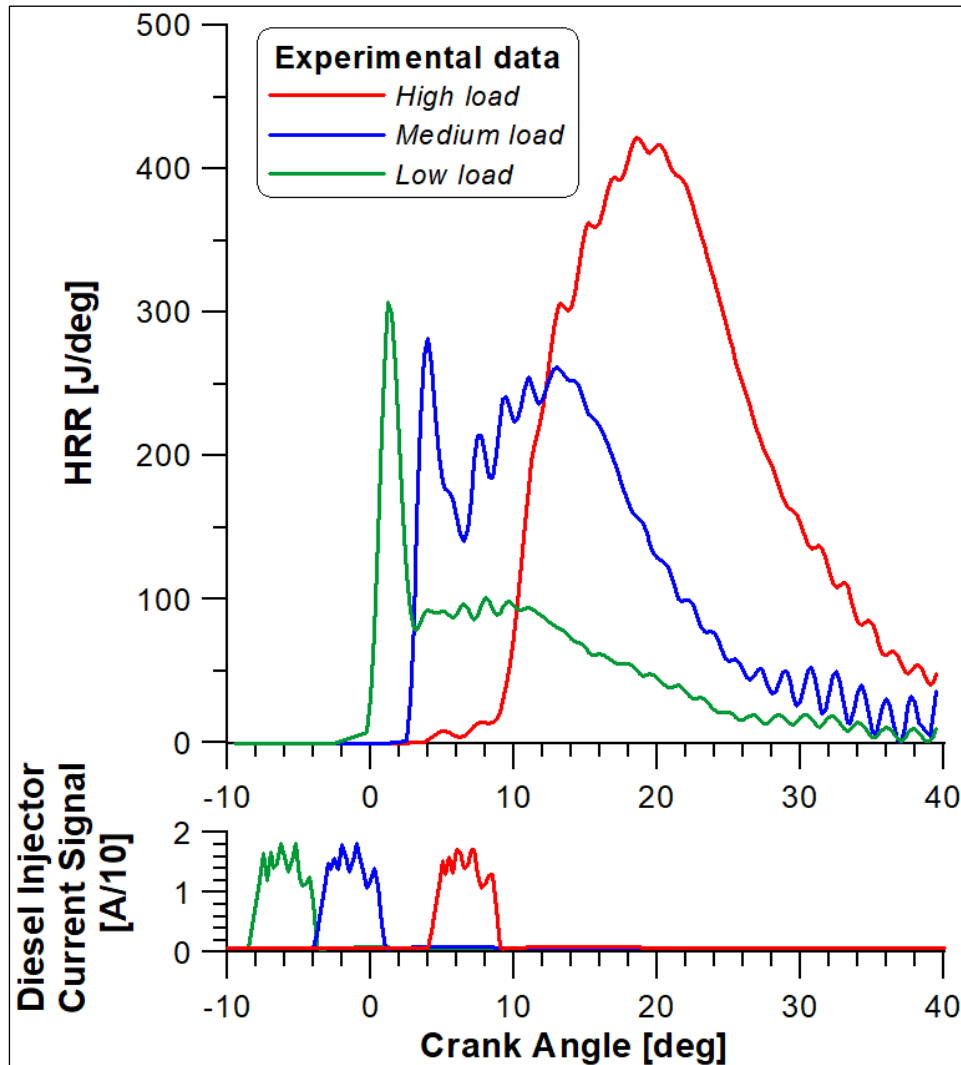


Fig. 6.6: Experimental heat of release rates and injection timings.

For the highest load level (75%) an increase of the HRR is evidenced even before the injection of the diesel oil, this means that the combustion of bulk natural gas has already started during the autoignition of the diesel vapour. This can be explained by the higher in-cylinder gas temperatures (Figure 6.5) that promote a faster compression ignition of the premixed NG fuel, close to the diesel SOI. However, a steep HRR increase takes place only after the ignition delay of the diesel fuel.

Finally, the measured emissions during the experimental are listed in Table 6.4.

Tab. 6.4: Experimental Emissions

[ppm]	Low Load	Medium Load	High Load
CH ₄	7483	3009	1011
UHC	7448	3035	1062
CO	2159	1258	628

6.3 CFD Methodology

In the previous chapter a more detailed scheme for the autoignition of methane, assumed as the only component of natural gas, was implemented, while the diesel oxidation was represented by a one-step reaction mechanism. Now, a new kinetic mechanism is introduced for the n-dodecane, still used as diesel oil surrogate, consisting of 100 species and 432 reactions introduced by Ra and Reitz in [103], and compared with the previous one. Although a simpler mechanism is preferable for the computational time reduction, the kinetic mechanism complication is also dictated by the necessity of a further knowledge of the various phenomena which characterise the combustion process. Based on the experimental activity, firstly a calibration, and secondly a validation of the kinetic mechanism has been made for cases at 50% (medium) and 75% (high) of the load performed with the 3D code ANSYS-FORTE.

Starting from a drawing of the stepped-lip piston bowl, displayed in Figure 6.7 [102], the profile of the combustion chamber was designed (Figure 6.8). The mesh was created with the K3PREPW tool, included in the KIVA-3V workbench, which is able to generate mesh grids that can be read by the ANSYS-FORTE solver. The K3PREPW is a software specialised in the creation of grids for internal combustion engine. However, only the

combustion chamber and the cylinder can be reproduced, allowing only the simulation of closed cycles from the intake valve closing to the exhaust valve opening. The not perfect assessment of the mass exchange inside the cylinder due to the absence of the valves and their opening period, is compensated by a significant reduction of computational efforts. Moreover, due to the circumferential periodicity the computational domain was limited to only a 45° sector and a further calculation time reduction is achieved (Figure 6.9). The final mesh consists of about 38,000 nodes.

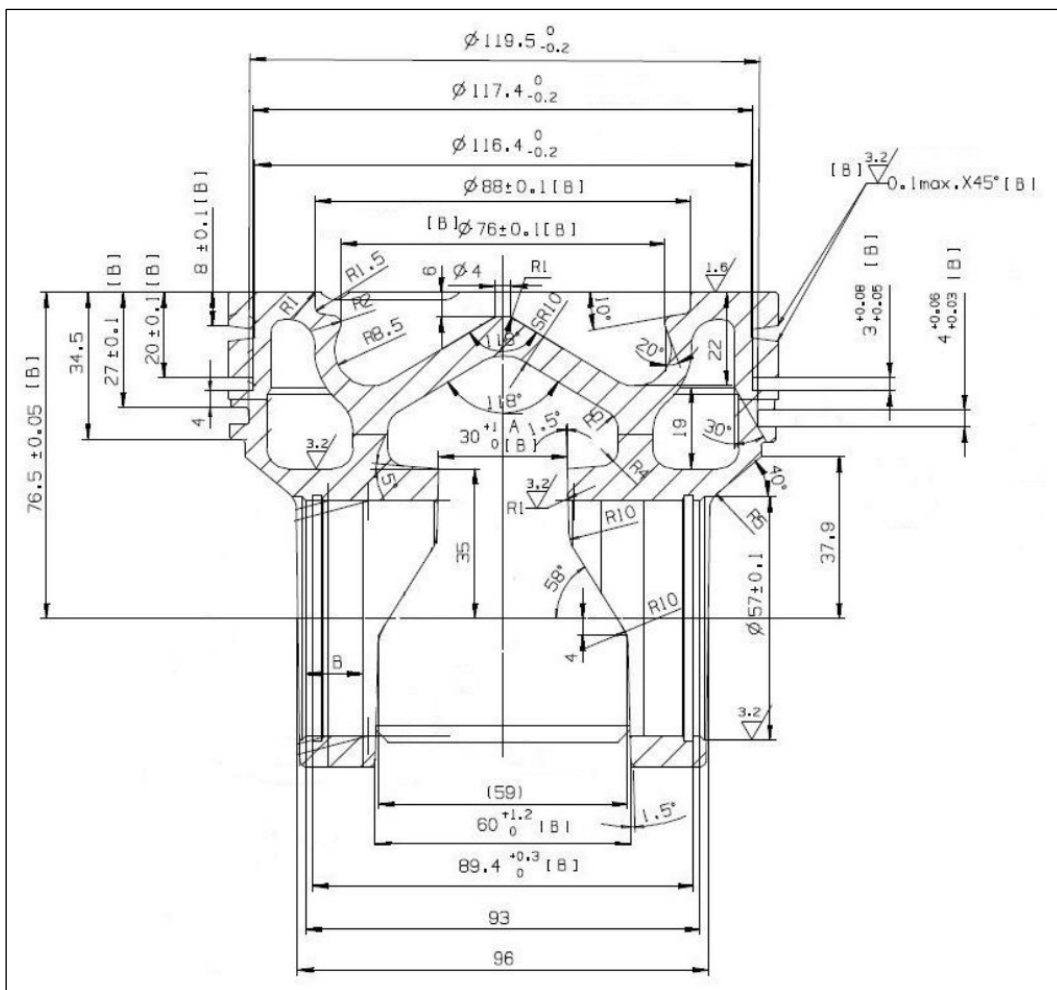


Fig. 6.7: Drawing of the piston cross-section [102].

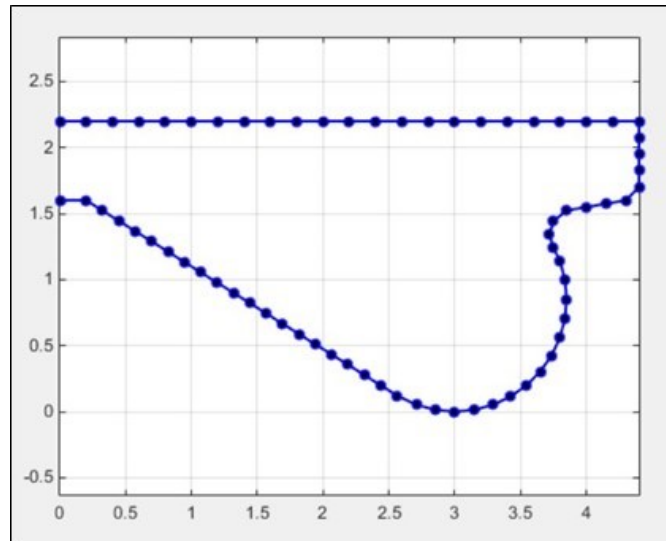


Fig. 6.8: Combustion bowl profile.

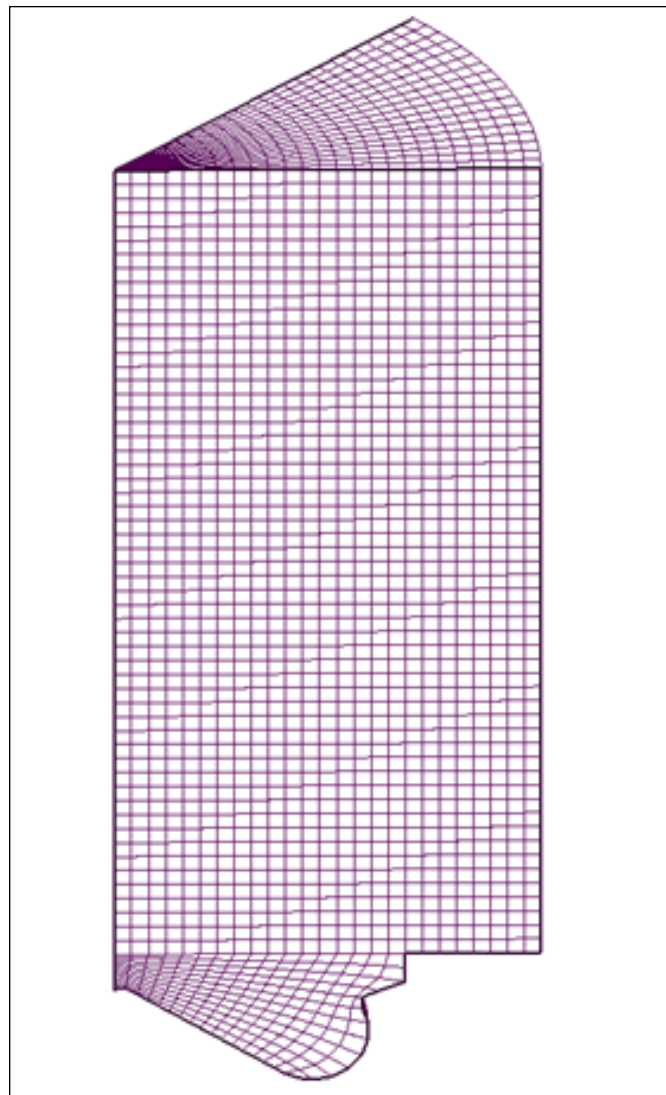


Fig. 6.9: 45° sector mesh.

The computational methodology founds on the integrated use of two solvers: KIVA-3V and ANSYS-FORTE. The first one is used only for the flow solution during the intake process on a similar geometry with open valve periods, in order to establish proper levels of turbulence and swirled flow parameters by making use of standard k-ε equations. More specifically, this solver provides the values of Turbulent Kinetic Energy and Turbulent Length Scale that are required by FORTE as turbulence initial conditions. This second solver is exploited for its advanced features in terms of complex kinetic mechanisms, turbulence-chemistry interaction and droplet breakup modelling.

In Table 6.5 the boundary condition for the CFD simulation are listed. The initial conditions are set at 40° BTDC. Indeed, as already said, the engine is equipped with a VVA system that varies the IVC and this crank angle was chosen for all the case.

Tab. 6.5. Simulation initial conditions at 40° BTDC.

Load	Medium	High
Diesel Start of injection [CAD]	-1.523	6.477
Duration of Diesel injection [deg]	5.03	5.02
Diesel Injected Mass [g/cycle]	0.0274	0.0421
Natural Gas mass fraction (NG%)	2.51	2.93
Pressure [bar]	17.7	24.21
Temperature [K]	667	699
Turbulent Kinetic Energy [cm ² /s]	1.0×10 ⁵	1.0×10 ⁵
Turbulent Length Scale [cm]	0.422	0.422

The Droplet breakup computation in FORTE is carried out by the combined Kelvin Helmholtz – Rayleigh Taylor approach.

Recalling Table 6.3, it is possible to observe that even at 75% load operation, the natural gas – air equivalence ratio is close to the lower flammable limit. For this reason, the effects of the turbulent flame propagation can be neglected and, once again it seems to be more appropriate to base the combustion process for both fuels on the turbulence – chemistry interaction.

The first kinetic mechanism is the same used in the previous chapter (Tables 5.6 and 5.7) consisting of the one-step reaction for the oxidation of n-dodecane and the 9-reaction mechanism presented by Li and Williams. Also, in these simulations, NG composition is assumed to be made of 100% methane contents, due to simplified composition of the gaseous fuel used during the experimental tests (Table 6.2).

Tab. 6.6: Detailed Species present in the mechanism.

1	DF2	7	H ₂	13	HO ₂
2	O ₂	8	O	14	CH ₃
3	N ₂	9	N	15	H ₂ O ₂
4	CO ₂	10	OH	16	CH ₂ O
5	H ₂ O	11	CO	17	CHO
6	H	12	NO	18	CH ₄

Differently from the previous chapters, the Zel'dovich mechanism for nitric oxides formation was not implemented in ANSYS-FORTE. Therefore, four species, i.e. N₂, O, N and NO, that are reported in Table 6.6 and that are not present in the kinetic scheme in Table 6.7, are, actually not used. For this reason, for these CFD simulations, the estimation of NO_x emissions is not included.

Tab. 6.7: Reaction mechanism.

RR1	$C_{12}H_{26} + 37/2 O_2 \rightarrow 12CO_2 + 13H_2O$
RR2	$CO + 1/2 O_2 \leftrightarrow CO_2$
RR3	$CH_4 + O_2 \rightarrow HO_2 + CH_3$
RR4	$CH_4 + HO_2 \rightarrow H_2O_2 + CH_3$
RR5	$CH_4 + OH \rightarrow H_2O + CH_3$
RR6	$CH_3 + O_2 \rightarrow CH_2O + OH$
RR7	$CH_2O + OH \rightarrow CHO + H_2O$
RR8	$CHO + O_2 \rightarrow CO + HO_2$
RR9	$CHO + M \rightarrow CO + H + M$
RR10	$H + O_2 + M \rightarrow HO_2 + M$
RR11	$H_2O_2 \rightarrow 2OH + M$
RR12	$CH_4 + 3/2 O_2 \rightarrow CO + 2H_2O$

The second kinetic mechanism consists of 100 species and 432 reactions for the complete oxidation of n-dodecane, implemented by Ra and Reitz. Actually, the new mechanism, includes a set of reactions for both methane formation from higher order hydrocarbons and methane oxidation via the CH_3 intermediate species. In Appendix a set of reactions for methane formation and oxidation via CH_3 is reported. Therefore, it appears to be suitable for a proper employment in a dual fuel problem.

6.4 CFD results

In this section, it is important to highlight that both medium and high load cases were simulated with the Li and Williams mechanism, while the Ra and Reitz mechanism was tested only in the 75% load case.

6.4.1 Medium Load: Li and Williams model

The in-cylinder pressure and temperature trends obtained by numerical calculations show a fair compliance with the experimental ones (Figure 6.10 and 6.11).

Figure 6.12 evidences that the two humps in the heat release rate for the medium load, already detected by experimental test, are more evident in the numerical simulation.

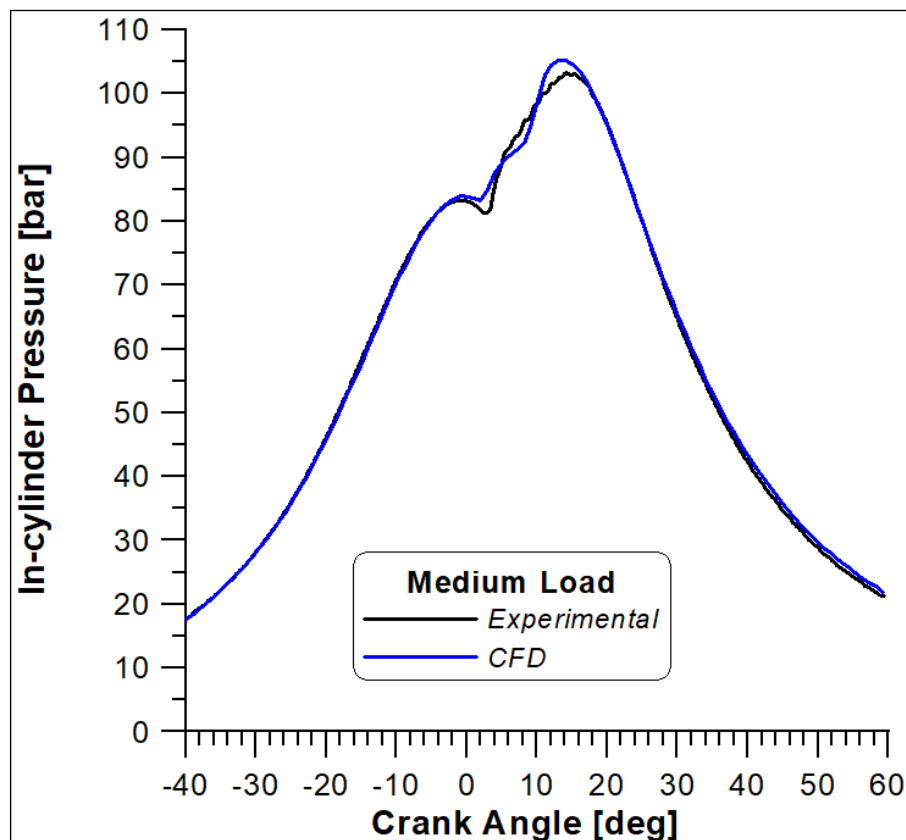


Fig. 6.10: Medium load pressure curves.

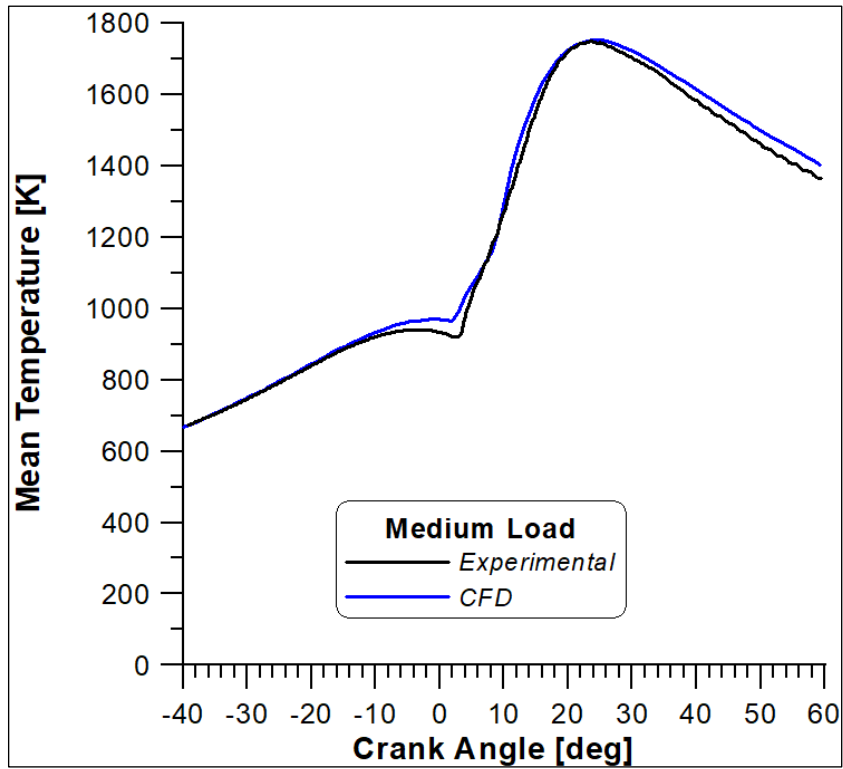


Fig. 6.11: Medium load temperature curves.

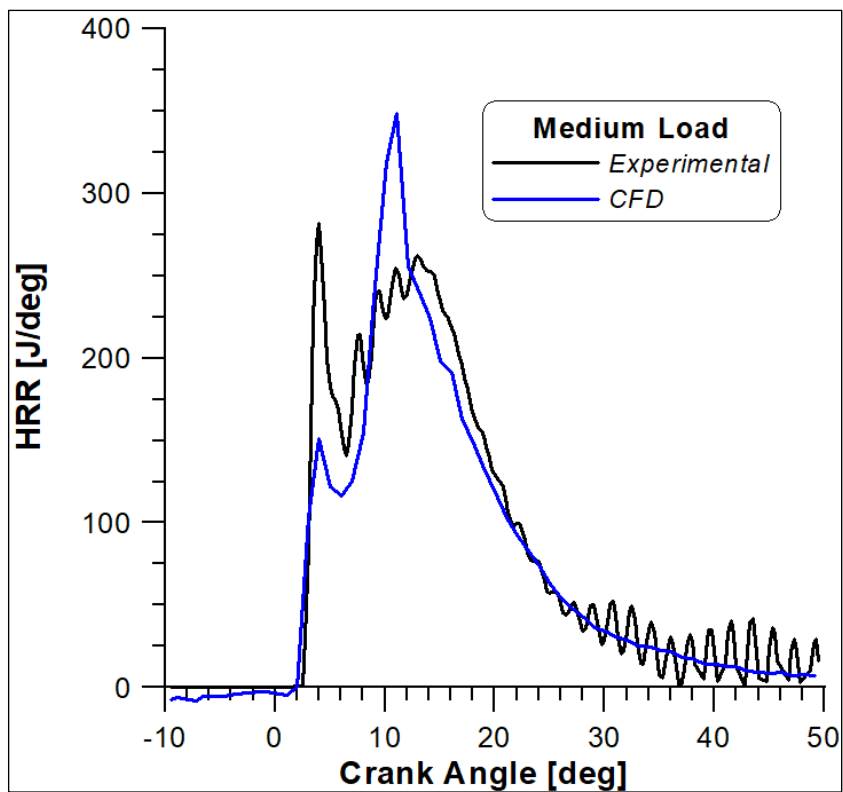


Fig. 6.12: Medium load heat of release rates.

An important result obtained from the same Figure is that experimental and numerical starts of combustion match perfectly. However, the two peaks, that highlight two distinct burning rates for diesel fuel and natural gas, are correctly detected in timing but their magnitude show opposite trends. Indeed, differently from the experimental tests, the first one is lower with respect to the second one and this implies a different increase to the maximum of pressure. Nevertheless, the final part of combustion is fairly reproduced.

6.4.2 High Load: Li and Williams model

The numerical pressure trend, displayed in Figure 6.13, differs from the experimental one only in the rise to the peak. In particular, a second lower hump is observed before the peak pressure. This is due to the fact that the Li and Williams model concerns only the methane autoignition, while the diesel vapour is converted directly in CO₂ through a single-step reaction. It appears that the two combustion processes are independent from each other. Therefore, the first hump is caused by the direct oxidation of n-dodecane and the second hump is the effect of the methane oxidation. Also, in Figure 6.14 the mean temperature does not present a straight rise to the peak, in accordance with the pressure trend. The validation of these considerations is provided by Figure 6.15, since the first peak in the heat release is comparable with the second one showing a different behaviour from the one previously observed in the medium load case. However, the experimental HRR, as explained in the experimental results section, is characterised by a single hump trend. Although, the numerical start of combustion is not perfectly detected, the estimation of combustion duration can be considered acceptable.

Finally, a perfect agreement of the expansion phase is shown in all Figures.

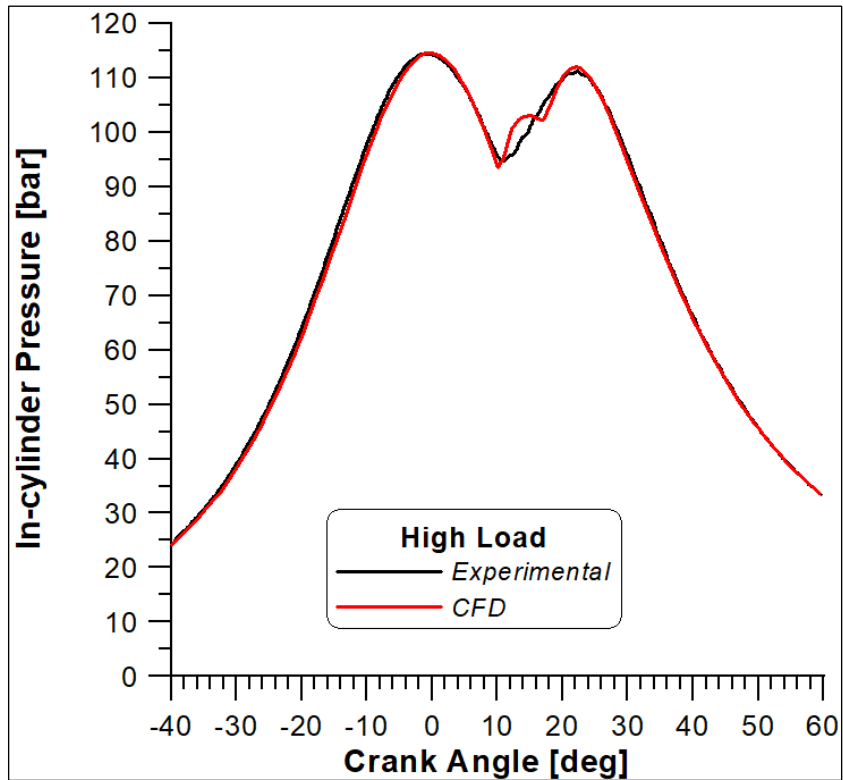


Fig. 6.13: High load pressure curves.

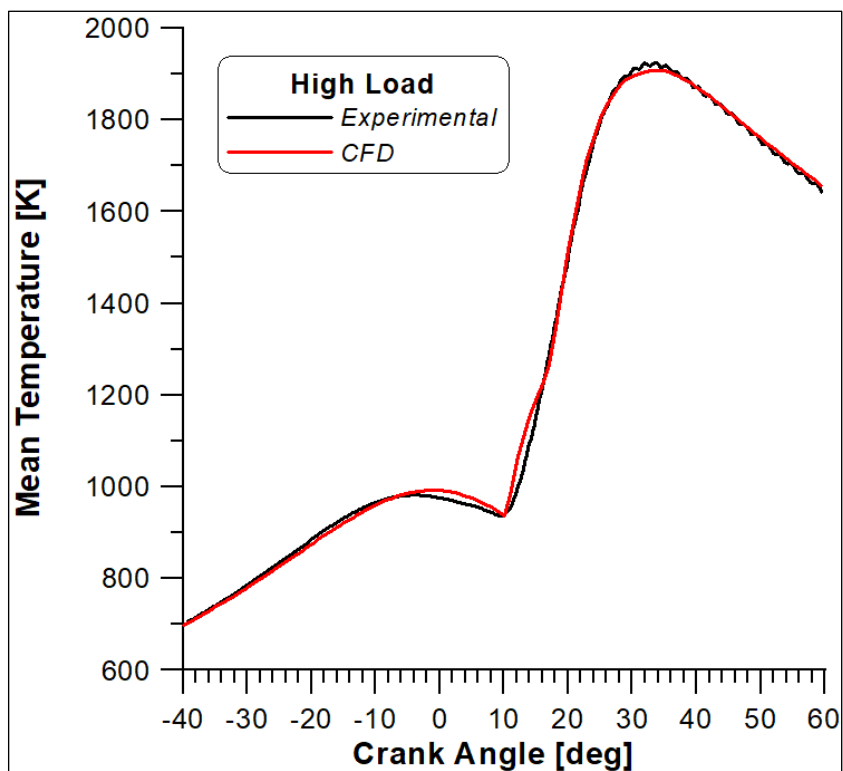


Fig. 6.14: High load temperature curves.

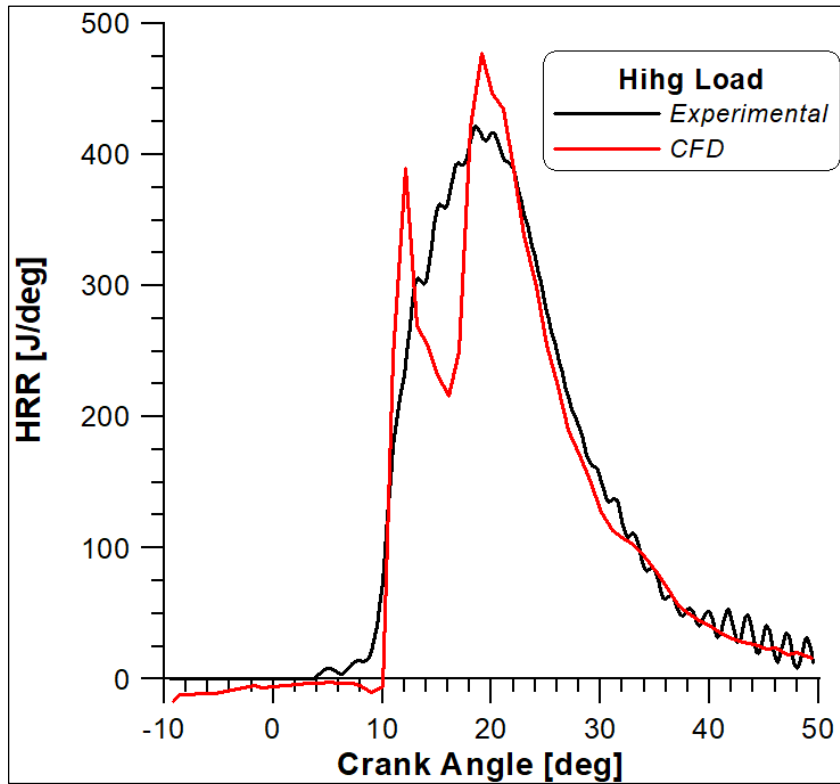


Fig. 6.15: High load heat of release rates.

6.4.3 High Load vs Medium load: Li and Williams

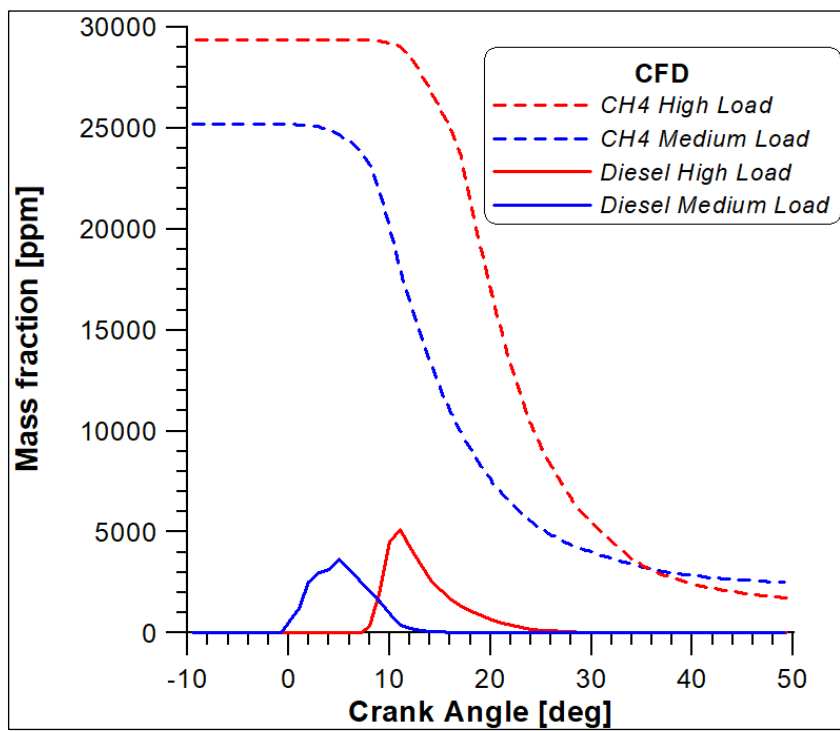


Fig. 6.16: Mass fractions of n-dodecane and methane comparison.

A comparison between the results of the two load levels can be an important mean to estimate the response of the model to different operating conditions, as reported in Figure 6.16 in terms of species consumption. A slower consumption for both n-dodecane and methane in medium load case is evidenced. Indeed, in this case, the lower temperature level and the anticipated injection start cause a longer delay for the diesel fuel ignition. Nevertheless, diesel vapour burns completely in both cases. On the other hand, CH₄ presents an incomplete combustion, especially for the medium load case, where the further reduced amount of fuel does not enable a proper ignition of the mixture.

6.4.4 High Load: Ra and Reitz model

In Figure 6.17 a comparison of the pressure curves obtained with the two different kinetic schemes is reported. With the Ra and Reitz model the start of combustion seems to be perfectly detected as well as the first part of pressure increase. However, at a certain point of the pressure rise the trend diverges considerably from the experimental one with a faster combustion and a peak slightly anticipated. Moreover, the expansion phase is no longer exactly reproduced. It is important to recall that methane is present as an intermediate species in this more complex reaction scheme, and this could be the reason why whole oxidation process is prolonged and consequently shows a different development.

Figure 6.18 displays that in both cases n-dodecane burns completely but with different timings. Indeed, in Ra and Reitz model C₁₂H₂₆ is firstly converted in a series of intermediate species that must be faster with respect to the direct oxidation in CO₂ of the one-step mechanism coupled with the Li and Williams model.

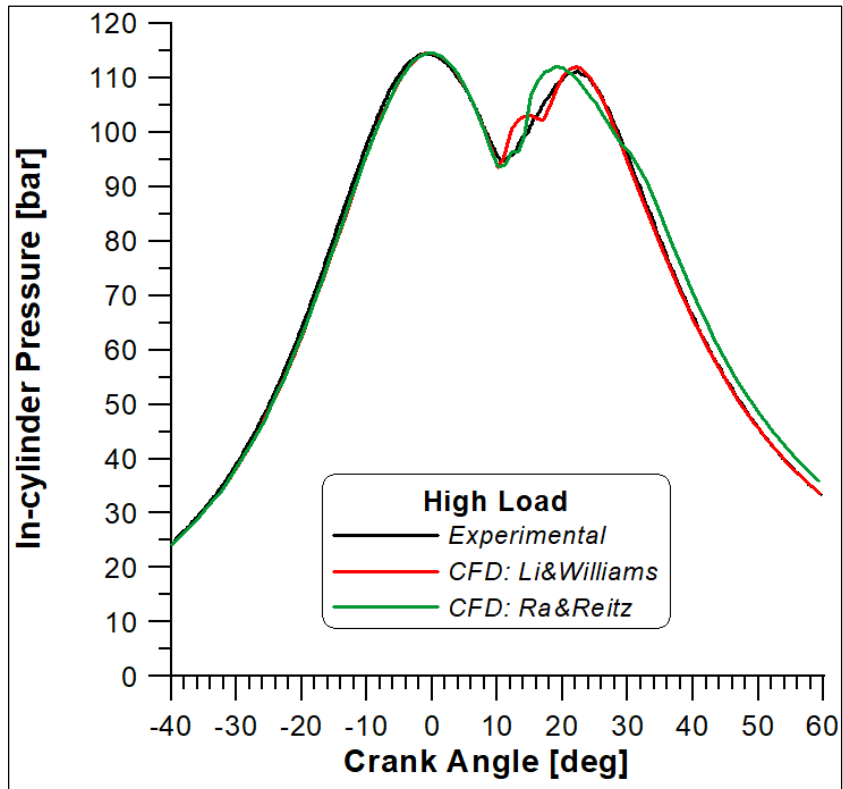


Fig. 6.17: High load pressure curves for the two reaction schemes.

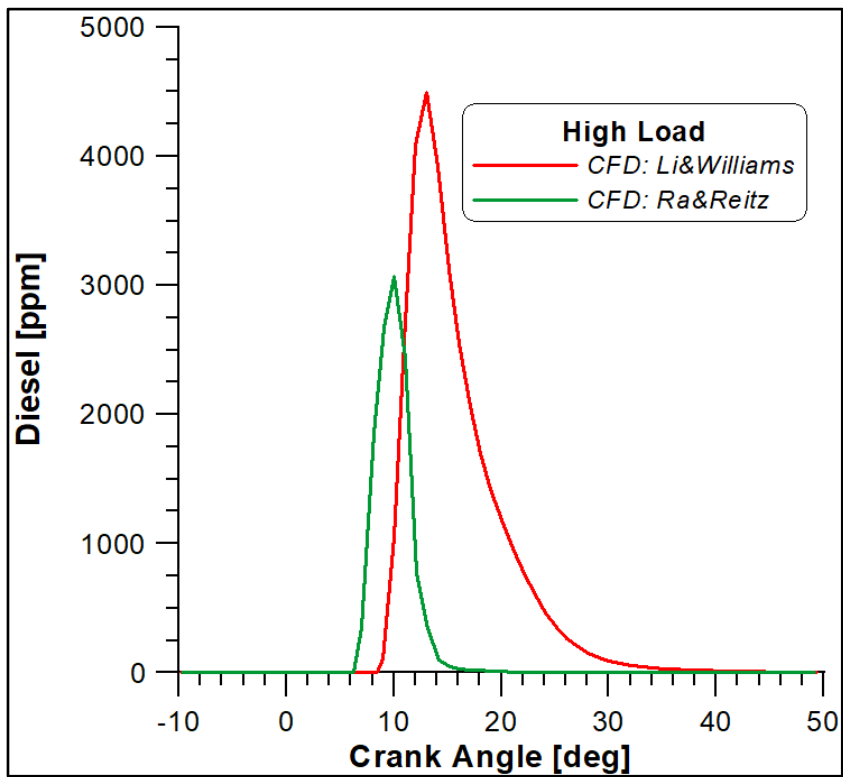


Fig. 6.18: High load diesel mass fractions for the two reaction schemes.

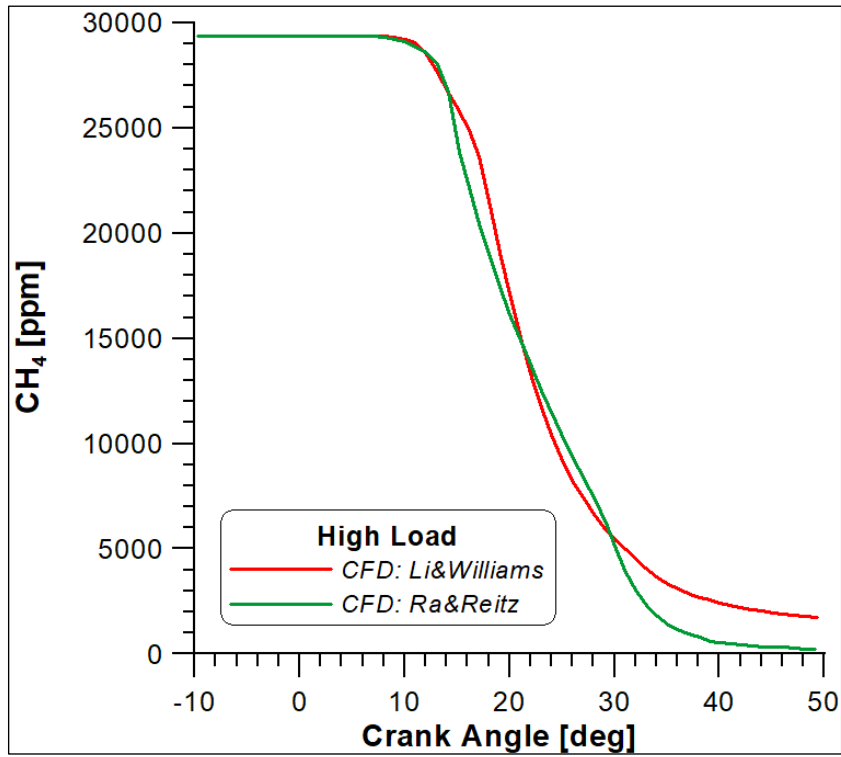


Fig. 6.19: High load methane mass fractions for the two reaction schemes.

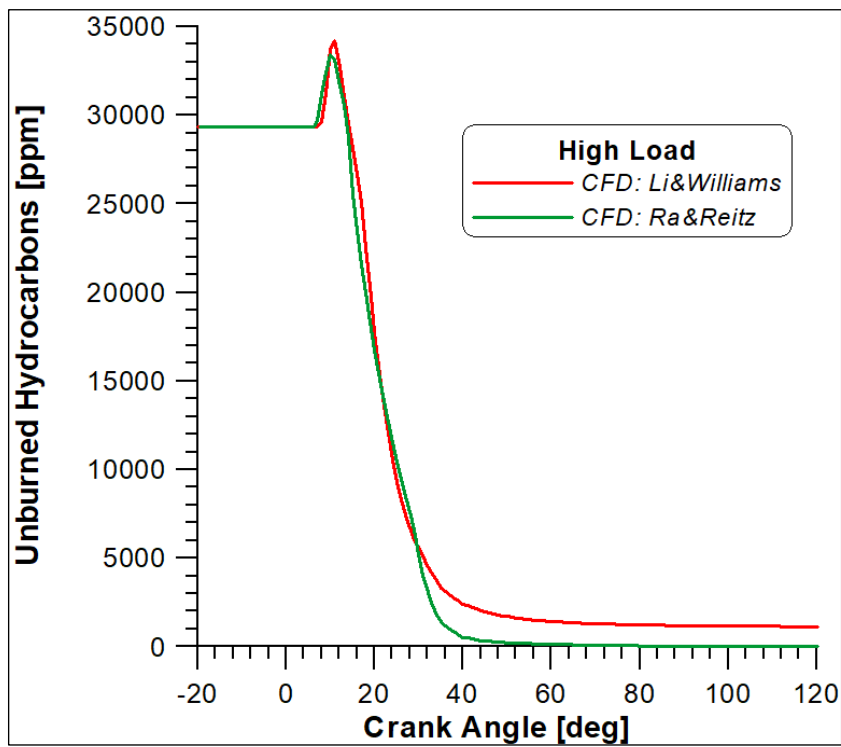


Fig. 6.20: High load CO mass fractions for the two reaction schemes.

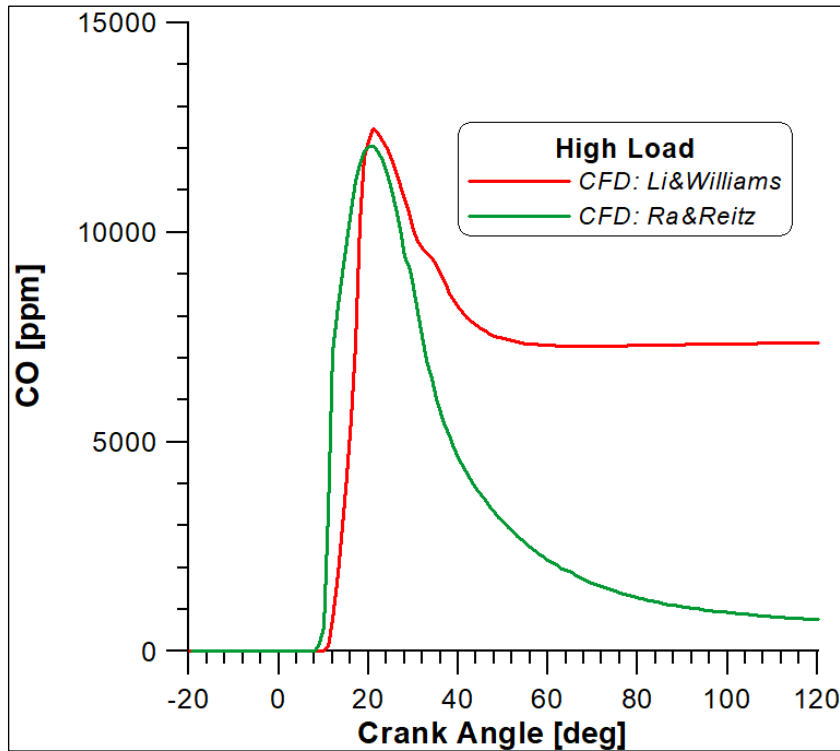


Fig. 6.21: High load UHC mass fractions for the two reaction schemes.

Methane consumption in Figure 6.19 highlights that with the Ra and Reitz model a faster and almost completed oxidation is achieved, explaining the anticipated peak in the pressure curve (Figure 6.17). Figure 6.20 confirms the complete oxidation of CH_4 since almost no unburned hydrocarbon are produced at the exhaust, being in contrast with the experimental measurements. Finally, Figure 6.21 points out a more efficient CO oxidation provided by the Ra and Reitz model.

6.4.5 Li and Williams vs Ra and Reitz model

In this last section an overall overview and a comparison of the experimental and numerical results are reported for a more comprehensive descriptions of the outcomes of the CFD analysis.

As evidenced in Table 6.8, Li and Williams kinetic model allows a correct prediction of methane combustion, while as already stated, the Ra and Reitz CH_4 and UHC results are in contrast with the well-known dual fuel

combustion problem represented by the relevant contents of these species in the exhaust. On the other hand, the Ra and Reitz model outcomes for CO species is in accordance with the experimental output. This seems to be reasonable since the first model deals with CO complete oxidation via a single reaction.

Tab. 6.8: High Load Emissions

[ppm]	Experimental	Li & Williams	Ra & Reitz
CH ₄	1011	1141	21
UHC	1062	1141	23
CO	628	7368	762

Temperature distributions in Figure 6.22 illustrate different combustion developments. In simulations based on the Li and Williams model, high temperature zones are detected near the wall of the combustion chamber. If comparing medium and high load cases with the Li and Williams model, this difference is due to the variation in injection timing. For the same load level, the higher temperature regions are located in correspondence of the higher presence of n-dodecane distributions as confirmed by Figure 6.23. Indeed, following the Li and Williams model, at 15° ATDC this species is still highly present (Figures 6.18 and 6.23), since, as already said the one-step reaction in the first mechanism describes a slower oxidation that occurs further than the Ra and Reitz one.

Moreover, with the Ra and Reitz model at 30° ATCD it is possible to observe zone at still high temperature, this means that combustion is still active. Therefore, a more efficient combustion process is taking place and consequently lower emissions of CH₄, UHC and CO are observed, as already widely previously pointed out.

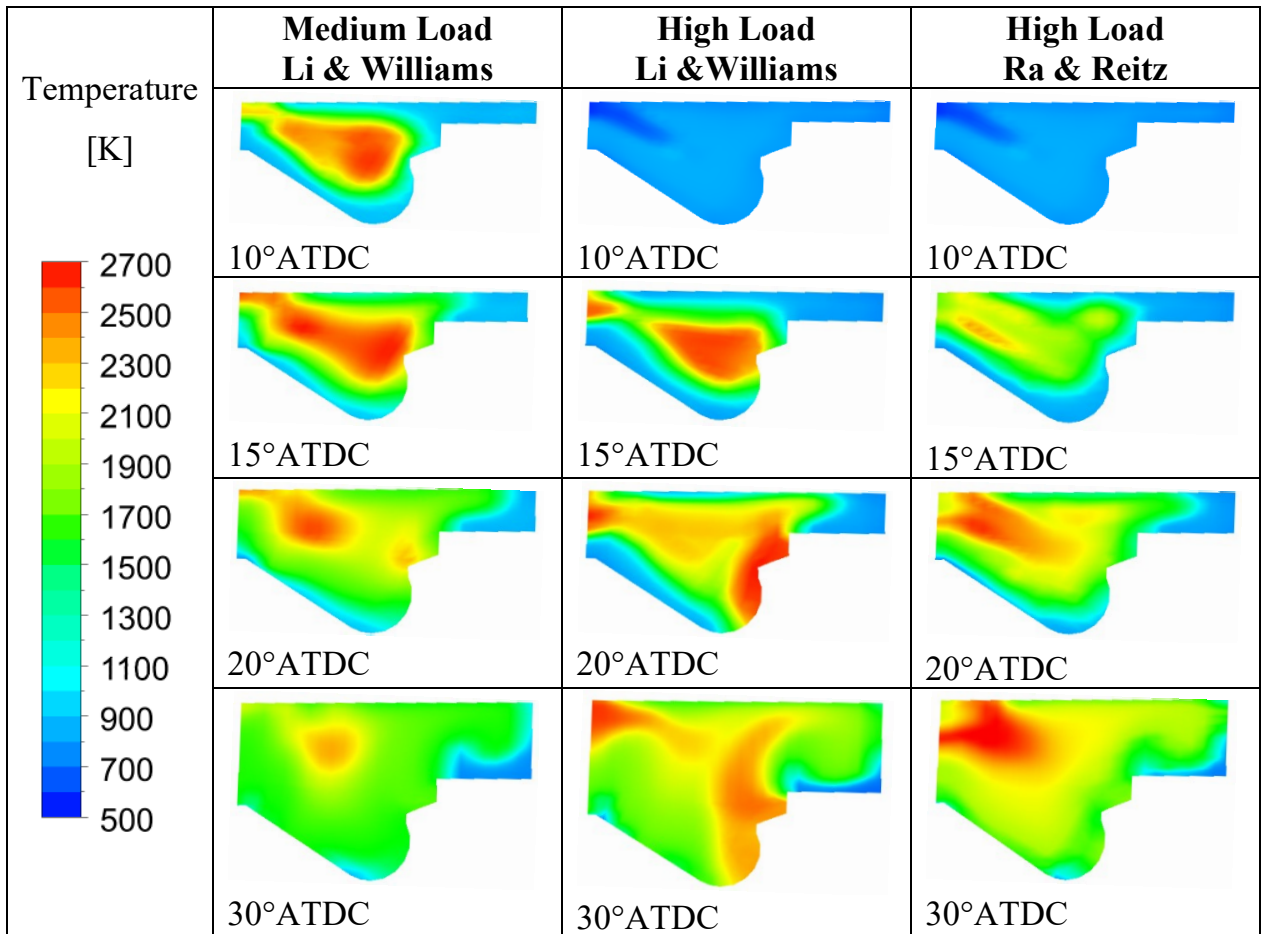


Fig. 6.22: Temperature contours.

The progress in CH₄ mass fraction decrease (Figure 6.24) appears to be consistent with the liquid jet propagation towards the walls of the domain.

Again, a faster methane consumption is achieved with the Ra and Reitz model, in accordance with Figure 6.19.

For all cases the higher amount of CH₄ is located in the squish zone. However, the Li and Williams model does not allow a complete oxidation also in the bowl as demonstrated by the higher CH₄ concentration zones still present at 30°ATDC, especially for the medium load case whose diesel injection is even anticipated.

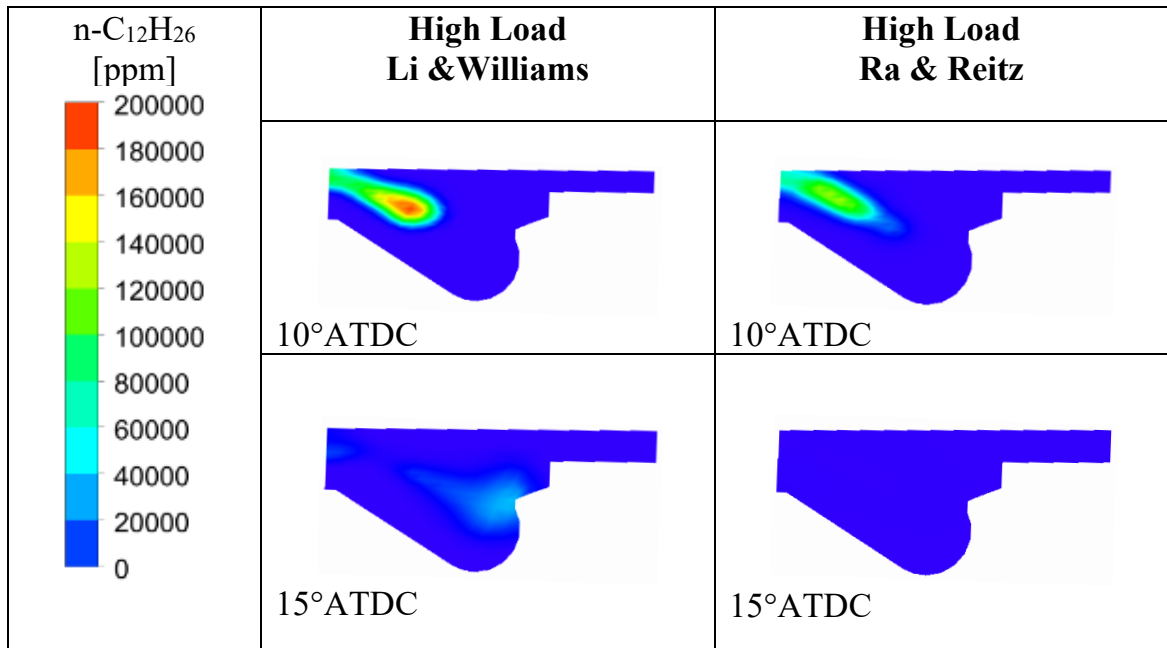


Fig. 6.23: Diesel mass fraction contours.

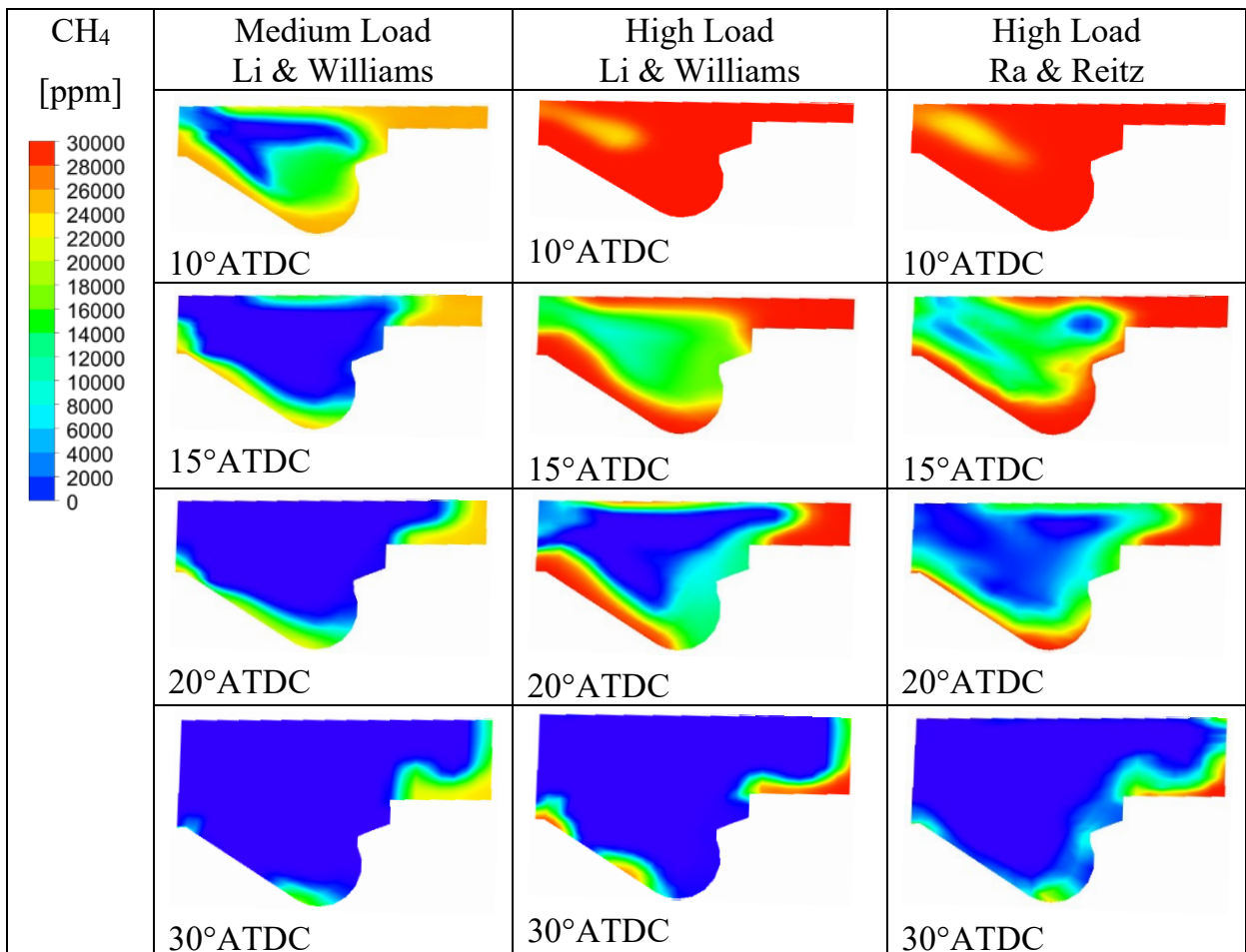


Fig. 6.24: Methane mass fraction contours.

Chapter 7

DEFINITE IMPROVEMENTS TO THE RESEARCH ENGINE SIMULATION

In this chapter the optically accessible single cylinder research engine [95] is again investigated. However, with respect to the results reported in Chapter 5 further improvements were made with the reproduction of the exact bowl geometry, with the deep investigation of the crevices issue that considerably affects this engine and with the testing of a model that seemed the most suitable to describe dual fuel combustion: Autoignition-induced Flame Propagation model.

7.1 Geometry

Since a grid of the complete geometry of the single cylinder engine including the gas exchange systems was not available yet, in Chapter 5 it was explained that the aim of the CFD investigation was to reproduce the experimental tests [95] in an in-cylinder domain with the same baseline geometrical features but with a bowl shape more consistent with those usually adopted for automotive application, and to prove the transferability of the experimental results to commercial diesel engines.

In order to limit the obvious differences between the numerical results and the experimental ones, the geometry of the flat bowl, already shown in Figure 5.2, and again displayed in Figure 7.1 with the related dimensions, was reproduced. Following the same methodology outlined in Chapter 6, the mesh was created with the K3PREPW tool and the ANSYS-FORTE solver was used for the calculations. In this case too, the domain consists of the

combustion chamber and the cylinder, so allowing only the simulation of closed periods.

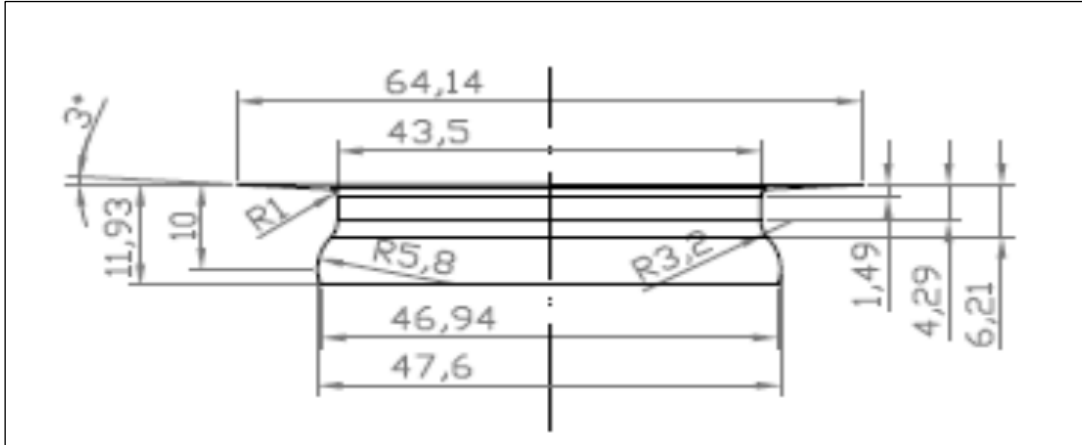


Fig. 7.1: Modified geometry of the combustion chamber.

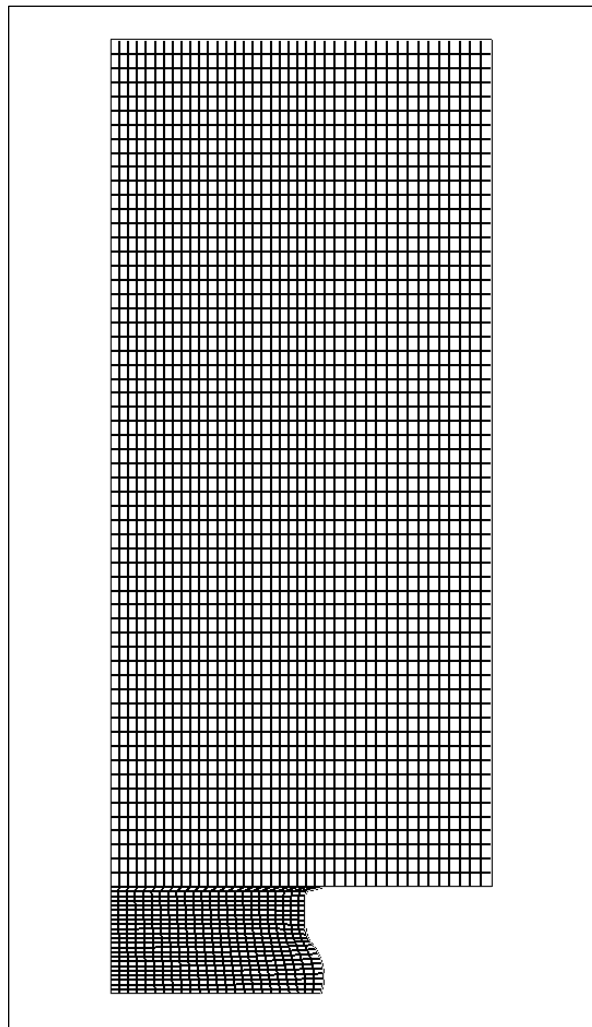


Fig. 7.2: Modified geometry of the combustion chamber.

The diesel injector has 7 holes (Table 5.2) periodically distributed approximately every 51.43° along the circumferential direction. Therefore, a sector with the same opening angle, having the jet radial direction as bisector, was considered for the computational domain. The final mesh displayed in Figure 7.2, consists of 64,166 nodes and 63,808 cells.

7.2 Crevices

The optically accessible research engine is affected by significant mass losses. Indeed, the adherence of the piston to the cylinder walls cannot be ensured with the use of lubricating oil that would prevent the visibility in the combustion chamber, but it is provided with particular rings, that allows the mass of the methane-air mixture to flow into the crevices region during the compression stroke and to return to the combustion chamber during the expansion phase. This phenomenon influences the estimation of the actual compression ratio. Indeed, in Table 5.1 it is reported a value of the geometric compression ratio equal to 16.5, but in the practice the pressure curve demonstrates that a lower effective value is reached during the end of the compression stroke. Therefore, in the simulations carried out in Chapter 5, the geometric compression ratio of the open valves mesh grid was calibrated in order to follow the pressure curve during the compression phase. However, this methodology cannot take into account the variations of equivalence ratio that is consequent to the mass loss. For this reason, in the present chapter a crevice model is added to the calculation set-up. In this way, it is possible to evaluate the behaviour of the combustion development when a part of the mass escapes and returns in the cylinder. Moreover, this model allows a better evaluation of the amount of mass involved in this process.

The crevice model, used by the FORTE solver, was implemented by Namazian and Heywood [104].

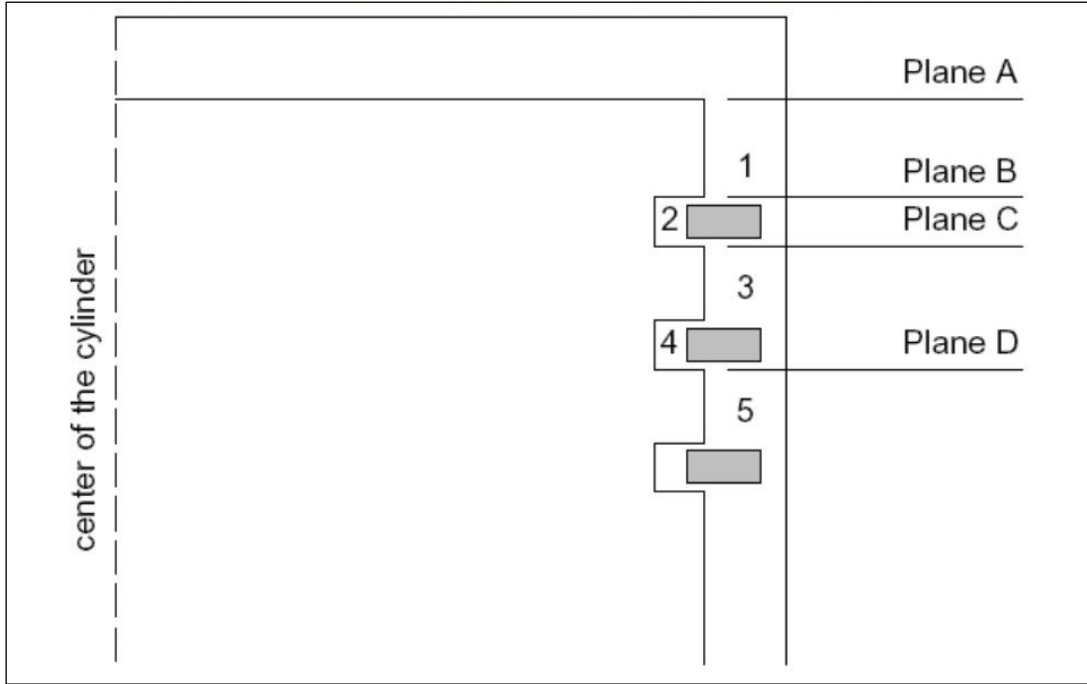


Fig. 7.3: Schematic diagram of the crevice volumes and planes used in the model [72].

In Figure 7.3 the diagram of the volumes and planes considered for the equations setting is reported. It is assumed that the flow in the crevice region 1 is a fully-developed laminar flow and the pressure is uniform and equal to the cylinder pressure. Also, regions 2, 3 and 4 each have a uniform pressure and the temperature is assumed to be equal to the wall temperature. The continuity equations for the region 2, 3 and 4 can be written as follow:

$$\frac{m_{o_2}}{p_{o_2}} \frac{dp_2}{dt} = \dot{m}_{12} - \dot{m}_{23}$$

$$\frac{m_{o_3}}{p_{o_3}} \frac{dp_3}{dt} = \dot{m}_{13} + \dot{m}_{23} - \dot{m}_{34} - \dot{m}_{35}$$

$$\frac{m_{o_4}}{p_{o_4}} \frac{dp_4}{dt} = \dot{m}_{34} - \dot{m}_{45}$$

The subscript “o” refers to a reference condition, m is the mass, p is the pressure, t is the time and the double subscript designates the flow from the first to the second numbered region.

The mass flow rate through the ring gap is calculated by the orifice flow equation:

$$\dot{m} = C_d A_g \rho c \eta$$

Where C_d is the discharge coefficient (0.6 – 0.86), A_g is the cross-sectional area available to the flow, ρ is the density, c is the speed of sound and η is the compressibility factor defined as:

$$\eta_i = \sqrt{\frac{2}{\gamma - 1} \left[\left(\frac{p_{i+1}}{p_i} \right)^{\frac{2}{\gamma}} - \left(\frac{p_{i+1}}{p_i} \right)^{\frac{\gamma+1}{\gamma}} \right]}$$

Where γ is the ratio of specific heats and the subscript “i” on the pressure terms denoted the region where the properties are calculated, with acceptable values running from 1 to 4.

In order to calculate the mass flow rate through the rings, the FORTE code requires some geometrical parameters as listed in Table 7.1. The values reported in the second column are obtained through a calibration process because the actual ones were unknown. In paper [104] Namazian and Heywood tested their model on an engine with similar characteristics as those under investigation; hence, starting from the values reported in their work a progressive adjustment of the parameters was operated until the numerical compression curve reproduced the one measured during the experimental activity.

Tab. 7.1: Crevice model input parameter.

Engine Bore [mm]	85.0
Gas Temperature Inside Crevice [K]	600
Height of the crevice region between the top of the crevice and the first compression ring [cm]	3.0
Crevice Thickness between the Piston edge and the Cylinder Liner [mm]	0.64
Cross-sectional flow Gap Area – first ring [cm ²]	0.021
Cross-sectional flow Gap Area – second ring [cm ²]	0.021
Volume Behind Top Ring [cm ³]	0.2457
Volume Between Ring 1 and 2 [cm ³]	0.2548
Volume Behind Second Ring [cm ³]	0.2457
First Ring Thickness [cm]	0.1
Second Ring Thickness [cm]	0.1
First Ring lateral Width [cm]	0.1
Second Ring lateral Width [cm]	0.1
Mass of the First Ring [g]	10.0
Mass of the Second Ring [g]	10.0
Bottom Clearance – First Ring [mm]	0.025
Bottom Clearance – Second Ring [mm]	0.025
Top Clearance – First Ring [mm]	0.025
Top Clearance – Second Ring [mm]	0.025

7.3 Autoignition induced flame propagation

In previous calculations the Finite rate – Eddy Dissipation model seemed to be the most suitable for the combustion development description; indeed, due to poor equivalence ratio of the operating conditions, it was not possible to obtain a proper flame propagation. However, in this Chapter the RP = 22% case was tested with the autoignition induced flame propagation model

illustrated in Section 2.5. As already explained, this model uses the G-equation model in order to track the position and the propagation of the premixed turbulent flame. The flame is initiated by the source of ignition that, in this specific case, is the autoignition kinetics represented by the Ra and Reitz reaction scheme for the n-dodecane. As soon as the computational cells reaches a temperature higher than the critical value, set at 1,200 K, they become ignition sites.

The low value of equivalence ratio imposed to choose the Gülder correlation for the reference flame speed calculation.

$$S_{L,ref}^0 = \omega \phi^\eta \exp(-\xi(\phi - \sigma)^2)$$

The values of the coefficients holding for methane, are listed in Table 7.2

Tab. 7.2: Coefficients for methane [105].

ω [cm/s]	η	ξ	σ
42.2	0.15	5.18	1.075

The calculation was performed from 130° BTDC to 130° ATDC. In Table 7.3 the initial conditions are outlined.

Tab. 7.3: Engine operating conditions.

Premixed ratio	22
Engine speed [rpm]	1500
Diesel SOI	3° BTDC
Diesel inj. duration [μ s] (deg)	450 (4.05)
Diesel flow rate [mg/str]	8.9
P_{in} [bar]	1.562
T_{in} [K]	381.1
Methane flow rate [mg/str]	2.14
Air flow rate [kg/s]	33.4
Methane mass fraction	0.00287
Turbulent Kinetic Energy [cm ² /s ²]	1.9227×10^4
Turbulent Length Scale [cm]	0.2378

7.4 Results

In Figure 7.4 the comparison of numerical and experimental in-cylinder mean pressure is illustrated. As already explained, the perfect matching of numerical and experimental compression curves was the goal of the crevices parameters calibration. However, the first nearly horizontal part, the start of combustion and the rise to the peak are correctly detected, while numerical results evidence a peak and expansion phase pressure lower than those from the experimental measurements.

Figure 7.5 shows that an important mass loss occurs as the pressure increases, then the injection of diesel oil causes a slight mass increase. Just after the pressure peak, around 10° ATDC, the expansion phase begins, and the mass increases because the air trapped in the crevices volume returns into the cylinder consequently to the pressure drop. It is important to highlight that this model describes a complete restitution of the mass from the crevices. The mass fraction trend of n-dodecane in Figure 7.6 does not evidence any particular feature. On the contrary, methane mass fraction starts to decrease after diesel injection but more importantly a slight increase is observed during the expansion phase.

Figure 7.7 demonstrates that CO and UHC are mainly due, respectively, to diesel oil and methane oxidation since the former reaches an almost steady value, while the latter follows exactly the same trend as CH_4 already outlined in Figure 7.6.

Figure 7.8 plots the in-cylinder averaged values of laminar and turbulent flame speeds. As imposed by the model, the turbulent flame speed is proportional to the laminar one. The flame starts right after the diesel injection and develops within an interval of about 10 crank angle degrees.

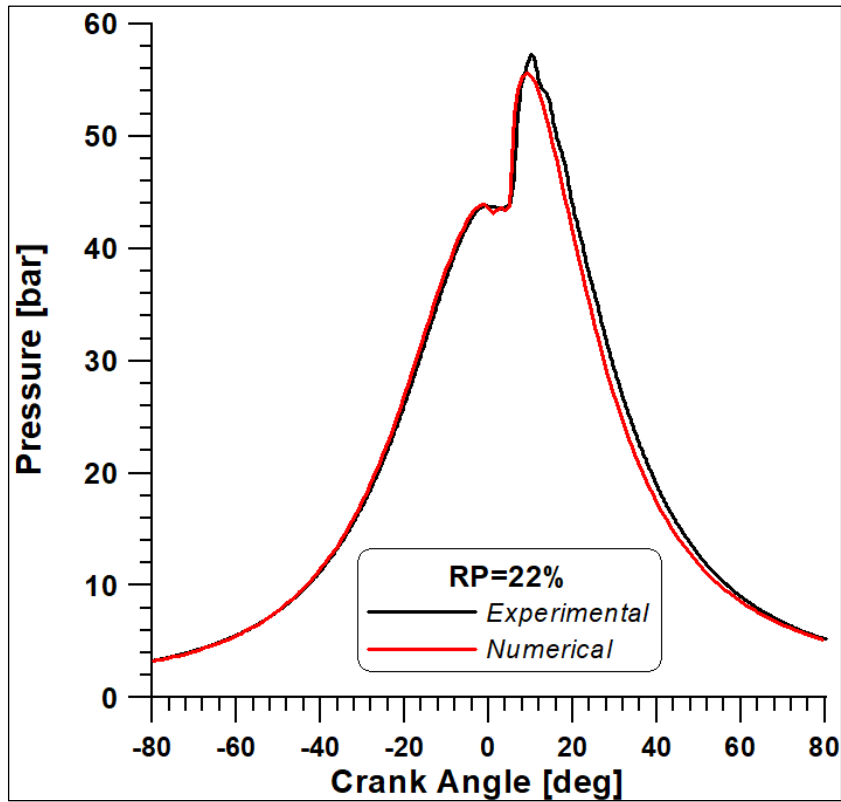


Fig. 7.4: In cylinder pressure for RP=22.

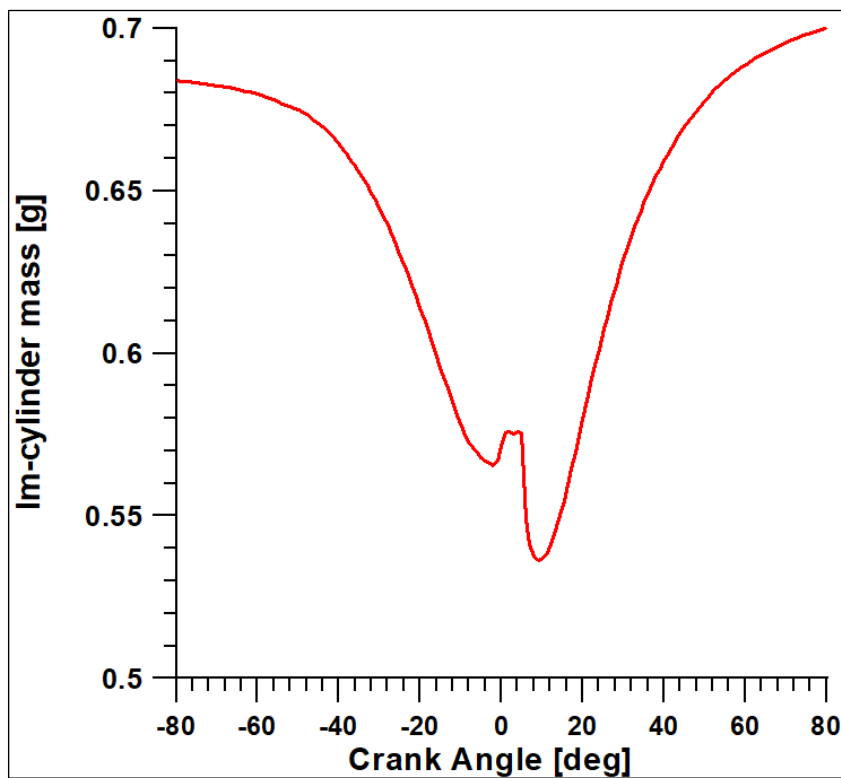


Fig. 7.5: In cylinder mass.

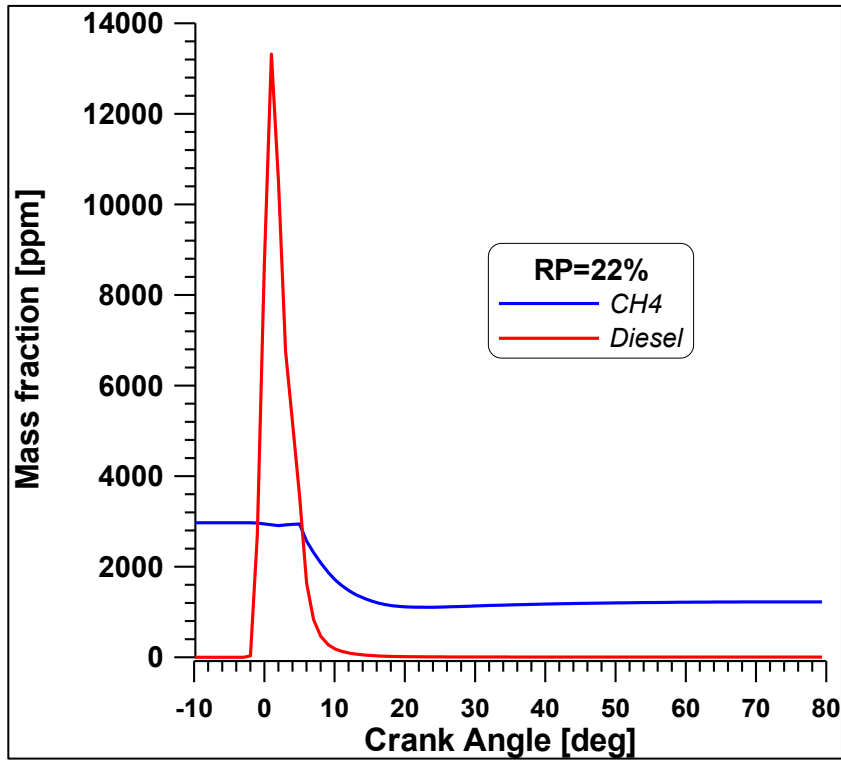


Fig. 7.6: Mass fractions of methane and n-dodecane.

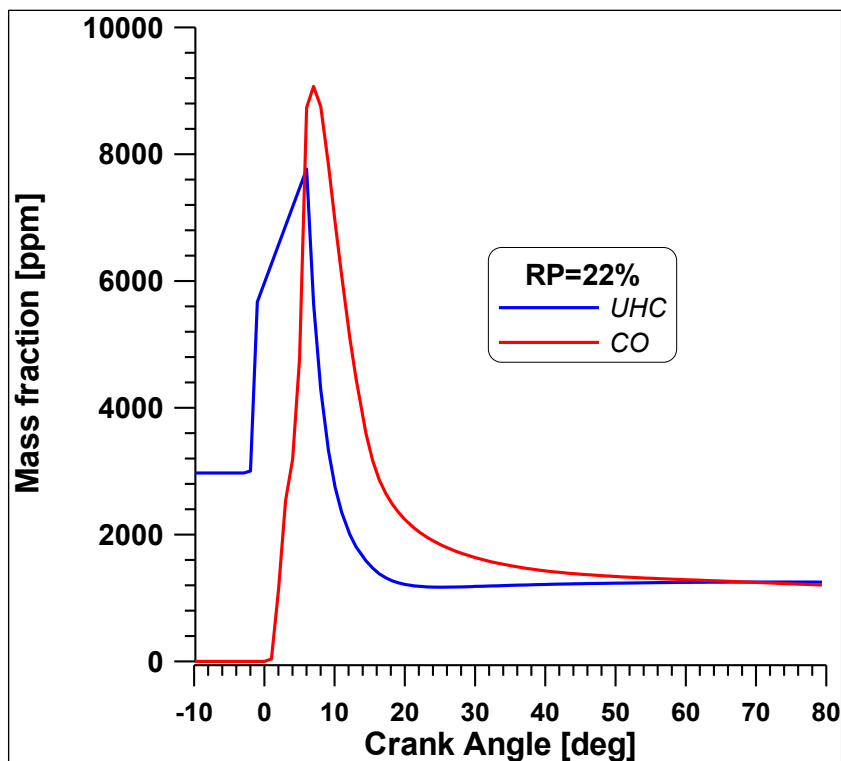


Fig. 7.7: Mass fractions of unburned hydrocarbons and carbon monoxide.

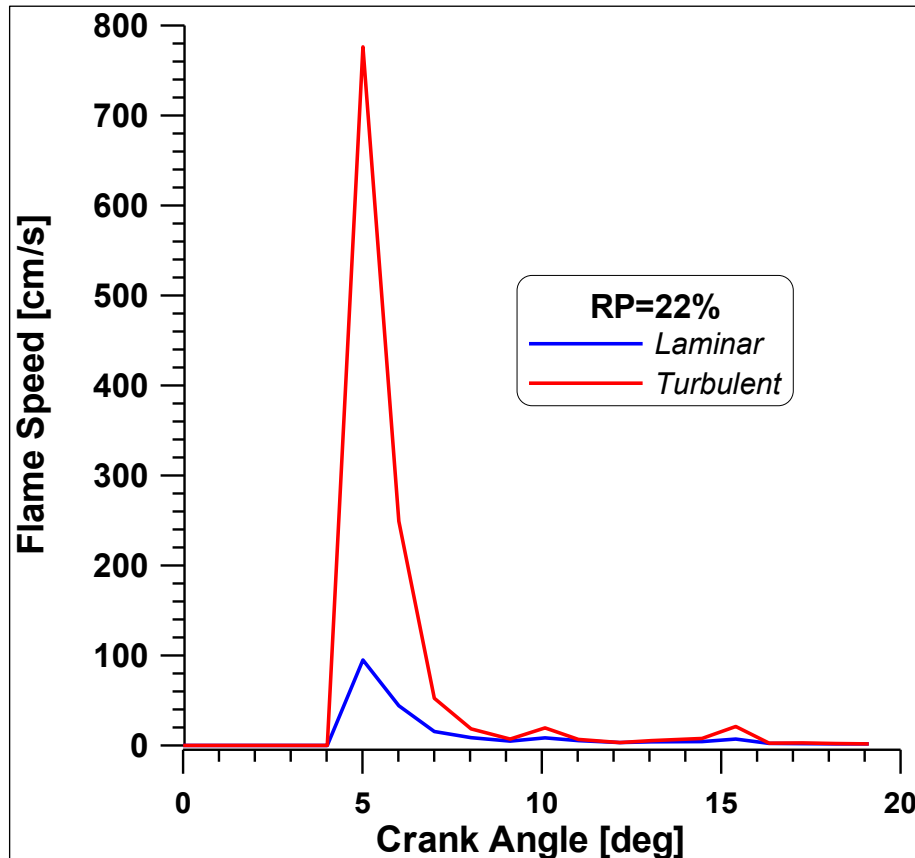


Fig. 7.8: Laminar and Turbulent flame speeds.

Figure 7.9 displays the temperature distributions at different crank angle degrees in a meridional plane passing through the jet radial direction. Just after TDC, higher temperatures are detected near the jet tips, recalling that in this test case the amount of methane energy supply is only of 22%, it seems reasonable that combustion start is mainly due to diesel vapour oxidation. However, a sort of front flame is able to quickly propagate after 5° ATDC (Figures 7.10 and 7.11). After this crank angle, higher concentration of methane remains in the furthest zone from the jets, especially in the squish zone, since during the expansion phase methane is released by the crevices (Figure 7.12).

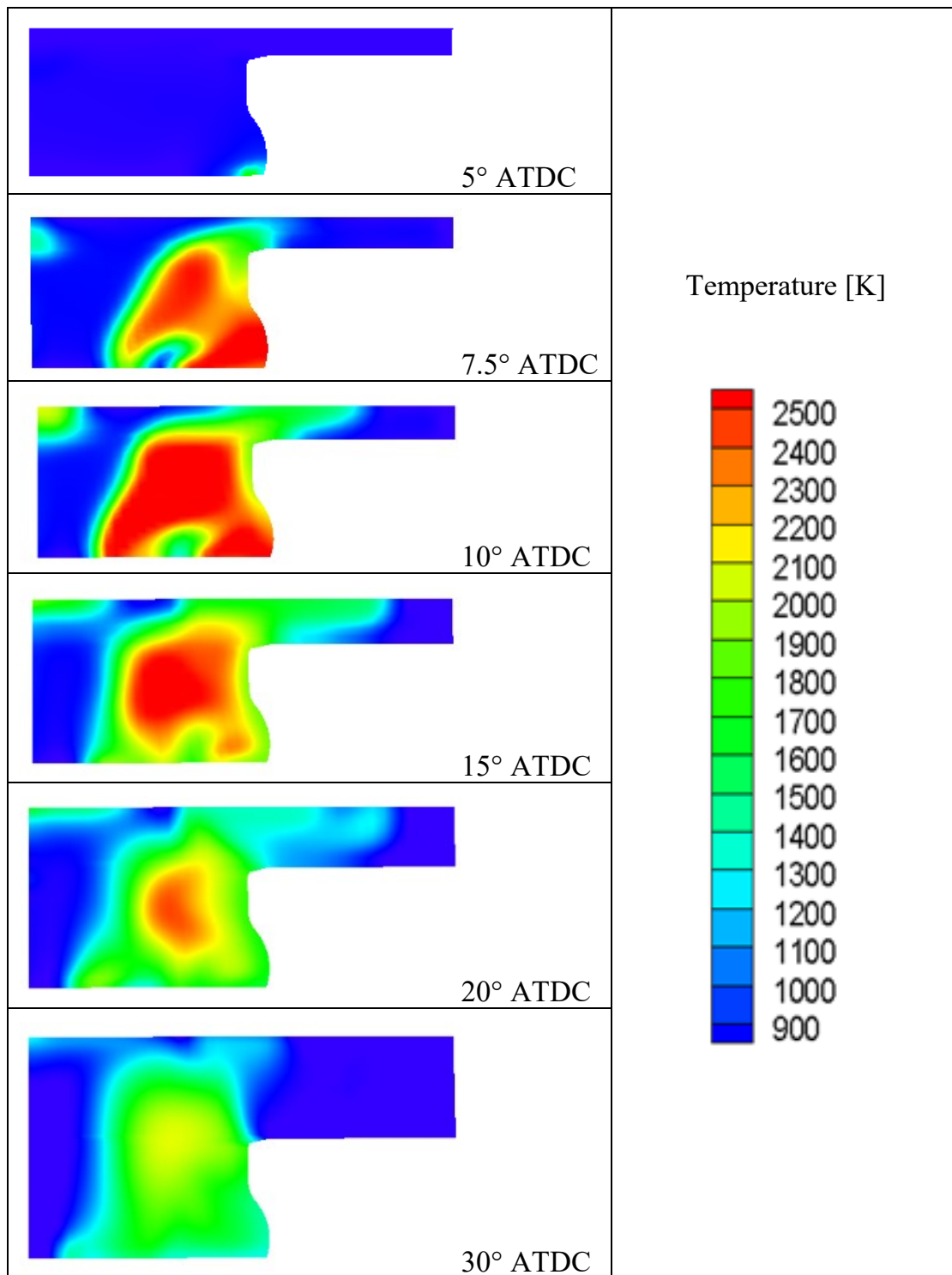


Fig. 7.9: In-bowl temperature distribution in a meridional plane at different crank angle degrees.

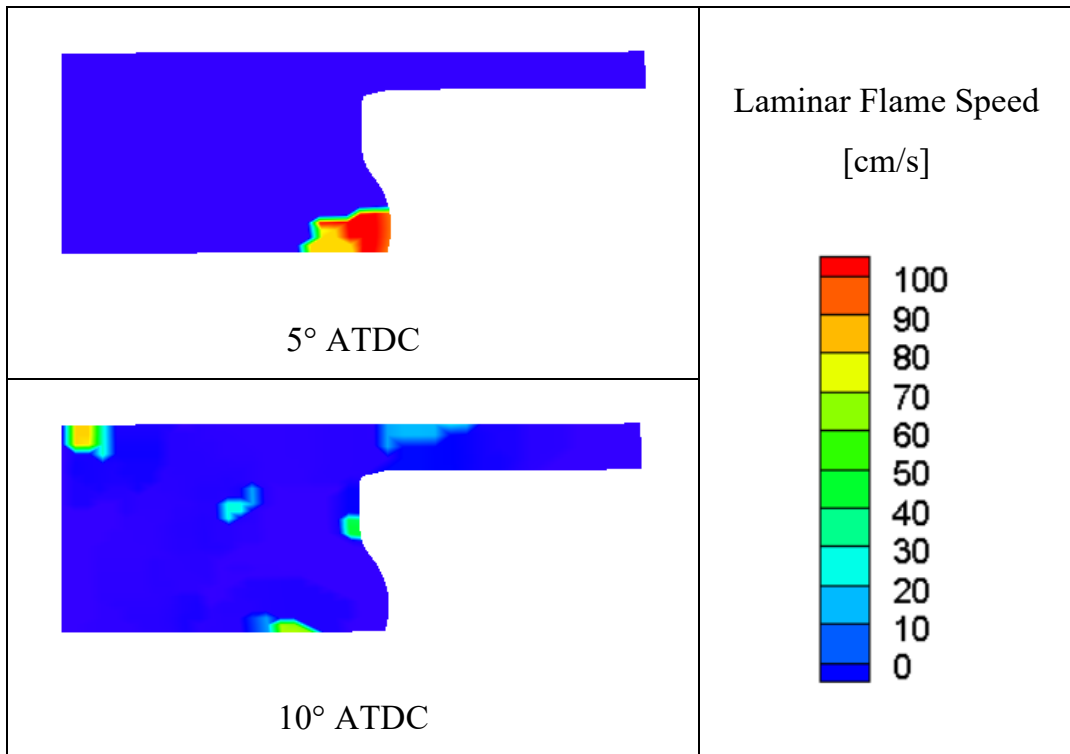


Fig. 7.10: Laminar flame speed contours at different crank angle degrees.

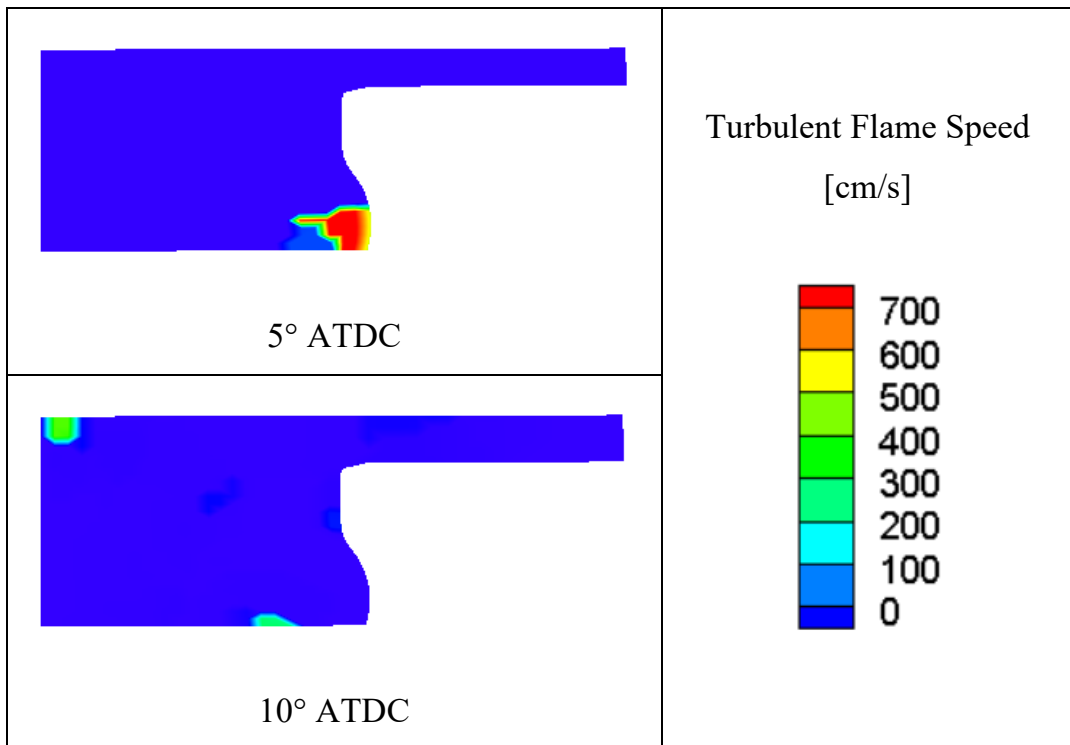


Fig. 7.11: Turbulent flame speed contours at different crank angle degrees.

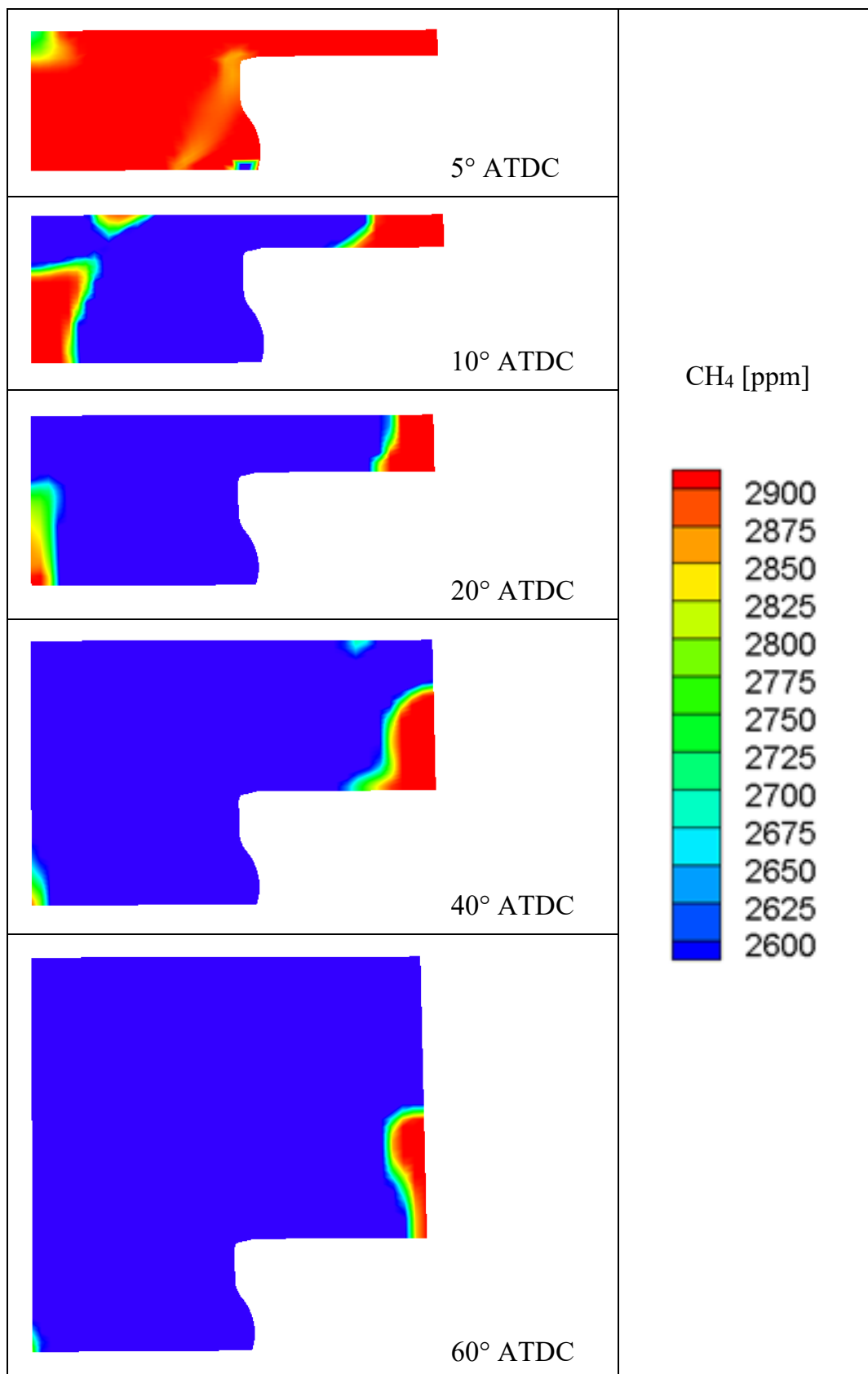


Fig. 7.12: Methane mass fraction contours at different crank angle degrees.

In conclusion, this final numerical set up provides a more comprehensive overview of the real phenomena affecting the dual fuel combustion in the research engine:

- The effect of the mass flow through the devices is correctly detected, in terms of actual in-cylinder mass trapped and, consequently, of effective fuel/air ratio in the early phases of the combustion processes.
- Taking into account for crevices flow also allows identification of the unburned methane location, which is mainly bounded in the squish region.
- The G-equation mechanism for flame activation puts into evidence that a sort of flame propagation takes place within a limited range of crank angles; after that, a quick flame extinguishment is observed, probably due to the very poor methane-air equivalence ratio. The latter gives an additional reason for the relevant amount of unburned species in this particular test case.

Conclusions

A CFD study of Dual Fuel combustion in a diesel engine was presented in this thesis. The aim was to investigate the main phenomena that characterise the combustion development, evidencing the criticalities that arise from the addition of a second fuel that introduced new issues to face in the description of the overall oxidation problem.

Due to the availability of experimental data used as an important validation tool in a wide range of operating conditions, it was possible to implement and test reliable computational models. In particular a progressive improvement of the methodology and more detailed kinetic mechanism were utilised to better comprehend the actual combustion mechanism and pollutants formation.

Firstly, an integrated numerical methodology between a one-dimensional and a three-dimensional code is developed for the prediction of the behaviour of a light duty common rail diesel engine, by varying injection advance in full diesel and dual fuel modes. In this phase, the aim was to build three correlations for pilot and three correlations for the main injection (start, peak and end of combustion) in order to extend the range of functioning and then, to provide the boundary conditions for the cases not experimentally tested to numerical simulations.

3D calculations were performed with ANSYS-FLUENT solver and the kinetic mechanism consisting of only one reaction for the diesel vapour oxidation and three reactions for the methane oxidation. A comparison between the trends of the IMEP for the examined cases in full diesel and dual fuel mode, evidences that in FD mode the IMEP decreases significantly with a reduction of the injection advance, while in DF mode it can be considered

almost constant. For this reason, in dual fuel mode a right choice of SOP can be suggested as a function of the only reduction of the pollutants. However, the most important result, is that the CO₂ emission index in DF mode is always lower with respect to FD mode confirming that this technology can be an effective mean to reduce the carbon dioxides emissions

Secondly, based on the experimental activity carried out on an optically accessible single cylinder research engine, it was possible to visualise the phenomena that occur inside the cylinder, focusing the attention on the fundamental features of the combustion. Indeed, the experimental tests were characterised by an increasing addition of methane and a constant amount of diesel oil. In this way it was possible to analyse the effects of the methane presence on the combustion. The KIVA-3V code was used for the numerical simulations, where the Li and Williams scheme for the autoignition of methane was implemented and compared with the previously cited kinetic mechanism. Results showed a fair compliance with experimental measurement, especially for OH distributions; since this radical represents an important signal of the combustion rate intensity and location, CFD simulations have proven to be capable to reproduce the real phenomena that occur inside the cylinder. Moreover, another important achievement is attained by the good agreement between the trends of numerical and experimental NO fraction levels in the exhaust, although a slight overestimation for the former with respect to the latter.

Finally, a further improvement was obtained during the study of the heavy duty diesel engine, whose actual geometry was reproduced with the K3PREPW mesh tool. In this phase, the Li and Williams model was compared with the far more detailed kinetic mechanism presented by Ra and Reitz. Results, obtained with the ANSYS-FORTE code, evidence that the Li and Williams kinetic model allows a correct prediction of methane combustion, while the Ra and Reitz CH₄ and UHC results are in contrast with

the well-known dual fuel combustion problem represented by the relevant contents of these species in the exhaust. On the other hand, the Ra and Reitz model outcomes for CO species is in accordance with the experimental output.

In conclusion, it is possible to affirm that results showed a good agreement with experimental data, highlighting important features that characterise Dual Fuel combustion. However, much work has still to be done in order to predict the whole behaviour of the system as the latest outcomes outlined that both models evidenced limits in the assessment of pollutant emissions. Moreover, a mechanism for nitric oxides formation should be re-introduced. In this sense, the completion of this study is currently addressed to the setup of a more comprehensive mechanism based on the combined use of the Ra and Reitz and Grimech 3.0 schemes, in order to obtain the best prediction of the behaviour of both fuels. At the same time, this approach could lead to a proper evaluation of NO_x formation.

In each section of this study, it was affirmed that the equivalence ratio of natural gas was lower than the flammability limits and, consequently, the choice of the combustion model favoured the turbulence-chemistry interaction. Nevertheless, in the final part of this thesis, the use of a G-equation based model allowed identification of multiple flame nucleations from which a sort of flame propagation takes place.

Once reached a comprehensive assessment of all dual fuel based phenomena, future works should be oriented at utilise more eco-friendly fuels such as syngas or biogas.

Acknowledgments

The simulations presented in this thesis have been achieved thanks to a licensed version of the software ANSYS-FLUENT, FORTE and CHEMKIN.

References

- [1] <http://www.isprambiente.gov.it/files2018/area-stampa/comunicati-stampa/graficiemissioni.pdf>
- [2] https://en.wikipedia.org/wiki/Diesel_engine
- [3] Heywood John B. – Internal Combustion Engine Fundamentals
- [4] Migliaccio, M., Della Volpe, R., 1995, Motori a combustione interna per autotrazione.
- [5] Ferrari, G., Motori a combustione Interna, Il Capitello
- [6] https://en.wikipedia.org/wiki/Common_rail
- [7] https://en.wikipedia.org/wiki/Diesel_particulate_filter
- [8] https://en.wikipedia.org/wiki/European_emission_standards
- [9] <https://www.theguardian.com/cities/2017/apr/13/death-of-diesel-wonder-fuel-new-asbestos>
- [10] https://en.wikipedia.org/wiki/Diesel_emissions_scandal
- [11] <https://www.eea.europa.eu/highlights/no-improvements-on-average-co2>
- [12] <https://www.statista.com/statistics/425324/eu-car-sales-share-of-diesel-engines-by-country/>
- [13] <https://www.roadtraffic-technology.com/features/european-countries-banning-fossil-fuel-cars/>
- [14] Murugesu Pandian, M., Anand, K., “Comparison of different low temperature combustion strategies in a light duty air cooled diesel engine”, Applied Thermal Engineering 142, 2018, 380-390, <https://doi.org/10.1016/j.applthermaleng.2018.07.047>.
- [15] <https://www.cummins.com/engines/drilling/dual-fuel-engines-drilling>
- [16] Lozza, G., 2006, Turbine a Gas e Cicli Combinati, Bologna, ed. Progetto Leonardo.
- [17] https://en.wikipedia.org/wiki/Diesel_fuel

- [18] https://en.wikipedia.org/wiki/Natural_gas
- [19] <https://www.slideshare.net/ahmedshoman792/natural-gas-dehydration>
- [20] Frerichs, J. and Eilts, P., “Development of a Physically/Chemically Based Approach for 2-Stage Ignition Delay Calculation in Medium Speed Dual-Fuel Engines,” SAE Technical Paper 2019-24-0068, 2019, doi:10.4271/2019-24-0068.
- [21] Ahmed, S.A., Zhou, S., Zhu, Y., Feng, Y., “Performance and Emission Characteristics Analysis of Dual Fuel Compression Ignition Engine Using Natural Gas and Diesel” International Journal of Thermodynamics (IJoT) Vol. 21 (No. 1), pp. 16-25, 2018, doi: 10.5541/ijot.316300.
- [22] Kozarac, D., Bozic, M., Vucetic, A., Krajnovic, J. et al., “Experimental and Numerical Analysis of a Dual Fuel Operation of Turbocharged Engine at Mid-High Load,” SAE Technical Paper 2019-24-0122, 2019, doi:10.4271/2019-24-0122.
- [23] Eder, L., Ban, M., Pirker, G., Vujanovic, M., Priesching, P., and Wimmer, A., Development and Validation of 3D-CFD Injection and Combustion Models for Dual Fuel Combustion in Diesel Ignited Large Gas Engines, *Energies* 2018, 11, 643; doi: 10.3390/en1130643.
- [24] Merts, M. and Verhelst, S., “Literature Review on Dual-Fuel Combustion Modelling,” SAE Technical Paper 2019-24-0120, 2019, doi:10.4271/2019-24-0120.
- [25] Akbarian, E., Najafi, B., Jafari, M., Ardabili, S.F., Shamshirband, S., Chau, K., (2018) “Experimental and computational fluid dynamics-based numerical simulation of using natural gas in a dual-fueled diesel engine”, *Engineering Applications of Computational Fluid Mechanics*, 12:1, 517-534, DOI:10.1080/19942060.2018.1472670.
- [26] Huang, H., Zhu, Z., Chen, Y., Chen, Y., Lv, D., Zhu, J., Ouyang, T., “Experimental and numerical study of multiple injection effects on combustion and emission characteristics of natural gas–diesel dual-fuel engine”, *Energy Conversion and Management* 183 (2019) 84-96, doi: 10.1016/j.enconman.2018.12.110.
- [27] Shu, J., Fu, J., Liu, J., Ma, Y., Wang, S., Deng, B., Zeng, D., “Effects of injector spray angle on combustion and emissions characteristics of a natural

gas (NG)-diesel dual fuel engine based on CFD coupled with reduced chemical kinetic model”, *Applied Energy* 233-234 (2019) 182-195, doi: 10.1016/j.apenergy.2018.10.040.

[28] Zhou, H., Li, X., Lee, C.F., “Investigation on soot emissions from diesel-CNG dual-fuel”, *International Journal of Hydrogen Energy*, <https://doi.org/10.1016/j.ijhydene.2019.02.012>.

[29] Papagiannakis, R.G, Rakopoulos, D.C., C.D., “Evaluation of the Air Oxygen Enrichment Effects on Combustion and Emissions of Natural Gas/Diesel Dual-Fuel Engines at Various Loads and Pilot Fuel Quantities”, *Energies* 2018, 11, 3028; doi:10.3390/en11113028.

[30] Ghazal, O.H., “Air Pollution Reduction and Environment Protection Using Methane Fuel for Turbocharged CI Engines”, *Journal of Ecological Engineering*, Volume 19, Issue 5, September 2018, pages 52-58, doi: 10.12911/22998993/91276.

[31] Sremec, M., Taritaš, I., Sjerić, M., Kozarac, D., “Numerical Investigation of Injection Timing Influence on Fuel Slip and Influence of Compression Ratio on Knock Occurrence in Conventional Dual Fuel Engine”, *J. sustain. dev. energy water environ. syst.*, 5(4), pp 518-532, 2017, doi: 10.13044/j.sdewes.d5.0163.

[32] Tulwin, T., and Sochaczewski, R., “The dual-fuel CFD combustion model with direct and indirect CNG injection”, *ITM Web Conferences* 15, 07016 (2017) doi: 10.1051/itmconf/20171507016.

[33] Zoldak, P., Sobiesiak, A., Wickman, D., and Bergin, M., "Combustion Simulation of Dual Fuel CNG Engine Using Direct Injection of Natural Gas and Diesel," *SAE Int. J. Engines* 8(2):2015, doi:10.4271/2015-01-0851.

[34] Majczak, A., Baranski, G., Siadkowska, K., Sochaczewski, R., “cng injector research for dual fuel engine”, *Advances in Science and Technology Research Journal*, Volume 11, Iss. 1, 2017, pages 212-219, DOI: 10.12913/22998624/68458.

[35] Stettler, M.E.J., Midgley, W.J.B., Swanson, J.J., Cebon, D., Boies, A.M., “Greenhouse Gas and Noxious Emissions from Dual Fuel Diesel and Natural Gas Heavy Goods Vehicles”, *Environ. Sci. Technol.* 2016, 50, 2018-2026.

- [36] Mousavi, S.M., Saray, R.K., Poorghasemi, K., Maghbouli, “A numerical investigation on combustion and emission characteristics of a dual fuel engine at part load condition”, *Fuel* 166 (2016) 309-319, doi: 10.1016/j.fuel.2015.10.052.
- [37] Talekar, A., Lai, M.-C., Tomita, E., Kawahara, N. et al., “Numerical Investigation of Natural Gas-Diesel Dual Fuel Engine with End Gas Ignition”, SAE Technical Paper 2018-01-0199, 2018, doi:10.4271/2018-01-0199.
- [38] Barro, C., Nani, C., Hutter, R., and Boulouchos, K., "Spray Model Based Phenomenological Combustion Description and Experimental Validation for a Dual Fuel Engine", SAE Technical Paper 2017-24-0098, 2017, doi:10.4271/2017-24-0098.
- [39] Li, Y., Guo, H., and Li, H., "Evaluation of Kinetics Process in CFD Model and Its Application in Ignition Process Analysis of a Natural Gas-Diesel Dual Fuel Engine", SAE Technical Paper 2017-01-0554, 2017, doi:10.4271/2017-01-0554.
- [40] Kusaka, J., Tsuzuki, K., Daisho, Y., Saito, T., “A Numerical Study on Combustion and Exhaust Gas Emissions Characteristics of a Dual Fuel Natural Gas Engine Using a Multi-Dimensional Model Combined With Detailed Kinetics” SAE Technical Paper 2002-01-1750.
- [41] Cantore, G., Mattarelli, E., Rinaldini C.A. Savioli, T., Scignoli, F. “Numerical Optimization of the Injection Strategy on a Light Duty Diesel Engine Operating in Dual Fuel (CNG/Diesel) Mode”, *International Journal of Heat and Technology*, Vol. 37, No. 3, 2019, pp 682-688, <https://doi.org/10.18280/ijht.370303>.
- [42] Maghbouli, A., Saray, R.K., Shafee, S., Ghafouri, J., “Numerical study of combustion and emission characteristics of dual-fuel engines using 3D-CFD models coupled with chemical kinetics”, *Fuel* 106 (2013) 98-105, doi: 10.1016/j.fuel.2012.10.055.
- [43] Huang, H., Lv, D., Zhu, J., Zhu, Z., Chen, Y., Pan, Y., Pan, M., “Development of a new reduced diesel/natural gas mechanism for dual-fuel engine combustion and emission prediction”, *Fuel* 263 (2019) 30-42, doi: 10.1016/j.fuel.2018.08.161.

- [44] Kahila, H., Wehrfritz, A., Kaario, O., Vourinen, V., "Large-Eddy simulation of dual-fuel ignition: Diesel spray injection into a lean methane-air mixture", *Combustion and Flame* 199 (2019) 131-151, doi: 10.1016/j.combustflame.2018.10.014.
- [45] De Simio, L., Gambino, M., and Iannaccone, S., "Effects of Low Temperature Combustion on Particle and Gaseous Emission of a Dual Fuel Light Duty Engine," SAE Technical Paper 2017-24-0081, 2017, doi:10.4271/2017-24-0081.
- [46] Catapano, F., Di Iorio, S., Sementa, P., and Vaglieco, B., "Particle Formation and Emissions in an Optical Small Displacement SI Engine Dual Fueled with CNG DI and Gasoline PFI," SAE Technical Paper 2017-24-0092, 2017, doi:10.4271/2017-24-0092.
- [47] Vipavanich, C., Chuepeng, S., Skullog, S., "Heat release analysis and thermal efficiency of a single cylinder diesel dual fuel engine with gasoline port injection", *Case Studies in Thermal Engineering* 12, 2018, 143-148, <https://doi.org/10.1016/j.csite.2018.04.011>.
- [48] Zang R., Yao C., Yin Z., et al. (2016). "Mechanistic Study of Ignition Characteristics of Diesel/Methanol and Diesel/Methane. Dual Fuel Engine". *Energy & Fuels*, Volume 30, Issue 10, pag. 8630-8637.
- [49] Pedrozo, V.B., May, I., Dalla Nora, M., Cairns, A., Zhao, H., "Experimental analysis of ethanol dual-fuel combustion in a heavy-duty diesel engine: An optimisation at low load", *Applied Energy* 165, 2016, 166-182, <http://dx.doi.org/10.1016/j.apenergy.2015.12.052>.
- [50] Pedrozo, V., May, I., and Zhao, H., "Characterization of Low Load Ethanol Dual-Fuel Combustion using Single and Split Diesel Injections on a Heavy-Duty Engine," SAE Technical Paper 2016-01-0778, 2016, doi:10.4271/2016-01-0778.
- [51] Pedrozo, V.B., May, I., Lanzasova, T.D.M., Zhao, H., "Potential of internal EGR and throttled operation for low load extension of ethanol–diesel dual-fuel reactivity controlled compression ignition combustion on a heavy-duty engine", *Fuel* 179, 2016, 391-405, <http://dx.doi.org/10.1016/j.fuel.2016.03.090>.

- [52] Pedrozo, V.B., May, I., Zhao, H., “Exploring the mid-load potential of ethanol-diesel dual-fuel combustion with and without EGR”, *Applied Energy* 193, 2017, 263-275, <http://dx.doi.org/10.1016/j.apenergy.2017.02.043>.
- [53] Karagoz, Y., Guler I., Sandalci T. et al. “Effects of hydrogen and methane addition on combustion characteristics, emissions, and performance of a CI engine”. *International Journal of Hydrogen Energy*, 2016, Volume 41, Issue 2, pag. 1313-1325.
- [54] Alrazen H.A.; Abu Talib A.R.; Ahmad K.A., “A two-component CFD studies of the effects of H-2, CNG, and diesel blend on combustion characteristics and emissions of a diesel engine”. *International Journal of Hydrogen Energy*, 2016, Volume 41, Issue 24, pag. 10483-10495.
- [55] Stylianidis, N., Azimov, U., Kawahara, N., and Tomita, E., "Chemical Kinetics and Computational Fluid-Dynamics Analysis of H₂/CO/CO₂/CH₄ Syngas Combustion and NO_x Formation in a Micro-Pilot-Ignited Supercharged Dual Fuel Engine," SAE Technical Paper 2017-24-0027, 2017, doi:10.4271/2017-24-0027.
- [56] Meng, X., Tian, H., Long, W., Zhou, Y., Bi, M., Tian, J, Lee, C.F., “Experimental study of using additive in the pilot fuel on the performance and emission trade-offs in the diesel/CNG (methane emulated) dual-fuel combustion mode”, *Applied Thermal Engineering* 157, 2019, 113718, <https://doi.org/10.1016/j.applthermaleng.2019.113718>
- [57] Abagnale, C., Cameretti, M.C., De Simio, L., Iannaccone, S., Tuccillo, R., “Experimental and Numerical Study of a Diesel Engine Operating in Dual Fuel Mode”, *Proceeding 67° Congresso ATI* 2012.
- [58] Abagnale, C., Cameretti, M.C., De Simio, L., Gambino, M., Iannaccone, S., Tuccillo, R., “Numerical simulation and experimental test of dual fuel operated diesel engines”, *Applied Thermal Engineering* 65 (2014) 403-417, doi: 10.1016/j.applthermaleng.2014.01.040.
- [59] Abagnale, C., Cameretti, M.C., De Simio, L., Gambino, M., Iannaccone, S., Tuccillo, R., “Combined numerical-experimental study of dual fuel diesel engine”, *Energy Procedia* 45 (2014) 721-730, doi: 10.1016/j.egypro.2014.01.077.
- [60] Abagnale, C., Cameretti, M., Ciaravola, U., Tuccillo, R. et al., "Dual Fuel Diesel Engine at Variable Operating Conditions: A Numerical and

Experimental Study", SAE Technical Paper 2015-24-2411, 2015, doi:10.4271/2015-24-2411.

[61] M.C. Cameretti, U. Ciaravola, R. Tuccillo, L. De Simio, S. Iannaccone, "A numerical and experimental study of dualfuel diesel engine for different injection timings", Applied Thermal Engineering (2016), doi: 10.1016/j.applthermaleng.2015.12.071.

[62] https://en.wikipedia.org/wiki/Computational_fluid_dynamics

[63] <http://sustainabilityworkshop.autodesk.com/products/metrics-and-basics-fluid-flow>

[64] Ansys Fluent, 2009, Theory Guide.

[65] https://en.wikipedia.org/wiki/Numerical_analysis

[66] ANSYS, "Introduction to ANSYS CFD Professional".

[67] <https://www.comsol.com/multiphysics/mesh-refinement>

[68] <http://sageography.myschoolstuff.co.za/wiki/grade-12-caps/geomorphology/drainage-systems-in-south-africa/discharge-of-a-river/>.

[69] <https://user-images.githubusercontent.com/193367/38030812-f6c4f174-3299-11e8-91ed-30684ceae715.png>

[70] Magnussen, B.F. and Hjertager, B.H., 1977, On Mathematical Modeling of Turbulent Combustion with Special Emphasis on Soot Formation, 16th. Symposium on Combustion, The Combustion Institute, Pittsburgh.

[71] Course notes "Thermofluid-dynamics", Bozza, F., University of Naples.

[72] Ansys Forte, 2016, Theory Manual.

[73] Metghalchi, M., Keck, J. C., "Burning Velocities of Methanol, Ethanol and iso-Octane-Air Mixtures", 19th Symposium (International) on Combustion/ The Combustion Institute, p. 275, 1983.

[74] Gülder, O., "L. Correlations of laminar combustion data for alternative S.I. engine fuels", SAE paper 841000, 1984.

[75] Cameretti, M.C., and Tuccillo R., "Flowand Atomization Models for C.R. Diesel Engine CFD Simulation," Proceedings of ASME/IEEE 2007 Joint Rail Conference and Internal Combustion Engine Division Spring

Technical Conference. vol. ASME paper JRCICE2007-40068, p. 451-461, ISBN: 0791837955, Pueblo, Colorado, USA, March 2007, doi: 10.1115/JRC/ICE2007-40068.

[76] O'Rourke P.J., Amsden, 1987, A.A, The TAB Method for Numerical Calculation of Spray Droplet Break up, SAE paper 872089.

[77] Reitz R.D., Diwakar R., 1987, Structure of High-Pressure Fuel Sprays, SAE paper 870598.

[78] Reitz R.D, 1987, Modelling Atomisation Processes in High-Pressure Vaporising Sprays, *Atomisation and Sprays Tech.*, vol.3, pp. 309-337.

[79] Patterson, M.A., Kong, S.C, Hampson, G.J, Reitz, R.D.,:1994, "Modelling the Effect of Fuel Injection Characteristics on Diesel Engine Soot and NOx Emissions", SAE paper 940523.

[80] Belardini, P., Bertoli, C., Cameretti, M.C., 1998, "Numerical Analysis on the Influence of Jets Break-up Model Formulation on Diesel Engines Combustion Computations", in *ATOMIZATION AND SPRAYS*, vol.8, pp123-154, april 1998.

[81] Abagnale C., Cameretti M.C., De Robbio R., Tuccillo R, 2016, "CFD Study of a MGT Combustor supplied with Syngas", *Energy Procedia*, ed Elsevier, doi: 10.1016/j.egypro.2016.11.118.

[82] Abagnale C., Cameretti M.C., De Robbio R., Tuccillo R, 2017, "Thermal cycle and combustion analysis of a solar-assisted micro gas turbine", *ENERGIES*, vol. 10, ISSN: 1996-1073, doi: 10.3390/en10060773.

[83] Cameretti, M.C., De Robbio, R., Tuccillo, R., 2017, "CFD study of a micro - Combustor under variable operating conditions" *Proceedings of the ASME Turbo Expo*, 2017 DOI: 10.1115/GT2017-63661.

[84] De Robbio, R., 2017, "Innovative Combustion Analysis of a Micro-Gas Turbine Burner Supplied with Hydrogen-Natural Gas Mixtures". *ENERGY PROCEDIA*, vol. 126, p.858-866, doi: 10.1016/j.egypro.2017.08.295.

[85] Capstone Turbine Corporation, 2009, Technical Reference, Capstone MicroTurbine Fuel Requirements, Document No. 410002, California.

[86] Chen, J., Mitchell, M.G., Nourse, J.G., 2010, "Development of Ultra-Low Emission Diesel Fuel-Fired Microturbine Engines for Vehicular Heavy

Duty Applications: Combustion Modifications”, Paper GT2010-23181, ASME Turbo Expo, Glasgow, UK.

[87] Novosselov ,I. V., Malte, P. C., 2007, ”Development and Application of an Eight-Step Global Mechanism for CFD and CRN Simulations of Lean-Premixed Combustors”, ASME paper GT2007-27990.

[88] Jachimowski C. J., “An Analytical Study of Hydrogen-Air Reaction Mechanism with Application to Scramjet Combustion”, NASA-TP-2791, 1988.

[89] Zel’dovich, Y.B., Sadovnikov, P.Y., Frank-Kamenetskik, D.A., 1947, Oxidation of Nitrogen in Combustion, Academy of Science of SR, Institute of Chemical Physics, Moscow- Leningrad.

[90] Nicol, G.D., Malte, P.C., Hamer, A.J, Roby, R.J., and Steele, R.C., 1998, A Five-Step Global Methane Oxidation – NO Formation Mechanism for Lean Premixed Gas Turbine Combustion, ASME paper 98-GT-185.

[91] Stringer, F.W., Clarke A., E., and Clarke, J.S., 1970, The Spontaneous Ignition of Hydrocarbon Fuels in a Flowing System, proc. Instn Mech. Engrs, vol. 184, pt. 3J, 1969-1970.

[92] Spadaccini, L.J. , and TeVelde, L.J., 1982, Autoignition Characteristics of Aircraft Type Fuels, Comb. & Flame, 46:283-300.

[93] Li, S.C. and Williams, F.A, 2000, Reaction Mechanism for Methane Ignition, ASME paper no. 2000-GT-145

[94] Cameretti, M.C., De Robbio, R., and Tuccillo, R., "Performance Improvement and Emission Control of a Dual Fuel Operated Diesel Engine", SAE Technical Paper 2017-24-0066, 2017, doi:10.4271/2017-24-0066.

[95] Magno, A., Mancaruso, E., and Vaglieco, B., "Combustion Analysis of Dual Fuel Operation in Single Cylinder Research Engine Fuelled with Methane and Diesel," SAE Technical Paper 2015-24-2461, 2015, doi:10.4271/2015-24-2461.

[96] Mancaruso, E., Sequino, L., Vaglieco, B. M., Cameretti, M.C. et al., “CFD Analysis of the Combustion Process in Dual- Fuel Diesel Engine,” SAE Technical Paper 2018-01-0257, 2018, doi:10.4271/2018-01-0257.

- [97] Cameretti, M.C., De Robbio, R., and Tuccillo, R., "Ignition and Combustion Modelling in a Dual Fuel Diesel Engine". Accepted on the Journal Propulsion and Power Research.
- [98] Gaydon, A.G., "*The Spectroscopy of Flames*," (London, Chapman and Hall, 1957).
- [99] Assanis, D.F., Filipi, Z.S., Fiveland, S.B., and Syrimis, M., "A Predictive Ignition Delay Correlation Under Steady- State and Transient Operation of a Direct Injection Diesel Engine," *ASME* 125:450, 2003, doi:10.1115/1.1563238.
- [100] S.C. Li, F.A. Williams, Reaction Mechanism for Methane Ignition, *Journal of Engineering for Gas Turbines and Power*, Vol. 124, pag. 471-480, 2002, doi: 10.1115/1.1377871.
- [101] Cameretti, M.C., De Robbio, R., Tuccillo, R., Pedrozo, V. et al., Integrated CFD-Experimental Methodology for the Study of a Dual Fuel Heavy Duty Diesel Engine," SAE Technical Paper 2019-24-0093, 2019, doi:10.4271/2019-24-0093.
- [102] May, I., "An Experimental Investigation Of Lean-Burn Dual-Fuel Combustion in a Heavy Duty Diesel Engine", PhD Thesis.
- [103] Wang, H., Ra, Y., Jia, M., and Reitz, R. D., "Development of a Reduced N-Dodecane-PAH Mechanism and its Application for N-Dodecane Soot Predictions," *Fuel* 136:25-36, 2014, doi:10.1016/j.fuel.2014.07.028.
- [104] Namazian, M., Heywood, J. B., "Flow in the Piston-Cylinder-Ring Crevices of a Spark-Ignition Engine: Effect on the Hydrocarbon Emissions, Efficiency and Power".
- [105] Amirante, R., Distaso, E., Tamburano, P., Reitz, R.D., "Laminar flame speed correlations for methane, ethane, propane and their mixtures, and natural gas and gasoline for spark-ignition engine simulations", *International Journal of Engine Research* 2017, Vol. 18(9) 951-970, DOI: 10.1177/1468087417720018.

Appendix

!=====

ch3+h(+M)=ch4(+M) 2.14E15 -0.4 0.0E0
h2/2.0/
h2o/5.0/
co/2.0/
co2/3.0/
LOW/3.31E30 -4.0E0 2.10803E3/
TROE/0.0E0 1.0E-15 1.0E-15 4.0E1/
ch4+h=ch3+h2 1.727E4 3.0 8.22395E3
REV/6.61E2 3.0E0 7.74402E3/
ch4+oh=ch3+h2o 1.93E5 2.4 2.10612E3
REV/4.82E2 2.9E0 1.485994E4/
ch4+o=ch3+oh 2.13E6 2.21 6.47992E3
REV/3.557E4 2.21E0 3.91993E3/
ch3+ho2=ch4+o2 7.2E12 0.0 0.0E0
ch4+ho2=ch3+h2o2 3.42E11 0.0 1.928991E4
ch3+ho2=ch3o+oh 2.2E13 0.0 0.0E0
ch3+oh=ch2o+h2 2.25E13 0.0 4.29995E3
ch3+o=ch2o+h 8.0E13 0.0 0.0E0
ch3+o2=ch3o+o 1.995E18 -1.57 2.921009E4
ch2+h+M=ch3+M 2.107E11 1.0 -1.961998E4
REV/1.968E16 0.0E0 9.252008E4/
ch3+oh=ch2+h2o 3.0E6 2.0 2.5E3
ch3+o2=ch2o+oh 7.47E11 0.0 1.425E4
!-----